5-2016

Magnetic Local Positioning System with Supplemental Magnetometer-Accelerometer Data Fusion

Benjamin Scott Prothro
The University of Tennessee, Knoxville, bprothro@vols.utk.edu

To the Graduate Council:

I am submitting herewith a dissertation written by Benjamin Scott Prothro entitled "Magnetic Local Positioning System with Supplemental Magnetometer-Accelerometer Data Fusion." I have examined the final electronic copy of this dissertation for form and content and recommend that it be accepted in partial fulfillment of the requirements for the degree of Doctor of Philosophy, with a major in Electrical Engineering.

Benjamin J. Blalock, Major Professor

We have read this dissertation and recommend its acceptance:

Syed K. Islam, Charles L. Britton Jr., Vasilios Alexiades

Accepted for the Council:

Carolyn R. Hodges

Vice Provost and Dean of the Graduate School

(Original signatures are on file with official student records.)

Magnetic Local Positioning System with Supplemental Magnetometer-Accelerometer Data Fusion

A Dissertation Presented for the

Doctor of Philosophy

Degree

The University of Tennessee, Knoxville

Benjamin Scott Prothro

May 2016

To my wife...

Acknowledgments

I would like to thank all those who have supported and encouraged me during the course of this project. To my wife: There are no words...Thank you. To Dr. Blalock, whose devotion and self-sacrifice toward his students is superhuman: Thank you. To my committee—Dr. Islam, Dr. Britton, and Dr. Alexiades—for their advice and generosity: Thank you. To Jim Rochelle and Tum Sangsingkeow, without whose patience, support, and advice this project would not have been possible: Thank you. And lastly, to my little survey helpers, Abby and Maddie, who are growing up way too fast: Thank you.

Beauty will save the world

—Fyodor Dostoyevsky, *The Idiot*

Abstract

Geo-location and tracking technology, once confined to the industrial and military sectors, have been widely proliferated to the consumer world since early in the twenty-first century. The commoditization of Global Positioning System (GPS) and inertial measurement integrated circuits has made this possible, with devices small enough to fit in a cellular phone. However, GPS technology is not without its drawbacks: Its power use is high, and it can fail in smaller, obstructed spaces. Magnetic positioning, which exploits the magnetic field coupling between a set of transmitter beacon coils and a set of receiver coils, is an often overlooked, complementary technology that does not suffer from these problems.

Magnetic positioning is strong where GPS is weak; however, it has some weaknesses of its own. Namely, it is subject to distortions due to metal objects in its immediate vicinity. In much of the prior art, these distortions are ignored or either statically measured and then corrected.

This work presents a novel technique to dynamically correct for distorted fields. Specifically, a tri-axial magnetometer and a tri-axial accelerometer are integrated with the magnetic positioning system using a complementary Kalman filter. The end result resembles a tightly-coupled integrated GPS/inertial navigation system.

The results achieved by this integrated magnetic positioning system prove the viability of the approach. The results are demonstrated in a real-world environment, where both strong, localized distortions and spatially broad distortions are corrected.

In addition to the integrated magnetic position system, this work presents a novel scheme for calibrating the magnetic receiver; this technique is termed *application domain calibration*. In many real-world situations, low-level measurement and calibration will not be possible; therefore, this new technique uses the same set of demodulated and down-mixed data that is used by the magnetic positioning algorithms.

Table of Contents

List of Tables

List of Figures

Nomenclature

$\angle x$	The phase of x ($x \in \mathbb{C}$)
x^*	The conjugate of x
$\mathbf{X}^H$	The conjugate transpose of $\mathbf{X}$
$\mathbf{X}^T$	The transpose of $\mathbf{X}$
`Lorem Ipsum`	Software code snippet or software function name
MA	Magnetometer-accelerometer measurement unit
SPD	Symmetric Positive Definite
Beacon	The magnetic transmitter device
GPS	Global positioning system
IMU	Inertial measurement unit
INS	Inertial navigation system
KF	Kalman filter
MANS	Magnetometer-accelerometer navigation system
MARG	Magnetometer-accelerometer-rate-gyroscope
NA	Not applicable

Natural Basis	The orthonormal $\mathbb{R}^3$ basis aligned with the axes of a tri-axial sensor
RMS	Root mean square
SD	Secure digital
SPKF	Sigma-Point Kalman filter
UKF	Unscented Kalman filter

Chapter 1

Introduction

1.1 Motivation

The last decade or so has seen incredible growth of small-form-factor navigation and geo-location technology. What once was found only in the cockpit or on a ship's bridge can now be found in nearly every cellular phone. In fact, a complete satellite navigation system and an inertial navigation system (INS) can be contained in three small integrated circuits which take up less than an inch of circuit board space. These systems almost always consist of a global positioning system (GPS) receiver and an inertial measurement unit (IMU). Products span the commercial, industrial, consumer, and public sector with applications nearly endless in scope.

However, GPS based systems suffer from some major shortcomings that limit their use in many situations. Their limitations include the following:

- They have relatively slow update rates–one update per second is common.
- Satellite signals are subject to frequent drop-out–especially in areas without a clear view of the sky.
- GPS receivers consume relatively large amounts of power.

- Accuracy is on the order of a meter or larger without specialized hardware or processing.

These limitations are irrelevant for the applications for which GPS is envisioned, such as large scale navigation, but for small scale applications where rapid updates and high precision are required, GPS based systems prove insufficient. This is even more pronounced where the receiver is forced to operate indoors or to operate for long periods of time with a small battery.

Clearly, GPS is not an optimal solution in these situations; so, many other positioning techniques have been proposed. Liu et al. in [1] presents several alternatives; however, the majority of these approaches suffer weaknesses similar to GPS or introduce their own complications.

A positioning technique not included by Liu is the basis for this research project. It is first introduced by Jack Kuipers in [2] and then vastly improved by Frederick Raab in [3]. A very accessible presentation is given in textbook form in [4]. For the purposes of this document, this system will be referred to as a *magnetic positioning* system. It consists of a tri-axial magnetic coil transmitter (or beacon) and a tri-axial magnetic coil receiver. The coils in the transmitter are oriented orthogonally and each transmits a different signal creating three magnetic dipoles. The coils in the receiver are also oriented orthogonally, and the receiver is able to separate the received signals based on which transmitter coil generated them. Then, from the known radiation pattern of the transmitter dipoles, the position and orientation (collectively referred to as the *pose*) of the receiver can be determined relative to the transmitter.

This type of system has some advantages over a GPS based system. For one, because of the passive nature of the receiver coils, the system can be very low power. Also, the magnetic signals penetrate most common objects, and therefore, the system is not subject to dropout. Furthermore, the update rate can be relatively high, and sub-foot accuracies are possible.

1.2 Approach

Despite the advantages of a magnetic positioning system over a GPS based system, there is one paramount difficulty: magnetic distortions. These distortions are induced by the signals leaving the transmitter.

The receiver of the system is able to resolve a 3-D vector of each of the three transmitted fields. In other words, the system has nine measurements. The unknowns of the system are the position and orientation which can be represented with six quantities. Therefore, in the absence of distortion, it is possible to determine the position and orientation of the receiver. However, with distortion present, another nine unknowns are added to the system and it becomes under-determined.

In order to address this situation, other sensors, and therefore more information, are added to the system to aid in estimating position and orientation. Specifically, a tri-axial accelerometer and magnetometer are added. Collectively, these are referred to as the magnetometer-accelerometer (MA). Usually, gyroscopes are also used when attempting navigational tracking, but they are not used in this effort as will be discussed in what follows.

While the addition of the accelerometer and magnetometer introduce more information into the system, each sensor also adds more unknowns to the system. Therefore, the system remains under-determined, and something more is needed. An integrated navigation system built around a Kalman filter is designed to meet that need. The ubiquitous Kalman filter is first introduced in 1960 by R. E. Kalman [5]. To call it a filter is somewhat misleading; in fact, it is an iterative estimator. It is able to incorporate all of the past measurements of the system and thus take a system from being under-determined to being overdetermined. In addition, it provides a very elegant mechanism for fusing measurements from several different sensors.

1.3 Objective

The objective of this project is to develop a magnetic positioning and tracking system which remains robust in the presence of environmental distortion. In order to do this, the system uses two extra sensors. In addition to the typical magnetic positioning sensor, the system includes a tri-axial accelerometer and a tri-axial magnetometer. Measurements from these three sensors are fused together and result in estimates of both position and orientation of the receiver relative to the transmitter. In addition, the system also produces estimates of the errors seen by the sensors.

Before completing the above objective, it is necessary to calibrate the three receiver sensors. Therefore, a side-goal of the project is to design and develop calibration processes for the sensors.

1.4 Organization

The rest of this document gives details about the development of the magnetic positioning system. Chapter 2 describes the nature of the tracking problem in more detail. Chapter 3 examines some of the approaches to the problem found in the literature. Chapter 4 describes the prerequisite calibration procedures and algorithms. Chapter 5 looks in depth at the approach to solving the tracking problem. Chapter 6 presents the results achieved by the magnetic positioning system. And Chapter 7 presents some closing remarks.

Chapter 2

Background and Problem Description

This chapter gives an overview of magnetic positioning and describes some of the practical issues. Section 2.1 lays the foundation for approaching the problem. Section 2.2 describes the theory behind magnetic positioning without considering any non-ideal distortions or interferences. In Section 2.3, the techniques are re-examined in light of real world difficulties such as magnetic field distortions. Finally, in Section 2.4 the requirements and design objectives of the magnetic position system are summarized.

2.1 System Background

This section outlines the hardware of the system and some of the conventions that are adopted for approaching the magnetic tracking application. With regard to the hardware of the system, there are four main components: a magnetic coil transmitter, a magnetic coil receiver, a receiver accelerometer, and a receiver magnetometer. Each of these will be treated in a subsection below.

2.1.1 Magnetic Transmitter

The magnetic transmitter, or beacon, forms the backbone of the system. It is placed at the center of the tracking volume, and all positions and orientations are estimated relative to its position and orientation. In other words, it creates the frame of reference for the system. Its physical setup is fixed before the system is activated, and therefore, its orientation relative to the earth is constant. It is also assumed that this orientation is known or can be measured before the operation of the system. The orthogonal axes of the transmitter's frame of reference are denoted x, y, and z and make up a *right-forward-up* coordinate system.

Three orthogonal coils are held within the transmitter and are aligned along the transmitter's frame of reference. The coils are referred to as the x-coil, y-coil, and z-coil. This is illustrated in Figure 2.1. The three coils are close enough in space to be considered co-located. The z-coil is referred to as the vertical coil, although it is only nominally vertical. The other two coils are referred to as the horizontal coils because of their nominally horizontal orientation.

2.1.2 Magnetic Receiver

Like the transmitter, the receiver also contains three, orthogonal, co-located magnetic coils. For the purposes of this work, the axes of the receiver's frame of reference are denoted u, v, and w and make up a *right-forward-up* coordinate system. Each coil of the receiver is oriented along a corresponding axis of the receiver frame of reference. The coils are therefore referred to as the u-coil, v-coil, and w-coil. The coil setup for the receiver is illustrated in Figure 2.1. It is assumed that the direction of movement (i.e. heading) is nominally oriented more along the positive v-axis than any other axis. It is also assumed that the u-coil is nominally oriented to the right and the w-coil to the vertical. None of these assumptions are concrete, and normal operation allows for frequent deviations from this.

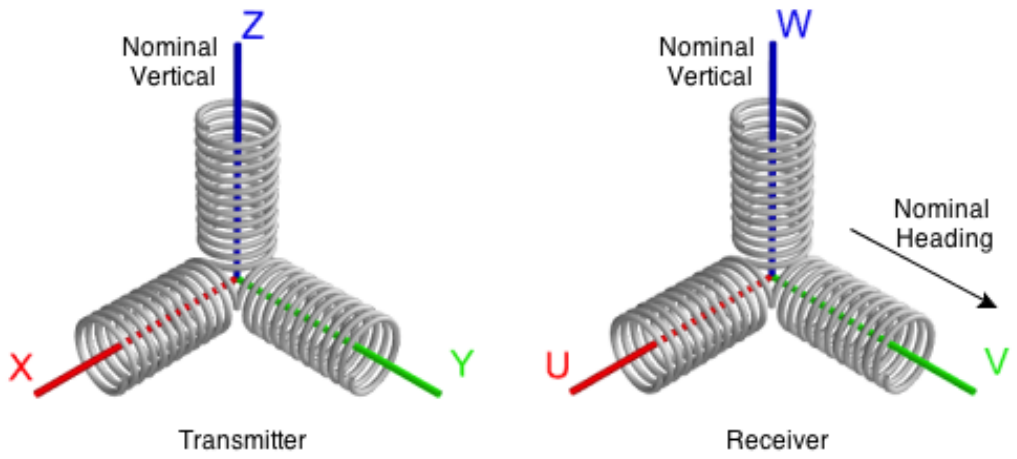

Figure 2.1: This diagram shows the orientation and labeling of the frames of reference and the coils of both the transmitter and receiver.

In addition to the coils, the receiver contains processing hardware that demodulates the received signals to base-band and records the measurements, which are complex-valued due to the time phase. This allows for off-line algorithm development during this research.

2.1.3 Magnetometer-Accelerometer

The main goal of this project is to fuse accelerometer and magnetometer measurements with magnetic location data, and so the receiver also contains an accelerometer and a magnetometer. These are referred to as the magnetometer-accelerometer (MA). For reasons explained elsewhere, no gyroscope is used, and the MA is an inexpensive one. The *ST Microelectronics LSM303DLHC* tri-axial accelerometer/magnetometer was chosen for use, and an evaluation board was fitted to the legacy receiver hardware. Its axes are aligned with those of the receiver coils. The specifications of both the accelerometer and magnetometer are somewhat configurable, but for this project they are fixed as given below:

The accelerometer specifications are as follows [6]:

- 12-bit digital output
- ±4-g full scale
- 2 mg/LSB sensitivity
- 60 mg zero-g offset
- Sample rate of 50 Hz

The magnetometer specifications are as follows [6]:

- 12-bit digital output
- ±1.3 Gauss full scale
- 2 mGauss resolution
- Sample rate of 15 Hz

2.1.4 Frames of Reference

There are three pertinent coordinate frames of reference in the magnetic tracking system: the receiver frame of reference, the transmitter frame of reference, and the earth frame of reference.

The receiver frame of reference is aligned with the receiver's primary sensor axes—u, v, and w. All the sensors on the receiver are aligned with this coordinate frame; therefore, all the measurements have this frame as their basis. Using traditional navigational language, this frame is referred to as the *body frame* [7].

The transmitter frame of reference is aligned with the three orthogonal transmitter coils—x, y, and z. Since they emanate from the transmitter, the magnetic beacon fields are native to this frame. This frame establishes the position and orientation reference for the magnetic tracking application. Using traditional navigational language, this is a *local-level* frame [7].

The earth frame of reference is an *east-north-up* right-handed coordinate frame centered at the transmitter. For simplicity in dealing with the magnetometer, this project uses magnetic north and east rather than true north and east. The "up" axis corresponds to the direction opposite the earth's gravity. The geo-magnetic field measured by the magnetometer and the gravity vector measured by the accelerometer are native to this frame, even though the measurements are made in the receiver frame. Because of this, the magnetometer and accelerometer measurements enable an estimate of the rotation between the receiver and the earth frame [8]. More will be said about this later in this document. Since this frame differs from the transmitter frame by only a rotation, it is also a local-level frame. It could be used as the position and orientation reference for the system, instead of the transmitter frame, but the analysis would be more difficult.

2.2 Magnetic Positioning in the Absence of Interference

As mentioned above, it is possible to glean position and orientation information from measurements of magnetic dipoles. This section attempts to describe how this can be done when the signals are pure and experience no interference. The magnetic transmitter and magnetic receiver are the only two components required to estimate the pose; with no interference, the accelerometer and the magnetometer are not needed.

The purpose of the transmitter coils is to establish a position reference and to generate the fields necessary for determining the pose of the receiver. Each of the transmitter coils creates a magnetic dipole. These dipoles are aligned along the x, y, and z coils of the transmitter, and they each have identical dipole moments. They

are expressed as

$$\mathbf{m}_x = m \begin{bmatrix} 1 \\ 0 \\ 0 \end{bmatrix}, \quad \mathbf{m}_y = m \begin{bmatrix} 0 \\ 1 \\ 0 \end{bmatrix}, \quad \text{and} \quad \mathbf{m}_z = m \begin{bmatrix} 0 \\ 0 \\ 1 \end{bmatrix}, \tag{2.1}$$

where $m = \|\mathbf{m}_x\| = \|\mathbf{m}_y\| = \|\mathbf{m}_z\|$.

The signal on each coil consists of a modulated, sine-wave carrier. The modulations on each coil are mutually orthogonal and unitary so that the receiver can distinguish between them. In other words,

$$\int_T a_x(t)a_y(t)dt = 0 \tag{2.2}$$

$$\int_T a_x(t)a_z(t)dt = 0 \tag{2.3}$$

$$\int_T a_y(t)a_z(t)dt = 0, \tag{2.4}$$

and

$$\int_T a_x(t)a_x(t)dt = 1 \tag{2.5}$$

$$\int_T a_y(t)a_y(t)dt = 1 \tag{2.6}$$

$$\int_T a_z(t)a_z(t)dt = 1, \tag{2.7}$$

where $a_x(t)$, $a_y(t)$, and $a_z(t)$ are the modulations applied to the x, y, and z coils, respectively; and T is the period of the modulation waveform. Figure 2.2 illustrates the signaling scheme for the transmitter, including the three modulation signals and the carrier sinusoid. (The carrier is shown as a complex exponential to ease analysis.)

The carrier frequency ($f_c = \frac{\omega_c}{2\pi}$) used for the transmitter is 27 kHz; therefore, the wavelength of the radiated field is much, much greater than the distance between the receiver and transmitter. This allows the near-field, quasi-static dipole models to be

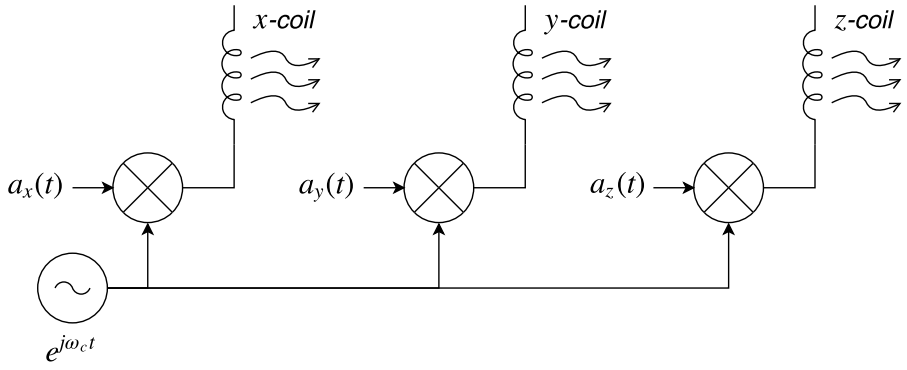

Figure 2.2: The transmitter signal path for each coil.

used. Thus, for each of the transmitter coils, the magnetic flux density at a position of $\mathbf{r} = \begin{bmatrix} x & y & z \end{bmatrix}^T$ can be modeled as

$$\mathbf{b}_x(\mathbf{r},t) = \frac{\mu_0}{4\pi r^5}\left(3\mathbf{r}(\mathbf{r}^T\mathbf{m}_x) - \mathbf{m}_x r^2\right) a_x(t)e^{j\omega_c t} \tag{2.8}$$

$$\mathbf{b}_y(\mathbf{r},t) = \frac{\mu_0}{4\pi r^5}\left(3\mathbf{r}(\mathbf{r}^T\mathbf{m}_y) - \mathbf{m}_y r^2\right) a_y(t)e^{j\omega_c t} \tag{2.9}$$

$$\mathbf{b}_z(\mathbf{r},t) = \frac{\mu_0}{4\pi r^5}\left(3\mathbf{r}(\mathbf{r}^T\mathbf{m}_z) - \mathbf{m}_z r^2\right) a_z(t)e^{j\omega_c t}, \tag{2.10}$$

where r is the magnitude of $\mathbf{r}$ and μ_0 is the permittivity of free space. Notice that these represent vector fields. A cross section of the shape of the vector field of a single coil resembles that shown in Figure 2.3.

As will be discussed below, the time dependence of (2.8)–(2.10) can be removed through mixing and demodulation. In that case, they become

$$\mathbf{b}_x(\mathbf{r}) = \frac{\mu_0}{4\pi r^5}\left(3\mathbf{r}(\mathbf{r}^T\mathbf{m}_x) - \mathbf{m}_x r^2\right) \tag{2.11}$$

$$\mathbf{b}_y(\mathbf{r}) = \frac{\mu_0}{4\pi r^5}\left(3\mathbf{r}(\mathbf{r}^T\mathbf{m}_y) - \mathbf{m}_y r^2\right) \tag{2.12}$$

$$\mathbf{b}_z(\mathbf{r}) = \frac{\mu_0}{4\pi r^5}\left(3\mathbf{r}(\mathbf{r}^T\mathbf{m}_z) - \mathbf{m}_z r^2\right), \tag{2.13}$$

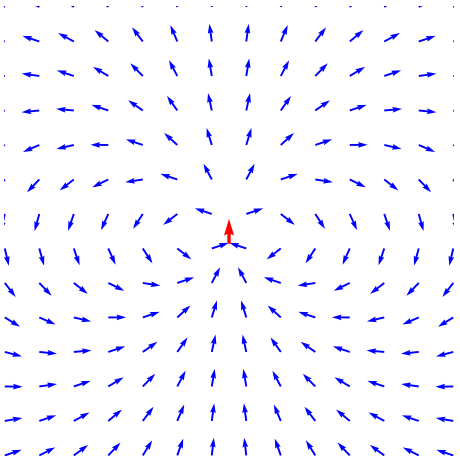

Figure 2.3: A cross section of the shape of the vector fields created by a transmitter coil. The dipole orientation is given by the red arrow.

With the time dependence removed, the vector fields are expressed as a column-matrix given by:

$$\mathbf{B}^t = \frac{k}{r^5}\left(3\mathbf{r}\mathbf{r}^T - \mathbf{I}r^2\right), \tag{2.14}$$

where k is the all-encompassing gain factor of the coils. In other words,

$$k = \frac{\mu_0 m}{4\pi}. \tag{2.15}$$

The superscript t indicates the transmitter's frame of reference. This equation can be expanded as,

$$\mathbf{B}^t = \frac{k}{r^5}\begin{bmatrix} 3x^2 - r^2 & 3xy & 3xz \\ 3xy & 3y^2 - r^2 & 3yz \\ 3xz & 3yz & 3z^2 - r^2 \end{bmatrix}. \tag{2.16}$$

This is referred to as the *field component matrix* or sometimes just the *field matrix*. Here, the matrix is expressed in the transmitter's frame of reference.

It should be noted that the above equation contains a hemispherical ambiguity. That is, the fields are equal at point $\mathbf{r}$ and its negative, $-\mathbf{r}$. This fact requires that the hemisphere be deduced by some other method or be established in advance. In practice, after a sufficient radial maneuver, this information can be deduced without much difficulty, and so it is not addressed further.

As stated above, every magnetic positioning system requires multiple transmitter coils as well as a magnetic receiver. The purpose of the receiver is to measure the dipoles produced by the transmitters. It has to be able to resolve the dipoles in three dimensions, and therefore, requires three coils with axes that span 3-D space. In this work, the u, v, and w coil axes are oriented along the orthogonal axes of a right-hand coordinate system.

The three separate receiver coils each measure the three transmitted dipoles producing a total of nine measurements. Each receiver coil has its own electronic processing channel to perform this. Figure 2.4 shows the processing for the u-coil. The other coils are identical. The first task of the coil processing is to down-mix to remove the carrier. Then the signal from the coil is multiplied by each modulation signal and integrated over a cycle. The result of each integration represents the intensity of the modulation signal which is picked up in the given coil.

The nine measurements make up the fields matrix in the receiver frame of reference given by:

$$\mathbf{B}^r = \begin{bmatrix} b_{xu} & b_{yu} & b_{zu} \\ b_{xv} & b_{yv} & b_{zv} \\ b_{xw} & b_{yw} & b_{zw} \end{bmatrix}, \tag{2.17}$$

where the elements of the matrix are the outputs of the demodulation process, with each column representing the outputs for a single transmitter coil modulation. It is trivial to see that if the orientation of the $u/v/w$ receiver coils are aligned with the $x/y/z$ transmitter coils, then $\mathbf{B}^r = \mathbf{B}^t$. If they do not align, then

$$\mathbf{B}^r = \underset{t:r}{\mathbf{R}}\mathbf{B}^t, \tag{2.18}$$

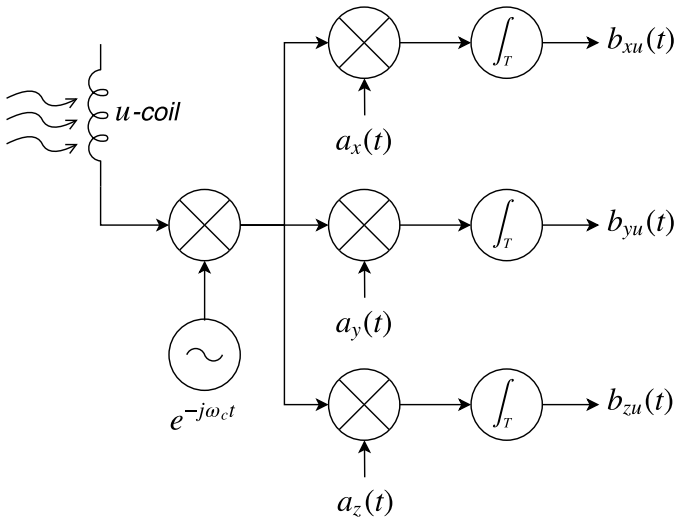

Figure 2.4: Down-mixing and demodulation. The down-mixing and demodulation signal flow for the u-coil channel.

where $\underset{t:r}{\mathbf{R}}$ is a rotation matrix that transforms from the transmitter's frame of reference to that of the receiver.

Using the field matrix, it is possible to calculate the position and orientation of the receiver relative to the transmitter. Within equation (2.18), there are six unknowns: x, y, z, and the three quantities required for the rotation matrix. There are several direct approaches that can be used to solve for the six unknowns: the Kuipers' algorithm from [4] is chosen for this project. However, this algorithm and all of the others become ineffective when distortions arise. The nature of these distortions will be covered in the next section.

2.3 Real-World Complications

Transmitted magnetic fields, such as those in the current work, have one paramount, practical difficulty. That is, every transmitted field produces parasitic fields in nearby

metal objects. In [9], when discussing the use of magnetic positioning systems for medical devices, the authors state:

> The problem of magnetic disturbances affecting the performance of electromagnetic tracking devices remains an extremely important limitation of these systems.

This is true whether the system is a medical system, which usually has a tracking volume on the order of a few square meters or less, or whether the system is a large area as envisioned in this application. In fact, it can be argued that a larger area will have more potential for magnetic disturbances just due to its size, and so the problem is more pronounced in this project.

This section describes the effects of the parasitic fields. It also discusses other practical complications and constraints related to available hardware and processing.

2.3.1 Ferromagnetic Effects

The induced interfering fields are of two different varieties. *Ferromagnetic* errors occur when a magnetic field couples to a ferrous metal. In this case, the impinging magnetic fields cause a parasitic magnetic field to be created inside the metal. This parasitic field then interferes with the transmitted field. Of the two types of errors, this type is dominant at lower frequencies and is present even with the geo-magnetic field. This means that the magnetometer measurements in this system are affected.

2.3.2 Eddy-Induced Errors

Eddy errors are present only when the transmitted field has a time-varying component, and they are due to Faraday's law. They occur with every type of conductor, not just ferromagnetic metals. In general, their direction is in opposition to the direction of the time-change of the impinging field.

For the purposes of this effort, eddy-induced errors are categorized as *bulk* or *acute* errors. Bulk errors occur when eddy-currents are induced in large metal objects;

acute errors occur when a larger eddy-current is induced in a highly localized metal conductor. Within the area where a receiver is operating, there are conductors such as buried cables or home wiring. If they form a loop or circuit, the transmitted signal couples into these conductors, and it creates a very acute interference. To illustrate how these errors might occur, the following simplified example is given:

Consider the effect of a circular loop of wire that lies perpendicular to a magnetic field coming from a single-coil transmitter. Assume that the loop has a radius of r_L and that the field is uniform over the loop. Also assume the transmitter flux density is sinusoidal and can be modeled by

$$\mathbf{B}_t = \alpha \sin \omega t.$$

By Faraday's law the induced electric field in the loop has the following relationship with the flux density:

$$\oint_L \mathbf{E}_t \cdot d\mathbf{l} = -\frac{\mathrm{d}}{\mathrm{d}t} \iint_S \mathbf{B}_t \cdot d\mathbf{S},$$

where L is the contour of the wire loop and S is the surface enclosed by the loop. With the given assumptions, $\mathbf{B}_t$ is uniform over the surface, and therefore $\mathbf{E}_t \cdot d\mathbf{l}$ will also be constant over the loop. Specifically, the following relationship holds

$$2\pi r_L E_t = -\pi r_L^2 \frac{\mathrm{d}B_t}{\mathrm{d}t},$$

where the vector designations of E_t and B_t are dropped with the understanding that a positive B_t is oriented in the direction of S and a positive E_t is oriented along the direction of the wire L. Therefore, the electric field in the wire is

$$E_t = -\frac{1}{2} r_L \alpha \omega \cos \omega t.$$

This electric field creates a current in the loop which induces an interfering magnetic field, sometimes called an eddy field. This effect is a manifestation of

Ampère's law. The interfering flux density due to the metal loop at a distance R away from the loop can be calculated from the following approximation

$$\oint_{2\pi R} \mathbf{B}_m \cdot d\mathbf{l} \approx \mu I_w,$$

where I_w is the current induced in the wire due to E_t and μ is the permeability of the medium. By Ohm's law

$$I_w = \sigma_w E_t A_w,$$

where σ_w is the conductivity of the wire, and A_w is the cross sectional area of the wire. The interfering flux density is then

$$B_m \approx -\frac{\mu_0 \sigma_w \alpha \omega r_L A_w}{4\pi R} cos\omega t. \tag{2.19}$$

A couple of interesting things can be gleaned from formula (2.19) above. First, the strength of the interfering field falls off inversely with the distance away from the conductor. Also, for a sinusoidal transmitted field, the interfering field is also sinusoidal and lags the transmitted signal by 90°. In the real world, this last observation may not hold due to the fact that any real-world current loops may have complex-valued impedance that will introduce some phase shift.

Figure 2.5 illustrates the relative orientations of the incoming field, the induced current, and the induced interfering field. Note that the induced signals are only present with a changing magnetic field (like the one in our example) and are oriented such that they oppose the change in the transmitted field.

2.3.3 Distortion Effects and Compensation

Regardless of whether a distortion is ferromagnetic or eddy-induced or whether it is bulk or acute, its effect will cause serious errors in the magnetic positioning system. Figure 2.6 shows the position as calculated from uncompensated magnetic data. It was collected by walking around an area that includes two locations with minor, acute

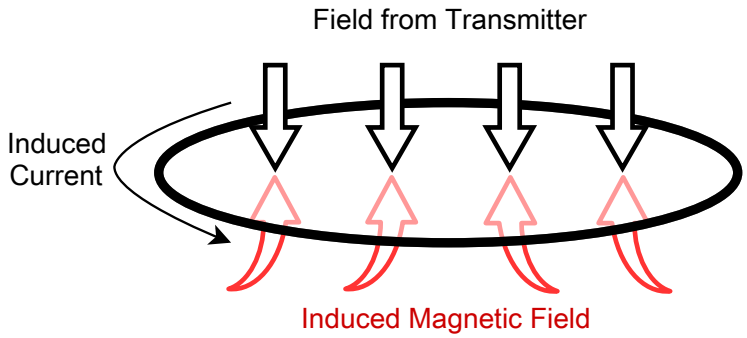

Figure 2.5: This diagram shows the orientations of the induced current and the induced magnetic field due to the transmitter field. Note that the induced signals are only present with a changing magnetic field and are oriented such that they oppose the change in the transmitted field.

eddy-interference. The most notable disturbance is in the lower left corner; the other is a single point at the top and toward the right.

The Kuipers algorithm [4] is used to calculate the position for this example. However, with distortions present, the nine measurements do not provide enough information to correctly solve the formula; and as can be seen, relatively minor distortions causes severe errors in the position.

In light of these real-world effects, it is obvious that more information is needed before accurate pose can be determined. The accelerometer and magnetometer help provide this information. Each of these sensors adds several more measurements, but they also each add more unknowns. The net effect is a decrease in the under-determined nature of the system. However, the system is still under-determined, and more must be done. The approach for this project is to add sensors and incorporate the complete time-history of measurements through the use of a Kalman filter.

2.3.4 Hardware and System Limitations

In addition to the measurement difficulties described above, several limitations are enforced in order to meet the needs of the magnetic tracking application. A magnetic

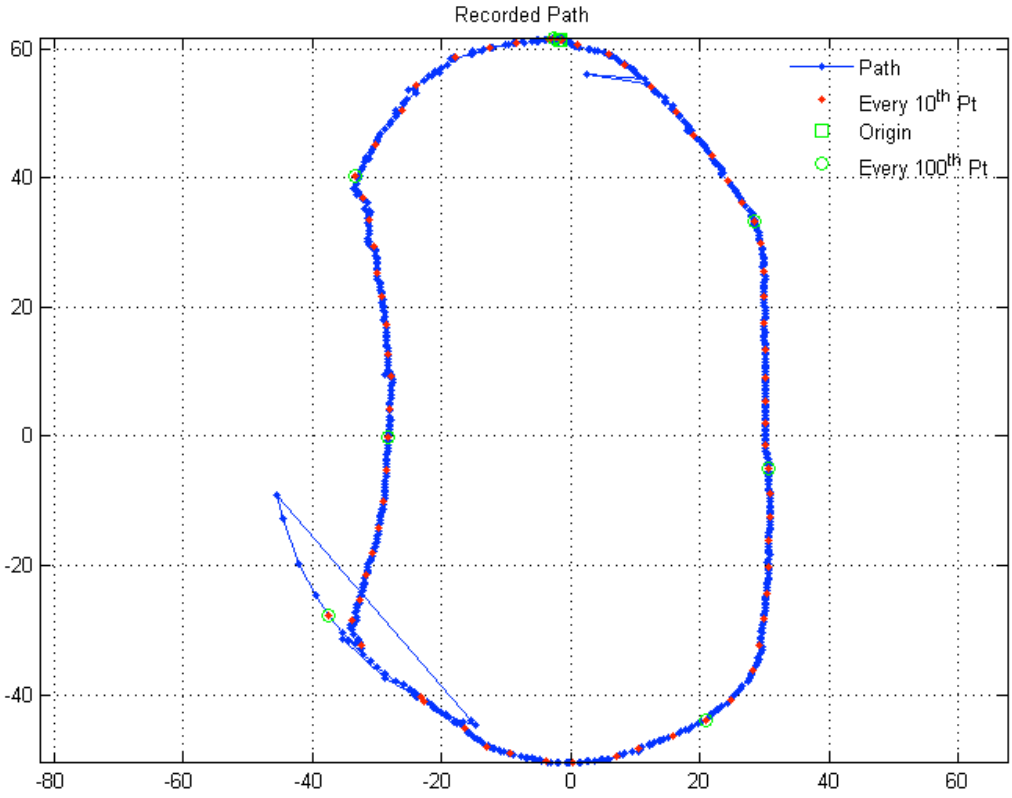

Figure 2.6: This real-world data shows two examples of acute interference. The left side of the data should have been straight and demonstrates the effects of bulk interference. Units are in feet with the transmitter at the origin.

positioning system can take many different forms, but for this project, the following objectives are targeted:

- **Low Power.** In one target use-case, a receiver will be worn on the body, possibly for days at a time without recharging. In this situation, it will be imperative that the system use as little power as possible. In addition, a non-intrusive package is required which precludes the use of large batteries and further hinders the power budget.

- **Compact Size.** Since the receiver might be worn on the body for long periods of time, it should be compact enough to not hinder the person wearing it.

- **Low Cost.** It is possible that dozens of receivers might be in operation with a single transmitter. Therefore, the cost of goods, especially in the receiver has to be kept low.

- **Relatively Long Range.** Most of the applications that employ magnetic positioning systems operate over small tracking volumes, sometimes as small as 1 meter on a side (*cf.* [10]). However, for the envisioned applications, a large tracking volume is needed–on the order of 60 meters on a side.

- **Rapid Reconfiguration.** The system should not be tied to a specific environment. In other words, if the system is moved from one location to another, setup should be very quick.

2.4 System Requirements and Objectives

The previous sections enumerate some of the limitations and constraints of a magnetic positioning system that will meet the needs of the envisioned applications. Using these limitations, it is possible to draft the system requirements and objectives. They are as follows:

1. Sensor *position* must be estimated, as well as *orientation*.

2. Low-performance inertial sensors must be used. High performance sensors tend to be large and expensive.

3. Gyroscopes can not be used. Usually, navigation sensor systems contain gyroscopes. In fact the cost, size, and function of gyroscopes will fit the needs of the system. However, their power use makes them unacceptable. While accelerometers and magnetometers draw on the order of 100 μA or less, gyroscopes can approach 10 mA; which for a system that must operate continuously for possibly days at a time on a small battery, this power draw is unacceptable.

4. Any compensation for induced interference must be done in real-time during operation. By contrast, in many applications, a calibration procedure is used (e.g. [11]) to create a signature or "fingerprint" of the magnetic field anomalies for a specific setup and area. This approach is not acceptable for this system due to the amount of setup work that must be to be done before operation.

5. In order to meet the need for long-range operation, the signaling used by the transmitter should have significant AC component. Since coils are used as the magnetic sensor, an electric field is induced in the receiver proportional to the time derivative of the transmitted field. This is in accord with Faraday's law. Therefore, the higher the frequency, the stronger the signal which is induced in the sensor.

6. With an AC type of signaling, there will be significant errors induced by eddy currents, for which compensation must be applied.

7. Anomalies in the geo-magnetic field due to ferromagnetic effects should be corrected.

8. The system should be rapidly reconfigurable. No long calibration routines or specific, detailed setup should be performed.

Chapter 3

Prior Art

This chapter summarizes the current state of the art relevant to this project. The concepts behind magnetic positioning have existed for more than 30 years, and much work has been done in the area up to the present. However, with regard to compensation for magnetic distortions, very few of the articles found could be considered comparables for this work. The reason for this lack of comparable work is unknown, but it may have to do with the fact that most of the deployed magnetic positioning systems have relatively small tracking volumes. Not only that, but these systems are usually set up once and rarely moved. The distortions experienced by these types of systems can be handled differently. To be more specific, the problem of magnetic distortion compensation is largely treated in two ways:

- It is ignored under the assumption that the operating environment can be cleared of distorting metal objects.
- Off-line measurement of the distortions is used to characterize the environment before deployment.

As should be clear from the last chapter, these two approaches are not acceptable for this project. In summary, the targeted application for the systems currently available have a much different paradigm than the application envisioned in this project, and this seems to result in only a couple of directly comparable works.

For this work, compensation is achieved through integration of magnetometer and accelerometer (MA) data. Only one other author (Roetenberg [12]) considers the use of an MA with a magnetic positioning system; and while he briefly mentions the use of MA data with magnetic positioning data, he is mostly focused on correcting distortions in the magnetometer. This work will be examined in more detail below.

3.1 Relevant Literature

3.1.1 Foundational Background

The patent by Kuipers in [2] describes one of the first methods to measure relative position and orientation of a device through magnetic fields. It uses coils to both transmit and receive magnetic fields. However, the configuration of the coils is not in two sets of three orthogonal coils. In [13], Kuipers expands his system to include an orthogonal, three-coil transmitter and receiver. Both of these systems, however, require a hard link between the transmitter and receiver in order to sync them in time and phase.

Building upon that, Raab in [3] presents a system whereby time-phase information is coded into the transmitted signal such that no hard link is required. He expands his system and adds a computational process for determining position and orientation in [14].

In [15], Raab *et al.* discusses the mathematical model for an orthogonal, tri-coil transmitter and an orthogonal, tri-coil receiver system that seeks to measure position and orientation. This is an oft-referenced paper and has set the foundation for much of the subsequent research. The hardware for this system is very similar to the hardware proposed in this document. Despite all this, the emphasis of the paper is a little dated as it attempts to linearize the system and make approximations so that the math processing will be tractable. This is not of paramount importance with the

processing hardware of today; however, it would be worthwhile when trying to trim down the processing time for use in an embedded system.

The most concise and clear presentation of the algorithms to extract position and orientation is given by Kuipers in [4]. In this book, he gives a brute force technique for solving the system, as well as an iterative technique which uses quaternions. This technique is directly adopted for this project, but for details, one should consult [4].

3.1.2 Induced Errors and Correction Techniques

As discussed in Section 2.3, transmitted magnetic fields induce parasitic fields in nearby metal objects. That interference is of two types: ferromagnetic effects due to ferrous metals, and eddy currents due to changing magnetic fields.

In [16], Nixon *et al.* examines in detail induced errors due to metal objects located in proximity to the positioning system's receiver and/or transmitter. A model is presented for the sensitivity of a measurement system as a function proportional to the distance to the fourth power. The work compares two commercial systems with different signaling schemes–one of them uses AC-signaling and the other a quasi-DC scheme. Much of the work is empirical in nature and agrees with relevant theory.

This paper also examines the effect of power line interference and computer monitor interferences. With an AC-signaling transmitter as presented herein, a high-pass filter prior to the ADC will eliminate these noise sources before they can do any harm. Reference [16] also notes that the proposed type of AC-signaling can benefit from the reduced permeability at higher frequencies and therefore reduced ferromagnetic effects.

The methods to deal with the induced-field problem fall into two categories within the literature: The first category is *off-line characterization*; the second is *real-time detection and correction.*

Off-Line Characterization

The most common method for correcting errors in magnetic fields is through characterization of the operating environment. This consists of an off-line process to record the signature of the magnetic environment and its anomalies. Correction can then be applied based on the recorded anomalies. Within the body of literature, this type of correction is often called calibration, which in this author's opinion is a misnomer. Examples of this type of correction are found in [17], [18] and [19]. Many of these techniques also require external hardware. For instance, [11] uses an optical tracking system to provide the "truth" for a calibration system. Similarly, [20] uses an ultrasonic distance measuring system.

For the project described in this document, none of these calibration procedures are acceptable as they require a pre-operational step to measure the interference and distortions. They also usually require separate hardware setups which are outside the purview of this project.

Dynamic Correction

Instead of off-line correction, this research implements a real-time (i.e. dynamic) correction technique. Two relevant techniques are found in the literature that are considered dynamic correction techniques.

The first technique is described in a series of papers by Prigge [21, 22, 23], with the most detail about the compensation technique being found in [23]. This paper presents a magnetic positioning system that consists of numerous magnetic transmitters that are distributed over a wide area. The position of each transmitter is known beforehand and is used to calculate the position.

One distortion mitigation technique the author uses is a natural outcome of the numerous distributed transmitters: That is, redundancy provided through many transmitters. In other words, the extra transmitters add more information to the system than is needed in an ideal sense. Also, because the transmitters are distributed

in space, the distortions that they induce have different signatures and affect the position measurement in different ways. In other words, a transmitter at a certain location may create an error that couples strongly with the receiver, while other transmitters may not create any errors. Therefore, the system has an inherent advantage over a system with three, co-located transmitter coils.

In this paper, Prigge treats eddy-induced errors and ferromagnetic errors in separate ways. The approach to eddy-current compensation is unique in the literature. Much of the uniqueness is reliant on a Code-Division Multiple Access (CDMA) signaling scheme which allows a measurement to be taken at the chipping rate of the system. This results in numerous measurements per cycle. These measurements are then used to compute a least squares solution for the system model. This is done twice: The first time, the solution is calculated with a system model that includes no eddy-induced errors; the second time, the model includes eddy-induced errors. If the two solutions differ by a certain amount, it is assumed that eddy-induced errors are present, and the corresponding model is used.

Prigge treats ferromagnetic errors differently than eddy-induced errors. In the ferromagnetic case, errors are detected by measuring the amount of disagreement between the multiple transmitters. Then the error is estimated such that it brought the transmitter measurements back into the best possible agreement. Obviously, this method depends on the fact that multiple, spatially-separated transmitters are available, and as such, this technique is not applicable with the hardware presented in this document.

The second dynamic correction technique found in the literature is described in a series of papers by Roetenberg *et al.* [24, 25, 10, 12].

In [12], the authors present a method of correcting for ferromagnetic induced errors in the geo-magnetic field. They achieve a very reliable estimate of the orientation of a device in the presence of parasitic fields using a Kalman filter to fuse the data from an inertial measurement unit –a tri-axial gyroscope, a tri-axial accelerometer, and

a tri-axial magnetometer. With their model, the Kalman filter is able to track and therefore compensate for geo-magnetic anomalies induced by ferromagnetic effects.

The techniques used in [12] show tremendous promise; however, there are several significant differences from what is accomplished in this project. For one, the system given by Roetenberg only estimates orientation; it does not estimate position. Furthermore, the system does not include a magnetic transmitter. Also, it uses a full magnetometer-accelerometer-rate-gyroscope (MARG) system, and since gyroscopes require too much power, they cannot be used for this research effort.

In [24] and [10], Roetenberg's technique is extended to include a magnetic transmitter to estimate position. However, the transmitter used is quasi-DC with very low update rate and is not suitable for the proposed system. Again, the author uses a Kalman filter to fuse the data, but it seems that the Kalman filter is used only in the same fashion as it is in [12]. In other words, the Kalman filter is used to fuse the MARG data with itself and to compensate for ferromagnetic errors in the geo-magnetic field; the filter is not used directly in the estimate of the position or to compensate for eddy-induced errors.

3.2 Limitations of Current Art

Numerous papers exist describing positioning from magnetic dipole transmitters, but most ignore or gloss over the magnetic anomalies induced from transmitted fields. These anomalies can cause drastic deviations from the ideal fields. Of the segment of the literature that addresses these deviations, the majority of them are off-line calibration methods that take place before the system is activated. Only a couple of works attempt to correct the problem in real-time. Of these, one ([23]) is tied to a specific system concept and cannot be easily extended to other concepts. The other ([12]) uses Kalman filters to fuse external data from a MARG; however, as previously discussed, the compensation is limited to the estimation of orientation rather than position.

Table 3.1 shows a summary of the most comparable literature. The numeral beside each category heading is a cross reference to the constraints and limitations for this project, which are listed in Section 2.4. This is done so that the reader can understand the weaknesses of each work with regard to the needs of this project. Each cell is color coded based on its applicability to the needs of this project. Green indicates it will meet the needs for this research; red indicates it will not; and yellow means it is unclear or unknown. "NA" stands for "Not Applicable" and indicates the reference does not address the topic.

As can be seen from the table, only Roetenberg even considers using inertial sensors in conjunction with a magnetic positioning system. As such, this author is the most comparable author, but the application is widely different than the one in this project, which results in some significant differences in technique. First, a short range system with quasi-DC signaling is used. Thus, negligible eddy currents are present, and so no eddy-compensation is considered. Second, in contrast to this project, the author is not as concerned with power, and so gyroscopes are used. The "Position Estimate" category is colored yellow because the author is mostly concerned with estimating orientation, and very little is presented with regard to estimating position.

From the table, it might appear that Prigge's work is very comparable to what is being proposed. However, the deployment of the author's system requires a complex setup phase where multiple transmitter coils are spread over an area. Not only that, but the receiver in the system needs a priori knowledge of that setup. So, while no off-line correction process is specifically required, extensive pre-configuration is necessary. Therefore, the author's approach to solving the problem at hand and the author's application are extremely different from the goal of this project.

Table 3.1: Comparable literature.

Authors	Position Estimate (1)	Low-Performance Inertial Sensors (2)	No Gyros (3)	Real-Time Correction (4)	Long Range (5)	Eddy Compensation (6)	Ferromagnetic Compensation (7)	Rapid Reconfiguration (8)
Raab *et al.* [14],[15]		NA	NA					
Prigge *et al.* [21],[22],[23]		NA	NA					
Roetenberg *et al.* [24],[25],[10],[12]								
Hu *et al.* [26]		NA	NA					
Ikits *et al.* [11] and others [17]		NA	NA					

Chapter 4

Receiver Calibration

The primary interest in this work is to track a magnetic receiver in the presence of environmental distortions, and the previous sections outline the problem and provide background literature. However, without reliable sensor measurements, the tracking problem is extremely difficult if not impossible. Therefore, before attacking the tracking problem, it is necessary to properly calibrate the receiver sensors.

In what follows, the calibration of each of the three sensors will be covered in its own section. Instead of having a separate chapter for the calibration literature, the relevant literature will be covered as it becomes pertinent within the analysis. The literature is fairly abundant with regard to calibration for accelerometers and magnetometers, but is almost non-existent for the coil receiver.

Because of this, the most substantial original contributions with regard to calibration are to be found in the section on coil calibration. At the time of this writing, there are several commercially available systems which contain coil receivers. Assuming they require calibration, it is likely done at the factory using dedicated fixtures and hardware, but no reports on coil calibration for these systems could be found in the literature. If they exist, these calibrations are probably performed at a very low level of the hardware, such as at the output of the coil amplifiers, or even lower than that, such as at the output of coils themselves. These low-level methods

are the most natural way of performing the calibration (e.g. [27]) and can lead to very good results. However, with fielded systems, such as the one described herein, calibration needs to be done with measurements which have been through the front-end down-mixing and demodulation. This is termed *application-domain calibration*, and having not been addressed in the available literature, it is a significant, original contribution of this research project.

4.1 Setup and General Procedure

This section describes the setup and procedures followed during the calibration process.

4.1.1 Environment and Receiver Location

Before the calibration can take place, data must be collected from each of the three sensors. This is done concurrently for each sensor; otherwise, the measurements could not be cross-referenced between the sensors. The following are the desired properties of the location to be chosen:

- Geo-magnetic fields must be relatively constant at the location. This precludes any areas near ferromagnetic metals.
- Transmitted fields must be relatively constant at the location. This precludes any areas very near large distorting objects or wires.
- The transmitted field signals must have a strong signal to noise ratio.
- The three transmitted field signals must be strongly anti-parallel with each other (i.e. nearly orthogonal). As will be explained later, this arrangement is needed for proper calibration of the coil receiver. With only minor distortion, this arrangement can be guaranteed if the receiver is positioned on or very near an axis of one of the transmitter coils.

The first two conditions are required because of the nature of the calibration process and the calibration fixture. The calibration process requires taking measurements at various receiver rotations while keeping its position constant. However, due to the mechanical setup of the receiver and the calibration fixture, it is unavoidable that the sensors will experience some change in position over the calibration process. This movement is kept within a distance of a few inches, but near distortions, a change in position of even a few inches can translate to a significant change in impinging field which will upset the calibration process. This is surprising; however, during the course of this research, this phenomenon was in fact encountered.

After taking a magnetic survey of the testing grounds (see section 6.1.3) and after trying a couple of other spots, the location shown in Figure 4.1 was chosen. It is located 36 feet away from the transmitter and on axis with the transmitter's x-coil; so the signal is strong, and the impinging field vectors are strongly anti-parallel. Also, this location is far from the metal building and other ferrous metals, so the geo-magnetic field is not disturbed. It is located within about twelve feet of a buried wire that causes serious distortions over much of the testing grounds. However, at this distance from the wire, the impinging transmitter beacon fields are constant. There is some distortion present, but it does not change enough over a few inches to cause a problem with the calibration process. Therefore, this location is well suited to collecting the calibration data.

4.1.2 Receiver Fixture

The receiver is affixed to a mounting fixture, which is affixed to a platform, which is affixed to a table. The receiver mounting fixture is made of wood with brass and nylon screws. The brass screws are non-ferromagnetic so that they will not disturb the geo-magnetic field; their induced effect on the impinging beacon fields is negligible. The platform is also made of wood and nylon and brass screws. The table is made with PVC legs, a wooden top, and is held together with brass screws.

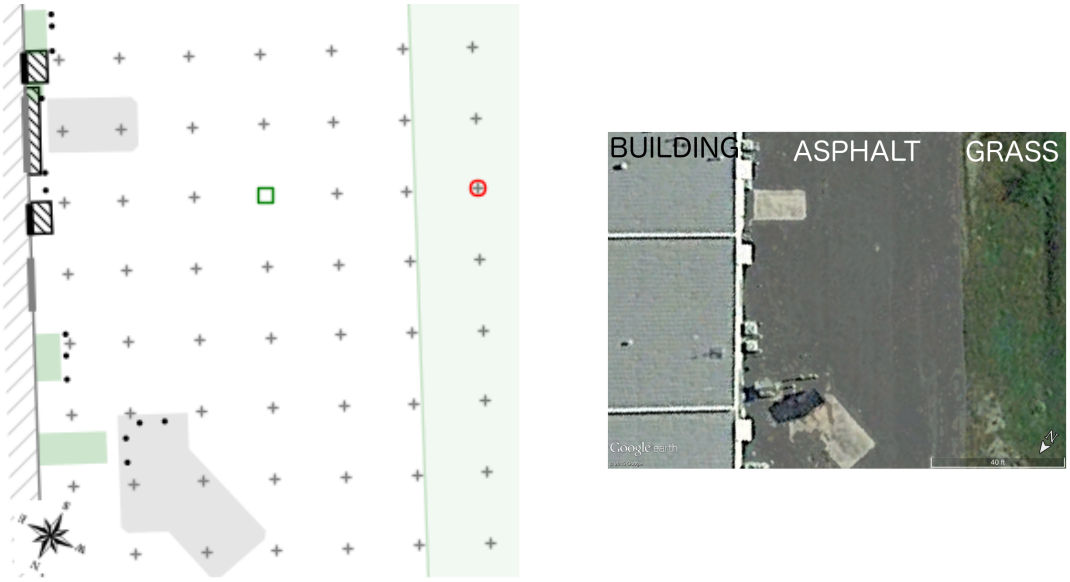

(a) Diagram **(b)** Photo [28]

Figure 4.1: The calibration environment. (a) The grid is oriented with the transmitter and is spaced at 12 feet. The green square is the transmitter, and the receiver is at the red circle 36 feet away. (b) A photo of the calibration environment. Note the asphalt, grass regions, and the building features including the dumpster and dumpster pad (lower left).

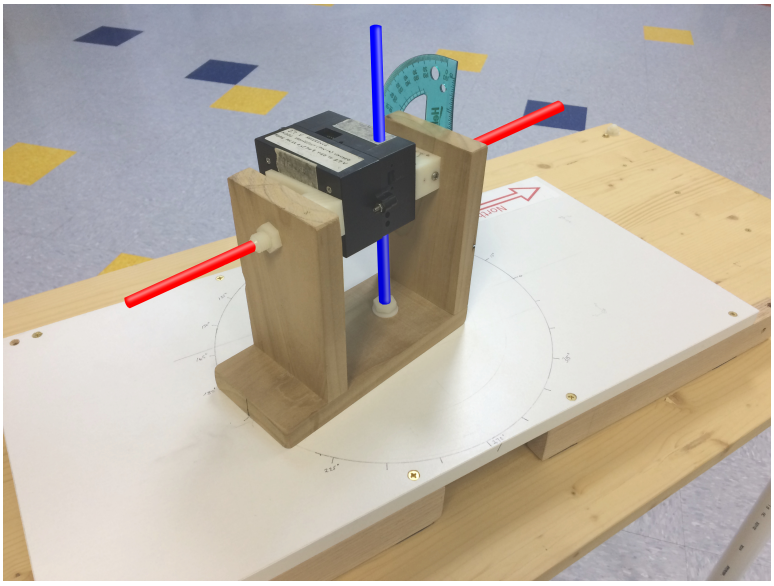

Figure 4.2: The fixture with the possible axes of rotation.

The entire fixture setup allows for rotation along two orthogonal axes. The fixture and the rotational axes are shown in Figure 4.2. The blue and red axes have their origin roughly at the centroid of coil triad of the receiver. The first axis of rotation is provided by the wooden receiver mount (the red axis in Figure 4.2). This mount is then allowed to rotate on the white, melamine platform (the blue axis). The rotation angle of the receiver in the wooden mount is indicated by a protractor mounted on the axis. The rotation angle of the mount on the platform is indicated by markings on the platform.

In addition to the two possible rotational axes, the platform itself can be mounted to the table either horizontally or vertically for even more variability. Without these two choices in platform mounting, the collected data would not be well formed enough to provide reliable calibration. Figure 4.3 shows a complete view of the fixture, platform, and table. It also shows the platform mounted both horizontally and vertically.

Being made with wood and PVC, this calibration fixture does not resemble a precision setup. However, this is not detrimental to the calibration outcome. The

(a) Table

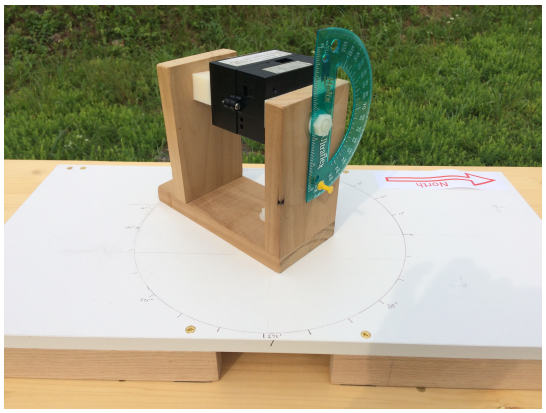

(b) Horizontal Mounting

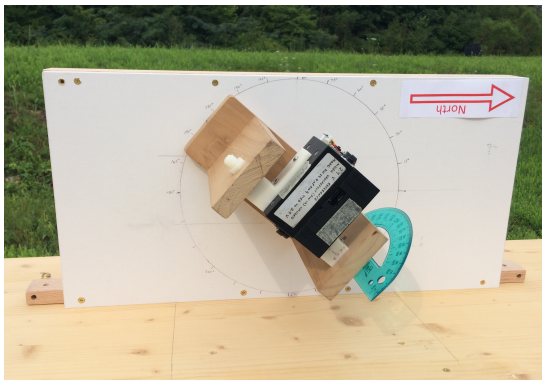

(c) Vertical Mounting

Figure 4.3: The calibration fixture. (a) The fixture table. (b) The platform mounted horizontally. (c) The platform mounted vertically.

magnetic positioning system is meant to operate over relatively large areas, spanning as much as 100 feet on a side. Therefore, small deviations due to imprecise fixture positioning are negligible. One might also object to the manual angle markings and rudimentary protractor angle indicator; but, as will be seen in the following sections, the angle indications are only used as guideposts rather than exact references. Therefore, they also do not have a negative effect the calibration outcome.

4.1.3 Collection process

Once the fixture is setup and in position, the data collection can take place. There are two possible axes of rotation as well as two platform mounting options. For each mounting option, data is continuously recorded while the following procedure is executed:

1. Fix the rotation of the receiver (red axis in Figure 4.2) by pinning the protractor to the wooden mount.
2. Rotate the mount by 360° over the melamine platform (i.e. around the blue axis in Figure 4.2).
3. Rotate the mount by 360° in the opposite direction over the melamine platform.
4. Move the protractor reading by 15° and re-pin.
5. Repeat the above steps until all desired rotations are complete.

As stated above, the mount is rotated by 360° twice in opposite directions. This is done to compensate for the accelerometer readings. For the best results, it is desirable that the accelerations experienced by the device be zero; but with the receiver being actively rotated, the device accelerations are finite albeit small compared to gravity. Subjecting the accelerometer to two opposite rotations serves to partially balance out the small accelerations.

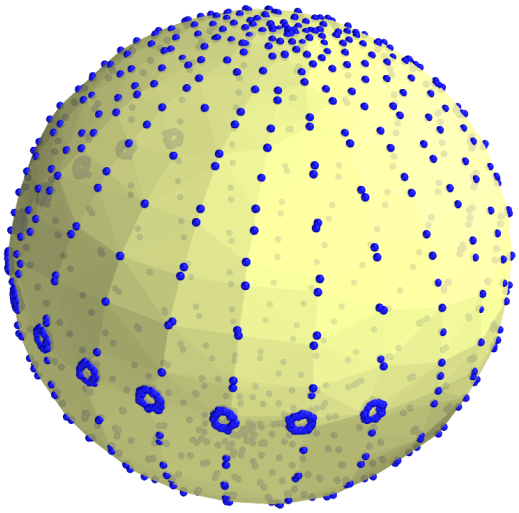

Figure 4.4: Accelerometer calibration samples. This figure demonstrates the density and coverage of the calibration sampling. The samples are in blue; the semi-transparent yellow ellipsoid is only a visual aid to show the shape of the samples.

The recording space available on the receiver cannot hold all of the data needed for the calibration. Therefore, the collection has to be stopped and re-started several times for the data to be downloaded. Also, the collection is paused when moving the platform from a horizontal to a vertical mounting.

Once the data is all collected, the files are collated and the data is resampled to reduce its size. During the resampling process, some averaging is applied to reduce the amount of noise present in the samples. The density and coverage of the calibration samples is demonstrated in Figure 4.4. The blue points are the samples from the accelerometer, and the semi-transparent yellow ellipsoid is only present as a visual aid to provide perspective.

The donut shaped locii in the figure illustrate the need for both horizontal and vertical mounting. They occurs when the platform is mounted in the horizontal position. In this case, the w-axis of the receiver always remains in the horizontal plane (roughly speaking). Therefore, it picks up very little of the gravity vector which is vertically aligned, and the samples have nearly zero value in the w-axis for

the entire collection when the platform is mounted horizontally. As will be seen in the later sections, calibration cannot be reliably performed unless the collection of points sufficiently sample the ellipsoid. For the accelerometer, this cannot be achieved without the vertical platform orientation.

4.2 Accelerometer Calibration

4.2.1 Analysis

The accelerometer considered in this work is made up of a triad of single-axis sensors. Ideally, each sensor axis has equal sensitivity and is aligned orthogonally to the other axes. An external vector stimulus applied to the accelerometer is projected upon each axis of the accelerometer to create a measurement. The measurements are normalized by the gain of the axes, which are nominally equal. As such, the vectors which are aligned with the physical sensor axes can be used as a basis for $\mathbb{R}^3$. Throughout this work, the orthonormal $\mathbb{R}^3$ basis aligned with the three sensor axes will be referred to as the *natural basis* for the sensor. For the accelerometer, this basis is denoted as $U' = \{\mathbf{u}', \mathbf{v}', \mathbf{w}'\}$. Therefore, a measurement taken from the sensor can be expressed as $\mathbf{a}' = a'_u\mathbf{u}' + a'_v\mathbf{v}' + a'_w\mathbf{w}'$ or simply $\mathbf{a}' = \begin{bmatrix} a'_u \\ a'_v \\ a'_w \end{bmatrix}$ when the U' basis is assumed. It should be noted that, since the U' basis is coincident with the accelerometer axes, it moves and rotates simultaneously with the receiver. As such, it is the foundation for the receiver reference frame.

With ideal sensors, U' is a right-handed, orthonormal basis, and $\mathbf{a}'$ can be used directly as a perfect representation of the accelerometer stimulus. Unfortunately, the three sensors in the accelerometer are subject to several errors, and so U' is not an orthonormal basis. Therefore, calibration is needed. Not considering random noise, the three main types of error experienced by the accelerometer are *bias error*, *scaling error*, and *non-orthogonality error*. The bias error arises from the accelerometer's

electronic system. It is additive in nature, and can be corrected by calibration although its value will drift somewhat with time and temperature. The scaling error arises from unequal gain between accelerometer axes. Finally, non-orthogonality error is due to non-orthogonal alignment among the three accelerometer axes. [29]

Taken together, the error model of the accelerometer is expressed by

$$\begin{bmatrix} \delta a_u \\ \delta a_v \\ \delta a_w \end{bmatrix} = \mathbf{b} + \mathbf{S} \begin{bmatrix} a_u \\ a_v \\ a_w \end{bmatrix} + \mathbf{M} \begin{bmatrix} a_u \\ a_v \\ a_w \end{bmatrix} \tag{4.1}$$

where $\mathbf{b}$ represents the bias error, $\mathbf{S}$ represents the scaling error, $\mathbf{M}$ represents the non-orthogonality error, $\mathbf{a} = \begin{bmatrix} a_u \\ a_v \\ a_w \end{bmatrix}$ represents the true sensor stimulus, and $\delta\mathbf{a} = \begin{bmatrix} \delta a_u \\ \delta a_v \\ \delta a_w \end{bmatrix}$ is the total accelerometer error such that

$$\begin{bmatrix} a'_u \\ a'_v \\ a'_w \end{bmatrix} = \begin{bmatrix} a_u \\ a_v \\ a_w \end{bmatrix} + \begin{bmatrix} \delta a_u \\ \delta a_v \\ \delta a_w \end{bmatrix} \tag{4.2}$$

[29].

With the above in mind, it is desirable to find an expression for the true sensor stimulus based on the sensor measurements. Combining (4.1) and (4.2) gives

$$\mathbf{a}' = (\mathbf{I} + \mathbf{S} + \mathbf{M})\,\mathbf{a} + \mathbf{b}. \tag{4.3}$$

Rearranging gives an expression for the calibrated sensor stimulus

$$\mathbf{a} = (\mathbf{I} + \mathbf{S} + \mathbf{M})^{-1}\,(\mathbf{a}' - \mathbf{b})\,. \tag{4.4}$$

Rather than separately describing $\mathbf{S}$ and $\mathbf{M}$, it is more convenient to describe the combined form. Let $\mathbf{K} = \mathbf{I} + \mathbf{S} + \mathbf{M}$. After the bias error is removed, the matrix $\mathbf{K}$ can be seen as the transform between an orthonormal basis, $U = \{\mathbf{u}, \mathbf{v}, \mathbf{w}\}$, and the non-orthonormal basis U'. It should be obvious that there are an infinite number of forms $\mathbf{K}$ can take; however, it is desired to have an orthonormal basis which is near U'. Again, there are an infinite number of ways to do this, but only a few make sense (see [30] and [31] for a couple of sensible options). For the purposes of this work, the following convention is adopted which is used by [32] and [33] :

- The first vector of the basis U, has the same direction as the first vector of U'. In other words, the direction of $\mathbf{u}$ equals the direction of $\mathbf{u}'$.
- The second vector of U, $\mathbf{v}$, is the nearest vector to $\mathbf{v}'$ which is also orthogonal to $\mathbf{u}$ and which is coplanar with $\mathbf{u}$ and $\mathbf{v}'$.
- The third vector's ($\mathbf{w}$) direction is fixed such that a right-hand basis is formed.

The above conditions can be restated in matrix form using three scaling factors, α_1, α_2, and α_3, and three angle perturbations, β, $gamma$, and η:

$$\begin{aligned}\mathbf{K} &= \begin{bmatrix} \alpha_1 & 0 & 0 \\ \alpha_2 \sin\beta & \alpha_2 \cos\beta & 0 \\ \alpha_3 \sin\eta & \alpha_3 \sin\gamma \cos\eta & \alpha_3 \cos\gamma \cos\eta \end{bmatrix} \\ &= \begin{bmatrix} \alpha_1 & 0 & 0 \\ 0 & \alpha_2 & 0 \\ 0 & 0 & \alpha_3 \end{bmatrix} \begin{bmatrix} 1 & 0 & 0 \\ \sin\beta & \cos\beta & 0 \\ \sin\eta & \sin\gamma \cos\eta & \cos\gamma \cos\eta \end{bmatrix}\end{aligned} \tag{4.5}$$

The definition of the angles is illustrated in Figure 4.5. In practice, the scaling factors are close to unity, and the angle perturbations are small. Therefore, it should be observed that both terms of $\mathbf{K}$ as well as the whole of $\mathbf{K}$ are close to the identity matrix. Also, it can be observed that $\mathbf{K}$ maps points on a sphere to points on an

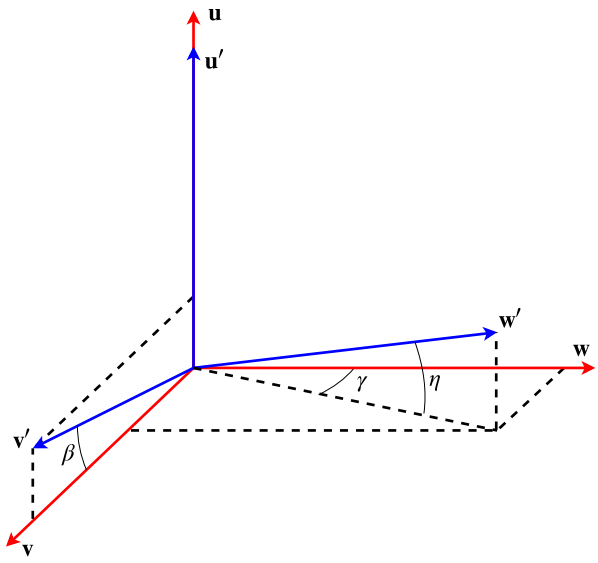

Figure 4.5: Definition of angle parameters with respect to the orthonormal and non-orthonormal bases

ellipsoid. (See [34] for a proof.) The shape of the ellipsoid is determined by **K**, whereas the center of the ellipsoid is determined by **b**.

As is previously noted, the choice of basis determines the form of **K**. If a different basis is chosen, the ellipsoid will not change—only its representation will change. An alternative and familiar representation of an ellipsoidal mapping uses a symmetric, positive-definite (SPD) matrix [35] rather than a lower triangular matrix. This form is mathematically similar and can be used with equal outcome. Because of the weak off-diagonal elements and strong diagonal elements of **K**, the ellipsoid will be nearly spherical. Because of this, the SPD form will also have weak off-diagonal elements and strong diagonal elements. If the basis of the SPD form is denoted as V, then it is obvious that only a small rotation is required to change from basis U to V. Therefore, in practice, the SPD form can be used with the expectation that its associated orientation is almost the same as that of the lower-triangular form. The benefit of using the lower-triangular form is in allowing the direct interpretation

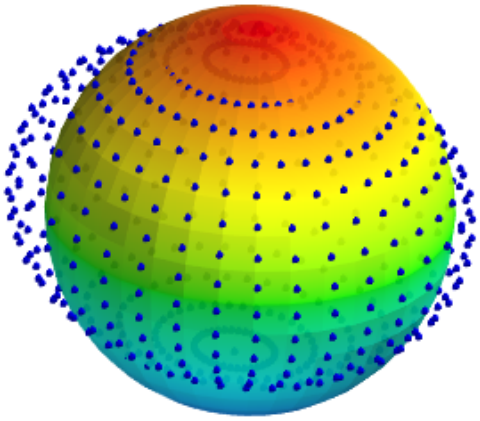

Figure 4.6: Uncalibrated accelerometer samples with a reference sphere

of the elements of **K**; the interpretation of the elements of the SPD matrix is less direct. However, this disadvantage is outweighed by the convenience of using the SPD form during implementation. Therefore, the SPD form is used, and thereafter, **K** is considered to be a symmetric, positive-definite matrix.

The ellipsoidal mapping of **K** is exploited to formulate the calibration procedure. With the accelerometer at rest (or with negligible accelerations) numerous points are collected, all with various rotations. They are denoted $\{\mathbf{a}'_n : n = 1 \dots N\}$, and it is obvious they are all represented in the receiver frame which changes relative to the earth frame. The gravity vector is constant in all of the measurements with respect to the earth frame; but in the receiver frame, the collected points appear as samples on an ellipsoid with a center corresponding to the accelerometer bias, **b**. If the accelerometer is perfectly calibrated, the points will be samples of a perfect sphere centered at the origin. In order to clarify these ideas, Figure 4.6 shows an example of what the uncalibrated samples will look like when compared to an ideal sphere.

To proceed with calibration after the data points are collected, it is necessary to find the parameters of the ellipsoid. Recall equation (4.4):

$$\mathbf{a} = \mathbf{K}^{-1}\left(\mathbf{a}' - \mathbf{b}\right). \tag{4.6}$$

where $\mathbf{a}'$ is a point on the ellipsoid, and $\mathbf{a}$ is a point on a sphere. Therefore,

$$\left(\mathbf{a}' - \mathbf{b}\right)^T \mathbf{T}_a^T \mathbf{T}_a \left(\mathbf{a}' - \mathbf{b}\right) = c \tag{4.7}$$

where $\mathbf{T}_a = \mathbf{K}^{-1}$ (also an SPD matrix) and c is a constant equal to the radius of the sphere. Because the sphere is defined by the gravity vector, c is equal to 1 standard gravity ($1\,G$). If $\mathbf{A} = \mathbf{T}_a^T \mathbf{T}_a$, then

$$\left(\mathbf{a}' - \mathbf{b}\right)^T \mathbf{A} \left(\mathbf{a}' - \mathbf{b}\right) = 1 \tag{4.8}$$

is the well known formula for an ellipsoid. Nine parameters are needed to solve for this ellipsoid—three bias parameters and six parameters for the SPD $\mathbf{A}$ matrix. Many sources in the literature estimate these parameters by directly fitting an ellipsoid to the data ([33]). They accomplish this through various techniques such as those presented in [36, 37, 32]. Rather than directly fitting an ellipsoid to the data, a more mathematically rigorous method to estimate the ellipsoid parameters is presented in [38] and [34], the latter of which presents an efficient maximum likelihood estimation technique.

An alternative, but equivalent, technique to direct ellipsoid fitting is what is referred to as scalar calibration [39, 40]. This technique is derived from the fact that the equation of an ellipsoid given by (4.7) is stated in terms of a constant scalar, in this case $1\,G$. Based on equation (4.7), scalar calibration consists in the application of the following constraint on the uncalibrated, collected points which lie on the ellipsoid [31]:

$$\left(\mathbf{a}'_n - \mathbf{b}\right)^T \mathbf{T}_a^T \mathbf{T}_a \left(\mathbf{a}'_n - \mathbf{b}\right) = 1 \quad \forall n = 1 \ldots N. \tag{4.9}$$

Several methods for optimizing against this constraint are available [39, 41]. The method presented in [31] is adopted for this work. It is specified by

$$\hat{\mathbf{T}}_a, \hat{\mathbf{b}} = arg\min_{\mathbf{T}_a, \mathbf{b}} \sum_{n=1}^{N} \left(\left(\mathbf{a'}_n - \mathbf{b} \right)^T \mathbf{T}_a^T \mathbf{T}_a \left(\mathbf{a'}_n - \mathbf{b} \right) - 1 \right)^2, \tag{4.10}$$

such that $\mathbf{T}_a = \mathbf{T}_a^T$ and $\mathbf{z}^T \mathbf{T}_a \mathbf{z} > 0$ for all $\mathbf{z} \in \mathbb{R}^3,\ \mathbf{z} \neq \mathbf{0}$.

It is instructive to consider the minimization of equation (4.10) in more detail. Rewriting the equation in terms of $\mathbf{A}$ gives

$$\hat{\mathbf{A}}, \hat{\mathbf{b}} = arg\min_{\mathbf{A}, \mathbf{b}} \sum_{n=1}^{N} \left(\left(\mathbf{a'}_n - \mathbf{b} \right)^T \mathbf{A} \left(\mathbf{a'}_n - \mathbf{b} \right) - 1 \right)^2. \tag{4.11}$$

such that $\mathbf{A} = \mathbf{A}^T$ and $\mathbf{z}^T \mathbf{A} \mathbf{z} > 0$ for all $\mathbf{z} \in \mathbb{R}^3,\ \mathbf{z} \neq \mathbf{0}$. Once this minimization is complete, $\hat{\mathbf{T}}_a$ can be found using

$$\hat{\mathbf{T}}_a = \sqrt{\hat{\mathbf{A}}}. \tag{4.12}$$

This is equivalent to performing the minimization of (4.10). However, $\sqrt{\hat{\mathbf{A}}}$, while guaranteed to exist if the accelerometer is operating properly, is not unique [35]. This is where the form that we chose for $\mathbf{K}$ becomes important. Because $\mathbf{T}_a$ is constrained to be SPD, there is only a single solution that satisfies (4.12) and is also SPD [35]. The other solutions to (4.12) differ only by an orthonormal matrix since for an orthonormal $\mathbf{R}$

$$\begin{aligned} \left(\mathbf{R}\hat{\mathbf{T}}_a \right)^T \mathbf{R}\hat{\mathbf{T}}_a &= \hat{\mathbf{T}}_a^T \mathbf{R}^T \mathbf{R} \hat{\mathbf{T}}_a \\ &= \hat{\mathbf{T}}_a^T \hat{\mathbf{T}}_a \\ &= \hat{\mathbf{A}}. \end{aligned}$$

Therefore, it is possible to calibrate the accelerometer to a sphere using

$$\mathbf{a} = \hat{\mathbf{T}}_a \left(\mathbf{a}' - \hat{\mathbf{b}} \right), \tag{4.13}$$

but it should be noted, that the "true" calibration cannot be determined without further constraints. That is, while a suitable calibration can be found when $\mathbf{T}_a$ is forced to be SPD, it is likely to be slightly rotated from the true, physical orientation. For the application described in this work, this uncertainty is unlikely to affect the outcome. It is only necessary that the accelerometer be aligned with the other sensors in the system. To do this, the calibrated orientation of the accelerometer is used as the baseline receiver orientation, and the other sensors will be calibrated to it. The methods for doing this will be covered in later sections.

4.2.2 Implementation and Results

To perform the calibration, widely available Python [42] libraries are used. The minimization of equation (4.10) is recognized as a non-linear least-squares minimization with 9 parameters. Therefore, the `leastsq` routine from SciPy Python optimization library is used [43]. According to its documentation, it uses the MINPACK `lmdif` algorithm [44].

The heart of the `leastsq` routine is the `residuals` function, which the user is required to supply. As implemented for the accelerometer, `residuals` does the following in order:

1. Parses the 9 parameters into a candidate calibration which includes a bias vector, $\hat{\mathbf{b}}$, and an SPD matrix, $\hat{\mathbf{T}}_a$.

2. Applies the candidate calibration to the N measurements to get

$$\left\{ \mathbf{a}_n = \hat{\mathbf{T}}_a \left(\mathbf{a}'_n - \hat{\mathbf{b}} \right) : n = 1, \ldots, N \right\}. \tag{4.14}$$

3. Computes the N residuals as

$$\left\{ r_n = \mathbf{a}_n^T \mathbf{a}_n - 1^2 : n = 1, \ldots, N \right\}. \tag{4.15}$$

It is then left to the Python-supplied `leastsq` algorithm to compute the squared sum of the N residuals. By making repeated calls to `residuals`, the `leastsq` routine is able to minimize over the 9-parameter space, thereby producing estimates for $\mathbf{T}_a$ and $\mathbf{b}$ in accord with equation (4.10).

The actual calibration procedure was carried out several times over the course of this project. This helped to overcome changes in the device response over long periods of time, such as might occur due to aging of the device or the changing of temperature with the seasons. Each time the calibration procedure was carried out, slightly different results were obtained, but the following results were typical:

$$\mathbf{T}_a = \begin{bmatrix} 0.99435 & -0.00019 & -0.00195 \\ -0.00019 & 1.00973 & -0.00137 \\ -0.00195 & -0.00137 & 1.01612 \end{bmatrix} \tag{4.16}$$

$$\mathbf{b} = \begin{bmatrix} -0.03007 & 0.02205 & -0.06373 \end{bmatrix} \tag{4.17}$$

These results are for a particular LSM303D accelerometer [6], which is used in this project.

Several conclusions are drawn from these results. The off-diagonal elements indicate non-orthogonality errors on the order of 0.1%. From the diagonal elements, it is deduced that the scale errors are more severe. The imbalance between the x and z axes is on the order of 2%. In general, over the course of the project, $\mathbf{T}_a$ proved to be fairly constant when the calibration procedure was re-run; however, $\mathbf{b}$ fluctuations were more significant. This information will become important at a later time when system models are developed.

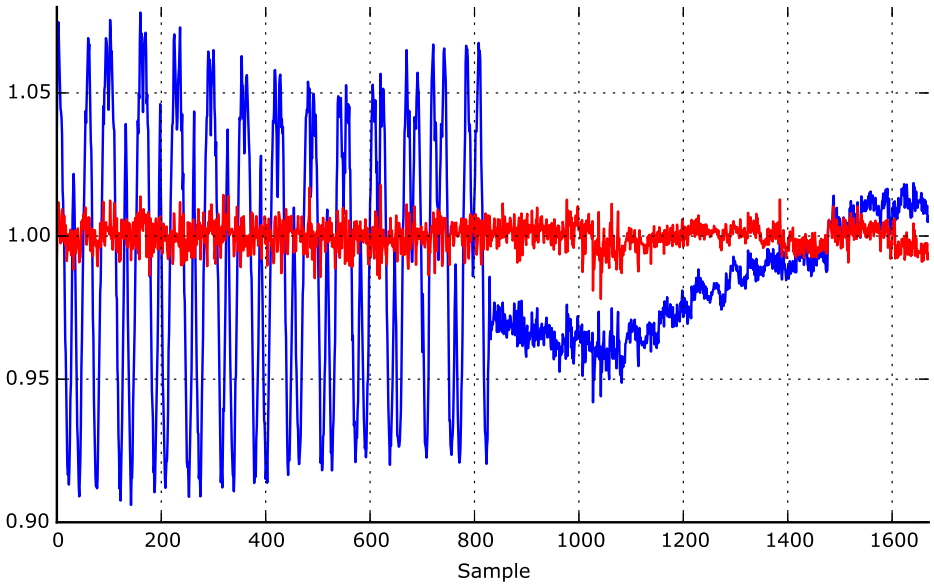

Figure 4.7: Gravity signal level. The magnitude of the accelerometer measurements in units of standard gravity are shown before (blue) and after (red) calibration.

When applied to the measurements, the calibration parameters presented above achieve the results shown in Figure 4.7. The blue signal corresponds to the magnitude of the uncalibrated measurements which were collected during the calibration process (see Figure 4.4). The red signal corresponds to the to the magnitude of the calibrated measurements.

The results clearly show the effectiveness of the calibration procedure. Each of the signals in the figure above represents the magnitude of the measured gravity vector plus noise. The strong deviation in the uncalibrated, blue signal shows that the ellipsoid surface differs from the ideal sphere by as much as 8%. With no noise, the ideal calibrated response will show a constant at $1\,G$ (or equivalently $32.174\,ft/s^2$ or $9.8\,m/s^2$). In this case, the "noise" consists of the usual electronic noise, as well as small accelerations experienced by the sensor during data collection. Around sample 850, a change is seen in the response of the uncalibrated signal. This is due

to a change in platform orientation: In the first part of the signal, the platform is mounted vertically; in the second part, it is mounted horizontally.

The calibrated samples have a standard deviation of less than 1%, and most of this deviation is attributed to noise and small accelerations during the collection process. In general, the ellipsoidal nature of the samples is effectively removed by the calibration process. This is evident in the nearly constant level of the red, calibrated signal.

4.3 Magnetometer Calibration

4.3.1 Analysis

The calibration of the magnetometer proceeds in much the same way as the accelerometer, but before describing the process, it is helpful to describe the error sources in a magnetometer measurement. Like the accelerometer, the tri-axial sensor of the magnetometer is subject to scaling, bias, and non-orthogonality errors—all of which are classified as intrinsic to the sensor electronics [33]. Recall the following:

- Scaling errors are due to gain mismatches on each axis of the sensor.
- Bias errors are offsets that occur due to electronic circuits in each axis of the sensor.
- Non-orthogonality errors arise due to mis-alignment between the sensor axes.

In addition, the magnetometer is subject to a few other possible errors; none of which are due to the magnetometer itself, but rather are extrinsic to it. They are *hard-iron* errors, *soft-iron* errors, and *mutual mis-alignment* errors [33]. Of these three extrinsic errors, hard-iron and soft-iron errors arise due to external, localized magnetic anomalies. Mutual mis-alignment errors arise when the magnetometer is not aligned with the other sensors (e.g. the accelerometer) on the receiver.

Hard-iron errors, $\mathbf{h}$, appear as constant offsets in the magnetometer measurement, but unlike the bias errors, these are extrinsic to the sensor. In other words, these errors affect the magnetic field impinging on the magnetometer, rather than occurring within the sensor itself. They are due to permanently magnetized ferrous materials which are mounted in the receiver near the magnetometer. As such, these interfering materials rotate with the magnetometer, and so they are constant in the receiver frame. Thus, they appear with the same form as the intrinsic bias errors. [33]

Like hard-iron errors, soft-iron errors are disturbances in the magnetic field which are created by materials mounted in the vicinity of the magnetometer. However, rather than being caused by permanently magnetized materials, they are induced in ferromagnetic materials by the impinging geo-magnetic field. As such, they are expressed as a constant, linear transformation of the impinging field denoted by, $\mathbf{C}_{si} : \mathbb{R}^3 \to \mathbb{R}^3$ [40].

The mutual mis-alignment error is external to the magnetometer electronics just like the hard-iron and soft-iron errors. However, it is not a magnetic field disturbance. Rather, it arises due to slight mounting and alignment errors between the magnetometer and the other sensors in the system. It is important that measurements from each sensor in the receiver be mutually aligned, else significant problems will arise [45, 31]. Recall, for purposes of this work, the receiver's natural basis (a.k.a. receiver frame of reference) is equated to the accelerometer's natural basis. Therefore, the mutual mis-alignment error is modeled as a slight rotation between the magnetometer natural basis and the receiver frame of reference, i.e the accelerometer natural basis. A simple rotation is all that is required to correct for mutual mis-alignment error.

To illustrate the effects of the errors, the model of the magnetometer measurement is developed step-by-step in what follows. (Much of the variable notation is shared with that from section 4.2. This is done for convenience because they have similar meanings. However, the context is different, and the variables in this section are distinct and should not be confused with those in 4.2.)

- Given the true impinging magnetic field, $\mathbf{m}$, and the hard-iron error, $\mathbf{h}$, the total impinging field is given by

$$\mathbf{m} + \mathbf{h}, \tag{4.18}$$

where $\mathbf{m}$ and $\mathbf{h}$ are both expressed in the receiver frame of reference.

- The magnetometer takes measurements in its natural basis, which is mis-aligned with the receiver basis; so the total impinging field in the magnetometer natural basis is given by

$$\mathbf{R}\left(\mathbf{m} + \mathbf{h}\right), \tag{4.19}$$

where $\mathbf{R}$ rotates from the receiver basis to the magnetometer natural basis.

- The total impinging field induces a distortion due to soft iron effects, which causes the total stimulus applied to the magnetometer to become

$$\mathbf{C}_{si}\mathbf{R}\left(\mathbf{m} + \mathbf{h}\right). \tag{4.20}$$

- The triad of sensors have a slightly, non-orthogonal orientation which affects the measurements by

$$\mathbf{C}_{\perp}\mathbf{C}_{si}\mathbf{R}\left(\mathbf{m} + \mathbf{h}\right), \tag{4.21}$$

where $\mathbf{C}_{\perp} = \begin{bmatrix} 1 & 0 & 0 \\ \sin\beta & \cos\beta & 0 \\ \sin\eta & \sin\gamma\cos\eta & \cos\gamma\cos\eta \end{bmatrix}$.

- The sensitivities of each axis are not ideal which distorts the measurements by

$$\mathbf{C}_{\alpha}\mathbf{C}_{\perp}\mathbf{C}_{si}\mathbf{R}\left(\mathbf{m} + \mathbf{h}\right), \tag{4.22}$$

where $\mathbf{C}_\alpha = \begin{bmatrix} \alpha_1 & 0 & 0 \\ 0 & \alpha_2 & 0 \\ 0 & 0 & \alpha_3 \end{bmatrix}$.

- Each axis has an electronic offset, $\mathbf{o}$, which distorts the measurements by

$$\mathbf{C}_\alpha \mathbf{C}_\perp \mathbf{C}_{si} \mathbf{R} (\mathbf{m} + \mathbf{h}) + \mathbf{o}. \tag{4.23}$$

In total, the magnetic measurement, $\mathbf{m}'$, is given by

$$\mathbf{m}' = \mathbf{C}_\alpha \mathbf{C}_\perp \mathbf{C}_{si} \mathbf{R} (\mathbf{m} + \mathbf{h}) + \mathbf{o}. \tag{4.24}$$

The calibrated sample in the receiver basis is then:

$$\begin{aligned} \mathbf{m} &= \mathbf{R}^T \mathbf{C}_{si}^{-1} \mathbf{C}_\perp^{-1} \mathbf{C}_\alpha^{-1} (\mathbf{m}' - \mathbf{o}) - \mathbf{h} && (4.25) \\ &= \mathbf{R}^T \mathbf{C}_{si}^{-1} \mathbf{C}_\perp^{-1} \mathbf{C}_\alpha^{-1} (\mathbf{m}' - \mathbf{o} - \mathbf{C}_\alpha \mathbf{C}_\perp \mathbf{C}_{si} \mathbf{R} \mathbf{h}) && (4.26) \\ &= \mathbf{T}_m (\mathbf{m}' - \boldsymbol{\mu}), && (4.27) \end{aligned}$$

where $\mathbf{T}_m = \mathbf{R}^T \mathbf{C}_{si}^{-1} \mathbf{C}_\perp^{-1} \mathbf{C}_\alpha^{-1}$ and $\boldsymbol{\mu} = \mathbf{o} + \mathbf{C}_\alpha \mathbf{C}_\perp \mathbf{C}_{si} \mathbf{R} \mathbf{h}$ are both constant. The form of (4.27) is equivalent to the form of (4.4) derived for the accelerometer, except that $\mathbf{T}_m$ is no longer forced to be symmetric positive definite.

Having established a model for the magnetometer measurement, calibration can proceed. The first step of the calibration is to find the ellipsoidal mapping established by $\mathbf{T}_m$. In other words, $\mathbf{T}_m$ has to be found that satisfies

$$(\mathbf{m}' - \boldsymbol{\mu})^T \mathbf{T}_m^T \mathbf{T}_m (\mathbf{m}' - \boldsymbol{\mu}) = c, \tag{4.28}$$

where c is the ideal static magnetic field strength at the location where calibration is performed. The minimization proceeds in exactly the same way as for the

accelerometer with

$$\hat{\mathbf{A}}, \hat{\boldsymbol{\mu}} = arg \min_{\mathbf{A},\boldsymbol{\mu}} \sum_{n=1}^{N} \left((\mathbf{m'}_n - \boldsymbol{\mu})^T \mathbf{A} (\mathbf{m'}_n - \boldsymbol{\mu}) - c \right)^2. \tag{4.29}$$

such that $\mathbf{A} = \mathbf{A}^T$ and $\mathbf{z}^T\mathbf{A}\mathbf{z} > 0$ for all $\mathbf{z} \in \mathbb{R}^3,\ \mathbf{z} \neq \mathbf{0}$. Then

$$\hat{\mathbf{T}}_m = \sqrt{\hat{\mathbf{A}}} \tag{4.30}$$

is solved, but the solution is not unique.

Therefore, the question arises: What is the correct form for $\mathbf{T}_m$? With the accelerometer, the correct form for $\mathbf{T}_a$ is *defined* to be the SPD form, but this cannot be done for the magnetometer. In section 4.2, it is pointed out that a solution to the matrix square root differs from all of the other solutions by an orthonormal matrix. In other words, if $\hat{\mathbf{T}}_m$ is a solution, then so is $\mathbf{R}_m\hat{\mathbf{T}}_m$, where $\mathbf{R}_m$ is an orthonormal matrix. Assuming the magnetometer and accelerometer are nominally aligned, $\mathbf{R}_m$ is assumed to be a rotation matrix (i.e. $\det(\mathbf{R}_m) = 1$).

The second step of the magnetometer calibration consists in finding this rotation matrix. This is equivalent to finding the mutual mis-alignment error. The literature examines a few methods for accomplishing this. In [30] known rotations are applied to the receiver, and these rotations are used to recover the mis-alignment between the sensor axes and the receiver frame. Another interesting solution is given in [46]; here, the mutual mis-alignment is found at the same time as $\mathbf{T}_m$. A common, simple method is presented in [47] and [48]. In this method, the inner product between the calibrated accelerometer measurement and the partially calibrated magnetometer measurement is used to find the mis-alignment between them. This method is adopted for this project and will be described in what follows.

To outline the adopted method, consider the previously calibrated accelerometer measurement

$$\mathbf{a} = \mathbf{T}_a(\mathbf{a}' - \mathbf{b}) \tag{4.31}$$

and the partially calibrated magnetometer measurement, $\tilde{\mathbf{m}}$, given by

$$\tilde{\mathbf{m}} = \mathbf{T}_m \left(\mathbf{m}' - \boldsymbol{\mu} \right), \tag{4.32}$$

where the "hat" modifiers have been dropped, and it is understood that $\mathbf{T}_a$, $\mathbf{T}_m$, $\mathbf{b}$, and $\boldsymbol{\mu}$ are the values found through equations (4.11), (4.12), (4.29), and (4.30). The fully calibrated magnetometer measurement are

$$\mathbf{m} = \mathbf{R}_m \mathbf{T}_m \tilde{\mathbf{m}}, \tag{4.33}$$

where $\mathbf{R}_m$ is the rotation matrix required to realign the magnetometer's natural basis with the accelerometer's natural basis. Taking the inner product

$$\mathbf{a}^T \mathbf{m} = k \tag{4.34}$$

gives a constant k for all samples regardless of rotation. So the following least squares minimization is performed:

$$\hat{\mathbf{R}}_m = arg \min_{\mathbf{R}_m} \sum_{n=1}^{N} \left(\mathbf{a}_n^T \mathbf{R}_m \tilde{\mathbf{m}}_n - k \right)^2, \tag{4.35}$$

such that $\mathbf{R}_m \in \mathbb{R}^3$, $\mathbf{R}_m^T \mathbf{R}_m = \mathbf{I}$, and $\det\left(\mathbf{R}_m\right) = 1$. At first glance (4.35) appears to be a linear least squares problem, but $\mathbf{R}_m$ has only three degrees of freedom which are usually parametrized with three Euler angles. Therefore, the minimization is non-linear.

Having found $\mathbf{R}_m$, the magnetometer calibration parameters are completely specified. In summary, to apply the calibration to the magnetometer measurements, the following is used:

$$\mathbf{m} = \mathbf{R}_m \mathbf{T}_m \left(\mathbf{m}' - \boldsymbol{\mu} \right). \tag{4.36}$$

With this, the uncalibrated measurements can be transformed such that they can be used to determine the geo-magnetic field.

4.3.2 Implementation and Results

The calibration of the magnetometer proceeds in two steps, corresponding to the two minimizations that must be performed. These two minimizations are

1. The ellipsoidal minimization, described by equation (4.29)

2. The mutual mis-alignment minimization, described by equation (4.35)

Step one in the calibration is the magnetometer ellipsoidal minimization. This step, described by equation (4.29), and the minimization for the accelerometer, described by equation (4.10), share the same form and can be thought of in the same way. In the accelerometer case, the volumetric constant of minimization is known to be $1\,G^2$. However, in the magnetometer case, the constant c must be determined. This is due to the fact that the geo-magnetic field varies by location, date, and environment. It is not necessary to employ a calibrated instrument to provide a precise reading of the field because the tracking algorithms are primarily concerned with the *direction* of the magnetic field, not its magnitude. Therefore, any arbitrary constant can be used for c; but, for the sake of consistency and so that $\mathbf{T}_m$ is close to the identity matrix, the constant is determined using data from the National Centers for Environmental Information which is a data center for the National Oceanic and Atmospheric Administration (NOAA). Their website contains a calculator that reports the nominal geo-magnetic field for a given location and date [49]. For this project, the nominal field strength is determined to be $c = 0.507\,\text{Gauss}$.

With that determination, an attempt was made at ellipsoidal calibration, but some difficulties were encountered. Figure 4.8 contains the results of the calibration and demonstrates these difficulties. Some systematic errors are seen in the figure, especially in the neighborhood of sample number 600. From trial and error, it was

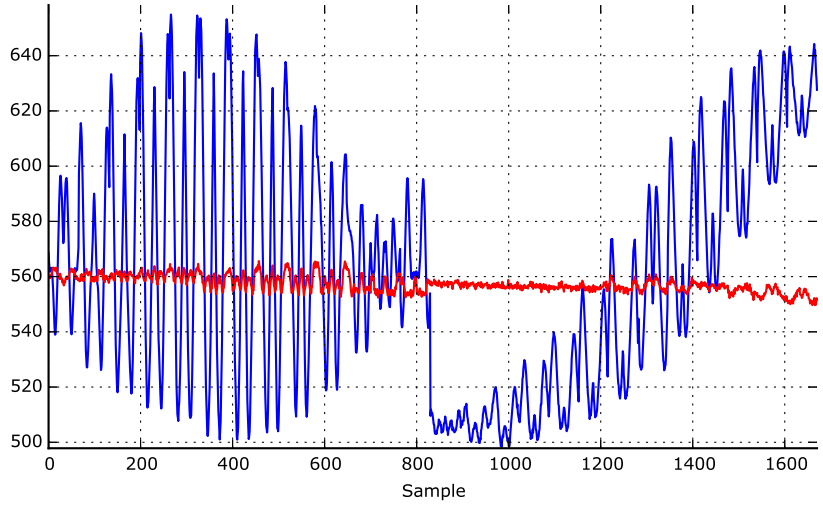

Figure 4.8: Magnetometer global minimization. The magnitude of the geo-magnetic field measurement vector is shown before (blue) and after (red) the first phase of calibration with global minimization applied. Some systematic errors are seen, especially in the neighborhood of sample number 600.

determined that these are due to gain variations during the calibration process, likely due to temperature changes over the course of the calibration. The gain variations are consistent over the three axes and cause what can be considered a volumetric expansion or contraction of the fitted ellipsoid. To compensate for this, an original technique is developed which is termed *adaptive-volume calibration*.

This technique adapts to the changing ellipsoidal volume by allowing c to vary over the course of the calibration. The required variation is slow; so c is broken up into numerous piecewise-constant segments. As delineated earlier in section 4.1.3, the collection process consists of fixing the axis of rotation; then rotating by 360°; and then rotating in the opposite direction by 360°. Each pair of 360° rotations is termed a *calibration segment* or just *segment*. These segments provide a natural boundary for breaking the calibration data into sections where negligible gain variations will occur. Therefore, over a given segment, c is held constant, but it is allowed to vary between segments. The set of all segments is $\{S_i : i = 1, \ldots, I\}$, where I is the total

number of segments and where S_i is the set of indices of all the measurements within segment i.

Adapting the ellipsoidal minimization of equation (4.29) to allow for piecewise-constant c gives:

$$\hat{\mathbf{T}}_m, \hat{\boldsymbol{\mu}} = arg \min_{\mathbf{T}_m, \boldsymbol{\mu}} \sum_{i=1}^{I} \sum_{n \in S_i} \left((\mathbf{m'}_n - \boldsymbol{\mu})^T \mathbf{T}_m^T \mathbf{T}_m (\mathbf{m'}_n - \boldsymbol{\mu}) - c_i \right)^2, \tag{4.37}$$

such that $\mathbf{T}_m = \mathbf{T}_m^T$ and $\mathbf{z}^T \mathbf{T}_m \mathbf{z} > 0$ for all $\mathbf{z} \in \mathbb{R}^3$, $\mathbf{z} \neq \mathbf{0}$ where c_i is the calibration constant for segment i.

The value of c_i is unknown for each segment, but it is approximated as the mean of the calibration signal over the segment. In other words, for a given segment, the value of c_i is computed as:

$$c_i = \frac{1}{N_i} \sum_{n \in S_i} (\mathbf{m'}_n - \boldsymbol{\mu})^T \mathbf{T}_m^T \mathbf{T}_m (\mathbf{m'}_n - \boldsymbol{\mu}), \tag{4.38}$$

where N_i is the number of samples in segment i. Note that at every iteration of the minimization, each c_i must be recomputed. In order to keep the minimization from converging to $\hat{\mathbf{T}}_m = 0$, it is necessary to constrain $\mathbf{T}_m$. This is done by forcing $\mathbf{T}_m[1,1] = 1.0$. When the minimization is complete, $\mathbf{T}_m$ is scaled such that the average calibrated sample value becomes equal to the nominal geo-magnetic field of 0.507 Gauss. This whole process can be thought of as minimizing the local deviations, and can be contrasted with minimizing the global deviations as expressed in equation (4.29).

Just like the accelerometer calibration (see Section (4.2.2)), the first phase of the magnetometer calibration makes use of Scipy's `leastsq` algorithm [43]. The goal is the minimization of equation (4.37) which has 8 degrees of freedom: 3 for $\boldsymbol{\mu}$ and 5 for the symmetric $\mathbf{T}_m$ since the $[1,1]$ element is fixed to 1.0. The `residuals` routine is the heart of the algorithm and performs the following in order:

1. Parses the 8 parameters into a candidate calibration which includes a bias vector, $\hat{\boldsymbol{\mu}}$, and an SPD matrix, $\hat{\mathbf{T}}_m$.

2. For each calibration segment S_i, does the following:

   (a) Applies the candidate calibration to the measurements within the segment to get

   $$\left\{\tilde{\mathbf{m}}_n = \hat{\mathbf{T}}_m \left(\mathbf{m}'_n - \hat{\boldsymbol{\mu}}\right) : n \in S_i\right\}. \tag{4.39}$$

   (b) Computes the mean squared norm of the calibrated samples within the segment as

   $$\left\{\overline{\tilde{\mathbf{m}}_n^T \tilde{\mathbf{m}}_n} : n \in S_i\right\} \tag{4.40}$$

   (c) Computes the residuals for the segment as

   $$R_i = \left\{\tilde{\mathbf{m}}_n^T \tilde{\mathbf{m}}_n - \overline{\tilde{\mathbf{m}}_n^T \tilde{\mathbf{m}}_n} : n \in S_i\right\} \tag{4.41}$$

3. Once the above is done for all I segments, the sets are joined to get the N residuals as

   $$R = \bigcup_{i=1}^{I} R_i \tag{4.42}$$

It is then left to the Python-supplied `leastsq` algorithm to compute the squared sum of the N residuals. By making repeated calls to `residuals`, the `leastsq` routine is able to minimize over the 8-parameter space. Once the minimization converges, $\hat{\mathbf{T}}_m$ is scaled so that it produces a field strength of 0.507 Gauss. Then the estimates for $\mathbf{T}_m$ and $\boldsymbol{\mu}$ are complete and in accord with equation (4.37).

The actual calibration procedure was carried out several times over the course of this project. This helped to overcome changes in the device response over long periods of time, such as might occur due to aging of the device or the changing of temperature with the seasons. Each time the calibration procedure was carried out,

slightly different results were obtained, but the following results were typical:

$$\mathbf{T}_m = \begin{bmatrix} 1.0026 & 0.01875 & 0.0198 \\ 0.01875 & 0.97809 & -0.0029 \\ 0.0198 & -0.0029 & 0.9891 \end{bmatrix} \tag{4.43}$$

$$\boldsymbol{\mu} = \begin{bmatrix} 19.1 & -70.5 & -5.1 \end{bmatrix} \tag{4.44}$$

These results are for the LSM303D magnetometer [6], which is used in this project. The units for $\boldsymbol{\mu}$ are the raw sensor units. (Divide by 1100 to get units in Gauss.) $\mathbf{T}_m$ is unit-less.

Several conclusions are drawn from these results. The off-diagonal elements indicate strong coupling between the u-axis and the the other axes. Assuming non-orthogonal errors are small, this is most likely due to soft-iron effects. From the diagonal elements, it is deduced that the scale errors are equally severe, also likely due to soft-iron effects. In general, over the course of the project, both $\mathbf{T}_m$ and $\boldsymbol{\mu}$ proved to be fairly constant when the calibration procedure was re-run.

Figure 4.9 shows the result of the first phase of the calibration. The blue curve is the norm of the uncalibrated data samples; the red curve is the calibrated samples. As can be seen, the improvement due to calibration is very significant. The local deviation in the calibrated samples is quite small–approximately 0.2% standard deviation. However, the global deviation is substantially greater. This effect is due to the gain variations within the magnetometer as discussed above and is the reason a piecewise-constant c_i is used.

A comparison between minimizing the global deviations and minimizing the local deviations is plotted in Figure 4.10. The result from minimizing globally is shown in blue, and the result from adaptive-volume minimization is shown in red. It is clear from the figure that minimizing the global deviation fails to remove some local, systematic variations. It is especially obvious around sample number 600.

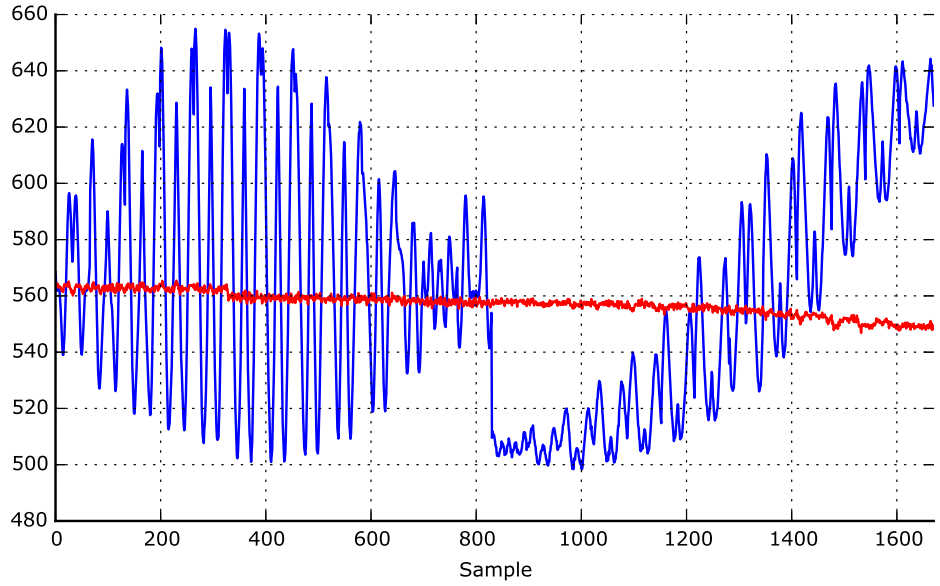

Figure 4.9: Geo-magnetic field signal level. The magnitude of the geo-magnetic field measurement vector is shown before (blue) and after (red) the first phase of calibration with adaptive-volume calibration.

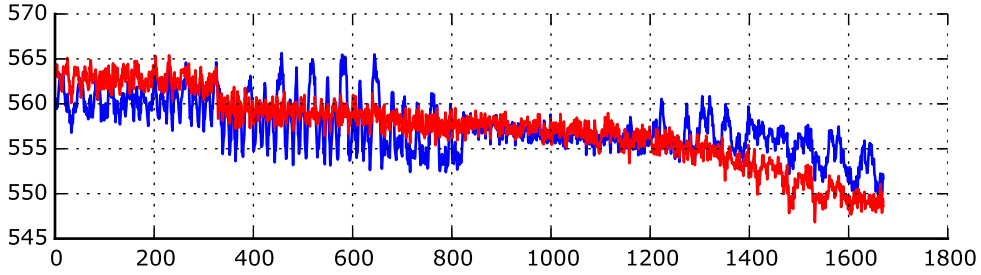

Figure 4.10: Global and adaptive minimization comparison. The adaptive-volume minimization (red curve) clearly eliminates the systematic errors that occur when global minimization is used.

These problems are remedied when local minimization is used (i.e. adaptive-volume minimization).

The adaptive-volume calibration technique described above is not found in the body of literature. Indeed, there are adaptive calibration techniques, but they work under a different set of assumptions. For example, [32] is adaptive to changing environmental conditions over much longer time periods. Likewise, [50] establishes and tracks changes in the calibration using a Kalman filter. This method again assumes much longer time periods, and it is unnecessarily complex for the gain variations seen during this effort. In [51], a technique is presented that adapts the calibration to short-term events which are detected and estimated using external information, such as dynamic current draws. It is possible that this technique could be used to compensate for the gain variations, but this would require extensive characterization of the variations and their causes. Therefore, this approach is not considered a practical alternative. While the adaptive-volume calibration technique is simple in its approach, without it, the quality of the calibration would suffer. As such, it is a valuable addition to the state of the art.

With the ellipsoidal minimization complete, the second phase of the calibration can be implemented. This phase is concerned with correcting the mutual misalignment between the magnetometer's natural basis and the receiver's basis. (Recall that the receiver's basis is defined to be the same as the accelerometer's natural basis.) Equation (4.35) is the minimization that is to be implemented.

Like what is done in the first phase of the magnetometer calibration, it is necessary to compensate for the varying gain of the magnetometer during the data collection. This is done in much the same way as before. Specifically, equation (4.35) is adapted to be

$$\hat{\mathbf{R}}_m = arg\min_{\mathbf{R}_m} \sum_{i=1}^{I} \sum_{n \in S_i} \left(\mathbf{a}_n^T \mathbf{R}_m \tilde{\mathbf{m}}_n - k_i \right)^2, \tag{4.45}$$

such that $\mathbf{R}_m$ is a rotation matrix. The value of k_i is unknown for each segment; but like before, it is approximated as the mean of the signal over the segment. Specifically,

$$k_i = \frac{1}{N_i} \sum_{n \in S_i} \mathbf{a}_n^T \mathbf{R}_m \tilde{\mathbf{m}}_n. \tag{4.46}$$

As noted previously, this minimization requires only three parameters to describe the rotation matrix; the three Euler angles are used for this purpose. Once again the `leastsq` algorithm [43] is used, which requires a `residuals` routine. The routine is created to do the following in order:

1. Parse the 3 parameters into 3 Euler angles and calculate the corresponding candidate rotation matrix $\hat{\mathbf{R}}_m$.

2. For each calibration segment S_i, do the following:

   (a) Apply the candidate rotation matrix to the partially-calibrated measurements within the segment to get

   $$\left\{ \mathbf{m}_n = \hat{\mathbf{R}}_m \tilde{\mathbf{m}}_n : n \in S_i \right\}. \tag{4.47}$$

   (b) Compute the mean of the calibration signal within the segment as

   $$\left\{ \overline{\mathbf{a}_n^T \mathbf{m}_n} : n \in S_i \right\} \tag{4.48}$$

   (c) Compute the residuals for the segment as

   $$R_i = \left\{ \mathbf{a}_n^T \mathbf{m}_n - \overline{\mathbf{a}_n^T \mathbf{m}_n} : n \in S_i \right\} \tag{4.49}$$

3. Once the above is done for all I segments, the sets are joined to get the N residuals as

   $$R = \bigcup_{i=1}^{I} R_i \tag{4.50}$$

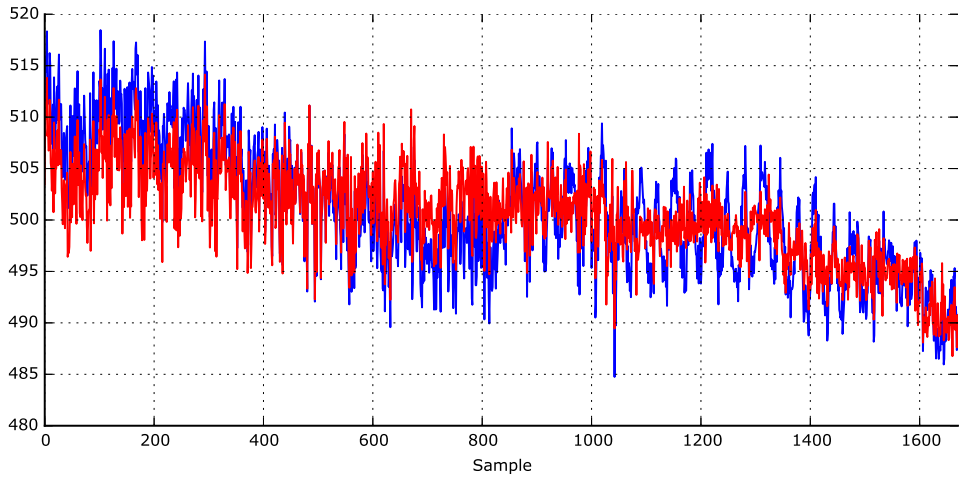

Figure 4.11: Magnetometer and accelerometer inner product. The mutual mis-alignment calibration effect is demonstrated by the inner product between the magnetometer and accelerometer measurement vectors. The blue signal is calibrated but does not include the final mutual mis-alignment calibration step; the red signal includes this step.

The Python-supplied `leastsq` algorithm is then allowed to do the minimization. When it finishes, an estimate of $\mathbf{R}_m$ is given, which compensates for the mutual mis-alignment errors in the measurement data. Based on the results, the mutual mis-alignment errors are not very severe. These are typical values for the $\mathbf{R}_m$ Euler angles expressed in degrees:

$$\text{Euler}\left(\mathbf{R}_m\right) = \begin{bmatrix} 0.25 & 1.07 & -0.57 \end{bmatrix}. \tag{4.51}$$

(The aerospace sequence of Euler angles is used as given in [4].) Figure 4.11 shows the improvement when the mutual mis-alignment correction is applied. The signals plotted are the inner product between the calibrated accelerometer measurements and the magnetometer measurements, both before (blue) and after (red) the mutual mis-alignment calibration. The blue signal shows some systematic error before the mutual mis-alignment calibration; in the red curve, much of this is corrected. This is seen more clearly in the last third of the samples. The variability remaining after

calibration is due to noise and the small accelerations present in the accelerometer measurements.

4.4 Coil Receiver Calibration

4.4.1 Analysis

The need for calibration in the receiver coil sensors is just as significant as with the magnetometer and accelerometer. However, very little is available in the literature with regard to calibration of tri-axial magnetic coil receivers. Many of the coil receivers specified in the literature are deployed in specialized, expensive systems or laboratory environments where brute force calibration is feasible [17, 52]. Also, specialized hardware and techniques have been employed that calibrate the sensors according to the specific needs of the system in question [9]. A large number of other authors approach the problem of calibration in terms of the operating environment (e.g. [17, 52, 11, 20, 19]). This approach serves to correct environmental distortions but does not address the calibration of the coil receiver itself. To this author's knowledge, a general-purpose sensor calibration procedure for tri-axial magnetic coil receivers has not been presented in the literature. Thus, the analysis and design outlined here is an original contribution of this work. Furthermore, the techniques that are adapted first started to appear with the proliferation of MEMS sensors in consumer electronics [53], which occur later in time than much of the work done on magnetic coil receivers. This further indicates that the techniques presented herein are original contributions.

The most obvious approach to calibrating the receiver coils is as follows:

1. Have the beacon emit a single magnetic field.

2. Measure the output of the coil amplifiers at numerous rotations, creating an ellipsoidal locus of measurements as with the magnetometer or accelerometer.

3. Complete the calibration using ellipsoid fitting as with the accelerometer and magnetometer.

4. Like with the magnetometer, use an inner product between the coil signals and the accelerometer to correct mutual mis-alignment errors.

This process can be referred to as calibration in the *raw-signal* domain because it uses measurements of the raw signals from the coil amplifiers. An example of raw-signal calibration can be found in [27].

There are a couple of problems with raw-signal calibration. Firstly, the raw, low-level data is incomplete, meaning it cannot be used to determine the receiver's location and rotation. Furthermore, this data will not always be available to the designer of a calibration algorithm. (Indeed, this is the case for this research project.) Therefore, the raw-signal calibration is not considered a general purpose approach, and something more must be formulated which uses the data available for a location and rotation tracking application. Because of this, the general purpose approach presented in this work is called calibration in the application domain.

Application-domain calibration has several advantages over raw-data calibration:

- It enables developers to do calibration who may have received systems without access to raw-data.

- It enables calibration in the field with only a transmitter and a receiver—no external measurement devices are required.

- It eases design requirements for new systems: It is no longer necessary to provide access to low-level data paths.

Before going further, it is helpful to review the nature of the signals which are detected by the receiver and are required for application domain calibration. There are three distinct, nominally orthogonal magnetic coils in the transmitter beacon. Each of these coils creates a magnetic dipole along its axis. The coils are all excited

by the same carrier signal, but each coil has its own modulation signal. Each of the modulation signals is orthogonal to the others; so that after demodulation, the signal from each beacon coil can be distinguished from the others.

Likewise, the receiver has three nominally orthogonal coils which detect the incoming magnetic fields and apply down-mixing and demodulation. Therefore, the three beacon signals are each sensed in 3-D space and converted to a triad of three-element vectors giving a total of nine measurements. The vector measurements of three beacon fields, corresponding to the three orthogonal excitations, are denoted by $\mathbf{b}_x$, $\mathbf{b}_y$, and $\mathbf{b}_z$, respectively. The three sensing coils of the receiver are denoted as the u-coil, v-coil, and w-coil, respectively. The nine measurements can be expressed in matrix form as

$$\mathbf{B} = \begin{bmatrix} b_{xu} & b_{yu} & b_{zu} \\ b_{xv} & b_{yv} & b_{zv} \\ b_{xw} & b_{yw} & b_{zw} \end{bmatrix} = \begin{bmatrix} \mathbf{b}_x & \mathbf{b}_y & \mathbf{b}_z \end{bmatrix}. \tag{4.52}$$

Ferromagnetic and eddy distortions introduce amplitude, direction, and phase deviations into the received fields. Since some phase distortion is present, the measurements do not all have the same time-phase, and down-mixing and demodulation must be done in the complex space. In other words, $\mathbf{B} \in \mathbb{C}^{3\times 3}$.

For the coil set, the errors which must be calibrated out are similar in form to that of the magnetometer. The types of errors experienced are bias errors, scaling errors, non-orthogonality errors, and mutual mis-alignment errors. The coil receivers are sensitive to signals around the carrier frequency of the transmitter and not to static fields created by permanently mounted devices; therefore, unlike the magnetometer, they do not experience hard-iron errors. However, field distortions are created by the interaction between the impinging fields and the metallic devices in the receiver; therefore, something akin to the magnetometer's soft-iron errors are present. These errors are referred to as the induced errors and denoted by $\mathbf{C}_{ind} \in \mathbb{C}^{3\times 3}$.

The bias error occurring in the field measurements is of a different nature than in the accelerometer and magnetometer. Each coil with its associated amplifier has

an electronic offset. The natural expression of the electronic offset is one real-valued constant for each coil amplifier. In other words, the offset is given as

$$\mathbf{o} = \begin{bmatrix} o_u \\ o_v \\ o_w \end{bmatrix} \in \mathbb{R}^3. \tag{4.53}$$

However, this bias is then forced through the demodulation process $f_{demod} : \mathbb{R}^3 \rightarrow \mathbb{C}^{3\times3}$ giving $\mathbf{O} = f_{demod}(\mathbf{o})$. It should be noted that the electronic offset $\mathbf{o}$ is constant with respect to time (i.e. DC), and in many cases, f_{demod} blocks all constant signals; therefore, in these instances, $\mathbf{O}$ is effectively zero and can be neglected.

There is one other systematic error that affects the fields. It is similar in nature to the non-orthogonality error. The x, y, and z modulations transmitted by the beacon are assumed to be orthogonal. That means that each of the three transmitted fields can be perfectly separated from the others. However, the type of modulation and the bandwidth of the channel affect how well this can be done in practice. Another non-orthogonality matrix can be introduced to correct for this error. This matrix is termed the *demodulation non-orthogonality matrix* and is denoted by $\mathbf{\Gamma}_\perp$. It describes how much of one modulation "bleeds" into the others. With small errors, this matrix is close to the identity matrix.

The complete model for the tri-axial coil receiver and its errors is given in what follows. (Much of the variable notation is shared with that from sections 4.2 and 4.3. This is done for convenience because they have similar meanings. However, the context is different, and the variables in this section are distinct and should not be confused with those in the other sections.)

- At a given location when the receiver is not moving, the impinging fields are constant except for a time varying phase which is due to the AC nature of the transmitted fields and/or imperfect down-mixing. Therefore, the three

impinging field vectors are given by

$$\mathbf{B}e^{j\omega t}, \tag{4.54}$$

where ω is the carrier frequency and $\mathbf{B}$ is expressed in the receiver's frame of reference.

- The measurements taken by the coils are in their natural basis which is slightly rotated from the receiver frame of reference; so the total impinging field in the coils' natural basis is given by:

$$\mathbf{RB}e^{j\omega t} \tag{4.55}$$

- The impinging field induces ferromagnetic and eddy distortions due to the metallic structures and devices on the receiver. Thus, the total stimulus sensed by the coils is given by

$$\mathbf{C}_{ind}\mathbf{RB}e^{j\omega t} \tag{4.56}$$

- The triad of coils are not mounted in a perfectly orthogonal manner; this is corrected by $\mathbf{C}_{\perp}$, where $\mathbf{C}_{\perp}$ is similar in form to that of (4.21). The measurements thus become

$$\mathbf{C}_{\perp}\mathbf{C}_{ind}\mathbf{RB}e^{j\omega t} \tag{4.57}$$

- The sensitivity is not identical for each coil and amplifier which distorts the measurements by

$$\mathbf{C}_{\alpha}\mathbf{C}_{\perp}\mathbf{C}_{ind}\mathbf{RB}e^{j\omega t} \tag{4.58}$$

- Including the offset term, the measured fields become

$$\mathbf{B}' = \mathbf{C}_{\alpha}\mathbf{C}_{\perp}\mathbf{C}_{ind}\mathbf{RB}e^{j\omega t} + \mathbf{O} \tag{4.59}$$

- As stated above, the modulation/demodulation process is not perfectly orthogonal. Incorporating this fact gives

$$\mathbf{B}' = \left(\mathbf{C}_\alpha \mathbf{C}_\perp \mathbf{C}_{ind} \mathbf{R} \mathbf{B} e^{j\omega t} + \mathbf{O}\right) \mathbf{\Gamma}_\perp \tag{4.60}$$

- With no effective loss in generality, the variable substitution is made $\mathbf{O}\mathbf{\Gamma}_\perp \rightarrow \mathbf{O}$. Then

$$\mathbf{B}' = \mathbf{C}_\alpha \mathbf{C}_\perp \mathbf{C}_{ind} \mathbf{R} \mathbf{B} \mathbf{\Gamma}_\perp e^{j\omega t} + \mathbf{O} \tag{4.61}$$

Given the above, recovery of the calibrated fields from the measured fields is then straightforward:

$$\mathbf{B} = \mathbf{R}^T \mathbf{C}_{ind}^{-1} \mathbf{C}_\perp^{-1} \mathbf{C}_\alpha^{-1} \left(\mathbf{B}' - \mathbf{O}\right) \mathbf{\Gamma}_\perp^{-1} e^{-j\omega t} \tag{4.62}$$

$$= \mathbf{T}_B \left(\mathbf{B}' - \mathbf{O}\right) \mathbf{\Gamma}_\perp^{-1} e^{-j\omega t}, \tag{4.63}$$

where $\mathbf{T}_B = \mathbf{R}^T \mathbf{C}_{ind}^{-1} \mathbf{C}_\perp^{-1} \mathbf{C}_\alpha^{-1}$ which is a constant. Thus the calibration model is expressed in a similar form as for the accelerometer and magnetometer, except with the extra term $\mathbf{\Gamma}_\perp^{-1}$ and a carrier phase term.

Once the necessary data is collected, the calibration proceeds. Four steps are required to complete the calibration. The first step is to find the the offset, $\mathbf{O}$. The second is to find $\mathbf{\Gamma}_\perp$. The third step is to find a suitable positive definite representation of $\mathbf{T}_B$. And the fourth step is to find the mutual mis-alignment error between the positive definite representation of $\mathbf{T}_B$ and the receiver frame of reference. Only the third step of the coil calibration is somewhat similar to what is done with the accelerometer and magnetometer; the rest are original to the coil calibration.

The first step in the calibration is to find the offset. In order to do this, $\mathbf{B}$ is set to zero by turning the transmitter off. The measurements are then equal to the offsets.

From equation (4.61) it is trivial to see

$$\mathbf{B}'\Big|_{\mathbf{B}=0} = \mathbf{O}. \tag{4.64}$$

As noted above, in many systems the offset is zero because the demodulation process often blocks DC signals.

After determining the $\mathbf{O}$, the next phase is to determine $\mathbf{\Gamma}_\perp$. The approach is to turn on one transmitter coil at a time; take a series of measurements while holding the receiver still; and use a linear least squares method to find the elements of $\mathbf{\Gamma}_\perp$. Before the details can be described, the following substitutions are made: $\tilde{\mathbf{B}}' = \mathbf{B}' - \mathbf{O}$ and $\tilde{\mathbf{B}} = \mathbf{C}_\alpha \mathbf{C}_\perp \mathbf{C}_{ind} \mathbf{R} \mathbf{B}$, where

$$\tilde{\mathbf{B}} = \begin{bmatrix} \tilde{b}_{xu} & \tilde{b}_{yu} & \tilde{b}_{zu} \\ \tilde{b}_{xv} & \tilde{b}_{yv} & \tilde{b}_{zv} \\ \tilde{b}_{xw} & \tilde{b}_{yw} & \tilde{b}_{zw} \end{bmatrix} = \begin{bmatrix} \tilde{\mathbf{b}}_x & \tilde{\mathbf{b}}_y & \tilde{\mathbf{b}}_z \end{bmatrix}. \tag{4.65}$$

Then (4.61) is rewritten

$$\tilde{\mathbf{B}}' = \tilde{\mathbf{B}} \mathbf{\Gamma}_\perp e^{j\omega t}. \tag{4.66}$$

The carrier-phase term is unneeded and should be removed. In order to do this, it is not necessary to know the phase exactly, but only to normalize the measurements so that the phase of each term remains constant over the course of measurements. There are several ways this can be done, which are covered in a different section of this document. Assuming, then, that the phase is normalized, the following holds:

$$\tilde{\mathbf{B}}' = \tilde{\mathbf{B}} \mathbf{\Gamma}_\perp. \tag{4.67}$$

This equation is a modified version of the demodulated measurements of the coil receiver. In other words, after removing the offset and the phase term, $\tilde{\mathbf{B}}'$ represents the nine complex measurements. The underlying structure of those measurements is given by $\tilde{\mathbf{B}} \mathbf{\Gamma}_\perp$.

The elements of $\mathbf{\Gamma}_\perp$ can be found by evaluating (4.67) with each of the three beacon coils excited one at a time. First, only the beacon coil with the x-modulation is excited; equation (4.67) becomes

$$\tilde{\mathbf{B}}' = \begin{bmatrix} \tilde{\mathbf{b}}_x & 0 & 0 \end{bmatrix} \mathbf{\Gamma}_\perp \tag{4.68}$$

$$= \begin{bmatrix} \tilde{b}_{xu}\gamma_{11} & \tilde{b}_{xu}\gamma_{12} & \tilde{b}_{xu}\gamma_{13} \\ \tilde{b}_{xv}\gamma_{11} & \tilde{b}_{xv}\gamma_{12} & \tilde{b}_{xv}\gamma_{13} \\ \tilde{b}_{xw}\gamma_{11} & \tilde{b}_{xw}\gamma_{12} & \tilde{b}_{xw}\gamma_{13} \end{bmatrix}, \tag{4.69}$$

where

$$\mathbf{\Gamma}_\perp = \begin{bmatrix} \gamma_{11} & \gamma_{12} & \gamma_{13} \\ \gamma_{21} & \gamma_{22} & \gamma_{23} \\ \gamma_{31} & \gamma_{32} & \gamma_{33} \end{bmatrix}. \tag{4.70}$$

Obviously, (4.68) does not have a unique solution, and so further constraints are required on $\mathbf{\Gamma}_\perp$. It is known that $\mathbf{\Gamma}_\perp$ is near the identity matrix when the errors are small; therefore, a reasonable choice is to set the diagonal elements of $\mathbf{\Gamma}_\perp$ to unity, i.e.

$$\mathbf{\Gamma}_\perp = \begin{bmatrix} 1 & \gamma_{12} & \gamma_{13} \\ \gamma_{21} & 1 & \gamma_{23} \\ \gamma_{31} & \gamma_{32} & 1 \end{bmatrix}. \tag{4.71}$$

An alternative choice is "power conserving", i.e.

$$\mathbf{\Gamma}_\perp = \begin{bmatrix} \sqrt{1 - \|\gamma_{12}\|^2 - \|\gamma_{13}\|^2} & \gamma_{12} & \gamma_{13} \\ \gamma_{21} & \sqrt{1 - \|\gamma_{21}\|^2 - \|\gamma_{23}\|^2} & \gamma_{23} \\ \gamma_{31} & \gamma_{32} & \sqrt{1 - \|\gamma_{31}\|^2 - \|\gamma_{32}\|^2} \end{bmatrix}, \tag{4.72}$$

but if the errors are small, the difference between these two choices is negligible. The unity diagonal choice of (4.71) maintains linearity in the γ coefficients; so it is used.

With this constraint imposed on $\mathbf{\Gamma}_\perp$, $\tilde{\mathbf{b}}_x = \tilde{\mathbf{b}}'_x$, and (4.68) have a unique solution. However, in the presence of measurement noise, it is better to take numerous measurements and construct a least squares problem. For N measurements, with only the x-coil turned on, the problem is divided into two least-squares problems with the solutions as follows:

$$\gamma_{12} = \frac{\beta_x^H \beta_y}{\|\beta_x\|^2} \quad \text{and} \quad \gamma_{13} = \frac{\beta_x^H \beta_z}{\|\beta_x\|^2}. \tag{4.73}$$

With only the y-coil activated, a similar derivation is performed giving:

$$\gamma_{21} = \frac{\beta_y^H \beta_x}{\|\beta_y\|^2} \quad \text{and} \quad \gamma_{23} = \frac{\beta_y^H \beta_z}{\|\beta_y\|^2}, \tag{4.74}$$

and with only the z-coil activated:

$$\gamma_{31} = \frac{\beta_z^H \beta_x}{\|\beta_z\|^2} \quad \text{and} \quad \gamma_{32} = \frac{\beta_z^H \beta_y}{\|\beta_z\|^2}, \tag{4.75}$$

where $\beta_x, \beta_y, \beta_z \in \mathbb{C}^{3N}$ are constructed by concatenating the N x, y, and z measurements, respectively. In other words,

$$\begin{aligned}
\beta_x &= \begin{bmatrix} \tilde{b}'_{xu,1} & \tilde{b}'_{xv,1} & \tilde{b}'_{xw,1} & \tilde{b}'_{xu,2} & \tilde{b}'_{xv,2} & \tilde{b}'_{xw,2} & \cdots & \tilde{b}'_{xu,N} & \tilde{b}'_{xv,N} & \tilde{b}'_{xw,N} \end{bmatrix}^T \\
\beta_y &= \begin{bmatrix} \tilde{b}'_{yu,1} & \tilde{b}'_{yv,1} & \tilde{b}'_{yw,1} & \tilde{b}'_{yu,2} & \tilde{b}'_{yv,2} & \tilde{b}'_{yw,2} & \cdots & \tilde{b}'_{yu,N} & \tilde{b}'_{yv,N} & \tilde{b}'_{yw,N} \end{bmatrix}^T \\
\beta_z &= \begin{bmatrix} \tilde{b}'_{zu,1} & \tilde{b}'_{zv,1} & \tilde{b}'_{zw,1} & \tilde{b}'_{zu,2} & \tilde{b}'_{zv,2} & \tilde{b}'_{zw,2} & \cdots & \tilde{b}'_{zu,N} & \tilde{b}'_{zv,N} & \tilde{b}'_{zw,N} \end{bmatrix}^T
\end{aligned} \tag{4.76}$$

This completes the solution of $\mathbf{\Gamma}_\perp$, and with the solution to $\mathbf{O}$ already complete, the next step is to find $\mathbf{T}_B$. This begins in much the same way as with the accelerometer and magnetometer. That is, this step seeks to minimize the deviation of the squared norm of the samples. In other words, with perfect samples and perfect calibration the following holds:

$$(\mathbf{B}' - \mathbf{O})^H \mathbf{T}_B^H \mathbf{T}_B (\mathbf{B}' - \mathbf{O}) = \mathbf{C}, \tag{4.77}$$

where $\mathbf{C}$ is constant. Therefore, the minimization proceeds in much the same way as for the accelerometer and magnetometer with

$$\hat{\mathbf{A}} = arg\min_{\mathbf{A}} \sum_{n=1}^{N} \left\| (\mathbf{B}'_n - \mathbf{O})^H \mathbf{A} (\mathbf{B}'_n - \mathbf{O}) - \mathbf{C} \right\|^2. \tag{4.78}$$

such that $\mathbf{A}$ is Hermitian positive definite, i.e. $\mathbf{A} = \mathbf{A}^H$ and $\mathbf{z}^H\mathbf{A}\mathbf{z} > 0$ for all $\mathbf{z} \in \mathbb{C}^3$, $\mathbf{z} \neq \mathbf{0}$. Once the minimization is complete, a solution for $\mathbf{T}_B$ can be found with

$$\hat{\mathbf{T}}_B = \sqrt{\hat{\mathbf{A}}}. \tag{4.79}$$

Equation (4.79) has many solutions; finding the correct one is the last step required to complete the calibration. With the magnetometer, the "true" solution differs from the positive definite one by a rotation matrix. Finding this is equivalent to finding the mutual mis-alignment error. For the coil receiver, complex numbers are involved, and so the "true" solution to (4.79) differs from the positive definite one by a unitary matrix rather than a rotation matrix. This is referred to as "finding the mutual mis-alignment error"; however, since complex phase is involved and not just a pure rotation matrix, using the term "mutual mis-alignment error" is not strictly correct. Nevertheless, this term suffices for the purposes of this work.

The mutual mis-alignment error is modeled as a complex, unitary matrix, $\mathbf{Q} \in U(3)$. Expressing $\mathbf{Q}$ in the context of the calibration equation of (4.63) gives

$$\mathbf{B} = \mathbf{Q}\mathbf{T}_B (\mathbf{B}' - \mathbf{O}) \boldsymbol{\Gamma}_{\perp}^{-1} e^{-j\omega t}. \tag{4.80}$$

(To keep the notation uncluttered, the hat is dropped from $\mathbf{T}_B$.) At this point in the derivation, $\mathbf{Q}$ is the only remaining unknown. To begin to find the solution for $\mathbf{Q}$, the calibrated coil signals are expressed in the earth frame of reference

$$\mathbf{B}^g = \underset{r:g}{\mathbf{R}}\mathbf{Q}\mathbf{T}_B (\mathbf{B}' - \mathbf{O}) \boldsymbol{\Gamma}_{\perp}^{-1} e^{-j\omega t}, \tag{4.81}$$

where $\underset{r:g}{\mathbf{R}}$ rotates from the receiver frame of reference to the earth frame of reference and is estimated via the TRIAD method [54, 55] which is described later. This effectively reverses the mechanical rotation performed during the data collection. The data which is needed to do the estimation consists only of the accelerometer and magnetometer measurements, both of which must be calibrated beforehand in order to give a reliable result.

Because the mechanical rotation is effectively removed by $\underset{r:g}{\mathbf{R}}$, there is no variation in $\mathbf{B}^g$ except for the carrier phase term, and if this term is also removed, there will be no variation at all when proper calibration has been achieved. Therefore, in order to complete the calibration process, the carrier phase term must be removed. The most obvious way to accomplish this is to estimate and then remove the phase as is done when finding $\mathbf{\Gamma}_\perp$. However, this cannot be done perfectly, so another method is sought.

Because of the imperfections in carrier phase *estimation*, a method of phase *cancellation* is sought. Since $\mathbf{B}^g$ is in the earth frame of reference, every element of $\mathbf{B}^g$ can be multiplied by a phase term composed of the phase of the conjugate of a specific element of $\mathbf{B}^g$. For instance, if the phase of b^g_{xu} is expressed by

$$e^{-j\angle b^g_{xu}} = e^{j\theta}e^{-j\omega t}, \tag{4.82}$$

where θ is the unknown constant phase term of b^g_{xu}, then

$$e^{j\angle b^g_{xu}}\mathbf{B}^g = \underset{r:g}{\mathbf{R}}\mathbf{Q}\mathbf{T}_B\left(\mathbf{B}' - \mathbf{O}\right)\mathbf{\Gamma}_\perp^{-1}e^{-j\theta}. \tag{4.83}$$

In this instance, each element of $\mathbf{B}^g$ is shifted in phase by a constant, but the variable phase term is canceled. This technique has an undesirable defect: namely, noise and errors in the estimation of $\underset{r:g}{\mathbf{R}}$ become phase cancellation errors.

To get around this defect, it is necessary to do phase cancellation before rotating to the earth frame of reference, i.e. by using equation (4.63). When this is done, the

phase cannot be canceled using the phase of an element of $\mathbf{B}$ since the phase of a given element changes with the mechanical rotation as well as with time. In other words, if for the b_{xu} element $e^{-j\angle b_{xu}} = e^{j\theta}e^{-j\omega t}$, then θ will not be constant with rotation. To get around this, $\mathbf{B}$ is transformed by a non-linear mapping $\{h\colon \mathbb{C}^{3\times 3} \mapsto \mathbb{C}^{3\times 3}\}$, where

$$h\Big(\begin{bmatrix}\mathbf{x} & \mathbf{y} & \mathbf{z}\end{bmatrix}\Big) = \begin{bmatrix}\mathbf{y}^* \otimes \mathbf{z} & \mathbf{z}^* \otimes \mathbf{y} & \mathbf{x}^* \otimes \mathbf{y}\end{bmatrix}, \quad \mathbf{x},\mathbf{y},\mathbf{z} \in \mathbb{C}^3, \tag{4.84}$$

and $\otimes$ is a simple adaptation of the cross product for $\mathbb{C}^3$ vectors. Specifically,

$$\mathbf{x} \otimes \mathbf{y} \triangleq (\mathbf{x} \times \mathbf{y})^* \quad \forall \mathbf{x},\mathbf{y} \in \mathbb{C}^3,$$

where $\times$ is the common cross product operator which uses complex multiplications rather than real multiplications. With conjugate appended to this definition, if $\mathbf{z} = \mathbf{x} \otimes \mathbf{y}$, then the expected orthogonal relationships hold

$$\mathbf{x}^H\mathbf{z} = 0 \quad \text{and} \quad \mathbf{y}^H\mathbf{z} = 0. \tag{4.85}$$

With the mapping of equation (4.84) defined, it is applied to $\mathbf{B}$

$$\mathbf{H} = h(\mathbf{B})\,. \tag{4.86}$$

Because of the conjugate operators in (4.84), the $e^{-j\omega t}$ term is canceled, and $\mathbf{H}$ varies only with mechanical rotation and is not dependent on t. Also, $\mathbf{H}$ is expressed in the receiver frame of reference just like $\mathbf{B}$.

It is important to ensure that $\mathbf{H}$ is well conditioned. This is done by choosing a proper location to perform the calibration procedure. If the location of the receiver is positioned along one of the physical axes of the transmitter and if only minor distortion is present at that location, the impinging transmitter fields are nearly orthogonal with only slight phase shifts between them. This means that $\mathbf{B}$ is close to orthogonal, and therefore, $\mathbf{H}$ will also be close to orthogonal. Using this setup for

the calibration procedure guarantees $\mathbf{H}$ to be well conditioned, and calibration can proceed.

At this point in the calibration process, all of the calibration factors except $\mathbf{Q}$ are established ($\underset{r:g}{\mathbf{R}}$, $\mathbf{T}_B$, $\mathbf{O}$, and $\mathbf{\Gamma}_{\perp}^{-1}$). Given the measurements $\mathbf{B}'$, the only remaining unknown is $\mathbf{Q}$; after it is established, the calibration will be complete. Therefore, the goal for this step of the calibration is to find $\mathbf{Q}$. With the carrier phase term canceled, $\mathbf{H}$ should be constant when it is expressed in the earth frame of reference. In other words $\mathbf{H}^g = \underset{r:g}{\mathbf{R}}\mathbf{H}$. should be constant. Therefore, the following minimization can be performed:

$$\hat{\mathbf{Q}} = arg\min_{\mathbf{Q}} \sum_{n=1}^{N} \|\mathbf{H}^g - \mathbf{C}\|^2 \tag{4.87}$$

$$= arg\min_{\mathbf{Q}} \sum_{n=1}^{N} \left\| \underset{r:g}{\mathbf{R}}\mathbf{H} - \mathbf{C} \right\|^2 \tag{4.88}$$

$$= arg\min_{\mathbf{Q}} \sum_{n=1}^{N} \left\| \underset{r:g}{\mathbf{R}}\, h(\mathbf{B}) - \mathbf{C} \right\|^2 \tag{4.89}$$

$$= arg\min_{\mathbf{Q}} \sum_{n=1}^{N} \left\| \underset{r:g}{\mathbf{R}}\, h\big(\mathbf{Q}\mathbf{T}_B\left(\mathbf{B}' - \mathbf{O}\right)\mathbf{\Gamma}_{\perp}^{-1}\big) - \mathbf{C} \right\|^2, \tag{4.90}$$

where $\mathbf{Q} \in U(3)$ and $\mathbf{C}$ is a constant whose value will be discussed in the next section.

With the mutual mis-alignment error term (i.e. $\mathbf{Q}$) having been found, the calibration parameters for the coil receiver are all determined. Applying them to the measurements $\mathbf{B}'$ in accord with equation (4.80) gives the calibrated measurements $\mathbf{B}e^{j\omega t}$. The full expression for the calibrated measurements is given by

$$\mathbf{B}e^{j\omega t} = \mathbf{Q}\mathbf{T}_B\left(\mathbf{B}' - \mathbf{O}\right)\mathbf{\Gamma}_{\perp}^{-1}, \tag{4.91}$$

where all terms are in the receiver frame of reference and $\mathbf{B}$ is not dependent on t. In general, $\mathbf{B}$ is the term of interest, and the carrier phase term is undesired. Therefore,

cancellation or estimation and correction of the carrier phase will be performed; and so, $e^{j\omega t}$ can be dropped from (4.91) without a loss of generality.

4.4.2 Implementation and Results

For the calibration of the coil receiver, there are four unknown parameters: $\mathbf{Q}$, $\mathbf{T}_B$, $\mathbf{O}$, and $\mathbf{\Gamma}_\perp$. Likewise, the process for calibration consists of four main steps, corresponding to the four parameters. The steps are as follows:

1. Finding $\mathbf{O}$. This consists of taking a series of measurements with the transmitter off

2. Finding $\mathbf{\Gamma}_\perp$. This consists of taking a series of measurements with only one transmitter coil turned on at a time and solving the least-squares systems of equations (4.73), (4.74), and (4.75).

3. Finding $\mathbf{T}_B$. This consists in solving the minimization of equation (4.78).

4. Finding $\mathbf{Q}$. This consists in solving the minimization of equation (4.87).

The calibration process begins with the first step, which is finding $\mathbf{O}$. In general, the technique for collecting the data for this step is different than what is described in section 4.1.3. Firstly, it is different in that the transmitter is powered off. Secondly, the amount of data required is not as great. Because no signal is present in the air, rotation of the receiver is not necessary; therefore, all the data can be collected at a single orientation. The amount of data is determined by the amount of data needed to effectively average out the electronic noise. For this project, 256 samples is sufficient.

As has been previously stated, calibration was repeated several times during the course of this project, and the results of this step did not change significantly over

that time. Typical results of this step of the calibration were

$$\mathbf{O} = \begin{bmatrix} -0.17 + j0.57 & -1.01 - j1.57 & -4.32 - j4.07 \\ -0.13 - j0.76 & -0.45 + j0.06 & -4.54 - j4.38 \\ -1.31 - j0.37 & -0.33 - j1.18 & -6.68 - j6.87 \end{bmatrix}, \tag{4.92}$$

in device-raw units. For the x-coil and y-coil signals (i.e. first and second columns), the offsets are all but insignificant. This indicates the demodulation process effectively blocks any DC offsets coming from the coil amplifiers for the x-type and y-type modulations. For the z-coil signal (i.e. third column), the offsets are small. With strong incoming signals, offsets the z-coil offsets are negligible, but, as the signal becomes weaker, the offsets become significant. This indicates that the demodulation process for the z-type modulation does not perfectly filter the DC portion of the coil amplifier output.

The second step in the process is to find the demodulation non-orthogonality matrix, $\mathbf{\Gamma}_\perp$. Again, the data collection technique is different from that in section (4.1.3). Three separate collections have to be made. During each of the collections, only one coil is excited, and the others are off. This is done once each for the x-coil, y-coil, and z-coil. It is inferred from equations (4.73), (4.74), and (4.75) that the solution is indifferent to the receiver rotation; therefore, data is only collected with one orientation.

Like $\mathbf{O}$, the results for this step in the calibration did not change significantly over the course of the project. Typical results were

$$\mathbf{\Gamma}_\perp = \begin{bmatrix} 1.0 & 0.00067 - j0.00055 & 0.00475 - j0.00038 \\ -0.00015 + j0.00049 & 1.0 & 0.00540 - j0.00137 \\ 0.00017 - j0.0001 & 0.00012 - j0.0146 & 1.0 \end{bmatrix}. \tag{4.93}$$

These results are interpreted as follows:

1. Based on the very small values in the first column, the x-type signals experience almost no cross-talk (i.e. interference) from the y- and z-type modulations.

2. The y-type signals experience almost no cross-talk from the x-type modulation, but it experiences substantial cross-talk from the z-type signals—approximately 1.5%. This interference is 90° out of phase with the z-coil signals which cause it. This is the highest level of cross-talk experienced between the modulations.

3. The z-type signals experience small but significant cross-talk from both of the other modulations—on the order of 0.5%. There is very little phase shift between the cross-talk and its cause.

The inter-modulation cross-talk and interference matrix display no symmetry or uniformity. In other words, the structure of $\mathbf{\Gamma}_{\perp}$ is somewhat unexpected. The cause of this result is unknown. A reasonable guess can be made based on prior knowledge of the modulation scheme, but no effort is exerted to find the true cause. This is deemed out-of-scope for this work and not necessary for this work's goals.

The third step in the calibration of the coil receiver is to find $\mathbf{T}_B$ through the minimization of (4.78). This equation is restated here for convenience and clarity:

$$\hat{\mathbf{T}}_B = arg\min_{\mathbf{T}_B} \sum_{n=1}^{N} \left\| \left(\mathbf{B}'_n - \mathbf{O}\right)^H \mathbf{T}_B^H \mathbf{T}_B \left(\mathbf{B}'_n - \mathbf{O}\right) - \mathbf{C} \right\|^2 . \tag{4.94}$$

such that $\mathbf{T}_B$ is Hermitian positive definite, i.e. $\mathbf{T}_B = \mathbf{T}_B^H$ and $\mathbf{z}^H \mathbf{T}_B \mathbf{z} > 0$ for all $\mathbf{z} \in \mathbb{C}^3$, $\mathbf{z} \neq \mathbf{0}$. This is similar to the scalar calibration or the ellipsoidal fitting minimization of the accelerometer and magnetometer; but, instead of minimization against a scalar constant, the minimization involves the squared norm of a matrix, for which the Frobenius norm is used [35].

The value of $\mathbf{C}$ is unknown with absolutely no practical way of determining its value. Therefore, it is treated in much the same way as the constant of minimization is for the magnetometer (see section (4.3.2)). Specifically, it is treated as a piecewise constant term over a calibration segment, and its value is taken to be the mean of

$(\mathbf{B}'_n - \mathbf{O})^H \mathbf{T}_B^H \mathbf{T}_B (\mathbf{B}'_n - \mathbf{O})$ over the calibration segment. With this approach, it is necessary to fix $\mathbf{T}_B[1,1] = 1.0$; otherwise, the minimization will converge to the trivial solution, $\mathbf{T}_B = 0$. With this adjustment, (4.94) is adapted to

$$\hat{\mathbf{T}}_B = arg \min_{\mathbf{T}_B} \sum_{i=1}^{I} \sum_{n \in S_i} \left\| (\mathbf{B}'_n - \mathbf{O})^H \mathbf{T}_B^H \mathbf{T}_B (\mathbf{B}'_n - \mathbf{O}) - \mathbf{C}_i \right\|^2, \tag{4.95}$$

where S_i, N_i, and I take the same meaning as in section 4.3.2, and

$$\mathbf{C}_i = \frac{1}{N_i} \sum_{n \in S_i} (\mathbf{B}'_n - \mathbf{O})^H \mathbf{T}_B^H \mathbf{T}_B (\mathbf{B}'_n - \mathbf{O}). \tag{4.96}$$

This step in the calibration again uses the Python `leastsq` algorithm [43] to minimize (4.95). The parameters are the elements of $\mathbf{T}_B$. Since the matrix is Hermitian positive definite and since $\mathbf{T}_B[1,1] = 1.0$ is fixed, eight parameters are required to specify the matrix. Included in this are two real diagonal elements and the three complex, off diagonal elements. For this implementation, the `residuals` routine performs the following:

1. Parse the 8 parameters into a candidate $\hat{\mathbf{T}}_B$.
2. For each calibration segment S_i, do the following:
   (a) Apply the candidate $\hat{\mathbf{T}}_B$ to the measurements within the segment to get

$$\left\{ \tilde{\mathbf{B}}_n = \hat{\mathbf{T}}_B (\mathbf{B}'_n - \mathbf{O}) : n \in S_i \right\}. \tag{4.97}$$

   (b) Compute $\mathbf{C}$ for the samples within the segment

$$\mathbf{C}_i = \left\{ \overline{\tilde{\mathbf{B}}_n^H \tilde{\mathbf{B}}_n} : n \in S_i \right\} \tag{4.98}$$

(c) Compute the residuals for the segment as

$$R_i = \left\{ \tilde{\mathbf{B}}_n^H \tilde{\mathbf{B}}_n - \overline{\tilde{\mathbf{B}}_n^H \tilde{\mathbf{B}}_n} : n \in S_i \right\} \tag{4.99}$$

3. Once the above is done for all I segments, the sets are joined to get the N residuals as

$$R = \bigcup_{i=1}^{I} R_i \tag{4.100}$$

It is then left to the Python-supplied `leastsq` algorithm to compute the squared sum of the N residuals. By making repeated calls to `residuals`, the `leastsq` algorithm is able to minimize over the 8-parameter space to get $\hat{\mathbf{T}}_B$.

This however does not represent the final value of $\hat{\mathbf{T}}_B$. Because $\hat{\mathbf{T}}_B[1,1] = 1.0$ is fixed, $\hat{\mathbf{T}}_B$ must be scaled to the correct value. This involves calculating the distance from the receiver to the transmitter using the Kuipers' algorithm [4]. The true distance is known to be 36 feet; so, based on the calculated value, $\hat{\mathbf{T}}_B$ is scaled to agree with the true value.

When doing this, it is apparent that the chosen location for performing the calibration is very important. If a location with strong distortions had been chosen, then the scaling factor would have been in error. Fortunately, this was anticipated, and a suitable location was chosen at the outset.

Over the course of the many calibrations that the coil receiver was put through, the following results were typical:

$$\mathbf{T}_B = \begin{bmatrix} 1.07888 & 0.02068 + j0.00051 & -0.05251 - j0.03968 \\ 0.02068 - j0.00051 & 1.07698 & 0.00126 + j0.00012 \\ -0.05251 + j0.03968 & 0.00126 - j0.00012 & 1.08161 \end{bmatrix}. \tag{4.101}$$

In general, this result shows that the coupling between the axes of the coil receiver is fairly strong, which makes calibration a vital step in achieving this project's goals.

At this step in the calibration process, it is beneficial to examine the effectiveness of the calibration so far. A *field calibration matrix* is defined as

$$\mathbf{M} = \sqrt{\tilde{\mathbf{B}}^H \tilde{\mathbf{B}}}, \tag{4.102}$$

such that $\mathbf{M} = \mathbf{M}^H$. Using the Kuipers' algorithm [4], this matrix will be all that is needed to determine the receiver's position. For this project, the receiver's orientation is also needed; therefore, calibration cannot stop at this step. However, examining $\mathbf{M}$ at this point does give a good indication of how well the Kuipers' position estimation will perform.

Figure 4.12 shows the diagonal elements of $\mathbf{M}$ both before and after calibration. The upper off-diagonal elements are shown in Figure 4.13 with both real and imaginary parts. (Because $\mathbf{M}$ is Hermitian positive definite, the lower off-diagonal elements are conjugates of the upper ones.)

An unusual effect can be seen in the plots, which is more pronounced in the imaginary parts of the off-diagonal elements. Sudden step-wise jumps followed by plateaus of constant value are seen in the data. During the data collection, the process had to be stopped temporarily to download the data. These stops and starts correspond to the location of the sudden jumps. As can be seen in the plots, the calibration effectively removes the rotational deviations, and only noise and these jumps remain. After studying the coil receiver front-end processing, it became apparent that these jumps are due to a problem in the startup configuration. As such, they are out-of-scope for this project and are considered a non-issue. So, neglecting the step-wise jumps, it is apparent that the calibration through this step is very effective. Errors on the order of 10% are reduced to sub-1% by calibration.

The fourth step in the calibration of the coil receiver is to find $\mathbf{Q}$ using equation (4.87) which is restated here for convenience.

$$\hat{\mathbf{Q}} = arg \min_{\mathbf{Q}} \sum_{n=1}^{N} \left\| \underset{r:g}{\mathbf{R}}\, h\left(\mathbf{Q}\mathbf{T}_B \left(\mathbf{B}' - \mathbf{O}\right) \mathbf{\Gamma}_{\perp}^{-1}\right) - \mathbf{C} \right\|^2, \tag{4.103}$$

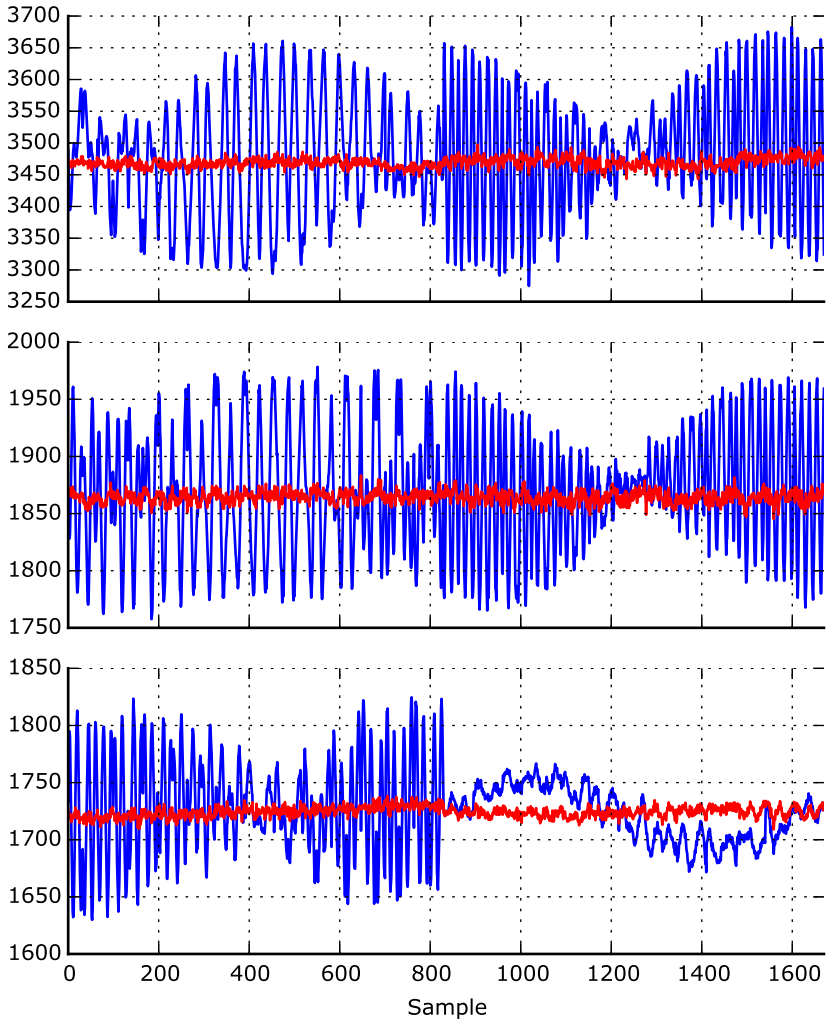

Figure 4.12: Field calibration matrix diagonals. The diagonal elements of the field calibration matrix are shown before (blue) and after (red) this step of calibration. In other words, the mutual mis-alignment error is not corrected for this plot. The figure is displayed in raw sensor units. The plots correspond to $\mathbf{M}_{1,1}$, $\mathbf{M}_{2,2}$, and $\mathbf{M}_{3,3}$, top-to-bottom, respectively.

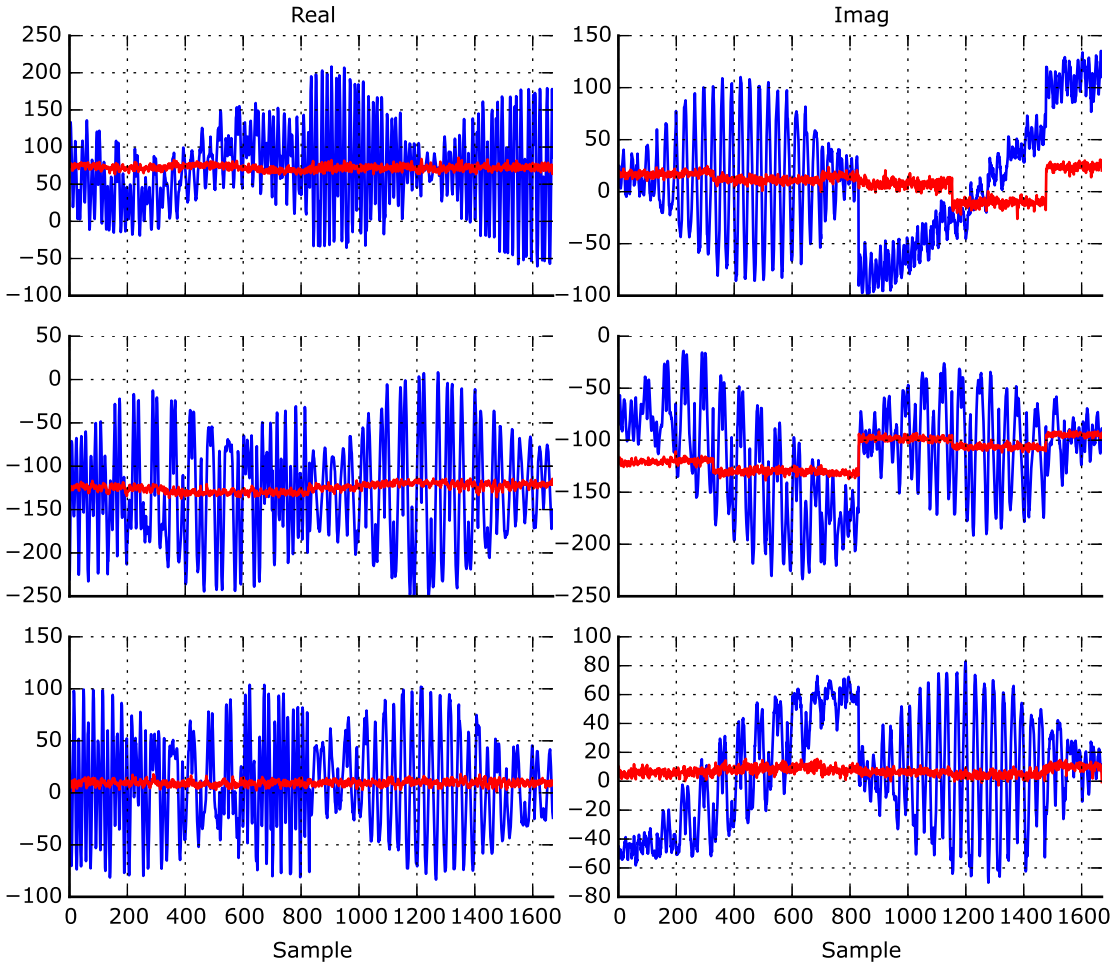

Figure 4.13: Field calibration matrix off-diagonals. Real and imaginary parts of the off-diagonal elements of the field calibration matrix are shown before (blue) and after (red) this step of calibration. In other words, the mutual mis-alignment error is not corrected for this plot. The figure is displayed in raw sensor units. The rows of the plots correspond to $\mathbf{M}_{1,2}$, $\mathbf{M}_{1,3}$, and $\mathbf{M}_{2,3}$, top-to-bottom, respectively.

where $\mathbf{Q} \in U(3)$ and $\mathbf{C}$ is the constant of minimization. This step is analogous to finding the mutual mis-alignment calibration in the magnetometer case, but $\mathbf{Q}$ is in $U(3)$ rather than a rotation matrix.

This step uses some of the same approaches that are used previously. Firstly, the minimization is applied in piecewise-constant fashion, where the constant of minimization, $\mathbf{C}_i$, is the mean for calibration segment i. Next, the Python `leastsq` tools are used [43]. Lastly, the Frobenius norm is used to compute the matrix norm.

The minimization seeks to find an estimate for $\mathbf{Q}$, which can be parametrized with eight real numbers [56]. With $\mathbf{C}_i$ changing with each calibration segment, it is necessary to fix the global phase of $\mathbf{Q}$ so that the calibration segments are consistent in phase with each other. This is done by forcing $\angle\mathbf{Q}[3,3] = 0$. There are numerous techniques for parametrizing $\mathbf{Q}$ [57, 58, 59, 60], but the simple approach from [61] is chosen. Using this, the `residuals` routine is designed to perform the following:

1. Parse the 8 parameters into a candidate $\hat{\mathbf{Q}}$ using code from [61].
2. For each calibration segment S_i, do the following:
   (a) Apply the candidate $\hat{\mathbf{Q}}$ to the measurements within the segment to get

$$\left\{ \mathbf{B}_n^g = \underset{r:g}{\mathbf{R}}\, h\Big(\hat{\mathbf{Q}}\mathbf{T}_B\left(\mathbf{B}' - \mathbf{O}\right)\mathbf{\Gamma}_\perp^{-1}\Big) \right\}. \tag{4.104}$$

   (b) Compute $\mathbf{C}$ for the samples within the segment

$$\mathbf{C}_i = \left\{ \overline{\mathbf{B}_n^g} : n \in S_i \right\} \tag{4.105}$$

   (c) Compute the residuals for the segment as

$$R_i = \left\{ \mathbf{B}_n^g - \overline{\mathbf{B}_n^g} : n \in S_i \right\} \tag{4.106}$$

3. Once the above is done for all I segments, the sets are joined to get the N residuals as

$$R = \bigcup_{i=1}^{I} R_i \tag{4.107}$$

It is then left to the Python-supplied `leastsq` algorithm to compute the squared sum of the N residuals. By making repeated calls to `residuals`, the `leastsq` algorithm is able to minimize over the 8-parameter space to get $\hat{\mathbf{Q}}$.

Over the course of the many calibrations that the coil receiver was put through, the following results were typical:

$$\mathbf{Q} = \begin{bmatrix} 0.99814 - j0.01297 & 0.00298 - j0.03826 & -0.02793 - j0.03598 \\ -0.00290 - j0.03886 & 0.99909 + j0.00215 & 0.01705 + j0.00073 \\ 0.02752 - j0.03566 & -0.01836 - j0.00048 & 0.99882 + j0.0 \end{bmatrix}. \tag{4.108}$$

This is the last piece of information needed to complete the coil calibration, but this numeric result is not easy to understand; therefore, a series of plots are shown to examine the effectiveness of the calibration algorithm. Each of the plots is made using the measurements of the field component matrix which were collected during the calibration. Also, each is made with the fields expressed in the earth frame of reference. Figure 4.14 shows the fields without any calibration applied. Figure 4.15 shows the fields with all steps of calibration except the mutual mis-alignment step. Figure 4.16 shows the fields with all steps including the mutual mis-alignment correction. (These figures each represent a version of the 3×3 field component matrix. Because of this, a 3×3 diagram is used to represent the matrix, with each sub-plot corresponding to the element in the respective position of the matrix.)

These results are quite telling. First, without any calibration, the variation in the signals is extreme. Using these signals in a tracking algorithm will give dubious results. Second, as is seen in Figure 4.15, after the first three steps of coil calibration, the signal variations are still very strong. This is the case even though the first

three steps of calibration are quite effective as shown in Figure 4.13. This indicates that the mutual mis-alignment calibration is of dire importance. Indeed, after it is applied, the results show vast improvement. Figure 4.16 shows that almost all of the variations have been removed. After this, the signals are indeed suitable for a tracking algorithm. (Note that this figure shows the step-wise jumps and plateaus as are present in Figure 4.13. This is a system issue and not a calibration problem.)

Figure 4.17 illustrates the overall effectiveness of the calibration using the before and after signals. For clarity, only the real parts are shown. A seemingly high level of noise is seen on some of the calibrated signals, for example, the lower-left figure ($\mathbf{B}^g[3,1]$). This is not an issue with the calibration procedure, but rather, it results from noise-like variations in $\underset{r:g}{\mathbf{R}}$. With this in mind, it is clearly seen that the calibration procedure is quite effective at removing systematic variations.

4.5 Conclusion

Without a doubt, the calibration of the three receiver sensors is a vital prerequisite for the development of a tracking algorithm. For the accelerometer, calibration is performed using well-known procedures. For the magnetometer, well-known tactics are again used. However, because of the drift of the magnetometer gain, an adaptive calibration technique is used to allow the magnetometer to achieve the best results. This technique is termed adaptive-volume calibration. To this author's knowledge, this sort of adaptive calibration has not been applied to MEMS tri-axial sensor device calibration; therefore, this is seen as an original piece of work.

The most significant original contribution from this chapter comes from the calibration of the tri-axial coil receiver, which is nearly all original work. The data available to a developer may not include the raw sensor coil measurements (as is the case in this project); therefore, calibration must be performed on demodulated data. This is termed "application-domain calibration", since the demodulated data is used

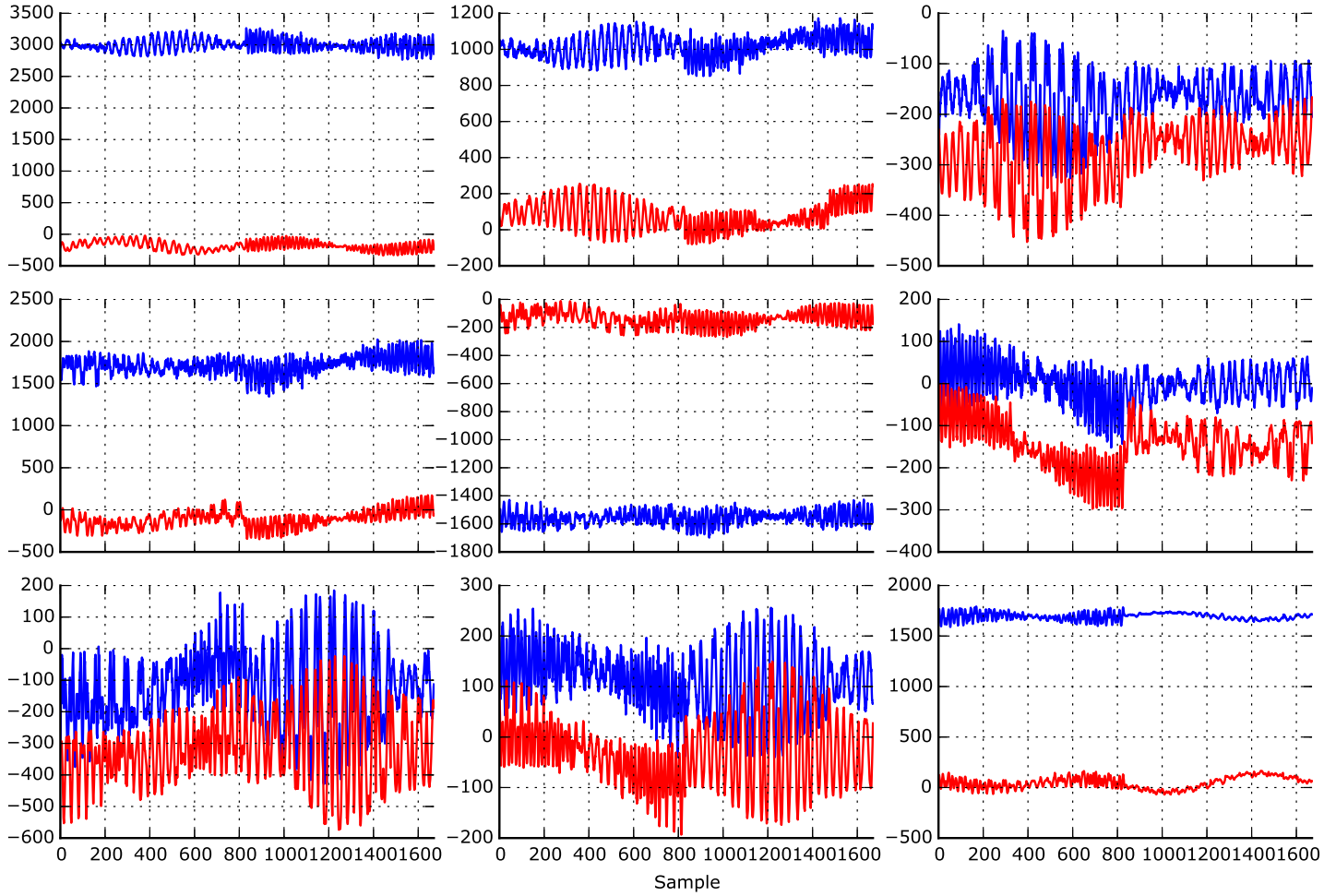

Figure 4.14: Field component matrix in the earth frame with no calibration. Elements of the field component matrix are shown in the earth frame with no calibration. Blue: Real part. Red: Imaginary part.

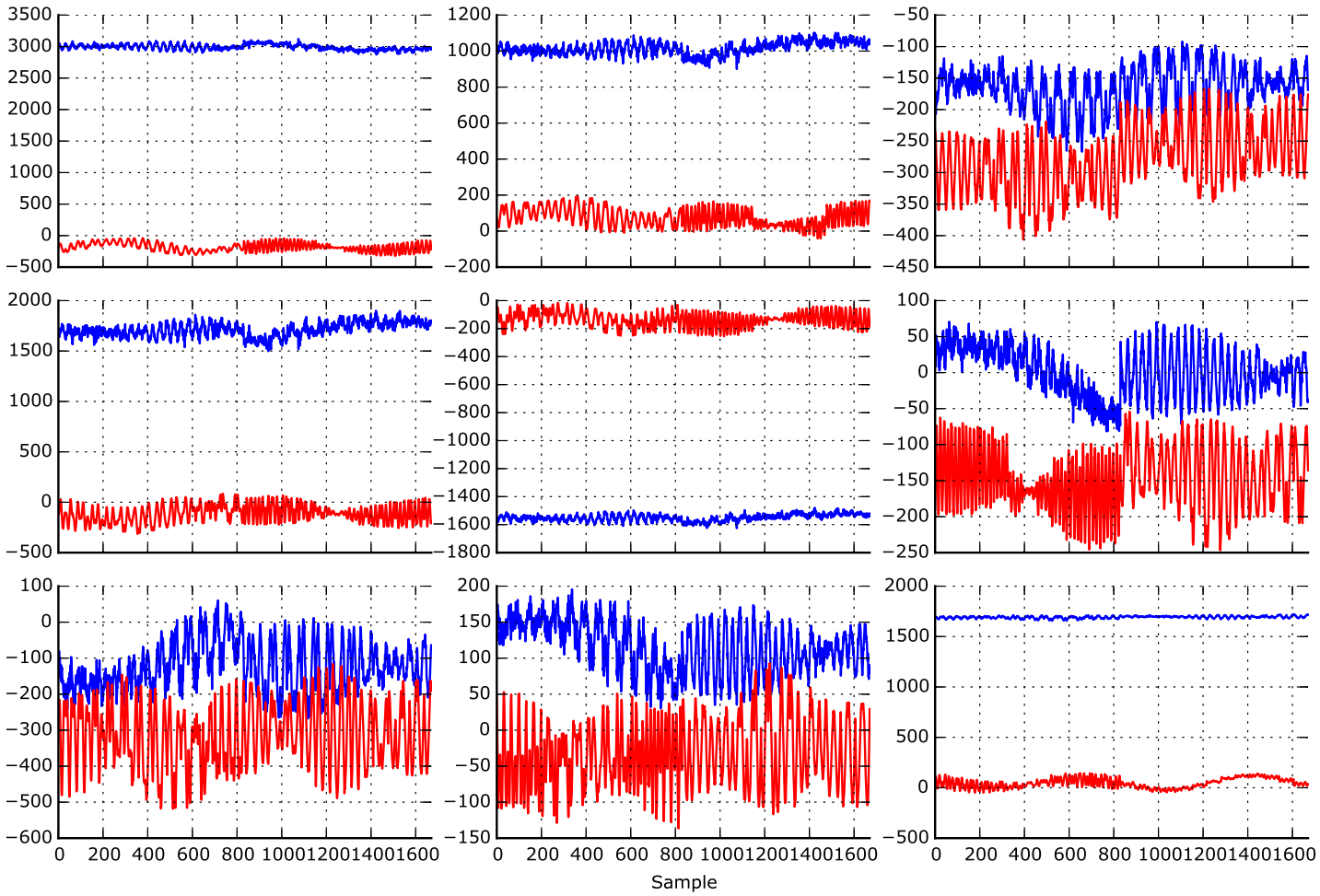

Figure 4.15: Field component matrix in the earth frame with partial calibration. Elements of the field component matrix are shown after all steps of calibration except mutual mis-alignment calibration. Blue: Real part. Red: Imaginary part.

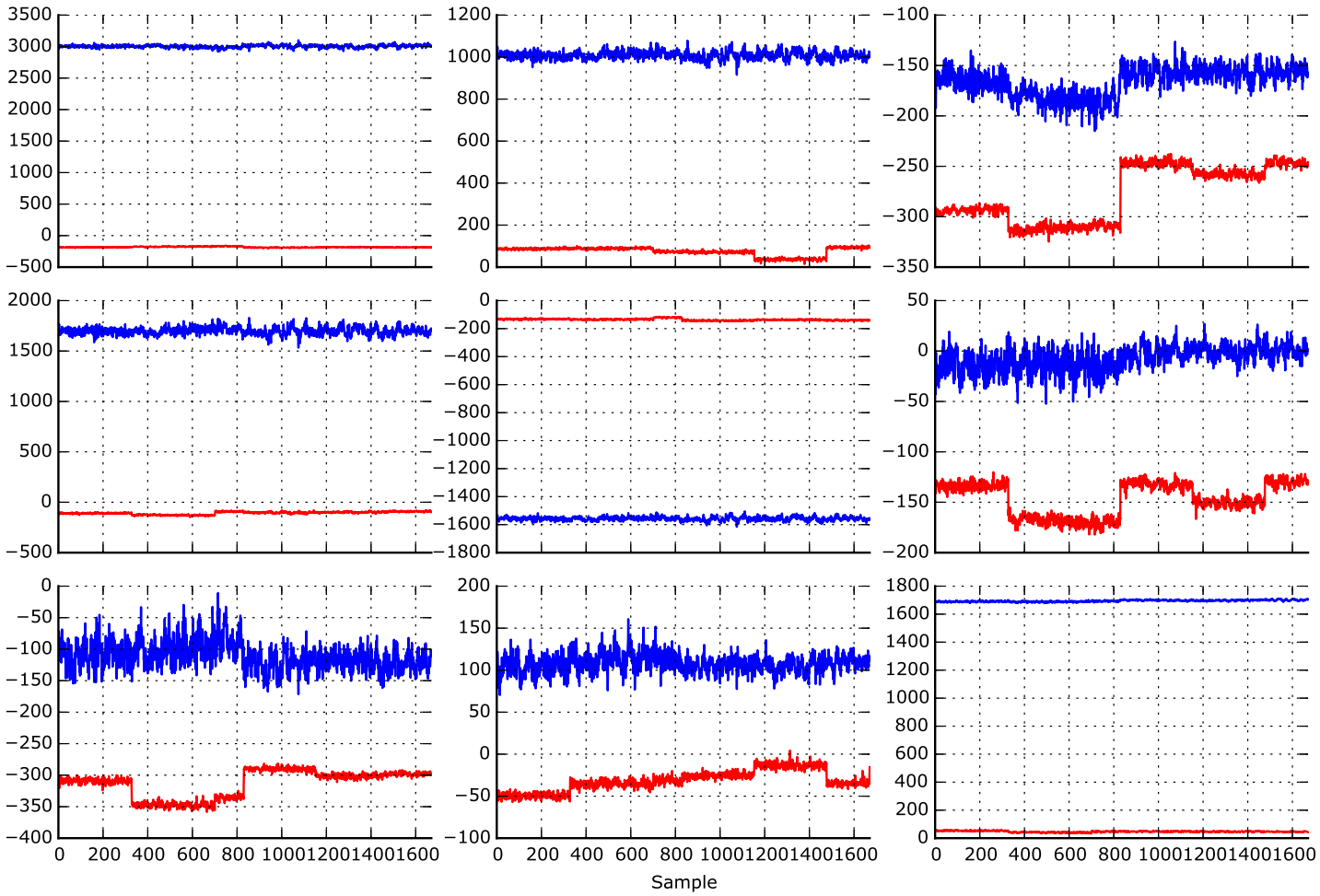

Figure 4.16: Field component matrix in the earth frame with full calibration. Elements of the field component matrix are shown in the earth frame with full calibration. Blue: Real part. Red: Imaginary part.

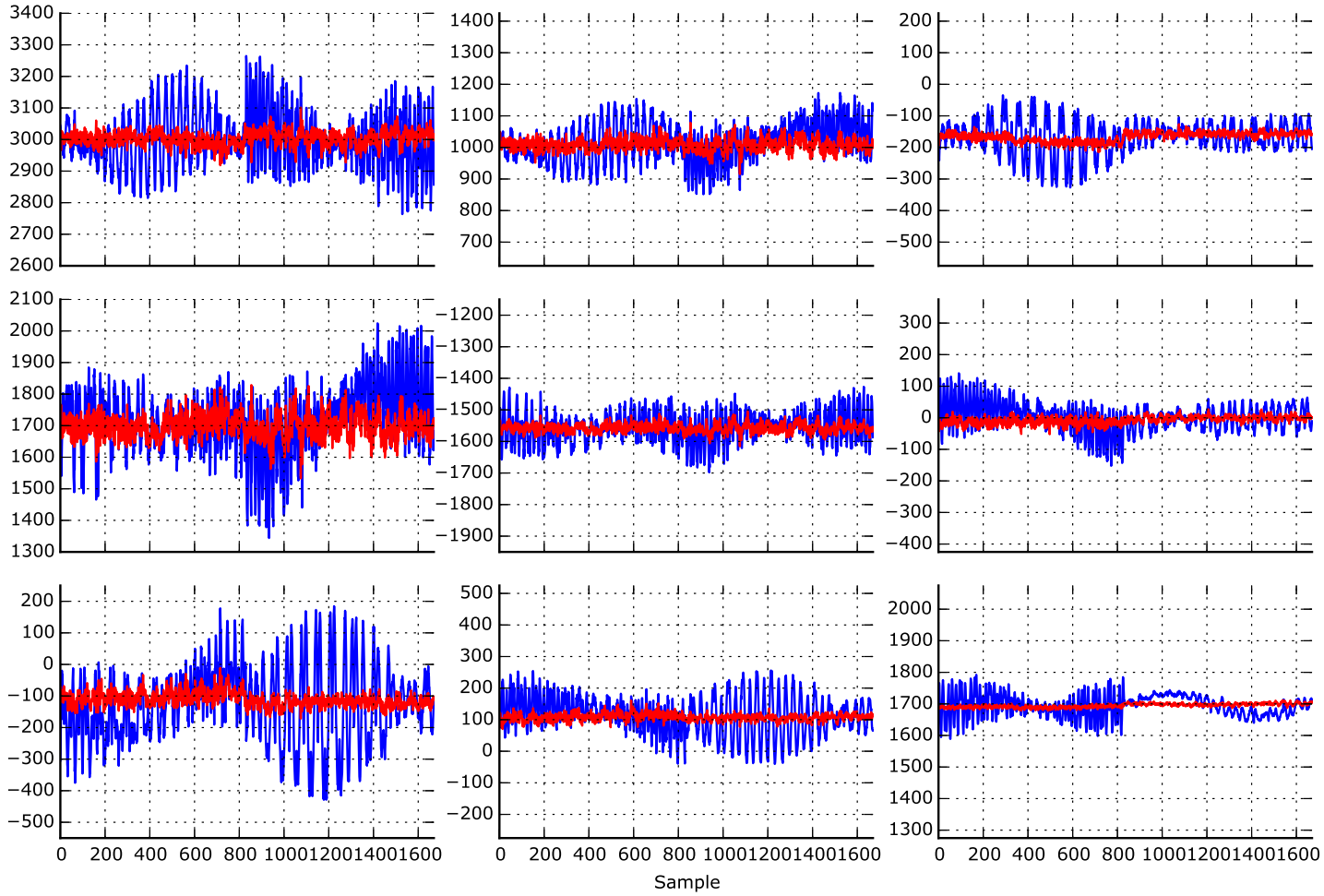

Figure 4.17: Field calibration matrix result. Results of calibration on the real part of the elements of the field calibration matrix are shown in the earth frame. Blue: No calibration. Red: Full calibration.

for the tracking application. It gives several advantages over raw-data calibration which is the default for many of the available systems:

- It enables developers to do calibration who may receive systems without raw-data access.
- It enables calibration in the field with only a transmitter and a receiver—no low-level measurement devices are required.
- It eases design requirements for new systems: It is no longer necessary to provide access to low-level data paths.

All three of the calibration procedures produce excellent results, as is demonstrated in this chapter. Indeed, without these calibration steps, implementing a tracking algorithm would be nearly impossible.

Chapter 5

Analysis and Design

In Section 2.4 the general requirements and objectives for this work are listed. To summarize in the most concise manner possible:

> The goal of this research is to extend a long-range magnetic positioning system to give robust position and orientation estimates, even in the presence of magnetic distortions, using methods that do not require extensive setup, excessive power, or expensive hardware.

Chapter 3 gives examples of other magnetic positioning systems which are comparable to the effort in this project–none of which meet all of the above objectives, and only few have explicit methods for dealing with magnetic distortions. The ones that do are mostly off-line correction routines that do not satisfy the goals of this project. Only one source was found that deals with the fusion of inertial sensors with magnetic positioning [12], and it also does not satisfy the goals of this project.

Therefore, this research seeks to meet the stated requirements and objectives by fusing magnetic positioning measurements with measurements from an accelerometer and a magnetometer to enable accurate estimates of position and orientation. The fusing of the data and the tracking of the receiver are achieved with an integrated navigation system, the heart of which is a discrete-time Kalman filter.

This chapter presents the analysis and formulation of the integrated navigation system and its Kalman filter. There are different types of Kalman filters, all with different strengths. Regardless of the type, every Kalman filter requires stochastic models for a set of observations and for the set of system states which the filter estimates. The observations can be thought of as the inputs to the filter and the states as the output of the filter. The filter design process consists of formulating the set of observations and states and determining how they are related to each other. In addition, stochastic models have to be assigned for each of the observations and states.

This chapter is organized as follows: Section 5.1 describes the sensors contained in the receiver and their operation. Section 5.2 develops the theory behind the architecture of the integrated navigation system. Finally, Section 5.3 describes the Kalman filter and derives the models necessary for its operation.

Before continuing, a reminder on notation should be given: Bold lower-case letters indicate vectors. Bold upper-case letters are matrices. Lower-case subscripts on a variable indicate its reference frame. The reference frame can be the reference frame of the receiver (subscript r), of the transmitter (subscript t), or of the earth. The earth frame is also referred to as the geo-frame and is denoted with a subscript g.

5.1 Sensor Models

The measurements of the three sensors on the receiver form the basis for the navigation system inputs. As such, it is critical to understand their operation and the content of their measurements. Each of the three sensors will be covered below in its own subsection. For each one, the measurements are assumed to be previously calibrated in accord with Chapter 4

5.1.1 Receiver Coils

The first model described is that of the magnetic field measurements at the receiver. Section 2.2 defines the ideal field component matrix using (2.16),(2.17), and (2.18). From this matrix, the position and orientation of the receiver can be deduced. In addition to the ideal field components, the coil measurements contain three sources of error:

1. System noise, denoted by $\mathbf{N}_B^r \in \mathbb{C}^{3\times 3}$.

2. Eddy and ferromagnetic distortions from the environment, denoted by $\mathbf{E}^r \in \mathbb{C}^{3\times 3}$ and called the *field error matrix*.

3. A phase term with a low-frequency, sinusoidal component due to imperfect down-mixing, denoted by $e^{j(\phi+\Delta\omega t)}$, where ϕ is the relative phase of the down-mixing signal and $\Delta\omega$ is the difference between the ideal and actual down-mixing frequency. In practice, the frequency mismatch between the ideal and actual is usually well below 1 Hertz, but it is never zero.

Including these error sources, the measured field matrix becomes

$$\tilde{\mathbf{B}}^r = \left(\begin{bmatrix} b_{xu} & b_{yu} & b_{zu} \\ b_{xv} & b_{yv} & b_{zv} \\ b_{xw} & b_{yw} & b_{zw} \end{bmatrix} + \mathbf{E}^r \right) e^{j(\phi+\Delta\omega t)} + \mathbf{N}_B^r. \tag{5.1}$$

$$= \left(\mathbf{B}^r + \mathbf{E}^r\right) e^{j(\phi+\Delta\omega t)} + \mathbf{N}_B^r, \tag{5.2}$$

where $\tilde{\mathbf{B}}^r$ is the measured field matrix and $\mathbf{B}^r$ is the actual value of the transmitted fields in the receiver frame. If the field matrix and field errors are expressed in the transmitter frame, the measurements become

$$\tilde{\mathbf{B}}^r = \underset{t:r}{\mathbf{R}} \left(\mathbf{B}^t + \mathbf{E}^t\right) e^{j(\phi+\Delta\omega t)} + \mathbf{N}_B^r, \tag{5.3}$$

where $\underset{t:r}{\mathbf{R}}$ is the rotation between the transmitter frame and the receiver frame. This version of the equation is preferred because $\mathbf{B}^t$ and $\mathbf{E}^t$ are constant at a given location regardless of receiver orientation. Also, $\mathbf{B}^t$ has a known form (symmetric and real) which is given in (2.16); it is repeated here for convenience.

$$\mathbf{B}^t = \frac{k}{r^5}\begin{bmatrix} 3x^2 - r^2 & 3xy & 3xz \\ 3xy & 3y^2 - r^2 & 3yz \\ 3xz & 3yz & 3z^2 - r^2 \end{bmatrix}. \tag{5.4}$$

The first task that must be accomplished is to remove the unnecessary and problematic phase term; this is referred to as *phase normalization*. Looking at the above equations and with $\mathbf{E}^t$ unknown, it is obvious that the phase term cannot be found without more information. However, there is no quantitative information that can be brought to bear. However, qualitatively speaking, there are a couple of options for approaching the problem:

1. Use a carrier recovery technique [62] to estimate $\Delta\omega$. Remove the frequency term, and then estimate ϕ based on some other criteria, such as maximum norm of real part.

2. At each step, lump the $\Delta\omega t$ term and the ϕ term together, and estimate them based on some criteria, such as maximum norm of real part.

The first option is complicated by the fact that the phase of the elements of $\tilde{\mathbf{B}}^r$ change not only with $\Delta\omega$, but also with the receiver's position and orientation. This makes carrier recovery techniques more complicated than they would be otherwise. After attempting the first option, the second option is adopted because it is much simpler to implement, and the results it achieves are just as effective as the first method.

Specifically, at each sample of time, t, the following minimization is performed to get an estimate of the phase correction to be applied:

$$\hat{\Phi} = arg \max_{\Phi} \left\| \Re\left\{ \tilde{\mathbf{B}}^r e^{-\Phi} \right\} \right\|. \tag{5.5}$$

Without a doubt, this is an ad hoc method of estimating the carrier phase, but there is little that can be done to improve on this without more information. Other optimization criteria were tried, but like this one, they were all simply guesses. Regardless, a ballpark estimate of the phase at each time point is achieved; and when the phase normalization is then applied, most of the energy is moved to the real part of the measurement.

Because phase normalization is always done immediately upon taking a measurement, it is assumed to be a part of the measurement process and is folded into the measurement, $\tilde{\mathbf{B}}^r$. In other words, from this point forward in this document, the meaning of $\tilde{\mathbf{B}}^r$ is redefined to indicate a phase normalized version. Therefore, the new, phase normalized definition of the field measurement matrix is expressed as

$$\underset{\text{new}}{\tilde{\mathbf{B}}^r} := \underset{\text{old}}{\tilde{\mathbf{B}}^r} e^{-\hat{\Phi}(t)}.$$

Then,

$$\tilde{\mathbf{B}}^r = \left(\mathbf{B}^r + \mathbf{E}^r\right) e^{j\Delta\phi} + \mathbf{N}_B^r \tag{5.6}$$

$$= \underset{t:r}{\mathbf{R}} \left(\mathbf{B}^t + \mathbf{E}^t\right) e^{j\Delta\phi} + \mathbf{N}_B^r, \tag{5.7}$$

where $\Delta\phi$ is the difference between the true phase and $\hat{\Phi}$. Note, the time dependence is implied in the above; in other words, the values of $\tilde{\mathbf{B}}^r$, $\mathbf{B}^r$, $\Delta\phi$, etc. change with each measurement. Also note that $\mathbf{N}_B^r$, being a random noise variable, is able to absorb the phase shift during the phase normalization process without changing its meaning.

Over the course of this project, it became obvious that the phase error term, $\Delta\phi$, is unobservable. In other words, without knowing $\mathbf{E}^t$, there is no way to determine $\Delta\phi$ due to the multiplication between them. Because of this and since $\mathbf{E}^t$ is going to be estimated by the Kalman filter, it can be assumed that $\Delta\phi$ is zero. The errors

which remain due to a non-zero $\Delta\phi$ are then folded into the estimate of $\mathbf{E}^t$. This results in the measurement becoming

$$\tilde{\mathbf{B}}^r = \underset{t:r}{\mathbf{R}} \left(\mathbf{B}^t + \mathbf{E}^t\right) + \mathbf{N}_B^r, \tag{5.8}$$

where the meaning of $\mathbf{E}^t$ is changed to absorb the errors from a non-zero $\Delta\phi$.

The question then arises: How do the phase errors affect the system performance? The following analysis addresses that question.

Start with the phase normalized measurements, and assume that the error between the normalizing phase and the true phase is small (e.g. $|\Delta\phi| < 10°$). Then the phase normalized measurements are (neglecting noise)

$$\tilde{\mathbf{B}}^r = (\mathbf{B}^r + \mathbf{E}^r)e^{j\Delta\phi} \tag{5.9}$$

$$\approx \mathbf{B}^r + \mathbf{E}^r + j\Delta\phi(\mathbf{B}^r + \mathbf{E}^r) \tag{5.10}$$

where, as usual, $\mathbf{B}^r \in \mathbb{R}^{3\times3}$ and $\mathbf{E}^r \in \mathbb{C}^{3\times3}$.

The measurements are reformulated in terms of the real and imaginary parts.

$$\Re(\tilde{\mathbf{B}}^r) \approx \mathbf{B}^r + \Re(\mathbf{E}^r) - \Delta\phi\Im(\mathbf{E}^r) \tag{5.11}$$

and

$$\Im(\tilde{\mathbf{B}}^r) \approx \Im(\mathbf{E}^r) + \Delta\phi\Re(\mathbf{E}^r) + \Delta\phi\mathbf{B}^r \tag{5.12}$$

$$\approx \Im(\mathbf{E}^r) + \Delta\phi\Re(\tilde{\mathbf{B}}^r) + \Delta\phi^2\Im(\mathbf{E}^r) \tag{5.13}$$

$$\approx \Im(\mathbf{E}^r) + \Delta\phi\Re(\tilde{\mathbf{B}}^r) \tag{5.14}$$

As can be seen, the real and imaginary parts of the phase normalized measurements each contain an error term that will disappear if the phase normalization is perfect. For the real part in (5.11), the error term is $-\Delta\phi\Im(\mathbf{E}^r)$. It is fair to assume that $\|\mathbf{E}^r\|$ is significantly smaller than $\|\mathbf{B}^r\|$; with the scaling by $\Delta\phi$, the

contribution of $-\Delta\phi\Im(\mathbf{E}^r)$ will be minimal. The error term in the imaginary part (5.14) is $\Delta\phi\Re(\tilde{\mathbf{B}}^r)$. It is expected that this factor will be more significant due to the larger value of $\tilde{\mathbf{B}}^r$. In both the real and imaginary cases, the Kalman filter is altered to allow for the expanded error content, thus compensating for the error terms.

As will be shown later in this document, the position state and rotation estimates are directly dependent on the real part of the measurements and not the imaginary parts. Fortunately, the expanded error content is most prominent in the imaginary part of the measurement and is quite subdued in the real part. Therefore, intuitively, the phase normalization error will have minimal impact on the position state estimates. Also, as can be deduced from (5.4), the effect of the position error goes by $\frac{1}{\sqrt[3]{\cdot}}$; and so the effect of the measurement error on the position state estimates is even further reduced.

In summary, imperfections during phase normalization will have a minimal impact on the overall system performance. In addition, the Kalman filter is more than capable of dealing with any errors introduced by the phase normalization process.

5.1.2 Accelerometer

This section describes the three-axis accelerometer and the content of its measurements. The measurements from the accelerometer are valuable in estimating linear motion and position as well as orientation. It is important to understand that the accelerometer does not directly measure acceleration. Rather, it measures the sum of the acceleration seen by the receiver and the earth's gravity vector [63]. Intuitively speaking, the accelerometer measures the receiver's deviation from a free-fall condition. In other words, when the accelerometer is at rest, it measures an upward-pointing vector with the magnitude of the earth's gravitational field. When it is moving, the measurements consist of the composite of this vector plus the receiver's acceleration.

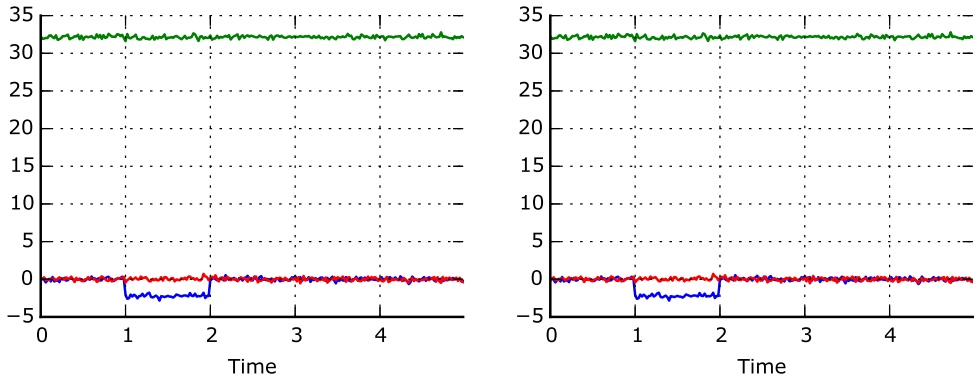

(a) Acceleration **(b)** Rotation

Figure 5.1: Acceleration vs. Rotation. This figure illustrates the difficulty in distinguishing accelerations from rotations. (a) Accelerometer measurements for a constant $-2.2 ft/s^2$ acceleration event. (b) Accelerometer measurements for a 4° rotation event. Blue: u-axis component; red v-axis component; green: w-axis component. Units: ft/s^2

This fact makes it difficult to deal with the accelerometer measurements. For determining orientation, the gravity vector is vital; but for measuring motion events, the gravity vector is a corrupting influence. Specifically, it is nearly impossible to distinguish small rotations from linear accelerations. Figure 5.1 demonstrates this idea. Shown in the figure are two separate scenarios; In the first, the receiver experiences a constant acceleration with a duration of 1 second along the u-axis. In the second, the receiver experiences a rotation of 4° around its v-axis. As is illustrated here, in the presence of noise, the signals are indistinguishable.

In order to resolve this ambiguity, all inertial navigation systems contain gyroscopes. Being sensitive only to rotations, the gyroscopes help differentiate between linear accelerations and rotations. Therefore, the gyroscopes effectively eliminate the issues caused by the gravity vector in the accelerometer measurements. Thus, with an accelerometer and a gyroscope, a full position and orientation solution can be given. [64]

As explained earlier, the system being described here cannot use gyroscopes, and so some other way of distinguishing rotations from accelerations is necessary. Indeed, compensating for the absence of a gyroscope is one of the primary difficulties of this research. Without doing this, the measurements of the accelerometer can provide very little information about the motion of the receiver. The combination of the magnetometer and the coil receiver fill this role within the framework of the Kalman filter. This is a primary contribution of this work and will be discussed in more detail later in this document.

The model of the accelerometer measurements would not be complete without considering the error sources. After, calibration, two main sources of error remain: accelerometer bias, $\mathbf{b}^r$, and electronic noise, $\mathbf{n}_a^r$. Even though the bias is included in the calibration, it varies enough with time and temperature to warrant being included in the measurement model. The quantities measured by the accelerometer include the acceleration, $\mathbf{s}^r$, and the gravity vector, $\mathbf{g}^g = [0\ 0\ g]^T$, where g is the specific gravity at the receiver's location. Including all of this, the total accelerometer measurement is given by

$$\tilde{\mathbf{f}}^r = \mathbf{s}^r + \underset{g:r}{\mathbf{R}}\mathbf{g}^g + \mathbf{b}^r + \mathbf{n}_a^r, \tag{5.15}$$

where all vectors are in $\mathbb{R}^3$, and $\underset{g:r}{\mathbf{R}}$ is the rotation matrix from the earth frame to the receiver frame of reference. This equation forms the basis for modeling the accelerometer within the navigation system framework and will be revisited later in this document.

5.1.3 Magnetometer

The three-axis magnetometer provides information about the orientation of the receiver. It measures the earth's magnetic field and any ferromagnetic distortions

induced by the geo-magnetic field. Its model is expressed as

$$\tilde{\mathbf{m}}^r = \mathbf{m}^r + \boldsymbol{\mu}^r + \mathbf{n}_m^r \tag{5.16}$$

$$= \underset{g:r}{\mathbf{R}} \left(\mathbf{m}^g + \boldsymbol{\mu}^g\right) + \mathbf{n}_m^r \tag{5.17}$$

where $\mathbf{m}^g$ is the actual magnetic field of the earth, $\boldsymbol{\mu}^g$ is any ferromagnetic distortion, $\mathbf{n}_m^r$ is an electronic noise term, and $\underset{g:r}{\mathbf{R}}$ is the rotation matrix from the earth frame to the receiver frame. Of the two equations above, it is preferable to use the one which references the ideal geo-magnetic field and the ferromagnetic distortion to the earth frame: Equation (5.17). This is due to the fact that $\mathbf{m}^g$ is a constant over the tracking volume, and its nominal value can be determined through the NOAA website [49]. Also, neither $\mathbf{m}^g$ nor $\boldsymbol{\mu}^g$ are dependent on the receiver orientation. Lastly, it is important to note that the distortion term, $\boldsymbol{\mu}^g$, will be zero when no ferromagnetic objects are nearby, but will begin to grow in the vicinity of such objects.

The magnetometer measurements taken together with the accelerometer measurements are used to get an estimate of the orientation of the receiver relative to the earth frame of reference. The geo-magnetic field is oriented toward the north, and the gravity vector points upward. As a result, the cross product between the geo-magnetic field and the gravity vector is an east-pointing vector. From these three vectors, the east-north-up orthonormal coordinate frame can be assembled with respect to the receiver's frame. The result corresponds to the rotation matrix from the earth frame to the receiver frame. In other words, it is possible to estimate $\underset{g:r}{\mathbf{R}}$ from the magnetometer and accelerometer measurement vectors. In fact, these two vectors provide more information than is needed to solve the problem. Therefore, there are several ways to do the estimation [65], each one with its strengths and weaknesses., For this project, the simple, deterministic *TRIAD* method [54, 55] is preferred.

Obviously, the orientation estimate is dependent on good measurements of the gravity vector and geo-magnetic field. That means that the dynamic accelerations of the receiver will corrupt the estimate. The same is true of magnetic distortions

Table 5.1: Measurement model summary

Measurement	Model	Relevance
Magnetic Coil Receiver	$\tilde{\mathbf{B}}^r = \underset{t:r}{\mathbf{R}}\left(\mathbf{B}^t + \mathbf{E}^t\right) + \mathbf{N}_B^r$	Receiver position/orientation; magnetic distortion
Accelerometer	$\tilde{\mathbf{f}}^r = \mathbf{s}^r + \underset{g:r}{\mathbf{R}}\mathbf{g}^g + \mathbf{b}^r + \mathbf{n}_a^r$	Receiver acceleration; receiver orientation; gravity vector
Magnetometer	$\tilde{\mathbf{m}}^r = \underset{g:r}{\mathbf{R}}\left(\mathbf{m}^g + \boldsymbol{\mu}^g\right) + \mathbf{n}_m^r$	Receiver orientation; Geomagnetic field; ferromagnetic distortion

and accelerometer biases. Of the three corrupting sources, the dynamic accelerations have the most negative impact, because of their large magnitude and quick changes. Compensating for all three of the error sources is one of the design goals for the Kalman filter described later in this document.

5.1.4 Summary of Sensor Measurements

Table 5.1 gives a summary of each of the measurements and its model. It also describes the relevance of each measurement. In other words, the information contained in each measurement is useful in determining the state of the system, and the "relevance" column gives the main informational contributions of the measurement. This will be discussed more when the navigation system architecture is presented.

5.2 System Architecture

The goal of this section is to establish the architecture of the integrated navigation system. Along with the calibration process presented in Chapter 4, this navigation system is one of the main contributions of this project. It meets all of the goals and

constraints of the research, and is original in the way it approaches the problem and in its final form.

Before the architecture can be presented, several background items are considered:

- The tracking application and the system configuration allow for several constraints to be fashioned that prove useful in the design of the filter. Subsection 5.2.1 describes these.
- Subsection 5.2.2 presents several design alternatives and the reasons why certain ones are preferred.
- Subsection 5.2.3 presents a couple of prerequisites necessary for analyzing the system.

After these background items are dealt with, the architecture is presented in Subsection 5.2.4. The details of the architecture and its components are presented and analyzed in the remainder of the subsections. One of the most important parts of the system is the integrating Kalman filter. Details of the Kalman filter are reserved for their own section. However, the input to the Kalman filter and the states it needs to track are derived in Subsection 5.2.7.

5.2.1 System Constraints and Assumptions

In Chapter 2 the description of the problem is addressed. This includes some specific constraints on the form that the system is allowed to take in Section 2.4. These are mostly constraints on the system hardware and hardware setup. In this section, several more constraints are added. In contrast to the hardware constraints, these are mostly operational in nature. In other words, these are assumptions and constraints of how the system will be used. They are generally qualitative in nature and are more like guidelines than strict constraints. They include the following:

1. *Significant ferromagnetic distortion is a low-probability event.* No quantitative constraint is imposed here, but the environment must be clean enough to allow

the system to properly estimate the earth's true magnetic field very soon after the system is turned on.

2. *Significant, acute distortion in the coils is a low-probability event.* Again, this is a concern during initialization and no quantitative constraint is imposed.

3. *The transmitter is aligned vertically.* No quantitative constraint is enforced. Rather, in general it is assumed that the positive z-axis is nominally perpendicular to the earth and pointing upward.

4. *The receiver's heading is usually in the direction of its v-axis.* Again, this is not a strict constraint, but it should be true that the heading of the receiver is usually more along its v-axis than along any other axis. This becomes important when modeling the linear motion dynamics of the system.

5.2.2 Design Alternatives

Many possible configurations for the integrated navigation system are available. Many of the configurations might have succeeded, but some narrowing of the design process was necessary beforehand. This subsection describes some of the choices that were made and the reasoning behind them.

Total-State vs. Error-State Filter

When used in a navigation and tracking application, the Kalman filter usually takes one of two forms. Those forms are total-state filtering and error-state filtering. Total-state filtering directly tracks the desired states, for example receiver position, $\mathbf{p}$. Error-state filtering is also called complementary filtering; it does not directly track $\mathbf{p}$, but rather, it tracks the error in position, $\delta\mathbf{p}$. It requires the ability to observe the error, which usually means there are two separate observations of the desired state, (e.g. $\mathbf{p}$). A practical example of a complementary filter would be an integrated INS-GPS navigation device. When operating in a complementary mode, the difference

between the location measurements of the two devices is used to track and correct the drift error of the INS. [66]

For the system in this project, as with most navigation systems, error-state Kalman filters are preferred. There are a couple of reasons for this. For one, the dynamics of a free-roaming system can be very severe and hard to model correctly. For example, the rotation of the receiver can change very quickly. The Kalman filter needs Gaussian models, but the dynamics do not fit a Gaussian model very well. One option would be to switch models based on the detected level of motion, and this is done in many applications [67]. A better option is to track the error states, such as the error in the rotation measurement. Depending on the specifics of the system involved, the error states can be much more easily and reliably modeled.

The second main reason for preferring error-state tracking is that the non-linearities of the system can sometimes be eliminated. For example, tracking rotations by using Euler angles is subject to non-linear interactions between the angles as well as numerical discontinuities. If the errors in the angles are tracked and if they remain small, then the system is approximately linear. For this reason, and for ease in modeling the dynamics, the error-state Kalman filter is preferred during this project.

Raw-Signal vs. Kuipers Output

Having established a preference for complementary Kalman filters, it is then necessary to make some choices about the input and output of the filter. With regard to the coil receiver, it is necessary to decide whether the raw, field matrix or the Kuipers algorithm output are to be used by the filter. Recall, the Kuipers algorithm decomposes the field matrix into position and orientation (i.e. pose) information [4]. This algorithm is iterative in nature and highly non-linear in nature. With significant error content in the field matrix, it is observed that the Kuipers algorithm will give unpredictable results. Since the Kalman filter needs its state variables to be reliably modeled, using the pose information from the algorithm does not seem to be viable. Therefore, the decision is made to use the raw field components in the filter.

Tightly vs. Loosely Coupled System

In many ways, the development of the system described in this document mirrors the development of integrated INS/GPS navigation systems. Integrated INS/GPS systems can be characterized by their level of integration between the INS and the GPS. For a *loosely* coupled system, the INS computes a navigation solution (i.e. position, velocity, attitude, etc.), and the GPS also computes a navigation solution, both largely independent from the other. The two solutions are then fused with a Kalman filter. For a *tightly* coupled system, the INS computes a navigation solution, but the GPS measurements are not used to compute a navigation solution. Rather, the GPS measurements are compared to what is predicted by the INS solution. From this comparison, the errors in the INS solution are computed and tracked with a Kalman filter. These errors are then used to correct the navigation solution of the INS. Once corrected, the INS solution is much more accurate and not subject to INS drifts. [68, 7]

The system in this work could be designed as either loosely or tightly coupled. Obviously, no INS or GPS is used, but the components can play similar roles: Instead of a GPS, this system has the magnetic coil receiver; and instead of the INS, this system has the magnetometer and accelerometer. For a loosely coupled system, the Kuipers pose would be fused with the MA pose using a Kalman filter. However, the Kuipers output is wildly non-linear and unpredictable in the presence of the field distortions. Therefore, the system is designed to be tightly coupled. In other words, the navigation solution of the magnetometer-accelerometer system is used to compute a field component matrix which is compared to the measured field component matrix. The comparison yields error terms that can be used to correct the MA navigation solution.

5.2.3 Prerequisites

Before the navigation system is designed, it is necessary to construct some overhead functions that will be used by the system. The two most important are the function to compute the rotation matrix, $\underset{r:g}{\mathbf{R}}$, and the function to compute the ideal field component matrix from a 3-D location.

The rotation matrix is computed via the the TRIAD method which is introduced in Section 5.1.3. The details of the method can be found in [54, 55]. This function needs four vector arguments: two measurement vectors in the receiver frame and two known ideal vectors in the the earth frame, which correspond to the two measurement vectors. From this information the rotation from the receiver to the earth frame can be estimated, subject to any noise or errors. The signature of the function is given by:

$$\underset{r:g}{\mathbf{R}} = \mathbf{\Psi}(\mathbf{x}_m^r, \mathbf{y}_m^r, \mathbf{x}_i^g, \mathbf{y}_i^g), \tag{5.18}$$

where $\mathbf{x}_m^r$ and $\mathbf{y}_m^r$ are the two measurement vectors in the receiver frame and $\mathbf{x}_i^g$ and $\mathbf{y}_i^g$ are the corresponding ideal versions in the earth frame.

The next most important overhead function is the field component matrix calculator. This function takes a 3-D location relative to the transmitter and returns the ideal field component matrix. It is called, $\boldsymbol{\beta}$, and it is computed as follows:

$$\boldsymbol{\beta}(\mathbf{p}^t) = \frac{k}{r^5}\begin{bmatrix} 3x^2 - r^2 & 3xy & 3xz \\ 3xy & 3y^2 - r^2 & 3yz \\ 3xz & 3yz & 3z^2 - r^2 \end{bmatrix}, \tag{5.19}$$

where $\mathbf{p}^t = [x\ y\ z]^T$ is the location, $r = \left\|\mathbf{p}^t\right\|$, and k is the known gain coefficient.

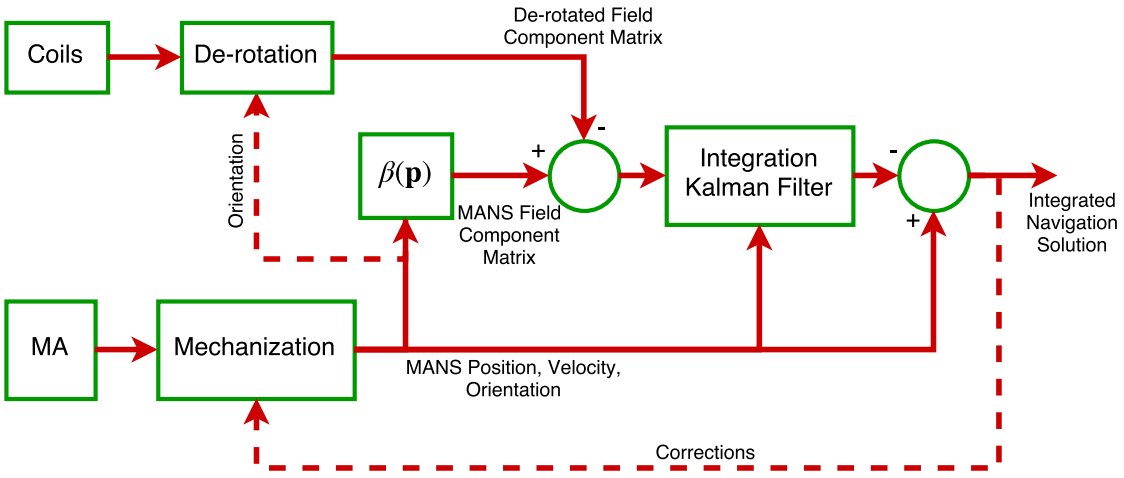

Figure 5.2: The integrated navigation system. Measurements from the coils and the MA are fused using a complementary Kalman filter.

5.2.4 Architecture

The overview of the navigation system architecture is shown in Figure 5.2. It is similar in nature to a tightly coupled INS/GPS navigation system. The heart of the system is the complementary Kalman filter which integrates the data from the coils and the MA.

As can be seen in the figure, two sets of measurements are captured: one by the coil receiver, and one by the MA. The MA measurements are put through a process called mechanization, which converts the measurements into position, velocity, and orientation information. In INS/GPS navigation systems, the inertial measurement unit combined with a mechanization process is commonly referred to as an inertial navigation system, or INS [7]. Following this naming scheme for the system in this project, the combination of the MA and the mechanization is referred to as a *magnetometer-accelerometer navigation system*, or *MANS*.

From the output of the MANS, it is possible to construct an ideal field component matrix for the computed position and attitude. It is desired that field component

matrices be compared in the transmitter frame of reference: Therefore, the fields measured by the coils are de-rotated to match the frame of reference of the MANS field matrix. The MANS version of the field component matrix is then subtracted from the measured, de-rotated field component matrix. This difference becomes the input to the Kalman filter, which fuses the coil and MANS output to get an estimate of the MANS error. The errors are subtracted to get a full navigation solution including position, velocity, and orientation. The following subsection describes the details of this process.

5.2.5 Mechanization

Mechanization for the MANS is the process of estimating the position, velocity, and orientation of the receiver. It uses the measurements from the accelerometer and the magnetometer. It also uses quantities estimated by the system from the previous cycle. After the mechanization is complete, position, velocity, and orientation estimates are treated as "measurements" from the MANS and then used in the Kalman filter.

The mechanization process for the MANS begins when a measurement is captured by the MA. The MA measurements are previously described and are given by (neglecting the noise terms):

$$\tilde{\mathbf{m}}^r = \underset{g:r}{\mathbf{R}} \left(\mathbf{m}^g + \boldsymbol{\mu}^g \right) \tag{5.20}$$

$$\tilde{\mathbf{f}}^r = \mathbf{s}^r + \underset{g:r}{\mathbf{R}} \mathbf{g}^g + \mathbf{b}^r. \tag{5.21}$$

The first step in the mechanization is to get the orientation of the receiver relative to the earth frame. This is done using the TRIAD method and requires measurements of the gravity vector and the geo-magnetic field. In order to get the best estimate of the rotation, the previous cycle's accelerometer bias and geo-magnetic field error are included. Since these values change slowly, the previous cycle's estimate is assumed

Table 5.2: Quantities used in the TRIAD method

Source	Receiver Frame	Earth Frame
Magnetometer	$\tilde{\mathbf{m}}_k^r$	$\mathbf{m}^g + \hat{\boldsymbol{\mu}}_{k-1}^g$
Accelerometer	$\tilde{\mathbf{f}}_k^r - \hat{\mathbf{b}}_{k-1}^r$	$\mathbf{g}^g$

to be almost equal to that of the current cycle. Recall that the TRIAD method requires four vectors: two vectors in the receiver frame and their equivalents in the earth frame. Incorporating the accelerometer bias ($\hat{\mathbf{b}}_{k-1}^r$) and the geo-magnetic field error ($\hat{\boldsymbol{\mu}}_{k-1}^g$) estimated in the previous cycle, the four vectors needed for the TRIAD method are given by the quantities shown in Table 5.2. Within this table, the cycle number is indicated with a subscript. Note that $\mathbf{m}^g$ and $\mathbf{g}^g$ are known, constant vectors.

Using the quantities in the table, the mechanized orientation for cycle k is calculated by

$$\underset{r:g_k}{\tilde{\mathbf{R}}} = \boldsymbol{\Psi}\left(\tilde{\mathbf{m}}_k^r\,, \tilde{\mathbf{f}}_k^r - \hat{\mathbf{b}}_{k-1}^r\,, \mathbf{m}^g + \hat{\boldsymbol{\mu}}_{k-1}^g\,, \mathbf{g}^g\right) \tag{5.22}$$

Compared to $\underset{r:g}{\tilde{\mathbf{R}}}$, the rotation from the receiver to the transmitter frames, $\underset{r:t}{\tilde{\mathbf{R}}}$ is more important. This matrix is computed using the estimated $\underset{g:t}{\mathbf{R}}$ of the previous cycle. In other words,

$$\underset{r:t_k}{\tilde{\mathbf{R}}} = \underset{g:t_{k-1}}{\hat{\mathbf{R}}}\,\underset{r:g_k}{\tilde{\mathbf{R}}}\,. \tag{5.23}$$

Because $\underset{g:t}{\mathbf{R}}$ is a fixed constant, its estimate will differ very little from cycle to cycle. Therefore, using the previous cycle's estimate is a valid approach, and the mechanized version becomes $\underset{g:t_k}{\tilde{\mathbf{R}}} := \underset{g:t_{k-1}}{\hat{\mathbf{R}}}$; therefore,

$$\underset{r:t_k}{\tilde{\mathbf{R}}} = \underset{g:t_k}{\tilde{\mathbf{R}}}\,\underset{r:g_k}{\tilde{\mathbf{R}}}\,. \tag{5.24}$$

With the rotation matrices computed, the next step is to compute the position and velocity. The acceleration can be extracted from the accelerometer measurement by

$$\tilde{\mathbf{s}}_k^t = \underset{r:t_k}{\tilde{\mathbf{R}}} \left(\tilde{\mathbf{f}}_k^r - \hat{\mathbf{b}}_{k-1}^r \right) - \underset{g:t_k}{\tilde{\mathbf{R}}} \, \mathbf{g}^g. \tag{5.25}$$

The velocity and position are then mechanized as

$$\tilde{\mathbf{v}}_k^t = \hat{\mathbf{v}}_{k-1}^t + \tilde{\mathbf{s}}_k^t \Delta t \tag{5.26}$$

$$\tilde{\mathbf{p}}_k^t = \hat{\mathbf{p}}_{k-1}^t + \hat{\mathbf{v}}_{k-1}^t \Delta t + \tilde{\mathbf{s}}_k^t \Delta t^2, \tag{5.27}$$

where Δt is the time period between cycles. With the position and velocity computed, the entire mechanization is complete and ready to be used by the rest of navigation system.

5.2.6 Field Differencing and Error Analysis

When the mechanization step is complete, the results are prepared for insertion into the Kalman filter. As can be seen in Figure 5.2, the first step in this process is to generate a field component matrix from the MANS output. This is achieved using the $\boldsymbol{\beta}$ function described above. Meanwhile, the measured fields are de-rotated by the MANS orientation; so that both field matrices are expressed in the same frame of reference. Then, they are differenced. In more specific terms, this process is

$$\tilde{\mathbf{B}}^t = \underset{r:t}{\tilde{\mathbf{R}}} \tilde{\mathbf{B}}^r \tag{5.28}$$

$$= \underset{r:t}{\tilde{\mathbf{R}}} \, \underset{t:r}{\mathbf{R}} \left(\mathbf{B}^t + \mathbf{E}^t \right) + \underset{r:t}{\tilde{\mathbf{R}}} \mathbf{N}_B^r \tag{5.29}$$

$$\approx \left(\mathbf{I} + \underset{r:t}{\boldsymbol{\Omega}^t} \right) \underset{r:t}{\mathbf{R}} \, \underset{t:r}{\mathbf{R}} \left(\mathbf{B}^t + \mathbf{E}^t \right) + \underset{r:t}{\tilde{\mathbf{R}}} \mathbf{N}_B^r \tag{5.30}$$

$$\approx \left(\mathbf{I} + \underset{r:t}{\boldsymbol{\Omega}^t} \right) \left(\mathbf{B}^t + \mathbf{E}^t \right) + \underset{r:t}{\tilde{\mathbf{R}}} \mathbf{N}_B^r, \tag{5.31}$$

where the orientation error is assumed to be small; such that $\underset{r:t}{\tilde{\mathbf{R}}} \approx (\mathbf{I} + \underset{r:t}{\boldsymbol{\Omega}^t})\underset{r:t}{\mathbf{R}}$ with $\underset{r:t}{\boldsymbol{\Omega}^t}$ being a skew-symmetric matrix with small off-diagonal elements given by

$$\underset{r:t}{\boldsymbol{\Omega}^t} = \begin{bmatrix} 0 & -\omega_z & \omega_y \\ \omega_z & 0 & -\omega_x \\ -\omega_y & \omega_x & 0 \end{bmatrix} \tag{5.32}$$

$$= \left[\underset{r:t}{\boldsymbol{\omega}^t}\right]_{\times}, \tag{5.33}$$

where $\underset{r:t}{\boldsymbol{\omega}^t} = [\omega_x\ \omega_y\ \omega_z]^T$, and $[\cdot]_{\times}$ indicate the cross-product matrix generated from the given vector.

The MANS version of the field matrix is derived from its position estimate and is given by

$$\tilde{\mathbf{B}}^t_{MANS} = \boldsymbol{\beta}\left(\tilde{\mathbf{p}}^t\right) \tag{5.34}$$

$$= \boldsymbol{\beta}\left(\mathbf{p}^t + \delta\mathbf{p}^t\right) \tag{5.35}$$

$$\approx \boldsymbol{\beta}\left(\mathbf{p}^t\right) + \frac{\partial\boldsymbol{\beta}\left(\mathbf{p}^t\right)}{\partial x}\delta x + \frac{\partial\boldsymbol{\beta}\left(\mathbf{p}^t\right)}{\partial y}\delta y + \frac{\partial\boldsymbol{\beta}\left(\mathbf{p}^t\right)}{\partial z}\delta z \tag{5.36}$$

$$\approx \mathbf{B}^t + \frac{\partial\boldsymbol{\beta}\left(\mathbf{p}^t\right)}{\partial x}\delta x + \frac{\partial\boldsymbol{\beta}\left(\mathbf{p}^t\right)}{\partial y}\delta y + \frac{\partial\boldsymbol{\beta}\left(\mathbf{p}^t\right)}{\partial z}\delta z, \tag{5.37}$$

where $\mathbf{p}^t$ is the true receiver position, and $\delta\mathbf{p}^t$ is the error in the mechanized version of the position which is given by $\delta\mathbf{p}^t = [\delta x\ \delta y\ \delta z]^T$.

Therefore, the field matrix difference becomes

$$\delta\mathbf{B}^t = \tilde{\mathbf{B}}^t - \tilde{\mathbf{B}}^t_{MANS} \tag{5.38}$$

$$\approx (\mathbf{I} + \underset{r:t}{\boldsymbol{\Omega}^t})\left(\mathbf{B}^t + \mathbf{E}^t\right) + \underset{r:t}{\tilde{\mathbf{R}}}\mathbf{N}^r_B - \left(\mathbf{B}^t + \frac{\partial\boldsymbol{\beta}\left(\mathbf{p}^t\right)}{\partial x}\delta x + \frac{\partial\boldsymbol{\beta}\left(\mathbf{p}^t\right)}{\partial y}\delta y + \frac{\partial\boldsymbol{\beta}\left(\mathbf{p}^t\right)}{\partial z}\delta z\right) \tag{5.39}$$

$$\approx \mathbf{E}^t + \underset{r:t}{\boldsymbol{\Omega}^t}\left(\mathbf{B}^t + \mathbf{E}^t\right) + \underset{r:t}{\tilde{\mathbf{R}}}\mathbf{N}^r_B - \frac{\partial\boldsymbol{\beta}\left(\mathbf{p}^t\right)}{\partial x}\delta x - \frac{\partial\boldsymbol{\beta}\left(\mathbf{p}^t\right)}{\partial y}\delta y - \frac{\partial\boldsymbol{\beta}\left(\mathbf{p}^t\right)}{\partial z}\delta z. \tag{5.40}$$

Equation (5.40) represents the main input to the Kalman filter, and it is of paramount importance for the system design. Note that all of the quantities on the right hand side of the equation are purely real except for $\mathbf{E}^t$. In other words, the imaginary part of $\mathbf{E}^t$ is superfluous with regard to analyzing the error in $\mathbf{B}^t$ and in the position. Therefore, only the real part of $\mathbf{E}^t$ is considered for the remainder of the project. In other words, from this point forward, $\delta\mathbf{B}^t, \mathbf{E}^t \in \mathbb{R}^{3\times 3}$.

Looking ahead to later parts of the design, it is necessary to perform error analysis on the mechanization of the position and velocity. This begins with the error analysis of $\tilde{\mathbf{s}}^t$.

$$\tilde{\mathbf{s}}_k^t = \underset{r:t_k}{\tilde{\mathbf{R}}} \left(\tilde{\mathbf{f}}_k^r - \hat{\mathbf{b}}_{k-1}^r\right) - \underset{g:t_k}{\tilde{\mathbf{R}}}\, \mathbf{g}^g. \tag{5.41}$$

$$\approx \left(\mathbf{I} + \underset{r:t\,k}{\mathbf{\Omega}^t}\right) \underset{r:t_k}{\mathbf{R}} \left(\tilde{\mathbf{f}}_k^r - \hat{\mathbf{b}}_{k-1}^r\right) - \left(\mathbf{I} + \underset{g:t\,k}{\mathbf{\Omega}^t}\right) \underset{g:t_k}{\mathbf{R}}\, \mathbf{g}^g \tag{5.42}$$

$$\approx \underset{r:t_k}{\mathbf{R}} \left(\tilde{\mathbf{f}}_k^r - \mathbf{b}_k^r\right) - \underset{g:t_k}{\mathbf{R}}\, \mathbf{g}^g + \underset{r:t_k}{\mathbf{R}} \left(\mathbf{b}_k^r - \hat{\mathbf{b}}_{k-1}^r\right) + \underset{r:t\,k}{\mathbf{\Omega}^t}\, \underset{r:t_k}{\mathbf{R}} \left(\tilde{\mathbf{f}}_k^r - \hat{\mathbf{b}}_{k-1}^r\right) - \underset{g:t\,g:t_k}{\mathbf{\Omega}^t \mathbf{R}}\, \mathbf{g}^g. \tag{5.43}$$

where $\underset{g:t}{\mathbf{\Omega}^t} = \left[\underset{g:t}{\boldsymbol{\omega}^t}\right]_\times$ is a small-angle, skew-symmetric matrix and $\underset{g:t}{\boldsymbol{\omega}^t} = [\omega_{g,x}\ \omega_{g,y}\ \omega_{g,z}]^T$. Therefore,

$$\delta\mathbf{s}_k^t = \tilde{\mathbf{s}}_k^t - \mathbf{s}_k^t \tag{5.44}$$

$$= \tilde{\mathbf{s}}_k^t - \underset{r:t_k}{\mathbf{R}} \left(\tilde{\mathbf{f}}_k^r - \mathbf{b}_k^r\right) - \underset{g:t_k}{\mathbf{R}}\, \mathbf{g}^g \tag{5.45}$$

$$= \underset{r:t_k}{\mathbf{R}} \left(\mathbf{b}_k^r - \hat{\mathbf{b}}_{k-1}^r\right) + \underset{r:t\,k}{\mathbf{\Omega}^t}\, \underset{r:t_k}{\mathbf{R}} \left(\tilde{\mathbf{f}}_k^r - \hat{\mathbf{b}}_{k-1}^r\right) - \underset{g:t\,g:t_k}{\mathbf{\Omega}^t \mathbf{R}}\, \mathbf{g}^g. \tag{5.46}$$

Using 5.26 and 5.27, it is trivial to show

$$\delta\mathbf{v}_k^t = \delta\hat{\mathbf{v}}_{k-1}^t + \delta\mathbf{s}_k^t \Delta t \tag{5.47}$$

$$\delta\mathbf{p}_k^t = \delta\hat{\mathbf{p}}_{k-1}^t + \delta\hat{\mathbf{v}}_{k-1}^t \Delta t + \delta\mathbf{s}_k^t \Delta t^2, \tag{5.48}$$

where $\delta\hat{\mathbf{p}}^t_{k-1}$ and $\delta\hat{\mathbf{v}}^t_{k-1}$ are the estimates from the previous cycle.

5.2.7 State Variables

The main input to the Kalman filter is established by (5.40). (The inputs of the filter are also called "observations".) From there it is necessary to derive the list of state variables that will be tracked by the Kalman filter. The system states form the core of what is tracked by the Kalman filter. During the prediction step of the filter (see Section 5.3), the system states are used to anticipate what the next observation will be.

Therefore, derivation of system states begins with the content of the observation as described in (5.40). Examining this equation indicates that the following quantities should be state variables:

- The field error matrix, $\mathbf{E}^t$.
- The error in the mechanized rotation from the receiver to the transmitter frame, $\underset{r:t}{\boldsymbol{\Omega}^t}$.
- The error in the mechanized position, $\delta\mathbf{p}^t$.

In addition, the model for the position error in (5.48) requires knowledge of the the velocity error, $\delta\mathbf{v}^t$; so it also needs to be a state variable.

After this, the mechanization quantities are examined to reveal any other needed state variables. Clearly, from the mechanization of $\underset{r:g}{\tilde{\mathbf{R}}}$, the accelerometer bias, $\mathbf{b}^r$, and geo-magnetic field error, $\boldsymbol{\mu}^g$, are needed. Looking then at the content of Equation (5.40), it is seen that $\mathbf{b}^r$ and $\boldsymbol{\mu}^g$ are not observable. In other words, even if every term of (5.40) is known, it will still not be possible to determine the values of $\mathbf{b}^r$ and $\boldsymbol{\mu}^g$. Therefore, more observations are needed.

The magnetometer and accelerometer measurements are used for this purpose. To fit within the error-state filter paradigm, the following complementary observations are defined

- From the accelerometer measurements

$$\delta\mathbf{f}^r = \tilde{\mathbf{f}}^r - \underset{g:r}{\tilde{\mathbf{R}}}\mathbf{g}^g \tag{5.49}$$

$$= \mathbf{s}^r + \mathbf{b}^r + \mathbf{n}_a^r + \underset{g:r}{\mathbf{R}}\mathbf{g}^g - \underset{g:r}{\mathbf{R}}\left(\mathbf{I} - \underset{r:g}{\boldsymbol{\Omega}^g}\right)\mathbf{g}^g \tag{5.50}$$

$$= \mathbf{s}^r + \mathbf{b}^r + \mathbf{n}_a^r + \underset{g:r\ r:g}{\mathbf{R}\boldsymbol{\Omega}^g}\mathbf{g}^g, \tag{5.51}$$

where $\underset{r:g}{\boldsymbol{\Omega}^g} = \left[\underset{r:g}{\boldsymbol{\omega}^g}\right]_\times$ is a small-angle, skew-symmetric matrix with a form similar to $\underset{r:t}{\boldsymbol{\Omega}^t}$.

- From the magnetometer measurements

$$\delta\mathbf{m}^g = \underset{r:g}{\tilde{\mathbf{R}}}\tilde{\mathbf{m}}^r - \mathbf{m}^g \tag{5.52}$$

$$= \left(\mathbf{I} + \underset{r:g}{\boldsymbol{\Omega}^g}\right)\underset{r:g}{\mathbf{R}}\left(\mathbf{m}^r + \boldsymbol{\mu}^r\right) + \underset{r:g}{\tilde{\mathbf{R}}}\mathbf{n}_m^r - \mathbf{m}^g \tag{5.53}$$

$$= \left(\mathbf{I} + \underset{r:g}{\boldsymbol{\Omega}^g}\right)\left(\mathbf{m}^g + \boldsymbol{\mu}^g\right) + \underset{r:g}{\tilde{\mathbf{R}}}\mathbf{n}_m^r - \mathbf{m}^g \tag{5.54}$$

$$= \underset{r:g}{\boldsymbol{\Omega}^g}\mathbf{m}^g + \left(\mathbf{I} + \underset{r:g}{\boldsymbol{\Omega}^g}\right)\boldsymbol{\mu}^g + \underset{r:g}{\tilde{\mathbf{R}}}\mathbf{n}_m^r. \tag{5.55}$$

With these two extra observations, $\mathbf{b}^r$ and $\boldsymbol{\mu}^g$ can be found. Speaking in Kalman filter terms, they become "observable".

However, with these two new observations, more state variables must be added. They are

- The error in the mechanized rotation from the receiver to the earth frame, $\underset{r:g}{\boldsymbol{\Omega}^g}$.
- The acceleration, $\mathbf{s}^r$.

Looking back at the first list of state variables, the quantity $\underset{r:t}{\boldsymbol{\Omega}^t}$ requires further analysis. From the mechanization discussion,

$$\underset{r:t}{\tilde{\mathbf{R}}} = \underset{g:tr:g}{\tilde{\mathbf{R}}\tilde{\mathbf{R}}}. \tag{5.56}$$

If the mechanized quantities are expressed in terms of their errors and their ideal values, then

$$\left(\mathbf{I}+\underset{r:t}{\boldsymbol{\Omega}^t}\right)\underset{r:t}{\mathbf{R}} \approx \left(\mathbf{I}+\underset{g:t}{\boldsymbol{\Omega}^t}\right)\underset{g:t}{\mathbf{R}}\left(\mathbf{I}+\underset{r:g}{\boldsymbol{\Omega}^g}\right)\underset{r:g}{\mathbf{R}}, \tag{5.57}$$

where all rotation errors are assumed to be small; therefore, from this equation it is easy to show that

$$\underset{r:t}{\boldsymbol{\Omega}^t} \approx \underset{g:t}{\boldsymbol{\Omega}^t} + \underset{g:t\ r:g\ g:t}{\mathbf{R}\boldsymbol{\Omega}^g\mathbf{R}^T}, \tag{5.58}$$

where second order terms are considered negligible. Therefore, from the three terms—$\underset{r:t}{\boldsymbol{\Omega}^t}$, $\underset{g:t}{\boldsymbol{\Omega}^t}$, and $\underset{r:g}{\boldsymbol{\Omega}^g}$—two are state variables, and the third can be found from the other two. Which two are used is a design choice. The quantity $\underset{g:t}{\boldsymbol{\Omega}^t}$ is used as one of the choices because its true value is a constant which represents the alignment error between the earth and transmitter frames, and modeling a constant quantity for the Kalman filter is trivial. The quantity $\underset{r:g}{\boldsymbol{\Omega}^g}$ is used as the other state variable since it is more directly linked to the accelerometer and magnetometer measurements (through the $\boldsymbol{\Psi}$ function).

However, with further analysis it is possible to also eliminate $\underset{r:g}{\boldsymbol{\Omega}^g}$ from the list of needed state variables. It is previously established that the mechanized rotation matrix from receiver to earth is

$$\underset{r:g_k}{\tilde{\mathbf{R}}} \approx \left(\mathbf{I}+\underset{r:g\ k}{\boldsymbol{\Omega}^g}\right)\underset{r:g_k}{\mathbf{R}}\ , \tag{5.59}$$

and

$$\underset{r:g_k}{\tilde{\mathbf{R}}} = \boldsymbol{\Psi}\left(\tilde{\mathbf{m}}_k^r\ , \tilde{\mathbf{f}}_k^r - \hat{\mathbf{b}}_{k-1}^r\ , \mathbf{m}^g + \hat{\boldsymbol{\mu}}_{k-1}^g\ , \mathbf{g}^g\right). \tag{5.60}$$

For the true version, the following holds:

$$\underset{r:g_k}{\mathbf{R}} = \boldsymbol{\Psi}\left(\tilde{\mathbf{m}}_k^r\ , \tilde{\mathbf{f}}_k^r - \mathbf{b}_k^r - \mathbf{s}_k^r\ , \mathbf{m}^g + \boldsymbol{\mu}_k^g\ , \mathbf{g}^g\right). \tag{5.61}$$

Table 5.3: The error-state variables of the navigation system.

Name	Symbol	Description
Position Error	$\delta\mathbf{p}^t$	Error in the position mechanization.
Velocity Error	$\delta\mathbf{v}^t$	Error in the velocity mechanization.
Acceleration	$\mathbf{s}^r$	Receiver acceleration.
Geo-Magnetic Field Error	$\boldsymbol{\mu}^g$	Distortion in the geo-magnetic field.
Field Error	$\mathbf{E}^t$	Field error matrix in the transmitter frame of reference.
Accelerometer Bias	$\mathbf{b}^r$	Bias in the accelerometer.
Frame Alignment Error	$\underset{g:t}{\boldsymbol{\Omega}^t}$	Error in the estimated rotation from the earth to the transmitter frame.

When this equation is combined with the mechanized version, $\underset{r:g}{\boldsymbol{\Omega}^g}$ can be calculated as

$$\underset{r:g}{\boldsymbol{\Omega}^g} = \underset{r:g_k}{\tilde{\mathbf{R}}}\ \mathbf{R}^T_{r:g_k} - \mathbf{I}. \tag{5.62}$$

Since every element in (5.61) is either known or is already identified as a state variable, Equation (5.62) can be used to calculate $\underset{r:g}{\boldsymbol{\Omega}^g}$. From this, it is seen that $\underset{r:g}{\boldsymbol{\Omega}^g}$ is completely derived from other state variables or mechanized quantities. Therefore, it can be removed from the list of needed state variables.

From the above reasoning, a final list of the required state variables is assembled; Table 5.3 describes them.

5.3 Filter Design

Concisely stated, the approach in this effort is to fuse magnetic positioning measurements with measurements from an accelerometer and a magnetometer in order to generate robust estimates of the receivers pose. Design and implementation of a navigation system to meet the stated requirements and objectives is the primary contribution of this work. With the architecture of the navigation system established in the last section, work began on the Kalman filter. This filter is the heart of the navigation system, and its design is the focus of a large portion of the research effort.

Before the Kalman filter can be implemented, two important sets of information must be specified: they are 1) the system observations models and 2) the system state variable models. Specifying these models is a subjective process and in some ways is more of an art than a science. Numerous choices are available, and there are probably at least a few choices that will be successful. For this project, the choices are made based on many factors, and these factors and the reasoning behind the design choices will be presented in this section.

5.3.1 Kalman Filter Overview

The Kalman filter is *the* ubiquitous technique for real-time tracking and sensor fusion applications. It has a long and illustrious history after being introduced in 1960 [5]. The body of relevant literature is understandably large, with many classic texts dedicated to its use, e.g. [66]. For a short tutorial see [69].

The Kalman filter as it is originally formulated is an optimal minimum-mean squared error (MMSE) state estimator for a stochastic linear dynamic system; but in order to function as the optimal estimator, several conditions are necessary. However, in practice, these conditions are almost never met, and some level of sub-optimal performance is allowed. [67]

The low-level operation of the filter will be addressed as needed, but for now it suffices to give an overview of its operation. The filter's main task is to estimate the

vector of system state variables. For this system, that consists of the variables in Table 5.3. The filter maintains and updates the state estimates based on successive incoming observations or measurements. Three main steps are involved which are repeated continually after an initialization step:

1. *Prediction.* This step makes a prediction of the system's state at the next time sample.

2. *Measurement.* This step records system observations derived from the system's sensors. (Together with the prediction step, this is also called *time update.*)

3. *Estimation.* This step compares and combines the measurements with the predictions to obtain an estimate of the system state. (This step is also called *state update.*)[66]

Every Kalman filter contains these steps, but the specific implementation is dependent on the objectives and requirements of the application being addressed. Even the work by Roetenberg in [10, 24, 25, 12], which is somewhat similar to this effort, presents a filter with very little in common with the one developed for this project. Therefore, the design choices for this project are unique to the type of observations and the states to be tracked.

This project's system of measurements and states for the Kalman filter requires a non-linear version of the Kalman filter. Non-linear Kalman filtering is by definition sub-optimal, but nonetheless, it has been used very successfully for decades. One of the oldest and most common of the non-linear adaptations is the extended Kalman filter (EKF). This method operates by linearizing the system about the current estimated state. As long as the state estimates are reliable, this filter will be reliable, but if the estimates suffer, the filter can diverge and fail. [66]

Another class of non-linear filters are sigma-point Kalman filters (SPKF). These filters use a deterministic sampling of the probability density function at the output of the filter to estimate the system states and covariances [70, 66, 71]. The most

common specific type of filter in this class is the unscented Kalman filter (UKF) [71]. In most all cases, this type of filter shows better adaptability when the non-linearities are strong and succeeds long after the EKF would have failed [72]. In addition, it requires much less off-line analysis to construct.

In this project, the Kalman filter is a tool to be used. The state models and measurement models are the parameters that define the filter and are the object of design. The type of filter (e.g. EKF, UKF, etc.) is also an object of design, but thereafter, the filter itself is treated largely as a black box. The unscented Kalman filter is chosen for this project due to its superior performance and ease of analysis. Fortunately, the Python community contains an open source implementation of the UKF in the PyKalman libraries [73].

The task of the UKF is to estimate the discrete-time non-linear system given by,

$$\mathbf{x}_{k+1} = \mathbf{f}\left(\mathbf{x}_k, \mathbf{v}_k\right) \tag{5.63}$$

$$\mathbf{z}_k = \mathbf{h}\left(\mathbf{x}_k, \mathbf{n}_k\right). \tag{5.64}$$

In this equation, $\mathbf{x}_k$ is the vector of system states, and $\mathbf{z}_k$ is the vector of observations. The subscript-k indicates sample number k. The random component of the update from sample k to $k+1$ is modeled by the *process noise* vector, $\mathbf{v}_k$. The *observation noise* vector is given by $\mathbf{n}_k$. The *time update* function, $\mathbf{f}\left(\cdot\right)$, describes how the system changes from one sample to the next given the current state and the current process noise. The *observation function*, $\mathbf{h}\left(\cdot\right)$, describes the relationship between the current observations and the current state and noise.

In order to use the UKF libraries, the time update function and the observation function must be supplied. In addition, like all Kalman filter implementations, the libraries need stochastic models for the observation noise and the state variable process noise. The design of these functions and stochastic models will be described in the following sections. But, first, the vector of states and observations will be formally defined.

5.3.2 Observation Vector

The cycle for the Kalman filter begins when a new measurement is taken. Those measurements are then processed to a form which will be useful to the Kalman filter. These new forms are called the *observations*, and they become the input to the Kalman filter. The observations are derived in the previous sections, but they are repeated here in summary form.

The primary observation comes from the difference of the measured field matrix and the MANS field matrix. Both the measured field matrix and the MANS field matrix contain noise terms. The MANS noise originates in the magnetometer and accelerometer and is propagated through the mechanization process. Compared to the noise from the measured field matrix, it is negligible and can be ignored. Therefore, the final observation of the field matrix difference is

$$\delta\mathbf{B}^t = \mathbf{E}^t + \underset{r:t}{\boldsymbol{\Omega}^t}\left(\mathbf{B}^t + \mathbf{E}^t\right) - \frac{\partial\boldsymbol{\beta}\left(\mathbf{p}^t\right)}{\partial x}\delta x - \frac{\partial\boldsymbol{\beta}\left(\mathbf{p}^t\right)}{\partial y}\delta y - \frac{\partial\boldsymbol{\beta}\left(\mathbf{p}^t\right)}{\partial z}\delta z + \underset{r:t}{\tilde{\mathbf{R}}}\mathbf{N}_B^r. \quad (5.65)$$

The other two observations come from the magnetometer and the accelerometer. They are given by

$$\delta\mathbf{m}^g = \underset{r:g}{\boldsymbol{\Omega}^g}\mathbf{m}^g + \left(\mathbf{I} + \underset{r:g}{\boldsymbol{\Omega}^g}\right)\boldsymbol{\mu}^g + \underset{r:g}{\tilde{\mathbf{R}}}\mathbf{n}_m^r \quad (5.66)$$

$$\delta\mathbf{f}^r = \mathbf{s}^r + \mathbf{b}^r + \underset{g:r\ r:g}{\mathbf{R}\boldsymbol{\Omega}^g}\mathbf{g}^g + \mathbf{n}_a^r, \quad (5.67)$$

where the measurement noise terms are included.

These three observations make up the entire signal input into the Kalman filter. As such they are of paramount importance throughout the design process. They compose the observation vector which is defined as,

$$\mathbf{z} = \begin{bmatrix} \text{vec}\left(\delta\mathbf{B}^t\right) \\ \delta\mathbf{m}^g \\ \delta\mathbf{f}^r \end{bmatrix} \in \mathbb{R}^{15}, \quad (5.68)$$

where vec $(\cdot)$ is the vectorization operator.

5.3.3 State Vector

The system states are derived in previous sections and summarized in Table 5.3. Therefore, the state vector which is used by the Kalman filter is given by,

$$\mathbf{x} = \begin{bmatrix} \delta\mathbf{p}^{t\,T} & \delta\mathbf{v}^{t\,T} & \mathbf{s}^{r\,T} & \boldsymbol{\mu}^{g\,T} & \text{vec}\left(\mathbf{E}^{t}\right)^{T} & \mathbf{b}^{r\,T} & \underset{g:t}{\boldsymbol{\omega}^{t\,T}} \end{bmatrix}^{T} \in \mathbb{R}^{27}. \tag{5.69}$$

5.3.4 Observation Function

The first of the required, user-supplied functions is the *observation function*. This function takes as input a state estimate and an observation noise; it returns a prediction of the observation based on these inputs. In other words, this function answers the question: For a given state and observation noise, what is the observation entering the filter?

The observation function is subdivided into three parts corresponding to Equations (5.65), (5.67), and (5.66), respectively. Therefore,

$$\mathbf{h}\left(\mathbf{x}, \mathbf{n}\right) := \begin{bmatrix} \text{vec}(\mathbf{h}_B(\mathbf{x}, \mathbf{n})) \\ \mathbf{h}_m(\mathbf{x}, \mathbf{n}) \\ \mathbf{h}_a(\mathbf{x}, \mathbf{n}) \end{bmatrix} \tag{5.70}$$

where $\mathbf{h}_B(\cdot)$, $\mathbf{h}_m(\cdot)$, and $\mathbf{h}_a(\cdot)$ correspond to the observation functions for the field matrix difference, the accelerometer error, and the magnetometer error, respectively. Each one of these will be defined separately below.

Observation Function for Field Matrix Difference

The field matrix difference is part of the observation vector and is given in Equation (5.65). Of the components in the equation, $\mathbf{N}_B^r$ comes from $\mathbf{n}$, and $\mathbf{E}^t$, ∂x, ∂y, and

∂z are state variables (i.e., they come from $\mathbf{x}$). The other terms are computed as follows:

- $\underset{r:t}{\boldsymbol{\Omega}}^t = \underset{g:t}{\boldsymbol{\Omega}}^t + \underset{g:t}{\tilde{\mathbf{R}}} \underset{r:g}{\boldsymbol{\Omega}}^g \underset{g:t}{\tilde{\mathbf{R}}}^T$ where $\underset{g:t}{\boldsymbol{\Omega}}^t$ is a state variables, $\underset{g:t}{\tilde{\mathbf{R}}}$ is from the mechanization process, and $\underset{r:g}{\boldsymbol{\Omega}}^g$ is computed from the state variables using Equation (5.62).
- $\mathbf{p}^t = \tilde{\mathbf{p}}^t - \delta\mathbf{p}^t$ where $\delta\mathbf{p}^t$ is a state variable and $\tilde{\mathbf{p}}^t$ is from the mechanization.
- The field matrix is computed as $\mathbf{B}^t = \boldsymbol{\beta}\left(\mathbf{p}^t\right)$.
- The partial derivatives of $\boldsymbol{\beta}\left(\mathbf{p}^t\right)$ are analytically computed from (5.19) and evaluated at $\mathbf{p}^t$.

Therefore, using these computations and Equation (5.65), the observation function for the field matrix difference is given by

$$\mathbf{h}_B(\mathbf{x}, \mathbf{n}) = \mathbf{E}^t + \underset{r:t}{\boldsymbol{\Omega}}^t \left(\mathbf{B}^t + \mathbf{E}^t\right) - \frac{\partial \boldsymbol{\beta}\left(\mathbf{p}^t\right)}{\partial x}\delta x - \frac{\partial \boldsymbol{\beta}\left(\mathbf{p}^t\right)}{\partial y}\delta y - \frac{\partial \boldsymbol{\beta}\left(\mathbf{p}^t\right)}{\partial z}\delta z + \underset{r:t}{\tilde{\mathbf{R}}}\mathbf{N}_B^r. \quad (5.71)$$

Observation Function for Magnetometer Error

The magnetometer error is part of the observation vector and is given in Equation (5.66). Of the components in the equation, $\boldsymbol{\mu}^g$ is a state variables, $\underset{r:g}{\boldsymbol{\Omega}}^g$ is computed via (5.62), $\mathbf{n}_m^r$ is the given noise, and $\mathbf{m}^g$ is a known constant. Using Equation (5.66), the observation function for the magnetometer error is given by

$$\mathbf{h}_m(\mathbf{x}, \mathbf{n}) = \underset{r:g}{\boldsymbol{\Omega}}^g \mathbf{m}^g + \left(\mathbf{I} + \underset{r:g}{\boldsymbol{\Omega}}^g\right)\boldsymbol{\mu}^g + \underset{r:g}{\tilde{\mathbf{R}}}\mathbf{n}_m^r. \quad (5.72)$$

Observation Function for Accelerometer Error

The accelerometer error is part of the observation vector and is given in Equation (5.67). Of the components in the equation, $\mathbf{s}^r$ and $\mathbf{b}^r$ are state variables, $\underset{r:g}{\boldsymbol{\Omega}}^g$ is computed via (5.62), $\mathbf{n}_a^r$ is the given noise, and $\underset{g:r}{\mathbf{R}}$ is computed from Equation (5.61). Using Equation (5.67), the observation function for the accelerometer error is given

by

$$\mathbf{h}_a(\mathbf{x}, \mathbf{n}) = \mathbf{s}^r + \mathbf{b}^r + \underset{g:r\ r:g}{\mathbf{R}\boldsymbol{\Omega}^g}\mathbf{g}^g + \mathbf{n}_a^r. \tag{5.73}$$

5.3.5 Observation Noise Model

With the observation function fully derived, the stochastic models for the observation noise are all that is needed to fully characterize the observations. Compared to the state process noise models which will be derived later, the measurement noise models are fairly straightforward. That being said, the process of providing the stochastic models is more of an art than science and requires a fair amount of guesswork. To get the best models, extensive characterization of the sensors and their internal workings would be necessary. Even then, the best models would not greatly increase the accuracy of the filter estimation [66]. Therefore, the objective is to provide models that approximate the real-world conditions in a broad sense.

The Kalman filter has several requirements that must be met in order for it to be an optimum estimator. One of these is that the measurement noise has a zero-mean, Gaussian distribution. This condition is assumed to be true for all three sets of observations. Therefore, in order to model the noise, it is only necessary to provide the observation noise covariance, $\mathbf{R} = \mathbb{E}\left[\mathbf{n}\mathbf{n}^T\right] \in \mathbb{R}^{15\times 15}$. Because the signal paths of each of the sensors is separate, each sensor is statistically independent from the others. This means that the covariance has a block diagonal form,

$$\mathbf{R} = \begin{bmatrix} \mathbf{R}_B & \mathbf{0} & \mathbf{0} \\ \mathbf{0} & \mathbf{R}_m & \mathbf{0} \\ \mathbf{0} & \mathbf{0} & \mathbf{R}_a \end{bmatrix}, \tag{5.74}$$

where $\mathbf{R}_B = \mathbb{E}\left[\text{vec}(\mathbf{N}_B^r)\text{vec}(\mathbf{N}_B^r)^T\right]$, $\mathbf{R}_m = \mathbb{E}\left[\mathbf{n}_m^r \mathbf{n}_m^{r\,T}\right]$, and $\mathbf{R}_a = \mathbb{E}\left[\mathbf{n}_a^r \mathbf{n}_a^{r\,T}\right]$ are the covariances for the field matrix measurement noise, the accelerometer noise, and the magnetometer noise, respectively.

Providing a model for each of the individual observations is the next step. The first to be modeled is the accelerometer error noise. For this observation, the noise term is equal to the noise in the accelerometer measurement. It is assumed that the noise in each axis of the accelerometer is of equal average power and is independent of the others. Therefore, the noise for the accelerometer error observation is modeled as

$$\mathbf{n}_a^r \sim \mathcal{N}(\mathbf{0}, \mathbf{R}_a) \tag{5.75}$$

$$\sim \mathcal{N}(\mathbf{0}, N_a\mathbf{I}) \tag{5.76}$$

where N_a is the standard deviation (i.e. RMS signal level) of each accelerometer sensor axis, and $\mathcal{N}$ indicates the normal random distribution. Therefore, $\mathbf{R}_a = N_a\mathbf{I}$.

For the magnetometer error observation, the same assumptions are made: the noise in each axis of the accelerometer is of equal average power and is independent of the others. Therefore,

$$\mathbf{n}_m^r \sim \mathcal{N}(\mathbf{0}, \mathbf{R}_m^r) \tag{5.77}$$

$$\sim \mathcal{N}(\mathbf{0}, N_m\mathbf{I}) \tag{5.78}$$

where N_m is the standard deviation of each magnetometer sensor axis.

Similarly, for the field matrix difference,

$$\mathbf{N}_B^r \sim \mathcal{N}(\mathbf{0}, N_B\mathbf{I})\,, \tag{5.79}$$

and $\mathbf{R}_B = N_B\mathbf{I}$.

With noise models for each of the three sets of observations, it is possible to construct the full model as

$$\mathbf{n} \sim \mathcal{N}(\mathbf{0}, \mathbf{R})\,. \tag{5.80}$$

where $\mathbf{R}$ is given above. The values used for N_B, N_m, and N_a are empirically determined. Their values are estimated to be

$$N_B = 43.8$$

$$N_m = 1.44\, mG$$

$$N_a = 0.137\, ft/s^2$$

Note that the covariance, $\mathbf{R}$, is a diagonal matrix. This is the simplest possible model for the observation noise. More complex and appropriate models could be constructed allowing for non-zero correlation between elements. In fact, this was attempted, but the results did not prove to be substantially better. Also, with more complex models, extensive characterization of the sensors would be necessary to guarantee that the model is generic enough to cover all possible cases. When comparing the performance of the system with the simple model and the more complex model, the performance improvement did not justify the level of effort needed to reliably construct the more complex models. Therefore, the simple model is used and proves sufficient.

5.3.6 State Variable Models

The models for the state variables contain two parts: the transition function—which describes the migration of the state from one sample to the next—and the process noise model—which describes the random component of the state migration. In accord with the requirements of the Kalman filter, the models are designed so that the process noise always has zero-mean; therefore, the process noise is entirely specified by its covariance.

It should be remembered that the covariances being derived here are generic in nature. In other words, two variables might be generically uncorrelated, but during a tracking session, certain situations might cause the state variables to become highly

correlated. These situations are the responsibility of the Kalman filter and are not the purview of the models being derived.

As with the observation models, the process of providing the transition covariance is more of an art than science and requires a fair amount of guesswork. Models can be either simple or complex, but the performance difference is not always substantial. For this project, the goal is to provide models that prove the viability of the integrated magnetic navigation system. Therefore, simpler models are preferred that approximate the real-world conditions in a broad sense. More complicated models that require extensive characterization and testing are avoided.

The analysis is subdivided roughly based on each individual state variable. Table 5.4 shows the subdivisions and gives an overview of the notation used for each subdivision.

Using these subdivisions, the transition function for the entire system is

$$\mathbf{f}(\mathbf{x}, \mathbf{v}) = \begin{bmatrix} \mathbf{f}_p(\mathbf{x}, \mathbf{v}) \\ \mathbf{f}_s(\mathbf{x}, \mathbf{v}) \\ \mathbf{f}_m(\mathbf{x}, \mathbf{v}) \\ \mathbf{f}_E(\mathbf{x}, \mathbf{v}) \\ \mathbf{f}_b(\mathbf{x}, \mathbf{v}) \\ \mathbf{f}_g(\mathbf{x}, \mathbf{v}) \end{bmatrix} \tag{5.81}$$

Similarly, the entire covariance matrix is

$$\mathbf{Q} = \begin{bmatrix} \mathbf{Q}_p & \mathbf{Q}_{ps}^T & \mathbf{Q}_{pm}^T & \mathbf{Q}_{pE}^T & \mathbf{Q}_{pb}^T & \mathbf{Q}_{pg}^T \\ \mathbf{Q}_{ps} & \mathbf{Q}_s & \mathbf{Q}_{sm}^T & \mathbf{Q}_{sE}^T & \mathbf{Q}_{sb}^T & \mathbf{Q}_{sg}^T \\ \mathbf{Q}_{pm} & \mathbf{Q}_{sm} & \mathbf{Q}_m & \mathbf{Q}_{mE}^T & \mathbf{Q}_{mb}^T & \mathbf{Q}_{mg}^T \\ \mathbf{Q}_{pE} & \mathbf{Q}_{sE} & \mathbf{Q}_{mE} & \mathbf{Q}_E & \mathbf{Q}_{Eb}^T & \mathbf{Q}_{Eg}^T \\ \mathbf{Q}_{pb} & \mathbf{Q}_{sb} & \mathbf{Q}_{mb} & \mathbf{Q}_{Eb} & \mathbf{Q}_b & \mathbf{Q}_{bg}^T \\ \mathbf{Q}_{pg} & \mathbf{Q}_{sg} & \mathbf{Q}_{mg} & \mathbf{Q}_{Eg} & \mathbf{Q}_{bg} & \mathbf{Q}_g \end{bmatrix}, \tag{5.82}$$

Table 5.4: State variable analysis subdivisions and notation.

Subdivision	**Variables**	**State Noise**	**Covariance**	**Transition Function**
Linear Motion Error	$\delta\mathbf{p}^t$, $\delta\mathbf{v}^t$	$\mathbf{v}_p$	$\mathbf{Q}_p$	$\mathbf{f}_p(\mathbf{x}, \mathbf{v})$
Acceleration	$\mathbf{s}^r$	$\mathbf{v}_s$	$\mathbf{Q}_s$	$\mathbf{f}_s(\mathbf{x}, \mathbf{v})$
Geo-Field Error	$\boldsymbol{\mu}^g$	$\mathbf{v}_m$	$\mathbf{Q}_m$	$\mathbf{f}_m(\mathbf{x}, \mathbf{v})$
Field Matrix Error	$\mathbf{E}^t$	$\mathbf{v}_E$	$\mathbf{Q}_E$	$\mathbf{f}_E(\mathbf{x}, \mathbf{v})$
Accelerometer Bias	$\mathbf{b}^r$	$\mathbf{v}_b$	$\mathbf{Q}_b$	$\mathbf{f}_b(\mathbf{x}, \mathbf{v})$
Frame Alignment Error	$\underset{g:t}{\boldsymbol{\omega}^t}$	$\mathbf{v}_g$	$\mathbf{Q}_g$	$\mathbf{f}_g(\mathbf{x}, \mathbf{v})$

where the off-diagonal matrices are the cross-covariances between the variables indicated in the subscripts.

By simple reasoning many of the off-diagonal covariances can be assigned a value of zero. Inspecting the system for zero covariance renders the following:

- The variables $\delta\mathbf{p}^t$ and $\delta\mathbf{v}^t$ are independent of the magnetic field error, $\mathbf{E}^t$.
- The acceleration, $\mathbf{s}^r$, is independent of $\boldsymbol{\mu}^g$, $\mathbf{E}^t$, $\mathbf{b}^r$, and $\underset{g:t}{\boldsymbol{\omega}^t}$.
- The geo-field error, $\boldsymbol{\mu}^g$, is independent of $\mathbf{s}^r$, $\mathbf{E}^t$, $\mathbf{b}^r$, and $\underset{g:t}{\boldsymbol{\omega}^t}$.
- The magnetic field error, $\mathbf{E}^t$, is independent of $\delta\mathbf{p}^t$, $\delta\mathbf{v}^t$, $\mathbf{s}^r$, $\boldsymbol{\mu}^g$, $\mathbf{b}^r$, and $\underset{g:t}{\boldsymbol{\omega}^t}$.
- The accelerometer bias, $\mathbf{b}^r$, is independent of $\mathbf{s}^r$, $\boldsymbol{\mu}^g$, $\mathbf{E}^t$, and $\underset{g:t}{\boldsymbol{\omega}^t}$.
- The frame alignment error, $\underset{g:t}{\boldsymbol{\omega}^t}$, is independent of $\mathbf{s}^r$, $\boldsymbol{\mu}^g$, $\mathbf{E}^t$, and $\mathbf{b}^r$.

Therefore, the total covariance can be written as

$$\mathbf{Q} = \begin{bmatrix} \mathbf{Q}_p & \mathbf{Q}_{ps}^T & \mathbf{Q}_{pm}^T & \mathbf{0} & \mathbf{Q}_{pb}^T & \mathbf{Q}_{pg}^T \\ \mathbf{Q}_{ps} & \mathbf{Q}_s & \mathbf{0} & \mathbf{0} & \mathbf{0} & \mathbf{0} \\ \mathbf{Q}_{pm} & \mathbf{0} & \mathbf{Q}_m & \mathbf{0} & \mathbf{0} & \mathbf{0} \\ \mathbf{0} & \mathbf{0} & \mathbf{0} & \mathbf{Q}_E & \mathbf{0} & \mathbf{0} \\ \mathbf{Q}_{pb} & \mathbf{0} & \mathbf{0} & \mathbf{0} & \mathbf{Q}_b & \mathbf{0} \\ \mathbf{Q}_{pg} & \mathbf{0} & \mathbf{0} & \mathbf{0} & \mathbf{0} & \mathbf{Q}_g \end{bmatrix} \tag{5.83}$$

As can be seen, the only non-zero, off-diagonal covariance is between the linear motion error and its dependencies. These are related through (5.46), (5.47), and (5.48).

The remainder of this section will define all of the non-zero quantities within the covariance matrix. It will also specify the transition functions for each of the subdivisions, thus completing the design of the Kalman filter.

Acceleration

The acceleration is one of the more difficult quantities to accurately model. This is because the mounting configuration and type of motion are contributing factors. For this project, the receiver is mounted at the end of a pole which is held in the hand during the tracking session. This results in its being suspended about 18 inches above the ground. It is assumed that the person holding the pole will walk at a moderate pace. If the receiver is mounted in a different way, the acceleration model will need to be changed to reflect the different forces experienced. Similarly, if the human begins to run, the model must also change to accommodate higher dynamics. Switching between different types of motion is a common practice in the Kalman filtering world [67], but to limit the scope of this project, only a moderate walking pace is considered.

Since it is expressed in the receiver frame, the acceleration is not uniform in each axis. To see this, recall some of the fundamental assumptions about the orientation of the receiver. Specifically, the receiver w-axis is nominally vertical; the v-axis is

nominally in the direction of motion; and the u-axis is nominally tangent to the direction of motion. The mechanics of the foot steps taken by the person holding the receiver cause the largest accelerations in the vertical axis (w-axis) with the second largest in the direction of motion (v-axis). The accelerations are modeled as first-order Gauss-Markov random processes with independence in each axis. Therefore, the state-space models are

$$\dot{\mathbf{s}}_u^r(t) = -\frac{1}{\tau_u}\mathbf{s}_u^r(t) + \sqrt{\frac{2\sigma_u^2}{\tau_u}} \tag{5.84}$$

$$\dot{\mathbf{s}}_v^r(t) = -\frac{1}{\tau_v}\mathbf{s}_v^r(t) + \sqrt{\frac{2\sigma_v^2}{\tau_v}} \tag{5.85}$$

$$\dot{\mathbf{s}}_w^r(t) = -\frac{1}{\tau_w}\mathbf{s}_w^r(t) + \sqrt{\frac{2\sigma_w^2}{\tau_w}}. \tag{5.86}$$

The parameters for modeling the motion are estimated by viewing the recorded data, and their values are assigned as

$$\sigma_u = 0.3\, ft/s^2$$

$$\tau_u = 0.1\, s$$

$$\sigma_v = 0.7\, ft/s^2$$

$$\tau_v = 0.2\, s$$

$$\sigma_w = 3.0\, ft/s^2$$

$$\tau_w = 0.7\, s$$

The Loan method described in [74, 66] is used to get the transition function and the transition covariance from the state-space representation. From this, the transition

function is

$$\mathbf{f}_s : \{\mathbf{x}, \mathbf{v}\} \mapsto \begin{bmatrix} 0.81991 & 0 & 0 \\ 0 & 0.90549 & 0 \\ 0 & 0 & 0.95157 \end{bmatrix} \mathbf{s}^r + \mathbf{v}_s, \tag{5.87}$$

where $\mathbf{s}^r$ and $\mathbf{v}_s$ are subvectors of $\mathbf{x}$ and $\mathbf{v}$, respectively. Also

$$\mathbf{v}_s \sim \mathcal{N}(\mathbf{0}, \mathbf{Q}_s), \tag{5.88}$$

where

$$\mathbf{Q}_s = \begin{bmatrix} 0.082 & 0 & 0 \\ 0 & 0.12 & 0 \\ 0 & 0 & 0.85 \end{bmatrix}. \tag{5.89}$$

Geo-Field Error

The modeling of the geo-field error is more complex than might be expected. There are a couple of reasons for this. First, the error has a zero mean and can be very small, or it can be quite large. Also, when the speed of the receiver approaches zero, the error will be constant over time. That being said, the error is modeled as a first-order Gauss-Markov random process, but to solve these problems, the model must be adjusted based on the state of the receiver. More specifically, the standard deviation, σ_m, and time constant, τ_m, of the Markov model are adjusted to match the current conditions.

To correct for the varying magnitude of the error, a simple, ad hoc method is employed to adjust the standard deviation. More sophisticated methods could be used, such as those in [67], but for this project, the simple approach is sufficient. For

this method, two test quantities, a and b, are used:

$$a = h(\langle \tilde{\mathbf{f}}^r / \left\| \mathbf{g}^g \right\|, \tilde{\mathbf{m}}^r \rangle) - \langle \mathbf{g}^g / \left\| \mathbf{g}^g \right\|, \mathbf{m}^g \rangle$$
$$b = \left\| \tilde{\mathbf{m}}^r \right\| - \left\| \mathbf{m}^g \right\|,$$

where $h(\cdot)$ is a simple low-pass filter meant to remove some of the perturbations due to acceleration.

The standard deviation is allowed to take on a few different levels: $\{\sigma_{m,k} = (0.005)2^k : k = 0, 1, \ldots, 4\}$. These two quantities are compared to a threshold in order to determine whether to raise or lower σ_m. In order to raise it, one of the following must be true:

$$|a| > 2.5\sigma_{m,i} \tag{5.90}$$
$$|b| > 2.5\sigma_{m,i}, \tag{5.91}$$

where i is the current level. In order to lower the level, both of the following must be true continuously while the receiver travels a distance of 3 feet:

$$|a| < 1.75\sigma_{m,i-1} \tag{5.92}$$
$$|b| < 1.75\sigma_{m,i-1}. \tag{5.93}$$

In addition, a lowering of the level is not allowed until the receiver has traveled 6 feet beyond the point where it was last raised.

For adjusting the time constant, a conversion between space and time is necessary. The speed of the receiver, v, is used to do this very simply:

$$\tau_m = \frac{\chi_m}{v}. \tag{5.94}$$

The constant $\chi_m = 2.0$ feet is something like a time constant except in the spatial domain. It is a measure of how the Gauss-Markov autocorrelation decays as the

receiver moves away from a position. In order to ensure stability, the speed, v, is not allowed to vary continuously, which creates a feedback path that might cause the filter to diverge. Rather, the speed is quantized and only allowed to take on these values: $\{0.5, 1.0, 2.0, 3.0, 4.0\}$.

The geo-field error is deemed to have the same stochastic model in each spatial dimension—*east*, *north*, and *up*. Also, in an overall sense, the error in each dimension is uncorrelated with the the others. Therefore, the following is the state-space representation for each dimension:

$$\dot{\mu}_e^g(t) = -\frac{1}{\tau_m}\mu_e^g(t) + \sqrt{\frac{2\sigma_m^2}{\tau_m}} \tag{5.95}$$

$$\dot{\mu}_n^g(t) = -\frac{1}{\tau_m}\mu_n^g(t) + \sqrt{\frac{2\sigma_m^2}{\tau_m}} \tag{5.96}$$

$$\dot{\mu}_u^g(t) = -\frac{1}{\tau_m}\mu_u^g(t) + \sqrt{\frac{2\sigma_m^2}{\tau_m}}, \tag{5.97}$$

where $\boldsymbol{\mu}^g = [\mu_e^g \; \mu_n^g \; \mu_u^g]^T$. From this, the Loan method is used to compute the transition function and covariance. However, an analytical expression is also available for the transition function and covariance [66]

$$\mathbf{f}_m : \{\mathbf{x}, \mathbf{v}\} \mapsto e^{-\Delta t/\tau_m}\boldsymbol{\mu}^g + \mathbf{v}_m, \tag{5.98}$$

where $\boldsymbol{\mu}^g$ and $\mathbf{v}_m$ are subvectors of $\mathbf{x}$ and $\mathbf{v}$, respectively. Also,

$$\mathbf{v}_m \sim \mathcal{N}(\mathbf{0}, \mathbf{Q}_m), \tag{5.99}$$

where

$$\mathbf{Q}_m = \sigma_m^2(1 - e^{-2\Delta t/\tau_m})\mathbf{I}. \tag{5.100}$$

Field Matrix Error

The field matrix errors are modeled as first-order Gauss-Markov random processes. In general, each of the elements is uncorrelated with the others. The elements from the horizontal fields, x and y, are deemed to have equal statistics. However, the vertical field, z, is more likely to couple to in-ground wire loops and cause more severe acute distortion. Therefore, its standard deviation is higher than the other field errors. The state-space representation is

$$\dot{\mathbf{E}}^t(t) = -\frac{1}{\tau_E}\mathbf{E}^t(t) + \sqrt{\frac{2}{\tau_E}}\Sigma_E, \tag{5.101}$$

where τ_E is a scalar time constant and Σ_E is a matrix of standard deviations. Reflecting the higher values for the z signals, its value is

$$\Sigma_E = \begin{bmatrix} 0.12 & 0.12 & 0.3 \\ 0.12 & 0.12 & 0.3 \\ 0.12 & 0.12 & 0.3 \end{bmatrix}. \tag{5.102}$$

Like with the geo-field error (see Section 5.3.6), the calculation of the time constant is a transform from a "spatial constant" via the the velocity. In other words,

$$\tau_E = \frac{\chi_E}{v}, \tag{5.103}$$

where $\chi_E = 2.0$ feet. Again, the velocity is quantized in the same way as described in Section 5.3.6.

From the state-space representation, the transition function and covariance are calculated.

$$\mathbf{f}_E : \{\mathbf{x}, \mathbf{v}\} \mapsto e^{-\Delta t/\tau_E}\text{vec}(\mathbf{E}^t) + \mathbf{v}_E, \tag{5.104}$$

where $\text{vec}(\mathbf{E}^t)$ and $\mathbf{v}_E$ are subvectors of $\mathbf{x}$ and $\mathbf{v}$, respectively. Also,

$$\mathbf{v}_E \sim \mathcal{N}(\mathbf{0}, \mathbf{Q}_E), \tag{5.105}$$

where

$$\mathbf{Q}_E = \text{diag}(\text{vec}(\Sigma_E))^2(1 - e^{-2\Delta t/\tau_E}), \tag{5.106}$$

where "diag$(\cdot)$" forms a diagonal matrix using the elements of the vector argument as the diagonal values.

Accelerometer Bias

It is well known that the accelerometer bias is nominally zero with a very slow moving, almost constant value [6]. Therefore, the bias is modeled as a first-order Gauss-Markov random process with a very long time constant. For the bias, x, of a single axis, the state-space representation is

$$\dot{x}(t) = -\frac{1}{\tau}x(t) + \sqrt{\frac{2\sigma^2}{\tau}} \tag{5.107}$$

with the values

$$\sigma = 0.3\, ft/s^2$$
$$\tau = 300\, s$$

Using the Loan method, the corresponding transition function and variance are obtained. They are

$$f : \{x, v\} \mapsto 0.99993x + v \tag{5.108}$$
$$v \sim \mathcal{N}\left(0, 11.9 \times 10^{-6}\right). \tag{5.109}$$

The bias in each axis is assumed to be independent of the others. Therefore, considering all of the axes at once, the transition function and covariance are

$$\mathbf{f}_b : \{\mathbf{x}, \mathbf{v}\} \mapsto 0.99993\mathbf{b}^r + \mathbf{v}_b \tag{5.110}$$

$$\mathbf{v}_b \sim \mathcal{N}(\mathbf{0}, \mathbf{Q}_b) \tag{5.111}$$

$$\mathbf{Q}_b = 11.9 \times 10^{-6}\mathbf{I}, \tag{5.112}$$

where $\mathbf{b}^r$ and $\mathbf{v}_b$ are subvectors of $\mathbf{x}$ and $\mathbf{v}$, respectively.

Frame Alignment Error

The frame alignment error is a measure of the error in the stated rotation between the earth and transmitter frames of reference. In other words, the transmitter orientation is fixed for a tracking session. This orientation is measured or estimated before the tracking session begins. The frame alignment error state variable represents the difference between the true rotation and the rotation used by the navigation system. As such, this variable is an unknown constant. Therefore, its transition function is trivial, and its covariance is zero—albeit, it is given a small finite value for the sake of numerical stability. They are given as,

$$\mathbf{f}_g : \{\mathbf{x}, \mathbf{v}\} \mapsto \underset{g:t}{\boldsymbol{\omega}^t} + \mathbf{v}_g \tag{5.113}$$

$$\mathbf{v}_g \sim \mathcal{N}(\mathbf{0}, \mathbf{Q}_g) \tag{5.114}$$

$$\mathbf{Q}_g = (0.001^\circ)^2\,\mathbf{I}, \tag{5.115}$$

where $\underset{g:t}{\boldsymbol{\omega}^t}$ and $\mathbf{v}_g$ are subvectors of $\mathbf{x}$ and $\mathbf{v}$, respectively.

Linear Motion Error

To model the linear motion error it is necessary to provide the transition function and covariance matrices for $\delta\mathbf{p}^t$ and $\delta\mathbf{v}^t$. In order to do this, the state space model

needs to be derived. This is done with the assumption that the linear acceleration error, $\delta\mathbf{s}^t$, is constant over a sampling period. Any perturbations from the constant value over the sample period are assumed to be zero-mean, white, and Gaussian. These assumptions make up what is referred to as the *constant acceleration process model* [67]. (However, in this case, the acceleration error is being used instead of the acceleration itself.) Following the structure of the constant acceleration process model, the continuous-time state-space equation is

$$\delta\dot{\mathbf{p}}^t(t) = \delta\mathbf{v}^t(t) \tag{5.116}$$

$$\delta\dot{\mathbf{v}}^t(t) = \delta\mathbf{s}^t_k(\mathbf{x}_k) + \mathbf{n}_p(t), \tag{5.117}$$

where $\mathbf{n}_p \sim \mathcal{N}(\mathbf{0}, \mathbf{\Sigma_p})$ and $\delta\mathbf{s}^t_k(\mathbf{x})$ is a function which numerically computes the acceleration error for each cycle. This function is based on Equation (5.46), which is adapted as

$$\delta\mathbf{s}^t_k(\mathbf{x}_k) = \underset{r:t_k}{\hat{\mathbf{R}}}\left(\mathbf{b}^r_k - \mathbf{b}^r_{k-1}\right) + \underset{r:t\ k}{\mathbf{\Omega}^t}\underset{r:t_k}{\hat{\mathbf{R}}}\left(\tilde{\mathbf{f}}^r_k - \mathbf{b}^r_{k-1}\right) - \underset{g:t\ g:t_k}{\mathbf{\Omega}^t\hat{\mathbf{R}}}\,\mathbf{g}^g. \tag{5.118}$$

Several steps are involved to compute this equation:

1. Calculate the earth to transmitter rotation matrix:

$$\underset{g:t_k}{\hat{\mathbf{R}}} = (\mathbf{I} - \underset{g:t\ k}{\mathbf{\Omega}^t})\underset{g:t}{\tilde{\mathbf{R}}}, \tag{5.119}$$

   where $\underset{g:t\ k}{\mathbf{\Omega}^t} = [\underset{g:t\ k}{\boldsymbol{\omega}^t}]_\times$ and $\underset{g:t\ k}{\boldsymbol{\omega}^t}$ is a subvector of the state vector. Also, $\underset{g:t}{\tilde{\mathbf{R}}}$ is the known constant, nominal value of $\underset{g:t}{\mathbf{R}}$.

2. Calculate the receiver to transmitter rotation matrix, including several sub steps:

   (a) Calculate the estimated gravity vector in the receiver frame:

$$\hat{\mathbf{g}}^r_k = \tilde{\mathbf{f}}^r_k - \mathbf{b}^r_k - \mathbf{s}^r_k, \tag{5.120}$$

where $\mathbf{b}_k^r$ and $\mathbf{s}_k^r$ are subvectors of the state

(b) Calculate the receiver to earth rotation matrix:

$$\underset{r:g_k}{\hat{\mathbf{R}}} = \boldsymbol{\Psi}\left(\tilde{\mathbf{m}}_k^r\,, \hat{\mathbf{g}}_k^r\,, \mathbf{m}^g + \boldsymbol{\mu}_k^g\,, \mathbf{g}^g\right), \tag{5.121}$$

where $\boldsymbol{\mu}_k^g$ is a subvector of the state vector

(c) Finish the calculation of the receiver to transmitter rotation matrix:

$$\underset{r:t_k}{\hat{\mathbf{R}}} = \underset{g:t_k}{\hat{\mathbf{R}}}\,\underset{r:g_k}{\hat{\mathbf{R}}}\,. \tag{5.122}$$

3. Calculate $\underset{r:t\;k}{\boldsymbol{\Omega}^t} = \underset{r:t_k}{\tilde{\mathbf{R}}}\,\underset{r:t_k}{\hat{\mathbf{R}}}^T - \mathbf{I}$

With these steps complete, $\delta\mathbf{s}_k^t(\mathbf{x})$ is computed and inserted into the state-space model (5.117) for cycle k.

At this point, the only missing part of the state-space model is the covariance, $\boldsymbol{\Sigma}_\mathbf{p}$, of the noise. No analytical equation is available or sought. Instead the covariance is estimated numerically using the propagation of uncertainty technique [75, 76, 77]. The equation of interest is (5.118), which is dependent on several of the state variables: $\mathbf{b}^r$, $\mathbf{s}^r$, $\boldsymbol{\mu}^g$, and $\underset{g:t}{\boldsymbol{\omega}^t}$. Each of these state variables is independent of the others, and their covariance is known (see below). Knowing this, the variance is estimated for each component of $\delta\mathbf{s}^t$ using

$$\sigma^2_{\delta s_x^t} = \sum_{a_i}\left(\frac{\partial\left(\delta s_x^t\right)}{\partial a_i}\right)^2\sigma^2_{a_i} \tag{5.123}$$

$$\sigma^2_{\delta s_y^t} = \sum_{a_i}\left(\frac{\partial\left(\delta s_y^t\right)}{\partial a_i}\right)^2\sigma^2_{a_i} \tag{5.124}$$

$$\sigma^2_{\delta s_z^t} = \sum_{a_i}\left(\frac{\partial\left(\delta s_z^t\right)}{\partial a_i}\right)^2\sigma^2_{a_i}, \tag{5.125}$$

where $a_i \in \left\{ \mathbf{b}^r, \mathbf{s}^r, \boldsymbol{\mu}^g, \underset{g:t}{\boldsymbol{\omega}^t} \right\}$. The partial derivatives are not analytically derived, but are numerically approximated using

$$\frac{\partial \left(\delta s_x^t(\mathbf{x}) \right)}{\partial a_i} \approx \frac{\delta s_x^t(\mathbf{x} + \Delta\mathbf{x}) - \delta s_x^t(\mathbf{x})}{\Delta a_i} \Big|_{\Delta a_i = \sigma_{a_i}}, \tag{5.126}$$

where $\mathbf{x} + \Delta\mathbf{x}$ is the state vector perturbed in the component corresponding to a_i. The magnitude of the perturbation is equal to $\Delta a_i = \sigma_{a_i}$.

Using these calculations, the full covariance of the state-space model can be approximated as

$$\boldsymbol{\Sigma}_{\mathbf{p}} = \begin{bmatrix} \sigma^2_{\delta s_x^t} & 0 & 0 \\ 0 & \sigma^2_{\delta s_y^t} & 0 \\ 0 & 0 & \sigma^2_{\delta s_z^t} \end{bmatrix}. \tag{5.127}$$

Since there is no correlation between axes and to make the analysis simpler, the state-space model is separated into three distinct, identical models—one for each axis. For brevity, the analysis below uses the x-axis, but the others are identical.

$$\delta \dot{p}_x^t(t) = \delta v_x^t(t) \tag{5.128}$$

$$\delta \dot{v}_x^t(t) = \delta s_{x,k}^t(\mathbf{x}_k) + n_{p,x} \tag{5.129}$$

$$n_{p,x} \sim \mathcal{N}(0, \sigma^2_{\delta s_x^t}). \tag{5.130}$$

From the well-known constant acceleration model (using just the x-axis), the transition from one cycle to the next is governed by

$$\begin{bmatrix} \delta p_{x,k+1}^t \\ \delta v_{x,k+1}^t \end{bmatrix} = \begin{bmatrix} 1 & \Delta t \\ 0 & 1 \end{bmatrix} \begin{bmatrix} \delta p_{x,k}^t \\ \delta v_{x,k}^t \end{bmatrix} + \mathbf{v}_{p,x}, \tag{5.131}$$

where $\mathbf{v}_{p,x} \sim \mathcal{N}(\mathbf{0}, \mathbf{Q}_{p,x})$ with the covariance given by

$$\mathbf{Q}_{p,x} = \sigma^2_{\delta s_x^t} \begin{bmatrix} \frac{\Delta t^3}{3} & \frac{\Delta t^2}{2} \\ \frac{\Delta t^2}{2} & \Delta t \end{bmatrix}. \text{ [67]} \tag{5.132}$$

Incorporating all of the axes, the transition function is given by

$$\mathbf{f}_p : \{\mathbf{x}, \mathbf{v}\} \mapsto \begin{bmatrix} \mathbf{I} & \mathbf{I}\Delta t \\ \mathbf{0} & \mathbf{I} \end{bmatrix} \begin{bmatrix} \delta\mathbf{p}^t \\ \delta\mathbf{v}^t \end{bmatrix} + \mathbf{v}_p \tag{5.133}$$

where $\delta\mathbf{p}^t$ and $\delta\mathbf{v}^t$ are subvectors of $\mathbf{x}$. Also, $\mathbf{v}_p$ is a subvector of $\mathbf{v}$. The covariance of $\mathbf{v}_p$ is

$$\mathbf{Q}_p = \begin{bmatrix} \sigma^2_{\delta s^t_x}\frac{\Delta t^3}{3} & 0 & 0 & \sigma^2_{\delta s^t_x}\frac{\Delta t^2}{2} & 0 & 0 \\ 0 & \sigma^2_{\delta s^t_y}\frac{\Delta t^3}{3} & 0 & 0 & \sigma^2_{\delta s^t_y}\frac{\Delta t^2}{2} & 0 \\ 0 & 0 & \sigma^2_{\delta s^t_z}\frac{\Delta t^3}{3} & 0 & 0 & \sigma^2_{\delta s^t_z}\frac{\Delta t^2}{2} \\ \sigma^2_{\delta s^t_x}\frac{\Delta t^2}{2} & 0 & 0 & \sigma^2_{\delta s^t_x}\Delta t & 0 & 0 \\ 0 & \sigma^2_{\delta s^t_y}\frac{\Delta t^2}{2} & 0 & 0 & \sigma^2_{\delta s^t_y}\Delta t & 0 \\ 0 & 0 & \sigma^2_{\delta s^t_z}\frac{\Delta t^2}{2} & 0 & 0 & \sigma^2_{\delta s^t_z}\Delta t \end{bmatrix}. \tag{5.134}$$

With the transition function and the covariance specified, the state model for the linear motion error is nearly complete. As is clear from (5.118), $\delta\mathbf{s}^t$ is dependent on the state variables $\mathbf{b}^r$, $\mathbf{s}^r$, $\boldsymbol{\mu}^g$, and $\underset{g:t}{\boldsymbol{\omega}^t}$. Because of this, $\delta\mathbf{p}^t$ and $\delta\mathbf{v}^t$ are correlated with these variables. Therefore, $\mathbf{Q}_{ps}$, $\mathbf{Q}_{pm}$, $\mathbf{Q}_{pb}$, and $\mathbf{Q}_{pg}$ are non-zero.

Like $\mathbf{Q}_p$, these quantities are derived using the propagation of uncertainties technique. Specifically, the covariances are estimated using

$$\sigma_{\delta s^t_x, a_i} = \frac{\partial\left(\delta s^t_x\right)}{\partial a_i}\sigma^2_{a_i} \tag{5.135}$$

$$\sigma_{\delta s^t_y, a_i} = \frac{\partial\left(\delta s^t_y\right)}{\partial a_i}\sigma^2_{a_i} \tag{5.136}$$

$$\sigma_{\delta s^t_z, a_i} = \frac{\partial\left(\delta s^t_z\right)}{\partial a_i}\sigma^2_{a_i}, \tag{5.137}$$

for each $a_i \in \left\{\mathbf{b}^r, \mathbf{s}^r, \boldsymbol{\mu}^g, \underset{g:t}{\boldsymbol{\omega}^t}\right\}$ [75, 76].

These expressions are valid in the continuous time domain, but in order to operate with the Kalman filter they must be discretized. The process of discretization is

described by the authors of [67]. They use it to derive the transition function (5.133) and the covariance (5.134) from the state-space model (5.116)-(5.117). In what follows, the same process is used to derive the covariance between the linear motion error terms and its correlated terms.

The analysis will begin with the covariance between δp_x^t and s_u^r. The noise terms associated with each of these variables are represented by $x(t)$ and $u(t)$, respectively. They are discretized in accordance with the method presented in [67] as

$$x_k = \int_0^{\Delta t} (\Delta t - \alpha) x(\alpha) d\alpha \tag{5.138}$$

$$u_k = \int_0^{\Delta t} e^{-\omega_0(\Delta t - \gamma)} u(\gamma) d\gamma, \tag{5.139}$$

where $\omega_u = \dfrac{1}{\tau_u}$ is the natural frequency associated with s_u^r (see Eq. (5.84)). Then, the discrete covariance is derived as

$$\sigma_{xu} = \mathbb{E}[x_k u_k] \tag{5.140}$$

$$= \mathbb{E}\left[\int_0^{\Delta t} (\Delta t - \alpha) x(\alpha) d\alpha \int_0^{\Delta t} e^{-\omega_u(\Delta t - \gamma)} u(\gamma) d\gamma\right] \tag{5.141}$$

$$= \int_0^{\Delta t} \int_0^{\Delta t} (\Delta t - \alpha) e^{-\omega_u(\Delta t - \gamma)} \mathbb{E}[x(\alpha) u(\gamma)]\, d\alpha d\gamma. \tag{5.142}$$

It is known that $\mathbb{E}[x(\alpha)u(\tau)] = \sigma_{\delta s_x^t, s_u^r} \delta(\alpha - \gamma)$, where $\delta(\cdot)$ is the Dirac delta function and $\sigma_{\delta s_x^t, s_u^r}$ is computed via the propagation of uncertainty technique as described above. Therefore, further simplification is possible:

$$\sigma_{xu} = \int_0^{\Delta t} \int_0^{\Delta t} (\Delta t - \alpha) e^{-\omega_u(\Delta t - \gamma)} \sigma_{\delta s_x^t, s_u^r} \delta(\alpha - \gamma) d\alpha d\gamma \tag{5.143}$$

$$= \int_0^{\Delta t} (\Delta t - \gamma) e^{-\omega_u(\Delta t - \gamma)} \sigma_{\delta s_x^t, s_u^r} d\gamma \tag{5.144}$$

$$= \frac{\sigma_{\delta s_x^t, s_u^r}}{\omega_u^2} \left[1 - e^{-\omega_u \Delta t} - \Delta t \omega_u e^{-\omega_u \Delta t}\right]. \tag{5.145}$$

After the discrete covariance is derived between the x-axis position error and s_u^r, it is necessary to derive the covariance between δv_x^t and s_u^r, where the noise term associated with δv_x^t is represented by $v(t)$. From [67],

$$v_k = \int_0^{\Delta t} v(\alpha) d\alpha. \tag{5.146}$$

Therefore,

$$\begin{aligned}
\sigma_{vu} &= \mathbb{E}[v_k u_k] && (5.147)\\
&= \mathbb{E}\left[\int_0^{\Delta t} v(\alpha) d\alpha \int_0^{\Delta t} e^{-\omega_u(\Delta t-\gamma)} u(\gamma) d\gamma\right] && (5.148)\\
&= \int_0^{\Delta t}\int_0^{\Delta t} e^{-\omega_u(\Delta t-\gamma)} \mathbb{E}[v(\alpha)u(\gamma)]\, d\alpha d\gamma && (5.149)\\
&= \int_0^{\Delta t} e^{-\omega_u(\Delta t-\gamma)} \sigma_{\delta s_x^t, s_u^r} d\gamma && (5.150)\\
&= \frac{\sigma_{\delta s_x^t, s_u^r}}{\omega_u}\left[1 - e^{-\omega_u \Delta t}\right]. && (5.151)
\end{aligned}$$

With this covariance derived, the complete covariance between $\mathbf{Q}_{ps}$ can easily be specified. For each component of $\delta \mathbf{p}^t$, the covariance is derived similarly to (5.145); and for each component of $\delta \mathbf{v}^t$, the covariance is derived similarly to (5.151). In order to keep the notation manageable, two helper functions are defined

$$\begin{aligned}
\chi : \{\sigma, \omega\} &\mapsto \frac{\sigma}{\omega^2}\left[1 - e^{-\omega\Delta t} - \Delta t \omega e^{-\omega \Delta t}\right] && (5.152)\\
\Upsilon : \{\sigma, \omega\} &\mapsto \frac{\sigma}{\omega}\left[1 - e^{-\omega\Delta t}\right]. && (5.153)
\end{aligned}$$

Thus, the complete covariance between the motion error and the acceleration is given by

$$\mathbf{Q}_{ps} = \begin{bmatrix} \chi(\sigma_{\delta s_x^t, s_u^r}, \omega_u) & \chi(\sigma_{\delta s_x^t, s_v^r}, \omega_v) & \chi(\sigma_{\delta s_x^t, s_w^r}, \omega_w) \\ \chi(\sigma_{\delta s_y^t, s_u^r}, \omega_u) & \chi(\sigma_{\delta s_y^t, s_v^r}, \omega_v) & \chi(\sigma_{\delta s_y^t, s_w^r}, \omega_w) \\ \chi(\sigma_{\delta s_z^t, s_u^r}, \omega_u) & \chi(\sigma_{\delta s_z^t, s_v^r}, \omega_v) & \chi(\sigma_{\delta s_z^t, s_w^r}, \omega_w) \\ \Upsilon(\sigma_{\delta s_x^t, s_u^r}, \omega_u) & \Upsilon(\sigma_{\delta s_x^t, s_v^r}, \omega_v) & \Upsilon(\sigma_{\delta s_x^t, s_w^r}, \omega_w) \\ \Upsilon(\sigma_{\delta s_y^t, s_u^r}, \omega_u) & \Upsilon(\sigma_{\delta s_y^t, s_v^r}, \omega_v) & \Upsilon(\sigma_{\delta s_y^t, s_w^r}, \omega_w) \\ \Upsilon(\sigma_{\delta s_z^t, s_u^r}, \omega_u) & \Upsilon(\sigma_{\delta s_z^t, s_v^r}, \omega_v) & \Upsilon(\sigma_{\delta s_z^t, s_w^r}, \omega_w) \end{bmatrix}^T . \tag{5.154}$$

The accelerometer bias and the geo-field error are also first-order Gauss Markov processes like the acceleration. Therefore, their covariances took identical forms:

$$\mathbf{Q}_{pb} = \begin{bmatrix} \chi(\sigma_{\delta s_x^t, b_u^r}, \frac{1}{\tau_{b_u^r}}) & \chi(\sigma_{\delta s_x^t, b_v^r}, \frac{1}{\tau_{b_v^r}}) & \chi(\sigma_{\delta s_x^t, b_w^r}, \frac{1}{\tau_{b_w^r}}) \\ \chi(\sigma_{\delta s_y^t, b_u^r}, \frac{1}{\tau_{b_u^r}}) & \chi(\sigma_{\delta s_y^t, b_v^r}, \frac{1}{\tau_{b_v^r}}) & \chi(\sigma_{\delta s_y^t, b_w^r}, \frac{1}{\tau_{b_w^r}}) \\ \chi(\sigma_{\delta s_z^t, b_u^r}, \frac{1}{\tau_{b_u^r}}) & \chi(\sigma_{\delta s_z^t, b_v^r}, \frac{1}{\tau_{b_v^r}}) & \chi(\sigma_{\delta s_z^t, b_w^r}, \frac{1}{\tau_{b_w^r}}) \\ \Upsilon(\sigma_{\delta s_x^t, b_u^r}, \frac{1}{\tau_{b_u^r}}) & \Upsilon(\sigma_{\delta s_x^t, b_v^r}, \frac{1}{\tau_{b_v^r}}) & \Upsilon(\sigma_{\delta s_x^t, b_w^r}, \frac{1}{\tau_{b_w^r}}) \\ \Upsilon(\sigma_{\delta s_y^t, b_u^r}, \frac{1}{\tau_{b_u^r}}) & \Upsilon(\sigma_{\delta s_y^t, b_v^r}, \frac{1}{\tau_{b_v^r}}) & \Upsilon(\sigma_{\delta s_y^t, b_w^r}, \frac{1}{\tau_{b_w^r}}) \\ \Upsilon(\sigma_{\delta s_z^t, b_u^r}, \frac{1}{\tau_{b_u^r}}) & \Upsilon(\sigma_{\delta s_z^t, b_v^r}, \frac{1}{\tau_{b_v^r}}) & \Upsilon(\sigma_{\delta s_z^t, b_w^r}, \frac{1}{\tau_{b_w^r}}) \end{bmatrix}^T , \tag{5.155}$$

and

$$\mathbf{Q}_{pm} = \begin{bmatrix} \chi(\sigma_{\delta s_x^t, \mu_e^g}, \frac{1}{\tau_{\mu_e^g}}) & \chi(\sigma_{\delta s_x^t, \mu_n^g}, \frac{1}{\tau_{\mu_n^g}}) & \chi(\sigma_{\delta s_x^t, \mu_u^g}, \frac{1}{\tau_{\mu_u^g}}) \\ \chi(\sigma_{\delta s_y^t, \mu_e^g}, \frac{1}{\tau_{\mu_e^g}}) & \chi(\sigma_{\delta s_y^t, \mu_n^g}, \frac{1}{\tau_{\mu_n^g}}) & \chi(\sigma_{\delta s_y^t, \mu_u^g}, \frac{1}{\tau_{\mu_u^g}}) \\ \chi(\sigma_{\delta s_z^t, \mu_e^g}, \frac{1}{\tau_{\mu_e^g}}) & \chi(\sigma_{\delta s_z^t, \mu_n^g}, \frac{1}{\tau_{\mu_n^g}}) & \chi(\sigma_{\delta s_z^t, \mu_u^g}, \frac{1}{\tau_{\mu_u^g}}) \\ \Upsilon(\sigma_{\delta s_x^t, \mu_e^g}, \frac{1}{\tau_{\mu_e^g}}) & \Upsilon(\sigma_{\delta s_x^t, \mu_n^g}, \frac{1}{\tau_{\mu_n^g}}) & \Upsilon(\sigma_{\delta s_x^t, \mu_u^g}, \frac{1}{\tau_{\mu_u^g}}) \\ \Upsilon(\sigma_{\delta s_y^t, \mu_e^g}, \frac{1}{\tau_{\mu_e^g}}) & \Upsilon(\sigma_{\delta s_y^t, \mu_n^g}, \frac{1}{\tau_{\mu_n^g}}) & \Upsilon(\sigma_{\delta s_y^t, \mu_u^g}, \frac{1}{\tau_{\mu_u^g}}) \\ \Upsilon(\sigma_{\delta s_z^t, \mu_e^g}, \frac{1}{\tau_{\mu_e^g}}) & \Upsilon(\sigma_{\delta s_z^t, \mu_n^g}, \frac{1}{\tau_{\mu_n^g}}) & \Upsilon(\sigma_{\delta s_z^t, \mu_u^g}, \frac{1}{\tau_{\mu_u^g}}) \end{bmatrix}^T , \tag{5.156}$$

respectively.

At this point, an expression for $\mathbf{Q}_{pg}$ is the only thing lacking. Recall that the frame alignment error is modeled as a constant, and its associated state noise is white Gaussian. Let the noise for its x-axis component be represented by $w(t)$. The discretized version is

$$w_k = \int_0^{\Delta t} w(\gamma) d\gamma. \tag{5.157}$$

Then, the discrete covariance with the position error is derived as

$$\begin{aligned}
\sigma_{xw} &= \mathbb{E}[x_k w_k] && (5.158)\\
&= \mathbb{E}\left[\int_0^{\Delta t} (\Delta t - \alpha) x(\alpha) d\alpha \int_0^{\Delta t} w(\gamma) d\gamma\right] && (5.159)\\
&= \int_0^{\Delta t}\int_0^{\Delta t} (\Delta t - \alpha)\mathbb{E}[x(\alpha)w(\gamma)]\, d\alpha d\gamma && (5.160)\\
&= \int_0^{\Delta t}\int_0^{\Delta t} (\Delta t - \alpha)\sigma_{\delta s_x^t, \omega_x^g}\delta(\alpha - \gamma) d\alpha d\gamma && (5.161)\\
&= \int_0^{\Delta t} (\Delta t - \gamma)\sigma_{\delta s_x^t, \omega_x^g} d\gamma && (5.162)\\
&= \sigma_{\delta s_x^t, \omega_x^g}\frac{\Delta t^2}{2}. && (5.163)
\end{aligned}$$

Similarly, for the covariance with the velocity error

$$\begin{aligned}
\sigma_{vw} &= \mathbb{E}[v_k w_k] && (5.164)\\
&= \mathbb{E}\left[\int_0^{\Delta t} v(\alpha) d\alpha \int_0^{\Delta t} w(\gamma) d\gamma\right] && (5.165)\\
&= \int_0^{\Delta t}\int_0^{\Delta t} \mathbb{E}[v(\alpha)w(\gamma)]\, d\alpha d\gamma && (5.166)\\
&= \int_0^{\Delta t}\int_0^{\Delta t} \sigma_{\delta s_x^t, \omega_x^g}\delta(\alpha - \gamma) d\alpha d\gamma && (5.167)\\
&= \int_0^{\Delta t} \sigma_{\delta s_x^t, \omega_x^g} d\gamma && (5.168)\\
&= \sigma_{\delta s_x^t, \omega_x^g}\Delta t. && (5.169)
\end{aligned}$$

Therefore, the full covariance is

$$\mathbf{Q}_{pg} = \begin{bmatrix} \sigma_{\delta s_x^t,\omega_{g,x}} \frac{\Delta t^2}{2} & \sigma_{\delta s_x^t,\omega_{g,y}} \frac{\Delta t^2}{2} & \sigma_{\delta s_x^t,\omega_{g,z}} \frac{\Delta t^2}{2} \\ \sigma_{\delta s_y^t,\omega_{g,x}} \frac{\Delta t^2}{2} & \sigma_{\delta s_y^t,\omega_{g,y}} \frac{\Delta t^2}{2} & \sigma_{\delta s_y^t,\omega_{g,z}} \frac{\Delta t^2}{2} \\ \sigma_{\delta s_z^t,\omega_{g,x}} \frac{\Delta t^2}{2} & \sigma_{\delta s_z^t,\omega_{g,y}} \frac{\Delta t^2}{2} & \sigma_{\delta s_z^t,\omega_{g,z}} \frac{\Delta t^2}{2} \\ \sigma_{\delta s_x^t,\omega_{g,x}} \Delta t & \sigma_{\delta s_x^t,\omega_{g,y}} \Delta t & \sigma_{\delta s_x^t,\omega_{g,z}} \Delta t \\ \sigma_{\delta s_y^t,\omega_{g,x}} \Delta t & \sigma_{\delta s_y^t,\omega_{g,y}} \Delta t & \sigma_{\delta s_y^t,\omega_{g,z}} \Delta t \\ \sigma_{\delta s_z^t,\omega_{g,x}} \Delta t & \sigma_{\delta s_z^t,\omega_{g,y}} \Delta t & \sigma_{\delta s_z^t,\omega_{g,z}} \Delta t \end{bmatrix}^T . \tag{5.170}$$

With every component of the state transition covariance specified and with each transition function specified, the models for the state variables are complete. Thus, all of the information required by the Kalman filter is defined, and the navigation system can be implemented.

5.4 Design Summary

The integrated navigation system presented in this chapter is one of the three primary contributions of this project. To this author's knowledge, no other systems like it exist. Not only is the final form original, but it seems to be the first time someone has approached the magnetic localization problem as an error-state tracking system. The system's final form resembles a tightly-coupled, INS/GPS integrated navigation system. However, instead of the INS, only a magnetometer and accelerometer are present. Also, instead of a GPS receiver, the magnetic coil receiver is used. To make up for a lack of gyroscope, both the magnetometer and the coil receiver are used.

The Kalman filter is the primary tool used to fuse the observations from the receiver sensors. The design of the filter does not deal with the filter's internals. Instead, the design is primarily concerned with modeling the system observations,

states, and dynamics. Once these models are derived, the design of the navigation is complete. The next chapter will present the results from this design.

Chapter 6

Testing and Results

This chapter presents the implementation and results of the integrated magnetic navigation system. The first section covers the setup and testing environment. Within this section, a magnetic survey of the testing site will be described which is a significant contribution of this research. The second section contains a demonstration of the navigation system technology which is presented in the previous chapter. The results achieved in this demonstration represent a massive improvement over the baseline magnetic positioning technology.

6.1 Setup and Environment

This section describes the hardware and software implementation of the integrated magnetic navigation system. In addition, the testing environment is described along with a magnetic fingerprint of the site used for testing.

6.1.1 Hardware

The features of the hardware are outlined previously, but they are reviewed here with some extra detail. The system hardware is made up of the transmitter beacon and

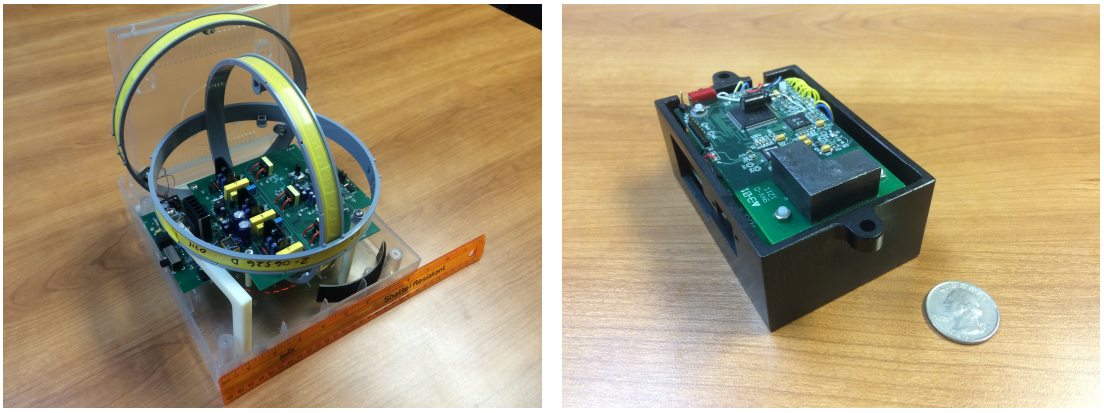

(a) Transmitter **(b)** Receiver

Figure 6.1: Transmitter and receiver hardware.

the receiver. The transmitter is a proprietary design created specifically for magnetic positioning applications. It contains three co-located, orthogonal coils.

The receiver is also a proprietary design, and it also contains three co-located orthogonal coils. The coils sense the magnetic field from the beacon and feed the signals into a circuit for demodulation, down-mixing, and amplification. The receiver also contains a tri-axial magnetometer and accelerometer. These are both part of the same integrated circuit—the LSM303D "Ultra compact high performance e-compass 3D accelerometer and 3D magnetometer module" [6].

In order to develop the navigation system algorithms, the sensor data from the coils and the MA must be be recorded. A Secure Digital (SD) flash memory card is used for this purpose. The brain of the receiver is an MSP430F5438 microcontroller from Texas Instruments [78]. This device is responsible for managing and collecting the sensor measurements and writing them to the SD card. During the collecting of the data, the receiver is mounted on a pole, which is held by the user. This results in the receiver being about 18 inches above ground when the data is collected.

The transmitter and receiver hardware are shown in Figure 6.1.

6.1.2 Software

The navigation system software is implemented with recorded data using the Python programming language [42]. Python allows for very concise and efficient programming practices. Even though it is known as a concise language, the Python code associated with this research effort consists of over 100,000 lines of code spread across more than 500 source files.

When possible, off-the-shelf python libraries are used (which are not included in the total line count). For mathematical and numerical routines, Scipy [79] and Numpy [80] are used. For plotting and display, Matplotlib [81] is the primary tool. The Kalman filter framework within the navigation system is taken from the Pykalman library [73]. All of the Python software is written using the jEdit code editor [82]. Debugging and executing are done with the standard, command-line Python toolset.

In addition to the software for the navigation system implementation, numerous supporting applications and routines are needed in the course of this project. They include

- A platform for continuous sensor data parsing, storing, loading, and anomaly correction.
- Single point survey data collection platform.
- Numerous 2-D and 3-D data visualization and analysis applications.
- Sensor noise measurement routines
- Field component phase normalization routines
- A field component matrix energy normalization
- The TRIAD algorithm.
- Routines for calculating and applying the calibration for each sensor.
- Numerous other mathematical routines, e.g. quaternion calculations.

In addition to the Python code, software was required to record and process the sensor data on the microcontroller. This was written in the C++ language and embedded on the microcontroller. The backbone of this software was done before the beginning of this research effort. However, the following features were added during this research:

- Magnetometer hardware interfacing capability.
- Accelerometer hardware interfacing capability.
- Continuous sensor data recording capability for the accelerometer and magnetometer.
- Single point survey data collection capability.
- Calibration data collection capability.

A few thousand lines of new C++ code were required to add these capabilities to the receiver's embedded microcontroller.

6.1.3 Testing Environment

Test Site

The test site consists of an asphalt parking lot behind a steel and block building in Knoxville, Tennessee. Adjacent to the parking lot is a grassy field. The transmitter is positioned towards the center of the parking lot and oriented roughly parallel to the building. Against the building there are several HVAC units, electrical units, conventional steel doors, steel overhead doors, steel awnings, and steel protective barrier posts. In addition, in the northeast corner, a steel dumpster sits on a concrete pad. Figure 6.2 shows photos of the test site and building.

In order to have true position data, a land survey was performed on the test site. Survey points were spaced on a nominally 12-foot grid. Additional points were taken

(a) From the grassy area

(b) From the northwest corner

(c) From the southeast corner

Figure 6.2: Photos of the building and testing site.

at the vertices of the building features, such as the HVAC units and the concrete pads. This allows a detailed diagram of the site to be constructed. Figure 6.3 shows this diagram and a corresponding aerial photo. The diagram shows the building with its features, the asphalt, and the grassy area. The key to interpreting the diagram is as follows:

- Gray crosses: survey grid points
- Gray patches: concrete pads
- Black hatched areas: steel awnings
- Solid black line segments: steel doors
- Dark gray line segments: steel overhead doors
- Black dots: steel and concrete barrier posts
- Green patches: HVAC and electrical units

The survey data is useful for visualizing the layout of the test site, but its primary purpose is to provide true position data for testing the magnetic location system. After the survey was taken, markers were left on the test site so that experiments could be referenced to known positions.

Magnetic Field Survey

Once the land survey of the test site was complete, a magnetic field survey of the site was performed. This consisted in measuring and recording the component magnetic field matrix and also the magnetometer measurement over the bulk of the test site. The end result is a magnetic field map of the test site. To this author's knowledge, no similar map of a large area exists for magnetic localization systems. As such, this map is a significant original contribution of this research.

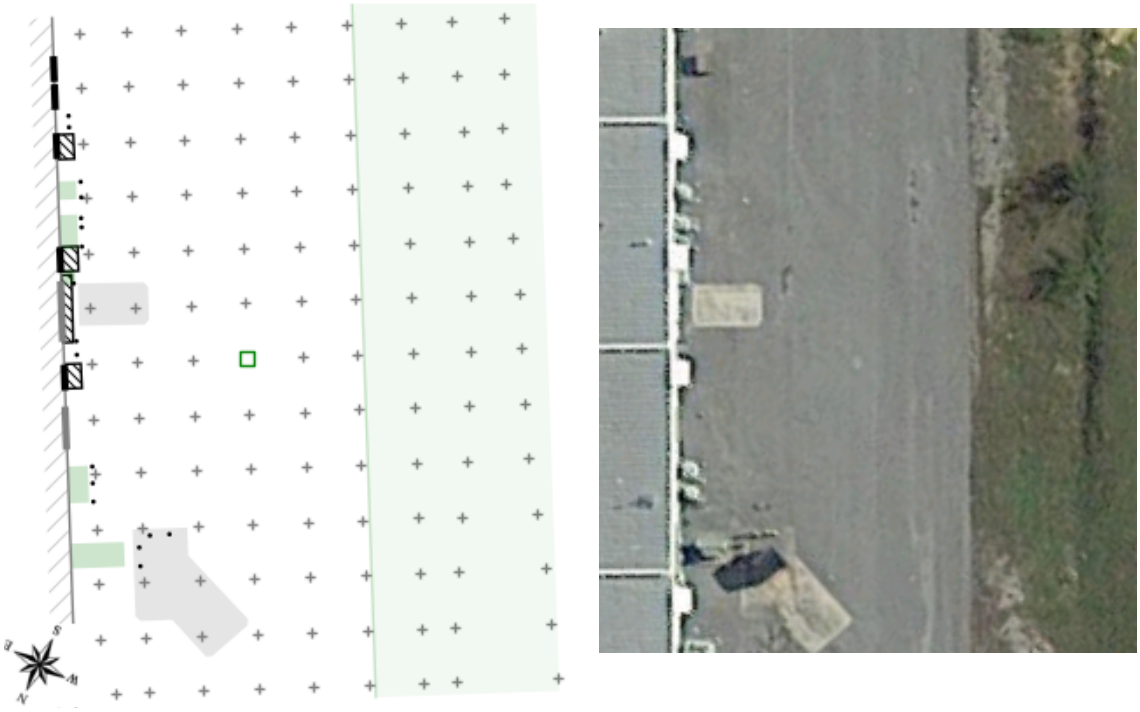

(a) Diagram and survey points. **(b)** Aerial photo. [28]

Figure 6.3: The testing site and survey. (a) The survey grid is oriented with the transmitter and is spaced at 12 feet. The green square is the transmitter location. (b) A photo of the site. Note the asphalt, grass regions, and the building features including the dumpster and dumpster pad (lower left), the HVAC units, and the steel door awnings.

The map is referenced to the site survey and is constructed with over 1400 sample points. It would have been desirable to densely sample the entire survey area, but for logistical reasons, only the central area of the site was densely sampled. A point spacing of 2 feet was used for this area. The transmitter has a minimum working distance inside of which the measurements are saturated and worthless; therefore, the area around the transmitter is excluded. To extend the map, samples were taken at each survey point not covered by the central area. Also, the 2 foot sample density was used to construct several lines of samples emanating from the central area. These extra samples helped reveal the whole magnetic fingerprint of the test site.

Because the magnetic field components have such a high dynamic range, they are normalized before being displayed. Using Equation (2.16), the following is trivial to show

$$\mathbf{B}^{tT}\mathbf{B}^{t} = \frac{k^2}{r^8}\begin{bmatrix} 3x^2+r^2 & 3xy & 3xz \\ 3xy & 3y^2+r^2 & 3yz \\ 3xz & 3yz & 3z^2+r^2 \end{bmatrix}. \tag{6.1}$$

Therefore,

$$\text{trace}(\mathbf{B}^{tT}\mathbf{B}^{t}) = \frac{6k^2}{r^6}, \tag{6.2}$$

and a normalization factor, c, is defined as

$$c = \frac{k}{r^3} = \sqrt{\frac{\text{trace}(\mathbf{B}^{tT}\mathbf{B}^{t})}{6}}. \tag{6.3}$$

Therefore, a normalized field component matrix is defined as

$$\mathbf{B}^{t}_{\|\cdot\|} = \frac{\mathbf{B}^{t}}{c} \tag{6.4}$$

$$= \begin{bmatrix} 3\hat{x}^2-1 & 3\hat{x}\hat{y} & 3\hat{x}\hat{z} \\ 3\hat{x}\hat{y} & 3\hat{y}^2-1 & 3\hat{y}\hat{z} \\ 3\hat{x}\hat{z} & 3\hat{y}\hat{z} & 3\hat{z}^2-1 \end{bmatrix}, \tag{6.5}$$

where $\hat{x}$, $\hat{y}$, and $\hat{z}$ are the components of the unit vector $\hat{\mathbf{r}} = \dfrac{\mathbf{r}}{\|\mathbf{r}\|}$. By inspection of $\mathbf{B}^t_{\|\cdot\|}$, the diagonal elements have a range of -1 to 2, and the off-diagonal elements have a range of -0.5 to 0.5. Normalizing the field component matrix in this way removes the dependence on the distance from the transmitter and makes viewing and processing the field component matrix much simpler. This process will be referred to as *range normalizing* for the remainder of this work.

To view the results of the survey, the range-normalized field component matrix is subtracted from the ideal, range-normalized field component matrix at a given survey point. This is done in the transmitter frame of reference, and the result is referred to as the *field component error matrix*. During the collection of the magnetic samples, the receiver was oriented in a known direction. Thus, transforming the measurements into the transmitter frame of reference is a matter of de-rotating by the known orientation. However, there is some human error involved in orienting the receiver during the sample collection. This error resembles noise and is low enough that the important information could be gleaned from the magnetic field map.

Figures 6.4, 6.5, and 6.6 show the elements of the 3×3 field component error matrix with one row of the matrix per figure. As would be expected, the samples show significant perturbation near the metal building due to eddy current distortions in the magnetic field.

The field error matrix also reveals a feature of the test site which is unexpected. A buried cable appears to be running from the building to the grassy area near the bottom of the central area. From there, it runs up the border of the grassy area and forms a loop by connecting back to the building. The indications are that it connects back to the building above the top edge of the surveyed area. Since the cable loop is oriented horizontally, its effects can be seen almost exclusively in the z-coil portion of the field error matrix (i.e. the third column). The estimated path of the loop is shown in Figure 6.7.

The implications of this buried loop should not be missed. Because most of the surveyed site falls within the loop, nearly all of it is subject to bulk eddy errors. This

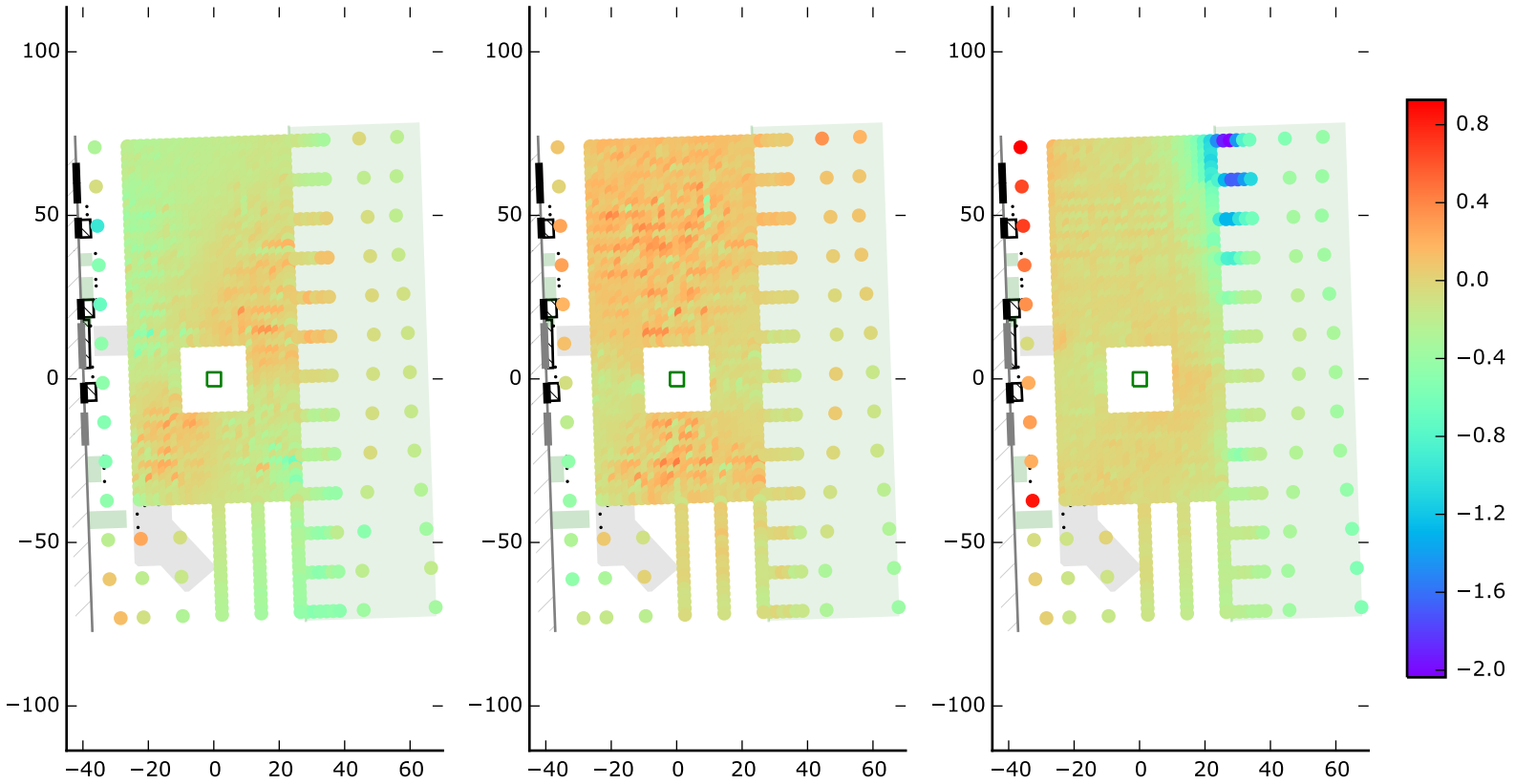

Figure 6.4: Field component error matrix: Row 1 of the 3×3 matrix. The elements of row 1 are shown as sampled on the survey points. Shown from left to right are the plots for row 1 column 1, row 1 column 2, and row 1 column 3, respectively.

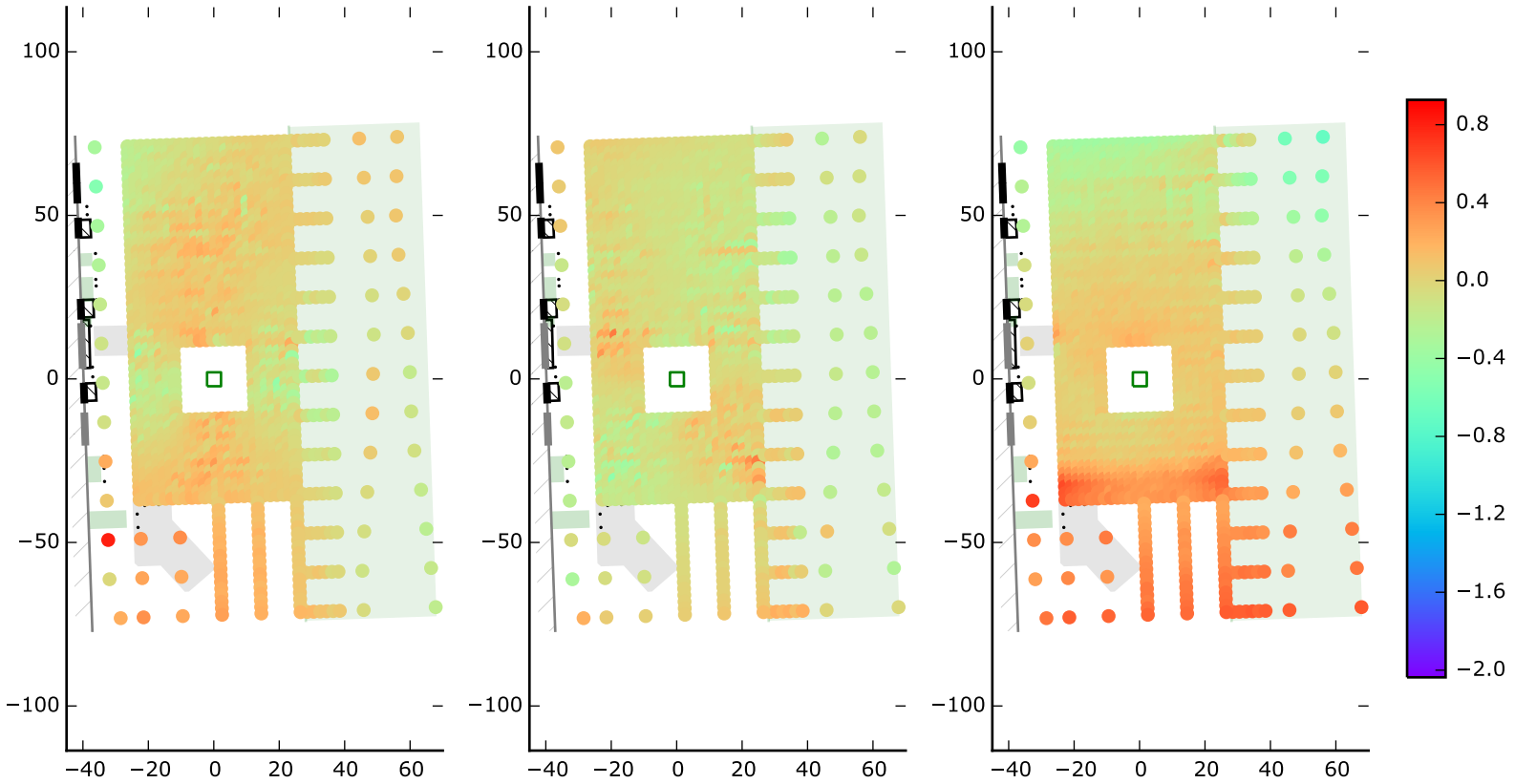

Figure 6.5: Field component error matrix: Row 2 of the 3×3 matrix. The elements of row 2 are shown as sampled on the survey points. Shown from left to right are the plots for row 2 column 1, row 2 column 2, and row 2 column 3, respectively.

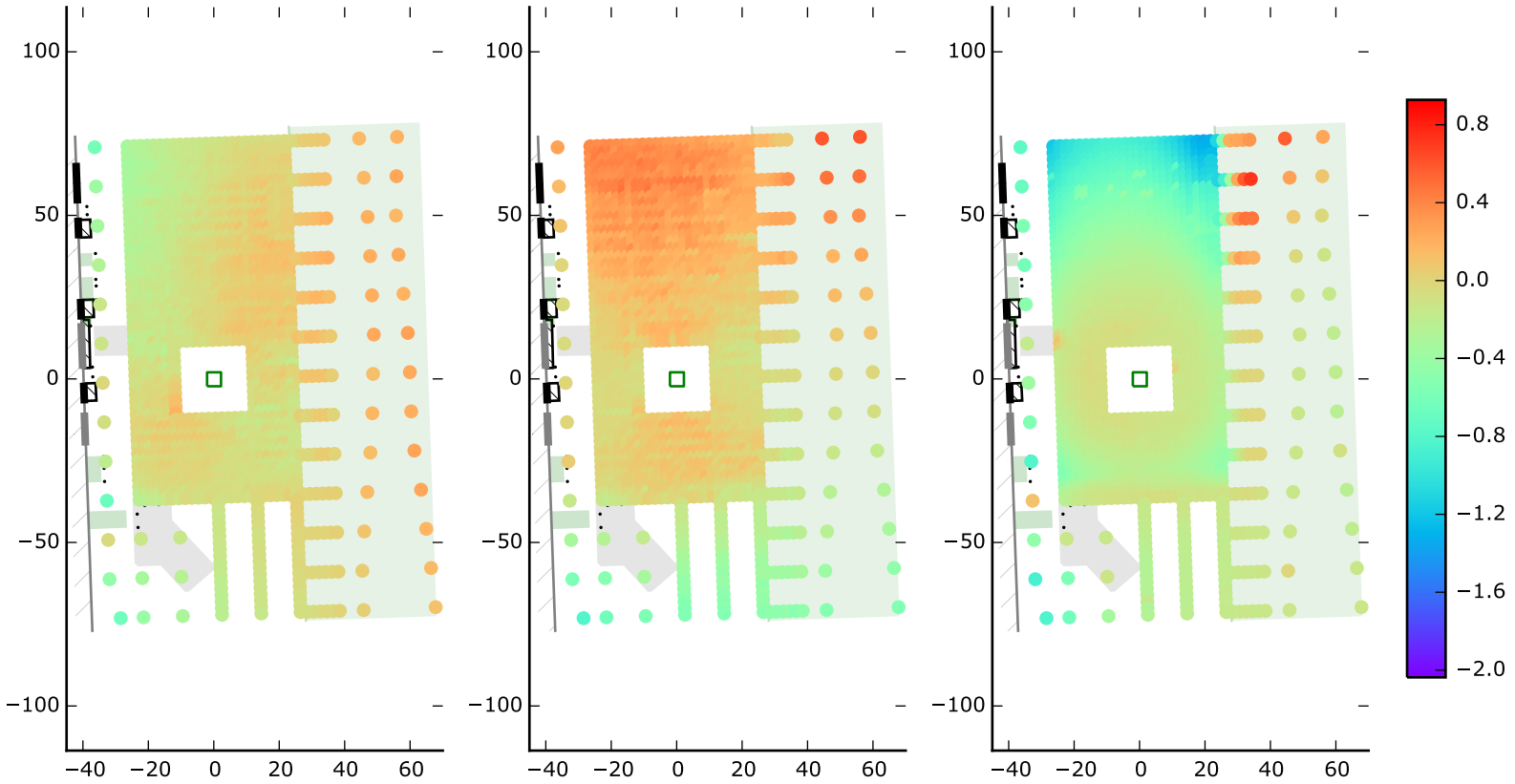

Figure 6.6: Field component error matrix: Row 3 of the 3×3 matrix. The elements of row 3 are shown as sampled on the survey points. Shown from left to right are the plots for row 3 column 1, row 3 column 2, and row 3 column 3, respectively.

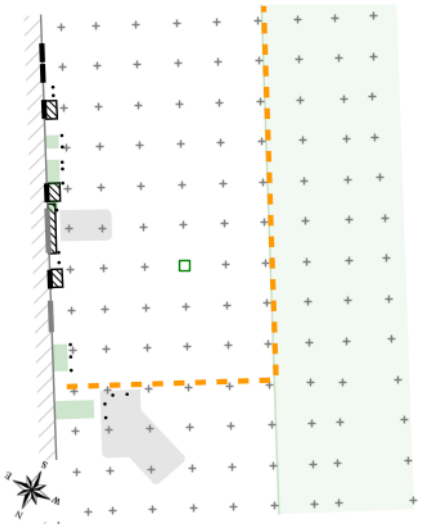

Figure 6.7: Estimated route of the buried cable. The survey grid is spaced at 12 feet in the asphalt area.

violates one of the design assumptions outlined in Chapter 2. Nevertheless, as will be seen in a later section, the system is able to overcome the violation of this assumption and still perform well.

Visualization of the field errors are easier to comprehend when the results are displayed as physical quantities. Therefore, the errors in position and rotation are derived using the Kuipers algorithm. The position result is shown in Figure 6.8. As can be seen, the eddy distortions cause severe, catastrophic errors in position. In the area with the strongest distortion, the z-axis and y-axis position error is nearly 60 feet, and the x-axis error is almost 40 feet. Once again, the area very near the building shows strong perturbations. While not as strong as those in the top-right corner, they are still very severe and seem to have a somewhat less predictable nature.

In addition to the Kuipers position error, the Kuipers rotation error is also calculated. Before describing these errors it is necessary to define the Euler angle convention. In accord with [4], the aerospace sequence is used. In this case, to transform from the transmitter frame of reference to the receiver frame of reference,

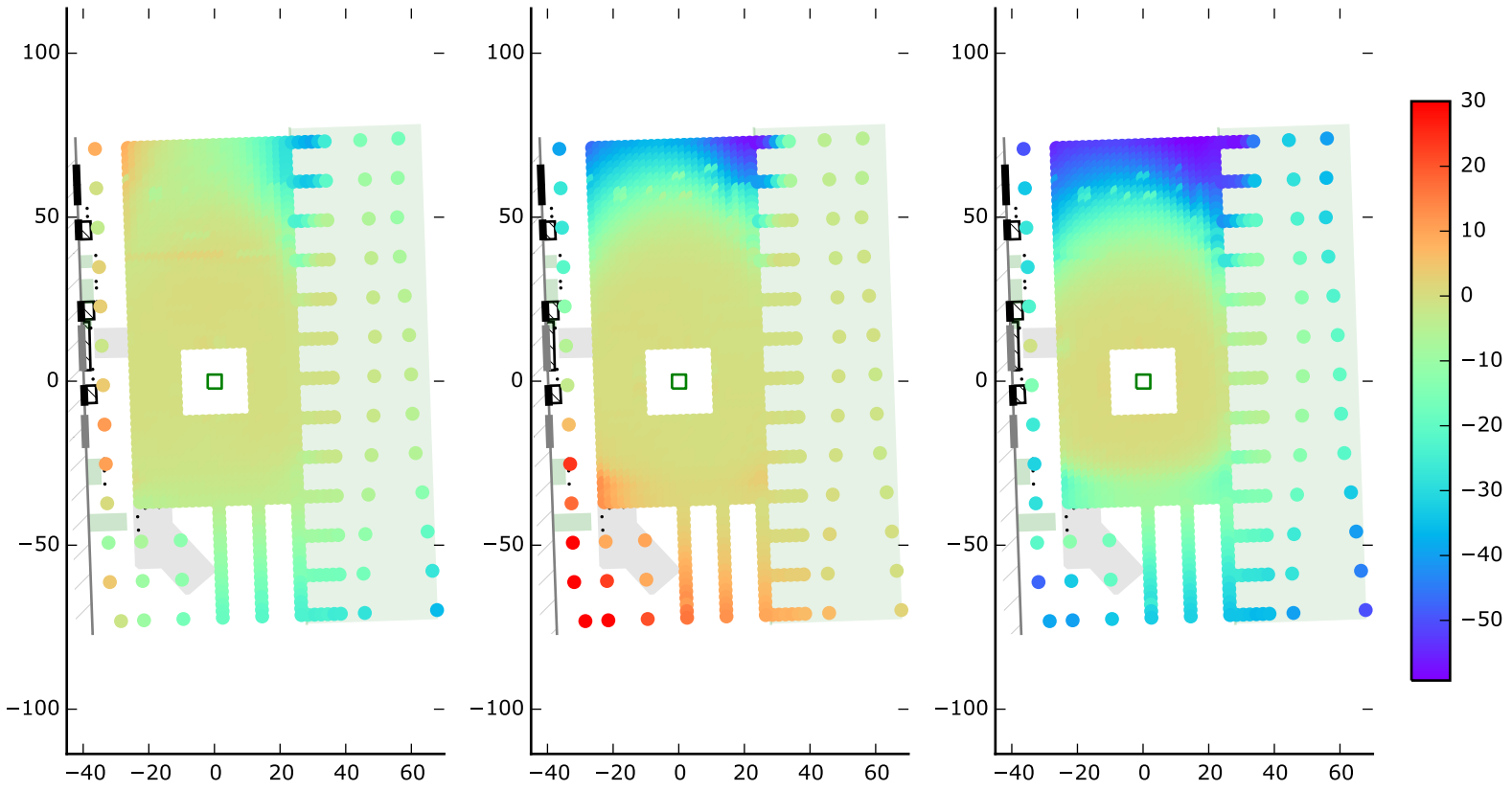

Figure 6.8: Survey Kuipers position error. From left to right, the figures represent the position errors in the x, y, and z dimensions, respectively. Units are in feet.

the coordinate frame is first rotated around the z-axis by an angle referred to as the *heading*. Next, the coordinate frame is rotated by the new y-axis by an angle referred to as the *elevation*. And finally, the coordinate frame is rotated by the newest x-axis by an angle referred to as the *bank-angle*. [4]

The terms heading, elevation, and bank-angle lose their meaning if the Euler angles come from a rotation matrix which transforms in the opposite way: *from* the receiver frame *to* the transmitter frame. However, in this case, it is still important to be able to talk about the Euler angles of that rotation matrix. Therefore, the heading, elevation, and bank-angle terms are dropped. Instead, it is just assumed that the sequence of the three Euler angles of a given rotation matrix are referred to the third principle axis, the new second principle axis, and the newest first principle axis, respectively. This Euler angle convention is used throughout this document.

For each point in the magnetic field map, this convention is used to evaluate the error in the Kuipers rotation. The true rotation at a point is approximately known (but subject to slight human error when orienting the receiver to take the measurement). Temporarily, let $\underset{t:r}{\mathbf{R}}$ refer to this orientation and $\underset{t:r}{\tilde{\mathbf{R}}}$ refer to the Kuipers calculated rotation. The error rotation matrix is then calculated as $\underset{t:r}{\delta\mathbf{R}} = \underset{t:r}{\tilde{\mathbf{R}}}\underset{t:r}{\mathbf{R}}^T$. The Euler angles of $\underset{t:r}{\delta\mathbf{R}}$ are denoted as $\delta\psi$, $\delta\theta$, and $\delta\phi$. These angles are plotted in Figure 6.9. In order to more effectively view the results, the errors are clipped at $\pm 60°$; however, in actuality, they go much higher in magnitude and even exceed $90°$.

These last two figures, Figure 6.8 and Figure 6.9, are a great representation of the problems encountered in real-world magnetic localization. Near the transmitter, where the signal is strong and the distorting objects are relatively distant, the performance is very good in both position and rotation. However, as the signal weakens and distorting objects move closer, the performance rapidly becomes catastrophically bad. These are the problems that have plagued magnetic positioning systems since their advent, and these are the problems this effort sought to address.

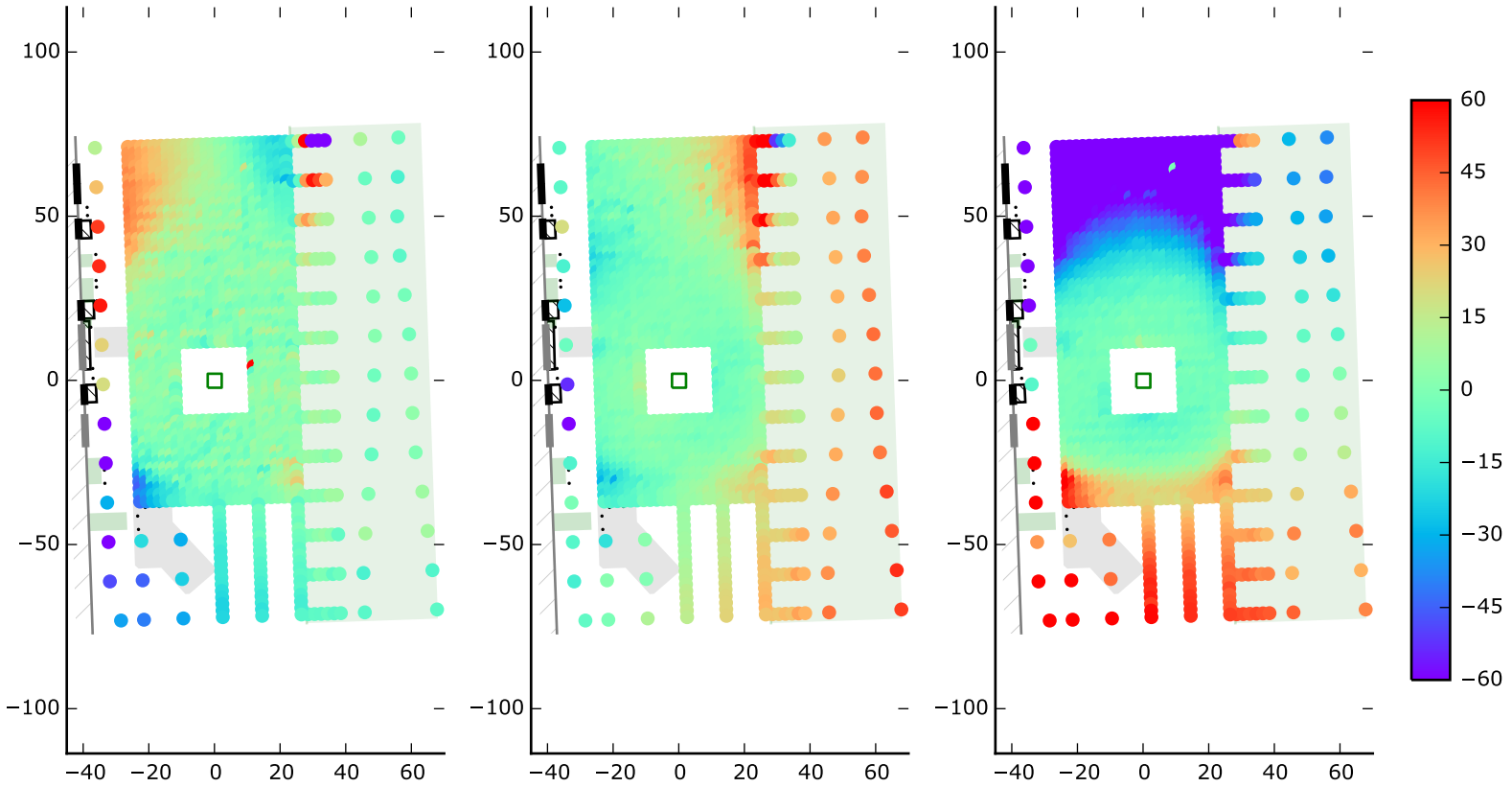

Figure 6.9: Survey Kuipers rotation error. The Euler angles of the error rotation matrix are shown. Units are degrees, but the error display is capped at $\pm 60^\circ$ to better show regions of smaller error. From left to right, the plots refer to $\delta\psi$, $\delta\theta$, and $\delta\phi$, respectively.

While collecting data for the magnetic field map, data was also collected from the magnetometer and accelerometer sensors. The data from the accelerometer is not very informative, but the magnetometer data is useful for discovering geo-magnetic field anomalies. The geo-magnetic compass heading and inclination from the magnetometer measurements are shown in Figure 6.10. (The magnitude of the measurements is the third component of the magnetometer, but it is left out because the gain of the magnetometer varies substantially with time and temperature (see Subsection 4.3.2).) The inclination is calculated with the accelerometer vector as a vertical reference, but the heading is subject to human error in the orientation of the receiver during the measurement. For reference, the nominal heading is 2° relative to the transmitter's y-axis, and the nominal inclination is 66°.

As expected, these results show reliable geo-magnetic fields over most of the test site. However, as the receiver nears ferromagnetic metal objects, the measurements become less dependable. This is especially obvious near the steel building, the HVAC units, and the metal dumpster.

Testing Environment Summary

The site survey and the accompanying data collection yield a much greater understanding of the challenges that face magnetic positioning systems. Indeed, the magnetic field signature of such a large, outdoor area is not found in the previously reported literature. As such, this information is a valuable contribution of this research.

The environmental distortions for the chosen site are much greater than expected. However, it shows promise as a location for testing: It has areas of bulk eddy distortion near the building, areas of acute eddy distortion near the buried cable, areas of ferromagnetic distortion near the building, and clean areas in the grass. In other words, all conditions that the receiver needs to compensate for are present at the site.

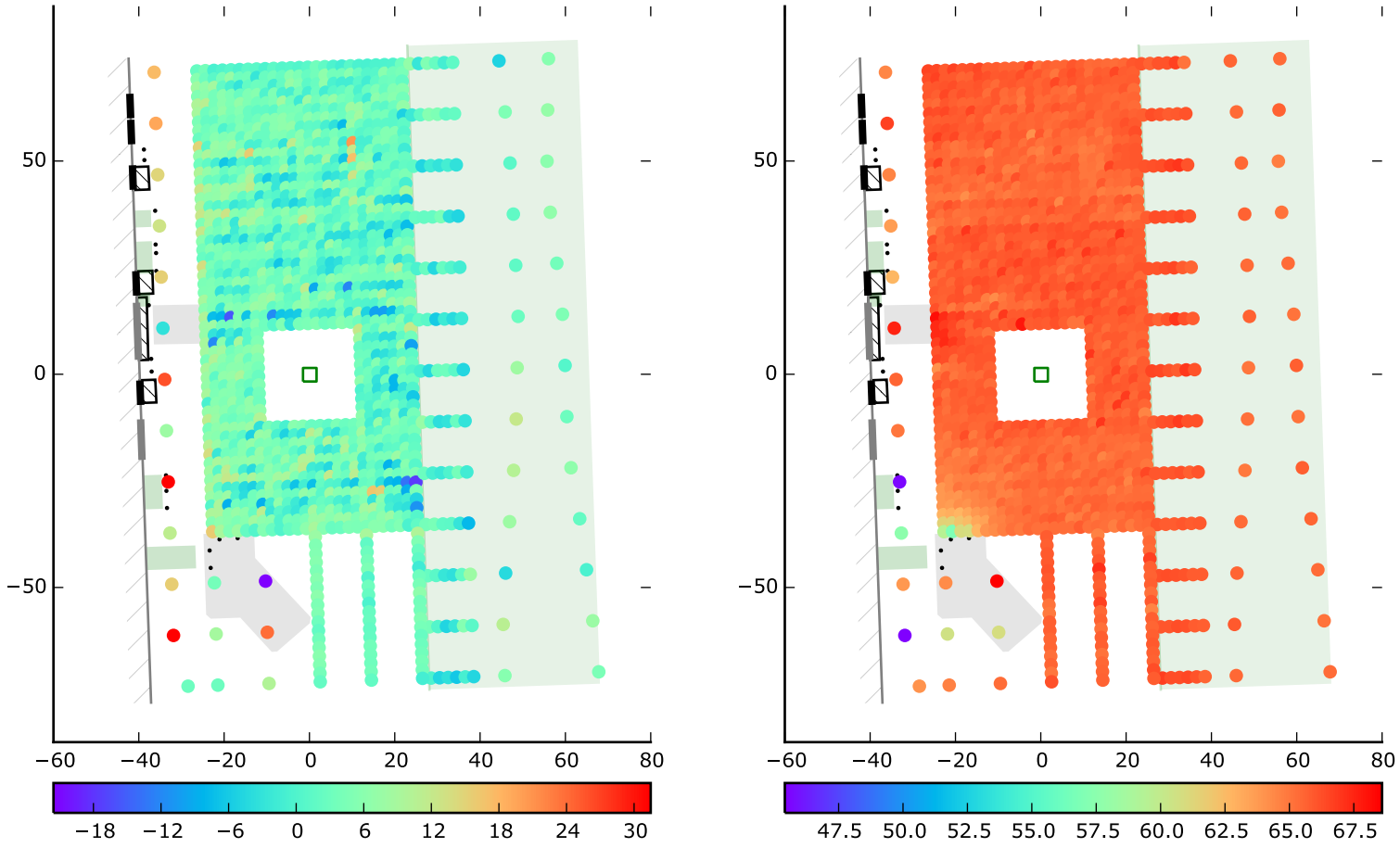

(a) Heading

(b) Inclination

Figure 6.10: Geo-field survey results. Unlike the inclination, the heading is subject to human error in the data collection process; so, it has more noisy results and some erroneous points.

6.2 Technology Demonstration

To prove the viability of the navigation system, a demonstration is performed in the same manner as in many other works (e.g. [83, 84, 10, 85]). The test site described in the last section is used as the proving grounds. The demonstration includes all of the environmental conditions that this effort sought to address. Specifically, the data includes clean areas, ferromagnetic distortion, and eddy distortion of both the acute and bulk varieties.

The demonstration seeks to incorporate all of these conditions. Also, a varied sequence of movements is used to illustrate the robustness to motion conditions. These include sharp turns, gradual turns, and straight segments of varying length. The path of travel is shown in Figure 6.11. The path begins (and ends) at the vertex indicated with a magenta circle, and it proceeds counterclockwise. The transmitter is located at the origin, and the axes are the principle axes of the transmitter frame of reference. The area in the grass is largely free of distortion. Ferromagnetic distortion is present when walking near the building. Acute eddy distortion is present at the crossing with the buried cable. Bulk eddy distortion is present nearly everywhere between the building and the buried cable.

6.2.1 Measurement Data

Data is recorded from each of the receiver sensors as the path is walked. The accelerometer measurements are shown in Figure 6.12. The magnetometer measurements are shown in Figure 6.13. The non-range-normalized field component matrix measurements are shown in Figure 6.14. All measurements are in the receiver frame of reference.

The magnetometer measurements are used to determine the level of geo-magnetic field distortion. The method to do this is described in Subsection 5.3.6. In Figure 6.15 the distortion levels are shown against the magnitude of the magnetometer measurement vector. As can be seen, serious distortions occur in the geo-magnetic

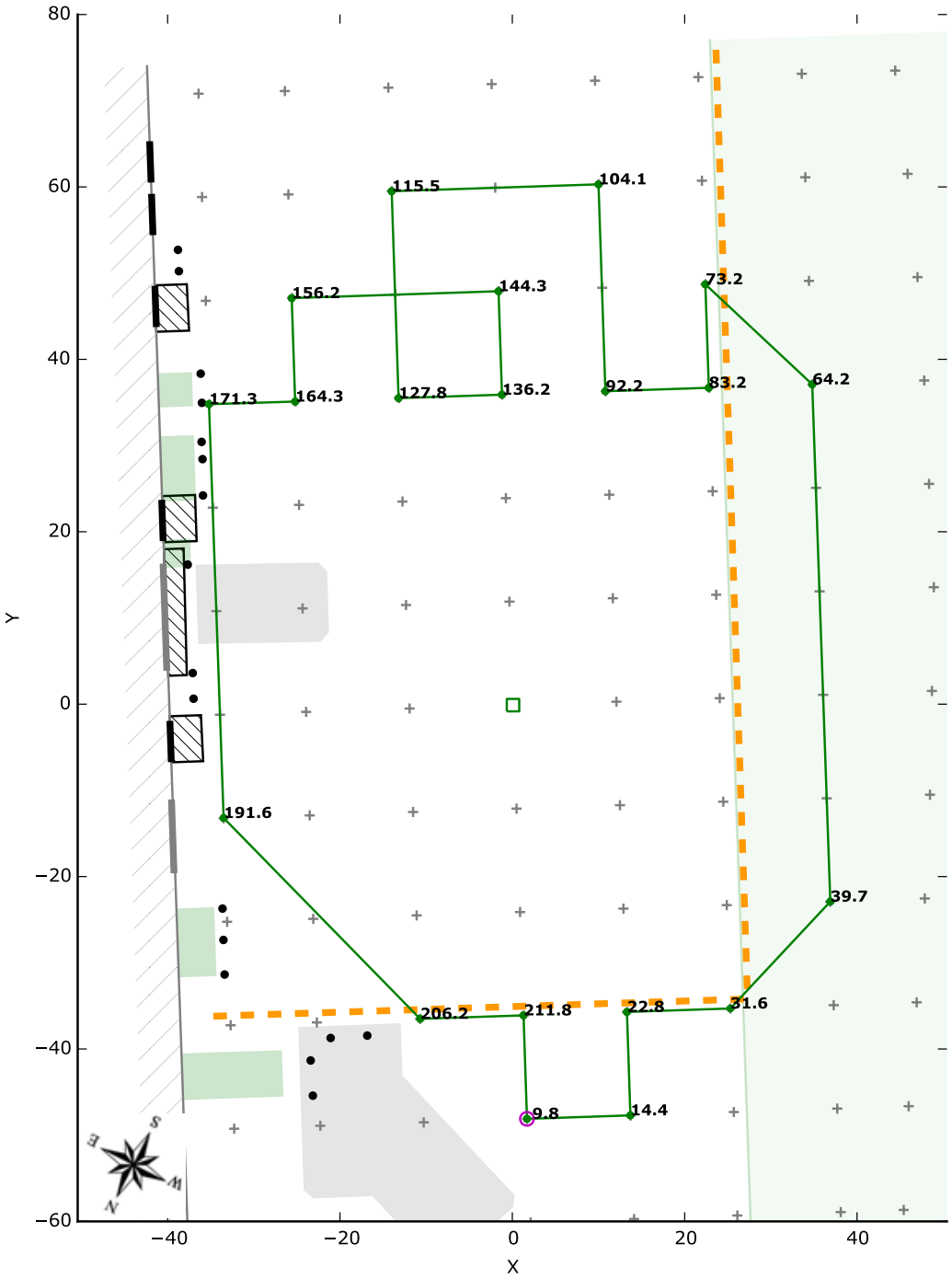

Figure 6.11: The test track. The path walked during the test is shown with the timestamps at each vertex. The starting vertex is indicated with a magenta circle. The figure is shown in the transmitter frame of reference. The survey grid is shown with the gray crosses; as can be seen, the survey grid is not perfectly aligned with the transmitter frame of reference.

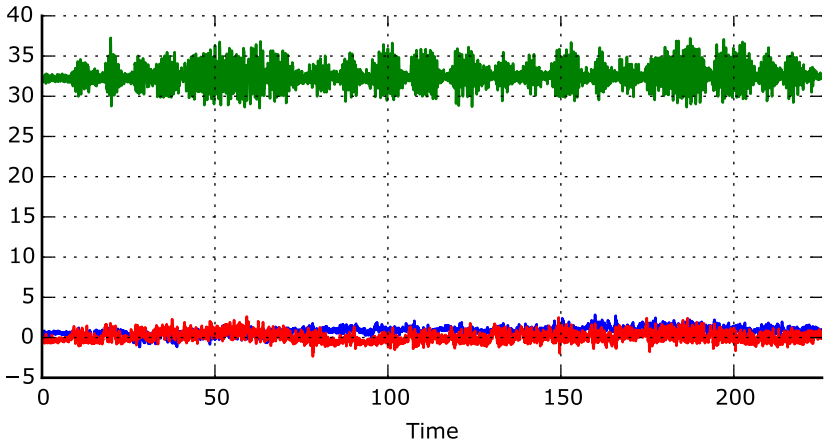

Figure 6.12: Accelerometer measurements. The u-, v-, and w-components are shown in blue, red, and green, respectively, with units of ft/s^2.

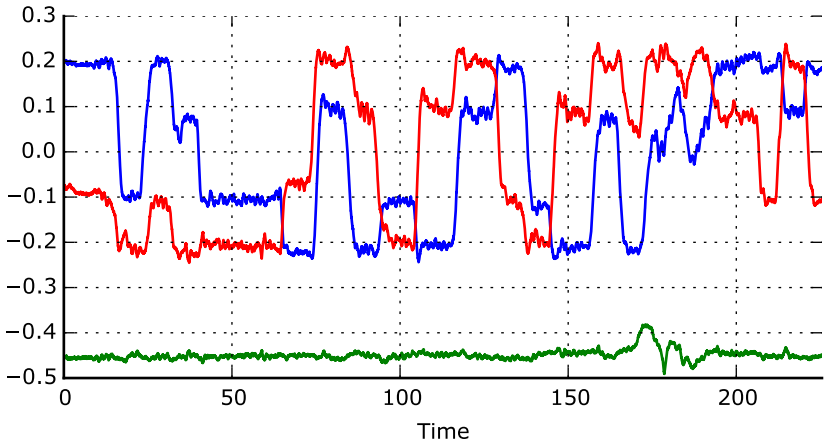

Figure 6.13: Magnetometer measurements. The u-, v-, and w-components are shown in blue, red, and green, respectively, with units of Gauss.

Figure 6.14: Measured fields. The 3×3 field component matrix as measured in the receiver frame.

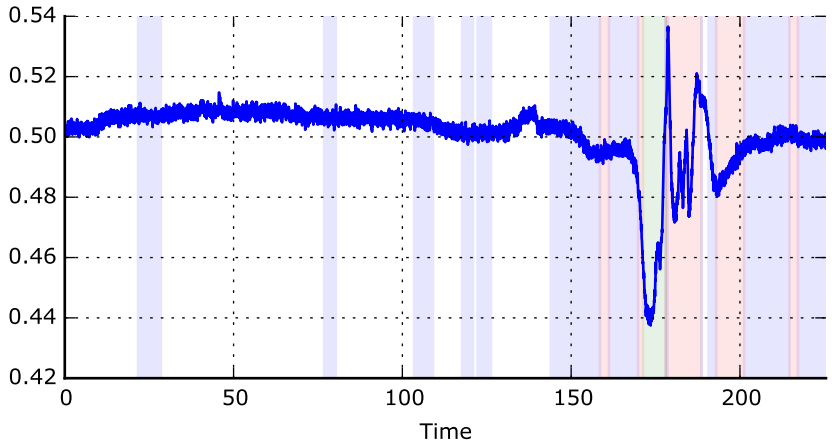

Figure 6.15: Magnetometer distortion metric and magnetometer measurement magnitude. The magnitude of the magnetometer measurements is shown with shading to indicate the levels of distortion as described in Subsection 5.3.6. In increasing order the levels are: no shading, blue, red, and green.

field from $t = 160$ seconds to nearly $t = 200$ seconds. This corresponds to the portion of the test adjacent to the wall of the steel building and within a couple of feet of large steel fixtures such as the HVAC units. For comparison, the magnetometer measurement magnitude is shown again in Figure 6.16. In this case, the plot is zoomed in on the area of large distortion, and the distance to the wall is shown in the second axis. This provides a good illustration of the influence of the steel wall and fixtures upon the magnetometer measurements.

Using the collected measurements, it is constructive to examine the performance of the Kuipers algorithm when applied to the coil measurements for the test path. Figure 6.17 shows the results of this operation. The effect of the distortion can be seen throughout the plot except for the grassy area. Once again, the area near the wall and its fixtures is the worst performing area. The severe errors evident in this plot demonstrate the challenges faced by the navigation system.

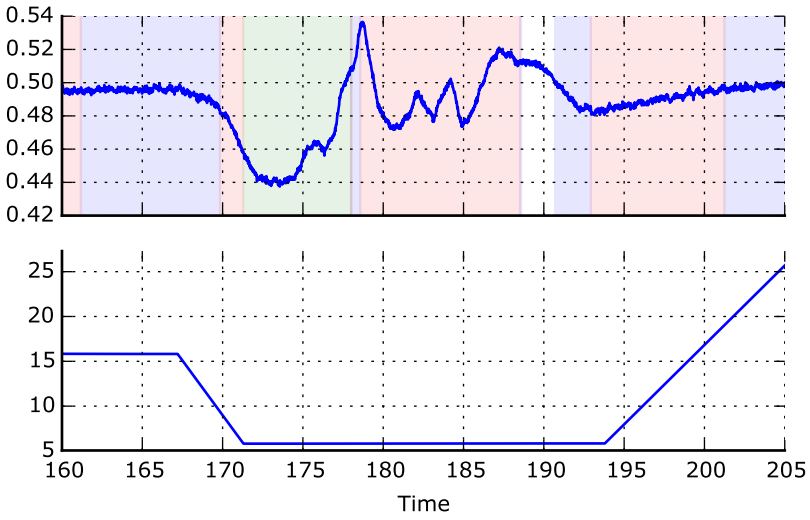

Figure 6.16: Magnetometer measurement magnitude with distance to the wall. A zoomed-in view of the magnitude of the magnetometer measurments is shown in the top axis with the distance to the wall (in feet) on the bottom axis.

6.2.2 Navigation System Output

This section describes the output of the navigation system. The variables to be presented include the magnetic field error matrix ($\mathbf{E}^t$), the geo-magnetic field error ($\boldsymbol{\mu}^g$), the position ($\mathbf{p}^t$), the velocity ($\mathbf{v}^t$), and the receiver rotation matrix ($\underset{r:t}{\mathbf{R}}$). These results show reliable tracking performance and demonstrate a massive improvement over unaided magnetic localization. As such, these results comprise a signficant contribution to the state of the art.

The magnetic field error matrix, $\mathbf{E}^t$, will be presented first. Also, as described before, the range-normalized version of the matrix is used in the implementation (see Subsection 6.1.3). Figure 6.18 shows the field errors. It also shows the observed field matrix difference, $\delta\mathbf{B}^t$, which is described by Equation (5.40). Recall that this quantity is the primary input to the Kalman filter, and it contains more error sources than just $\mathbf{E}^t$. Therefore, the two quantities shown in the figure do not track perfectly well. However, they do confirm the strong influence of $\mathbf{E}^t$ on $\delta\mathbf{B}^t$.

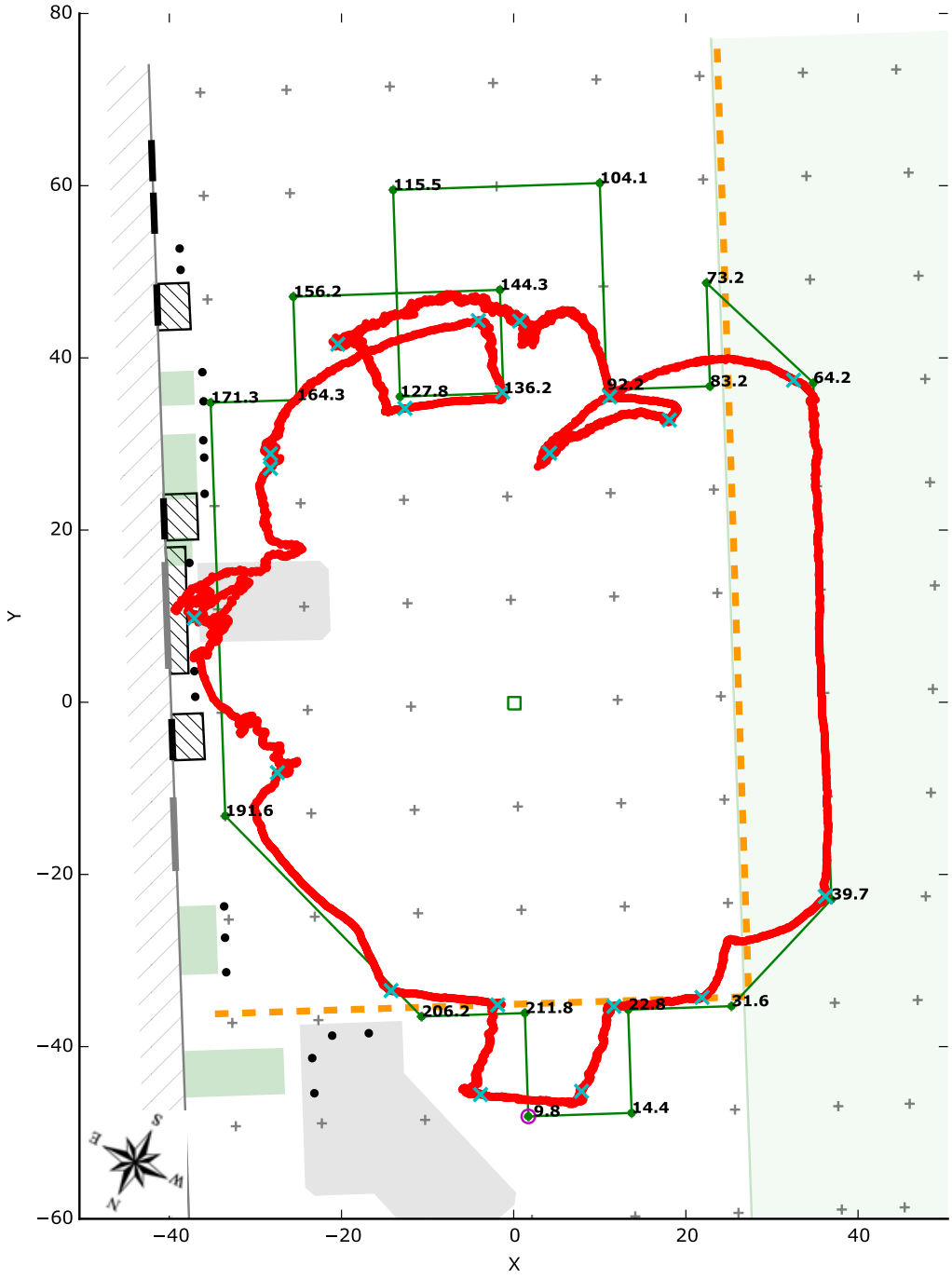

Figure 6.17: The test track with measurements. The Kuipers calculated position while walking the test path is shown in red. The cyan Xs correspond to the vertices of the ideal path.

Figure 6.19 shows $\mathbf{E}^t$ in a different context (green curves). The blue curves are the range-normalized values of $\tilde{\mathbf{B}}^t$ (see Eq. (5.28)). These values are the mechanized observations, and as such, they are uncorrected. The curves in red are the output of the navigation system which includes the corrections. These are calculated using Equation (5.31) (neglecting the measurement noise) as

$$\mathbf{B}^t = \left(\mathbf{I} - \underset{r:t}{\boldsymbol{\Omega}^t}\right) \tilde{\mathbf{B}}^t - \mathbf{E}^t. \tag{6.6}$$

The corrected field components show great agreement with the ideal field components which are calculated from the known receiver location. These two sets of signals are both shown in Figure 6.20.

As described previously, the magnetic field error matrix encapsulates a triad of distortion vectors, one for each type of transmitter modulation. As such, these variables have a physical interpretation: each distortion vector can be thought of as existing in 3-D space. In a similar way, the geo-magnetic error vector, $\boldsymbol{\mu}^g$, can also be thought of as existing in space. The results for this vector are presented next.

Figure 6.21 shows the components of the geo-magnetic field error vector. As expected, the area near the steel building and dumpster are the only areas where the ferromagnetic distortion is significant.

The effectiveness in estimating $\boldsymbol{\mu}^g$ is demonstrated by Figure 6.22. To generate this figure, a mechanized version of the geo-magnetic field vector in the earth frame of reference is obtained via

$$\tilde{\mathbf{m}}^g = \underset{r:g}{\tilde{\mathbf{R}}} \tilde{\mathbf{m}}^r \tag{6.7}$$

$$= \mathbf{m}^g + \delta\mathbf{m}^g, \tag{6.8}$$

where $\delta\mathbf{m}^g$ is expressed by Equation (5.66) and is largely dependent on $\boldsymbol{\mu}^g$. To show the reliability of the $\boldsymbol{\mu}^g$ estimation, the mechanized geo-magnetic field vector is plotted in blue. On top of that, the partially-corrected field vector is shown in red.

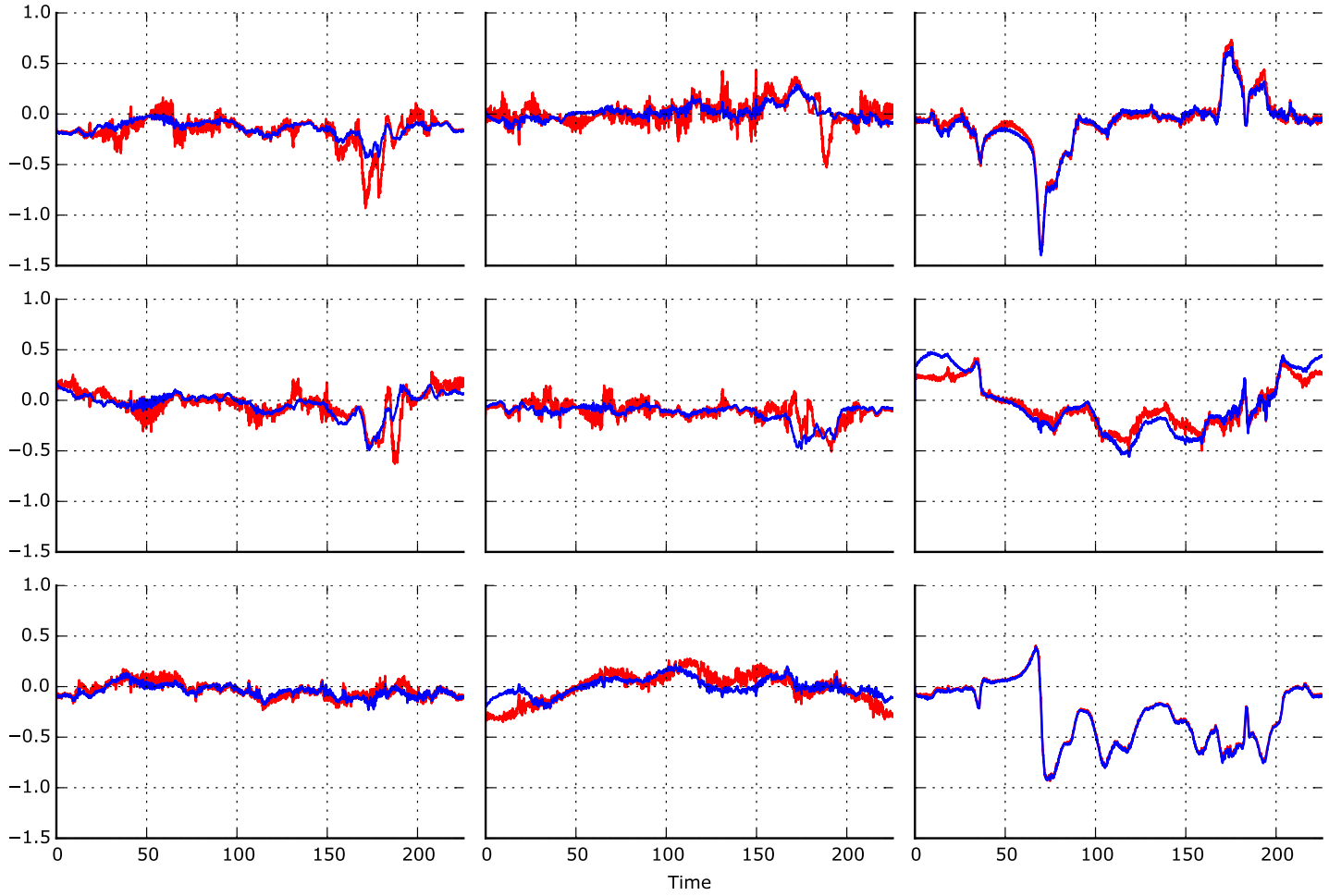

Figure 6.18: Range-normalized field component errors. The blue curves are the field component errors, $\mathbf{E}^t$, which are tracked by the navigation system. The red curves are the difference between the mechanized $\hat{\mathbf{B}}^t$ and the ideal $\mathbf{B}^t$. As such, the red curves include more error sources beyond $\mathbf{E}^t$, but they nevertheless indicate good agreement.

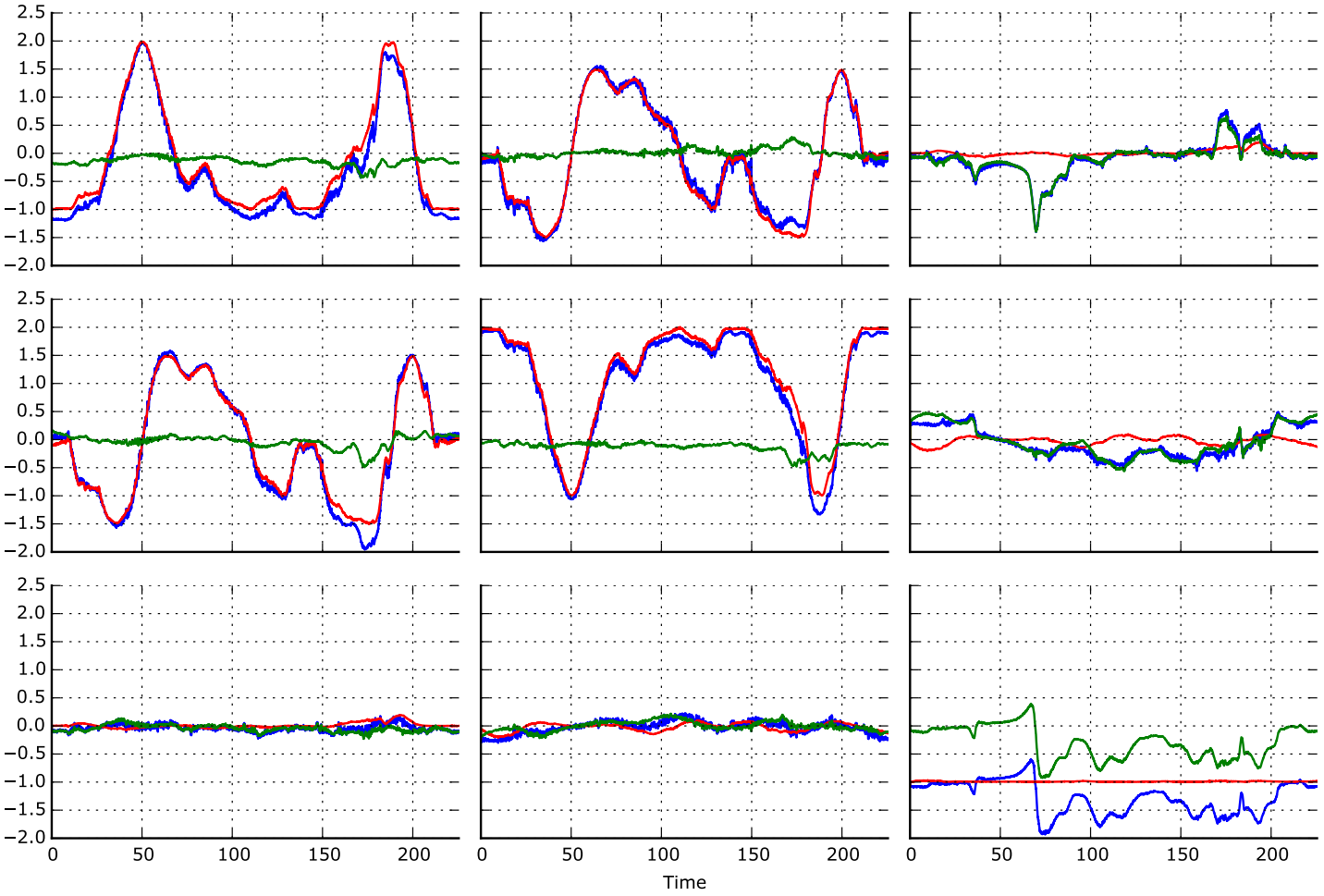

Figure 6.19: Range-normalized field component matrix and errors. This figure shows the field component matrix and the component matrix errors in the transmitter frame of reference. The error, which is tracked by the navigation system, is shown in green. The blue curves are the original field components, and the red curves are the corrected field components.

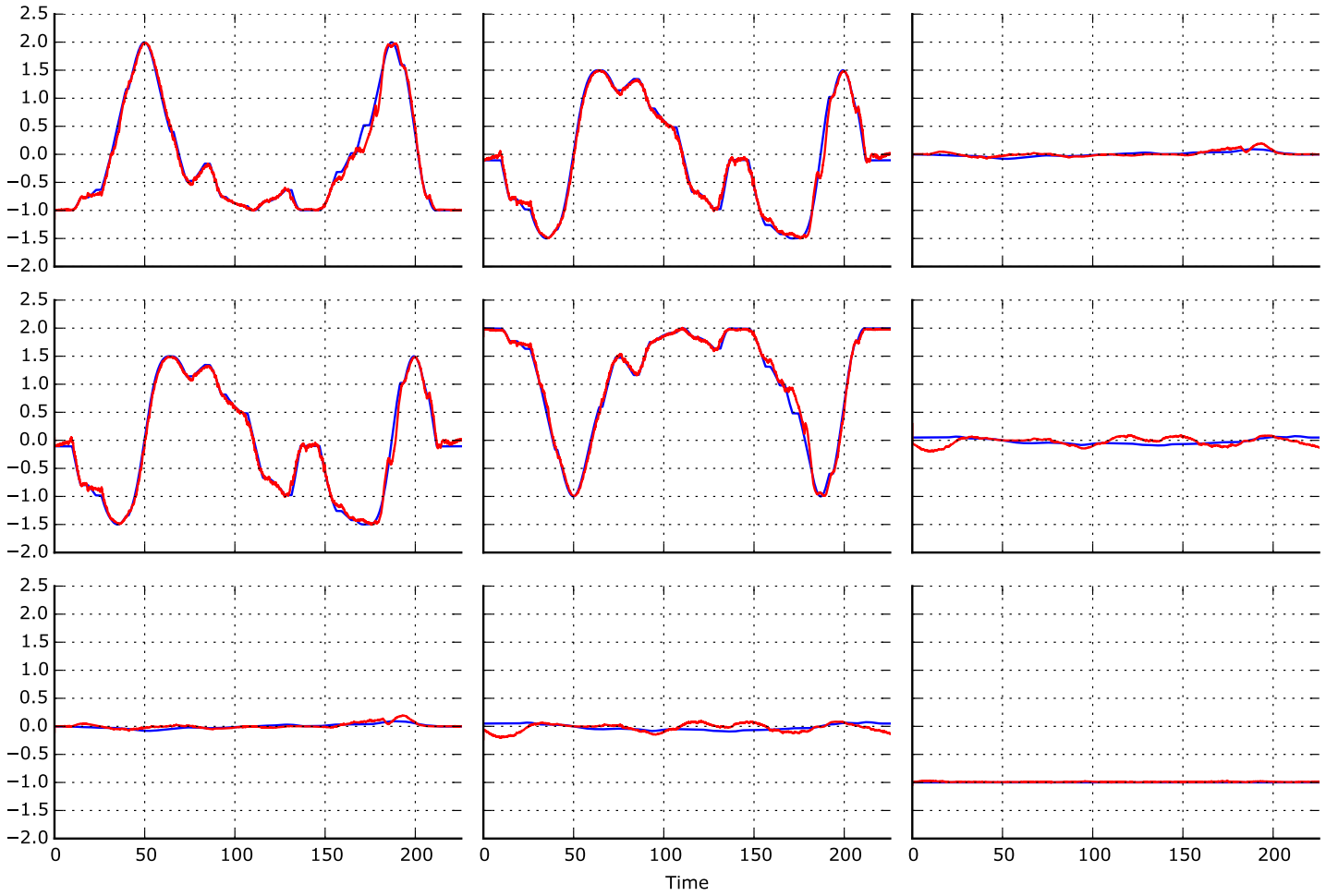

Figure 6.20: Range-normalized field component matrix vs. ideal. This figure shows the field component matrix from the navigation system (red) and the ideal field component matrix (blue).

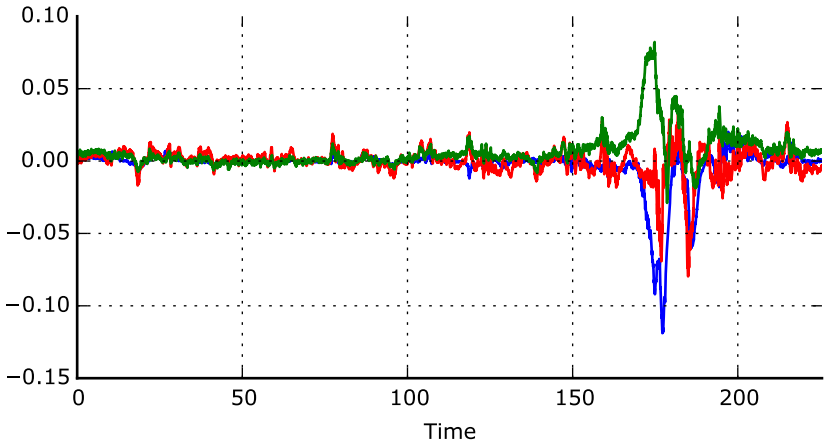

Figure 6.21: Geo-magnetic field error. The geo-magnetic error state variable, $\boldsymbol{\mu}^g$, found by the navigation system. The *east*-, *north*-, and *up*-components are shown in blue, red, and green, respectively.

This partial correction is done by subtracting the geo-magnetic field error vector from the mechanized field vector (i.e. $\tilde{\mathbf{m}}^g - \boldsymbol{\mu}^g$). If the correction were full, the red signals would be zero, but as it is, not all of the terms of Equation (5.66) are addressed by this correction. However, as can be seen, the correction is quite effective at canceling the geo-magnetic distortion. Therefore, it is simple to see that the navigation system reliably tracks the geo-magnetic field error.

The magnetic field error matrix and the geo-magnetic field error are important physical quantities that give great insight into the environment and the performance of the system. However, the position and orientation of the receiver are the physical quantities of paramount importance. These will be addressed next.

The position of the receiver as determined by the navigation system is shown first in Figure 6.23. This figure also shows the corresponding velocity. Each axis of motion is shown in its own column.

In Figure 6.24 the navigation system position results are compared against the Kuipers-generated position and the true position. The top row of plots show the position calculated by each method: The blue is from the navigation system, the

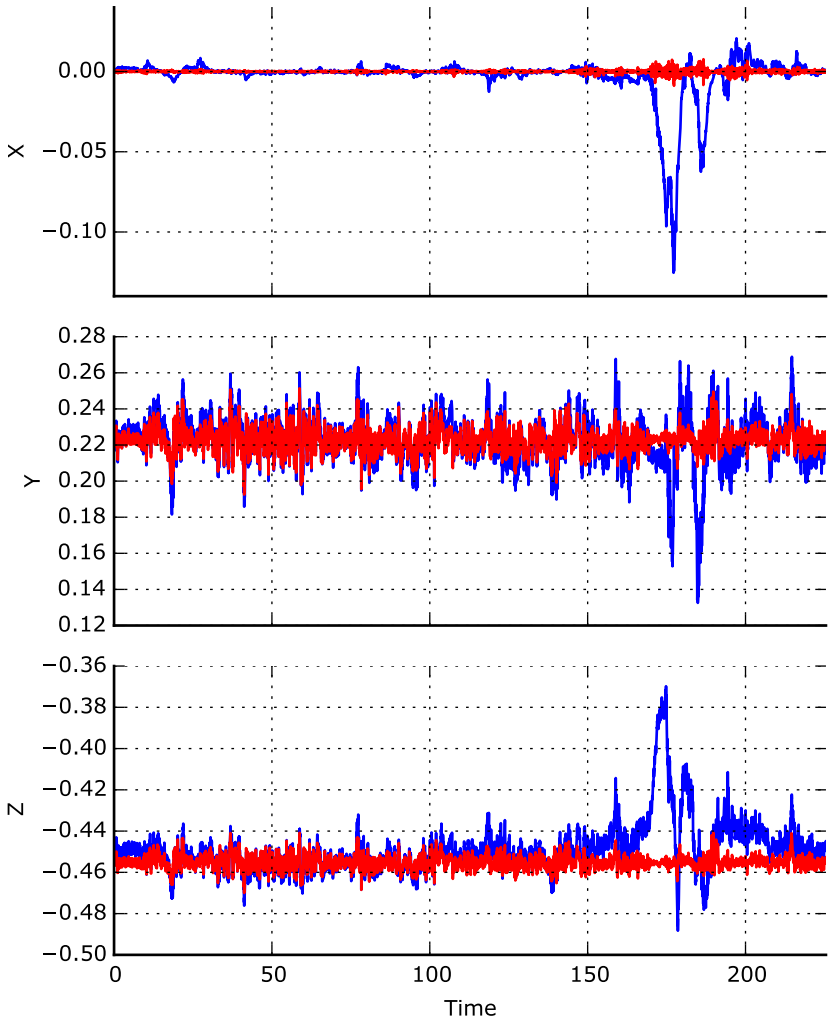

Figure 6.22: Geo-magnetic field correction. This figure shows the mechanized geo-magnetic field before correction (blue) and after correction (red). The correction is applied by subtracting the state variable $\boldsymbol{\mu}^g$ from the mechanized field. The *east*-, *north*-, and *up*-components are shown from top to bottom, respectively.

red is the baseline Kuipers solution, and the green is the true. The second row of plots shows the difference between the navigation solution and the true solution (blue curves). It also shows the difference between the Kuipers solution and the true solution (red curves). Figure 6.25 shows the position data projected onto the horizontal plane.

Both of these figures show the immense improvement of the navigation system over the baseline Kuipers positioning algorithm. The only area of marginal performance is near the steel building where there is extreme bulk and acute eddy distortion as well as ferromagnetic distortion; and even here, the results are acceptable. Overall, the position errors from the navigation system resemble a zero mean random variable. In contrast, the errors from the Kuipers algorithm are deterministically driven by the underlying distortion phenomena. As such, rigorous statistical comparison between the two techniques is not appropriate.

However, the histograms of the position error associated with the two techniques are shown in Figure 6.26. This figure helps demonstrate how the navigation system technique is robust against the systematic errors present in the Kuipers technique. The errors that remain in the navigation system's result resemble a zero-mean (colored) Gaussian noise. They have standard deviations of 1.3, 1.4, and 1.4 feet for the x-, y-, and z-axes, respectively.

The advantage of the navigation system over the Kuipers algorithm is obvious when it came to determining position. Likewise, similar improvements in the receiver orientation are seen with the navigation system. Figure 6.27 shows the Euler angles of the receiver orientation relative to the transmitter frame of reference for both the Kuipers algorithm and the navigation system.

Side-by-side plotting of the Euler angles of two rotation matrices, like in Figure 6.27, is not the best way to make a comparison. Rather, a rotation difference matrix should be constructed. For the Kuipers rotation matrix, a rotation difference matrix

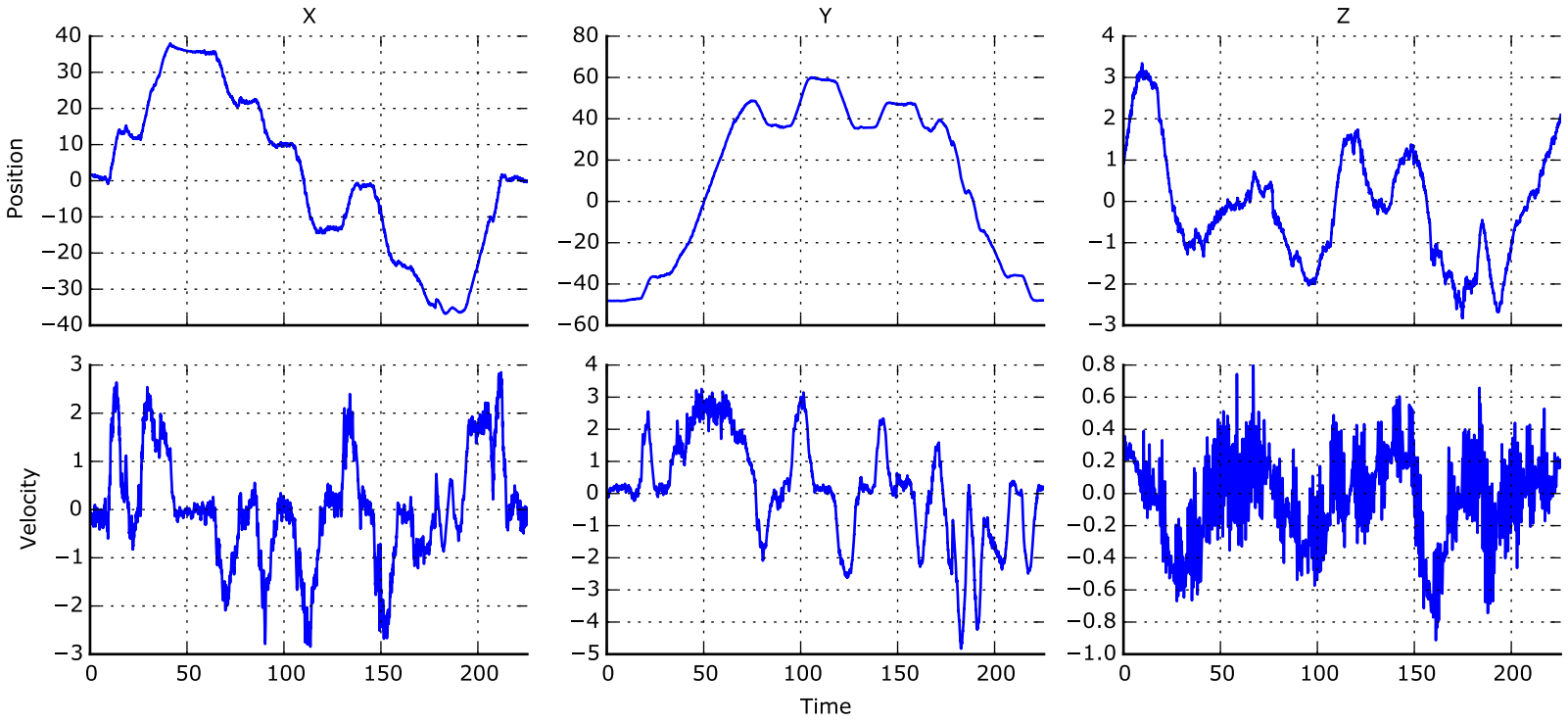

Figure 6.23: Position and velocity. The position calculated by the navigation system is shown in the top row. The corresponding velocity is shown in the bottom row.

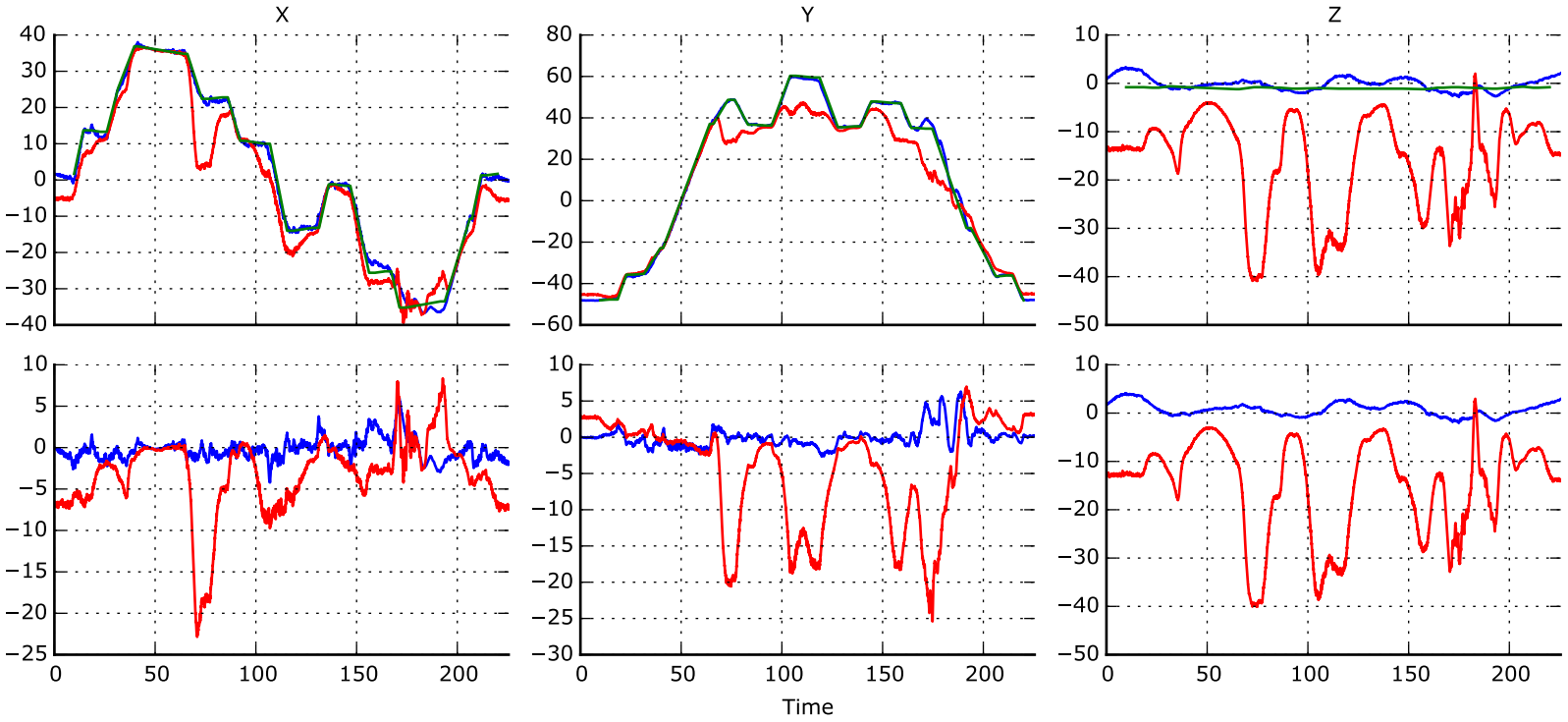

Figure 6.24: Position results and error. In the top row, the Kuipers-calculated position (red) and the navigation system results (blue) are shown alongside the true position (green) for each axis. The bottom row shows the difference from the true value for the Kuipers position (red) and the navigation system output (blue).

is constructed with the navigation system matrix as

$$\underset{t:r}{\delta\mathbf{R}} = \underset{t:r}{\mathbf{R}}\,\underset{t:r}{\mathbf{R}}^{T}. \tag{6.9}$$

Kuipers Nav. Sys.

Figure 6.28 shows the Euler angles of this rotation difference matrix. This is a more appropriate way of viewing the difference between the two rotation matrices.

Unfortunately, with regard to the receiver orientation, there is no way to know the ideal or true rotation. However, in general, the receiver is held horizontal, which means the second two true Euler angles (i.e. elevation and bank angle) are near zero. Also, the first Euler angle represents the heading of the receiver. Therefore, most of the variation is in this Euler angle. Despite not knowing the true Euler angles exactly, some comparisons and conclusions can still be made.

The first conclusion is that the Kuipers angles are wildly incorrect. This is obvious from the previous two figures. The errors are smaller but still large even in the parts of the data which correspond to the clean, grassy area of the test site. In contrast, the navigation system produces angles much more in line with expectations. To help visualize the correctness of the navigation system output, Figure 6.29 shows the receiver's heading vector at each point along the test path.

With regard to the receiver orientation, the solution produced by the navigation system is tremendously improved over the Kuipers algorithm. These results are at least as impressive as the improvements seen with regard to the receiver's position.

6.3 Testing and Results Summary

In the first part of this chapter, the testing setup and testing environment are presented. Of note, Subsection 6.1.3 presents the results of a large-scale, outdoor magnetic survey. This is the first known survey to cover a large, real-world scenario.

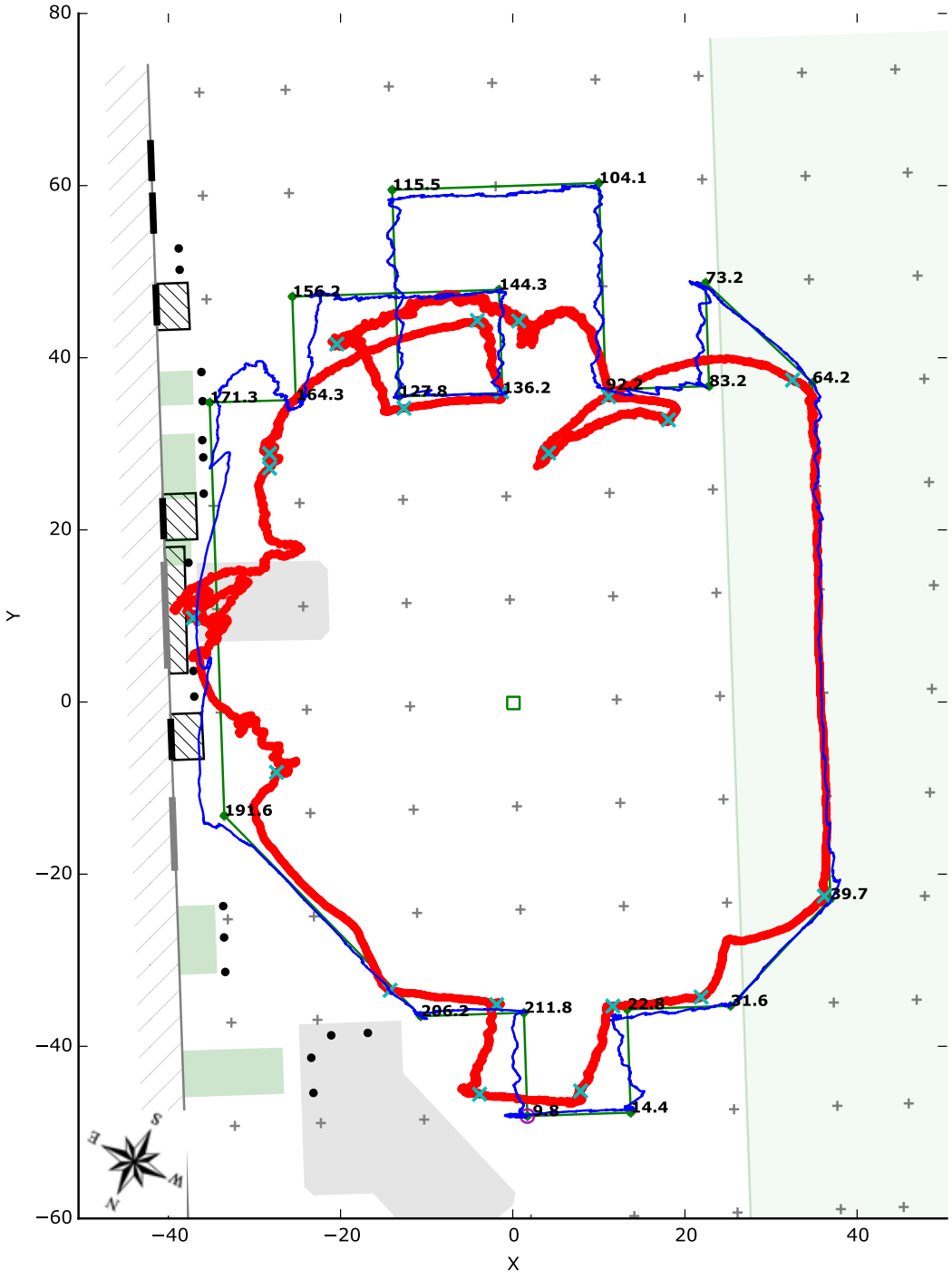

Figure 6.25: Navigation system position. This figure shows the position as output from the navigation system in blue. The red curve is the position from the Kuipers algorithm and the green curve is the actual path. Survey grid spacing is nominally 12 feet.

This real-world data contains some unforeseen phenomena and will prove useful to those seeking to implement magnetic positioning in such a scenario. Such is the case for the navigation system in this project, where the real-world data is invaluable. Therefore, the results from this survey are a significant contribution to the state of the art.

The second part of this chapter presents the results achieved by the navigation system which is developed in Chapter 5. Compared to the conventional algorithm, the results demonstrate a huge performance improvement even though the survey site has bulk eddy errors much higher than expected. The distortion effects in the test site render the Kuipers output almost useless. However, when using the navigation system developed in this research effort, the standard deviation of the position errors are less than 1.5 feet in each axis. Not only that, but the navigation system is able to avoid the massive orientation errors that are present when using the Kuipers algorithm.

With these positive results, the navigation system is deemed to have accomplished all of its goals. As such, it represents a significant contribution to magnetic positioning technology.

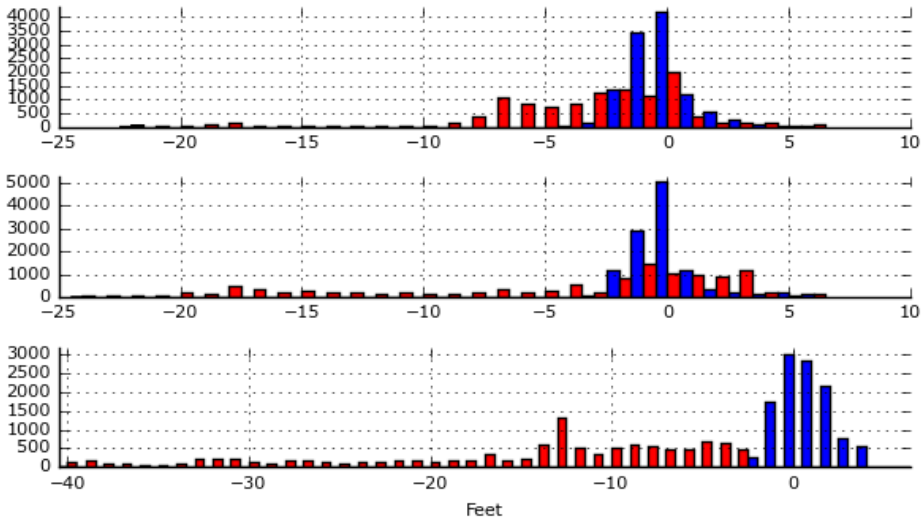

Figure 6.26: Position error histograms. Histograms are shown for each axis of the position with the x-, y-, and z-axes corresponding to the top, middle, and bottom plots, respectively. The red histogram is from the Kuipers positioning algorithm. The blue is from the navigation system. The bin-width is 1 foot.

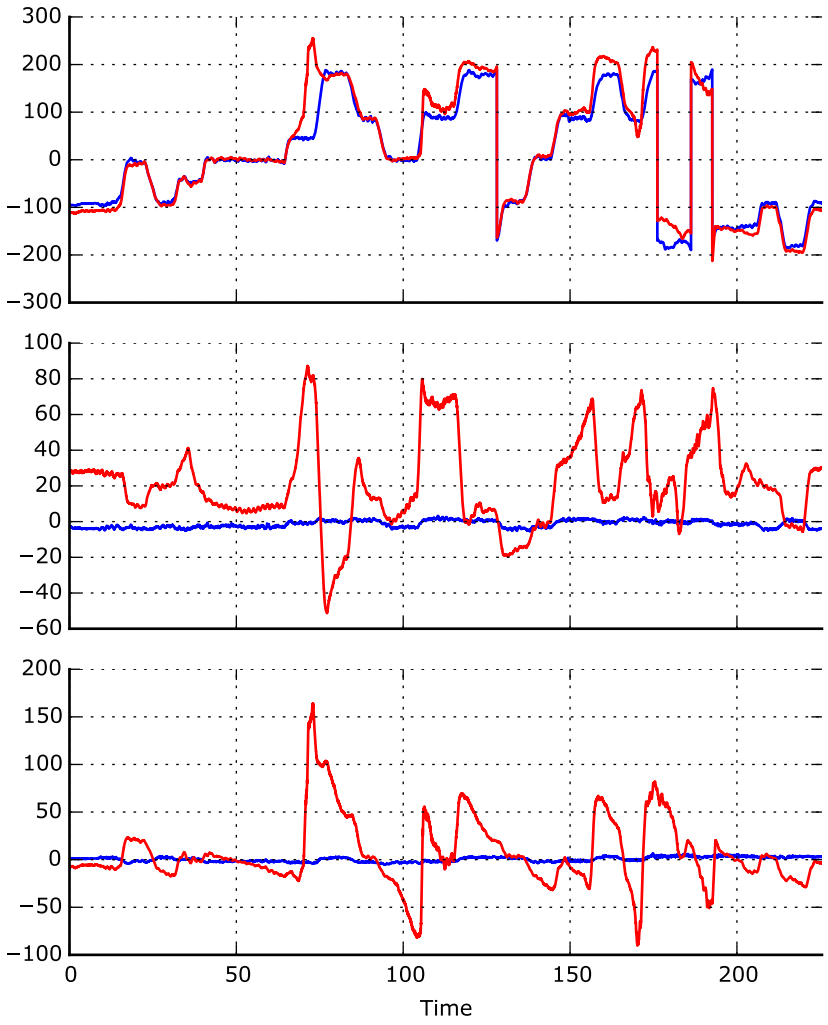

Figure 6.27: Transmitter-to-receiver Euler angles. From top to bottom, the plots show the three Euler angles for the transmitter-to-receiver rotation matrix. The red curves are the angles in degrees as calculated directly from the Kuipers algorithm; the blue curves are the corrected values as determined by the navigation system.

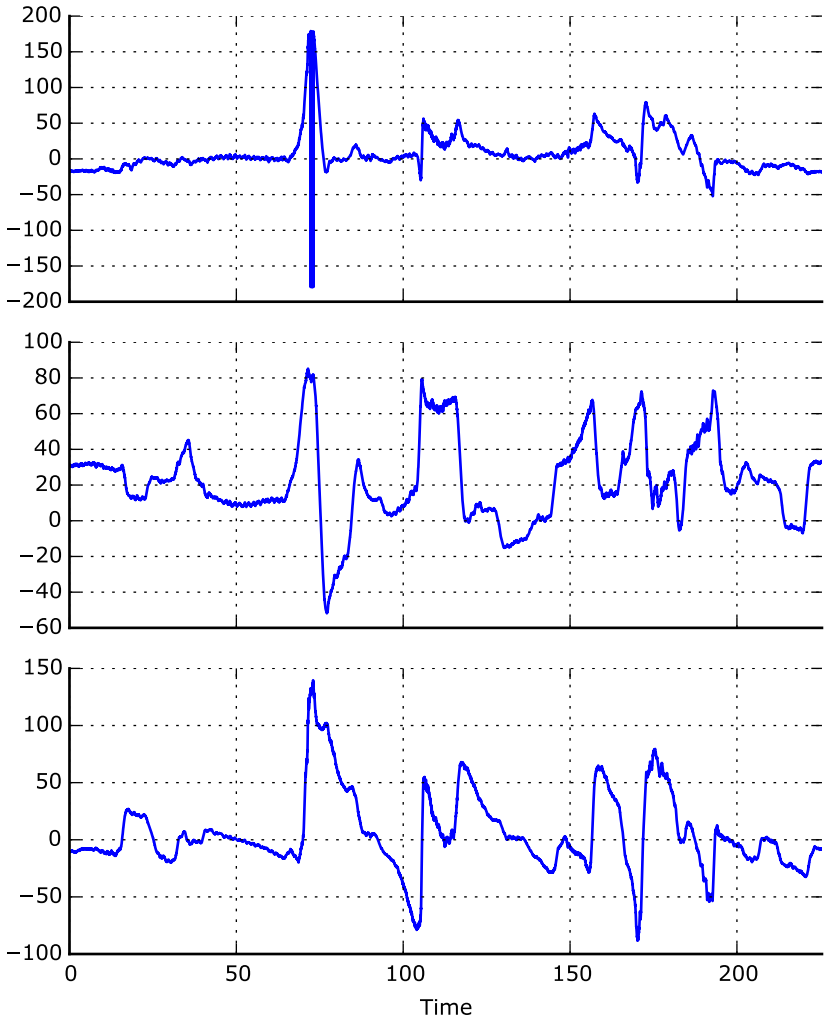

Figure 6.28: Euler angles of the transmitter-to-receiver rotation difference matrix. This plot shows the Euler angles of $\underset{t:r}{\delta\mathbf{R}}$ as calculated by Equation (6.9).

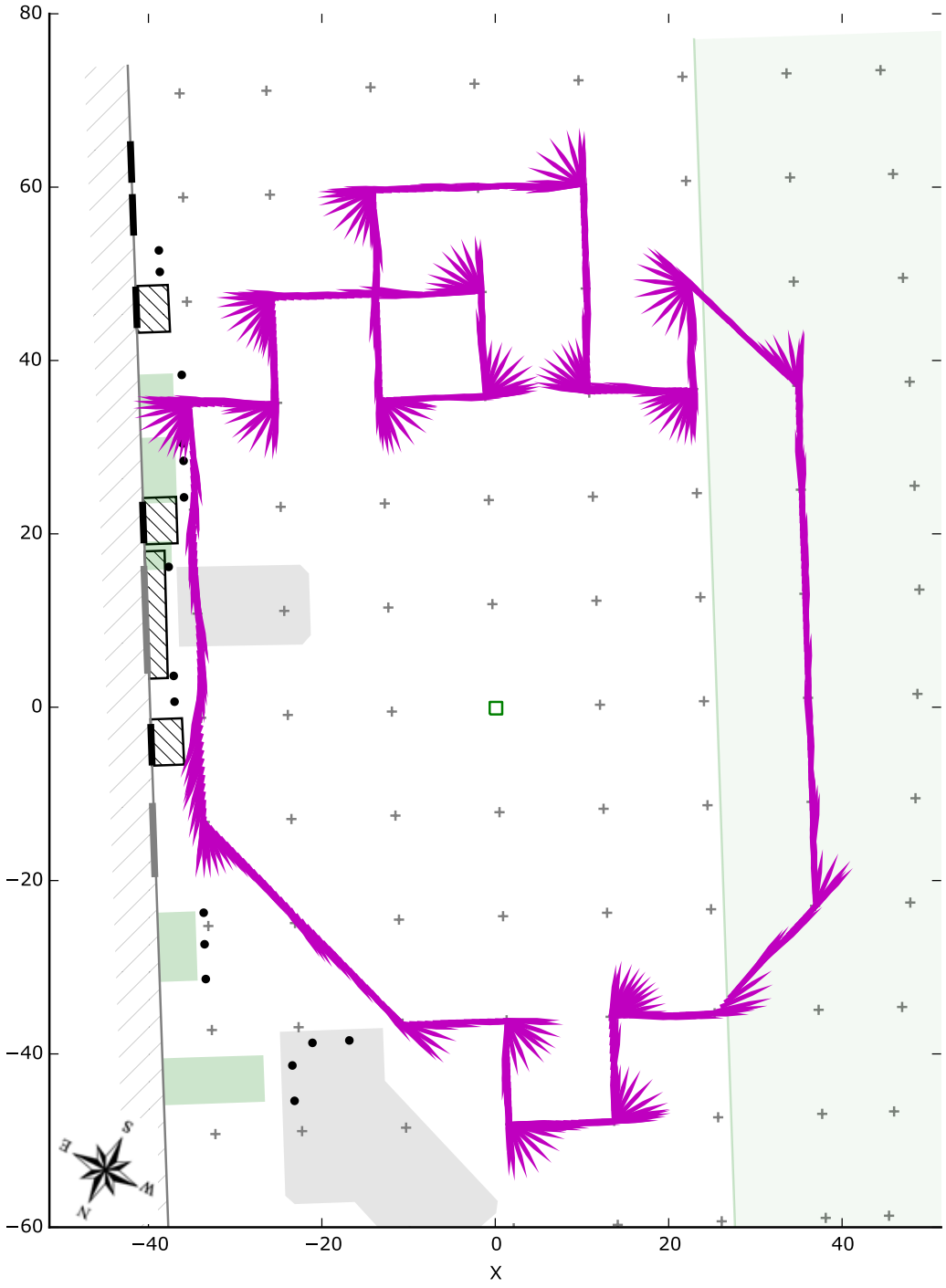

Figure 6.29: Receiver heading vector from the navigation system. The computed heading vector is plotted at each point along the path to give an idea of the correctness of the navigation system's orientation result.

Chapter 7

Conclusion

Magnetic positioning systems have existed for several decades but have never met their full potential due to the problem of environmental distortions. Recently—with the advent of small, cheap, integrated inertial and magnetic sensors—augmented magnetic positioning systems have become a possibility. This research effort sought to develop such a navigation system which integrated a magnetic positioning system with a magnetometer and accelerometer. The goal of the project was to be robust in the presence of environmental distortions.

The project meets its goals, even though the distortion experienced in testing was more extreme than was assumed at the beginning of the project. In the final demonstration, the baseline positioning system produces results that are wildly incorrect and basically worthless. In contrast, when using the integrated navigation system, the errors have a standard deviation of below 1.5 feet in each dimension.

7.1 Original Contributions

For this research effort, there are three main contributions to the state of the art: The integrated magnetic navigation system, the application-domain magnetic field calibration technique, and the large-scale, outdoor magnetic survey. Of these three, the navigation system directly meets the goals of the project. The other two play

a supporting role, but their importance to the advancement of magnetic positioning systems should not be underestimated.

With regard to the application-domain calibration, this technique fills a void in the available literature. With most magnetic positioning systems being commercial in nature, almost no calibration techniques have been reported. Not only that, but the proprietary, commercial techniques are most likely done by interfacing to low-level electronics using expensive measurement equipment. In contrast, the technique discovered in this research uses the demodulated and down-mixed measurements which are available to anyone developing magnetic positioning algorithms. In addition, the technique can be adapted for use in the field without any external equipment. When considering these advantages, the value of this technique is of wider, general appeal than any low-level technique.

The large-scale magnetic site survey is also of general interest and fills a void in the current state of the art. It reveals the types and effects of distortions in a semi-industrial outdoor environment. This data was invaluable in designing this navigation system, and it will also be valuable to others seeking to build similar systems.

In addition to these three main contributions, several minor contributions are also made by this research effort. Among them are the following:

1. A magnetometer calibration technique capable of performing in the presence of rapidly changing gain. This is termed adaptive-volume calibration.

2. Integrated navigation without gyroscopes. Gyroscopes are one of the key components of a conventional integrated navigation system, but they also use potentially much higher power than the other components in an INS. Many authors have sought to eliminate them from their designs (e.g. [86]), but none have done this within magnetic positioning systems.

3. Real-time estimation of the magnetic field component distortions. The magnetic field component error matrix is tracked by the navigation system, and it is due almost entirely to induced distortions.

4. Real-time estimation of geo-magnetic field distortion. The geo-magnetic field error vector is a state variable of the Kalman filter. Therefore, its value is tracked in real time.

7.2 Future Research

The successful completion of this project opens the door to many other avenues of study including:

1. Adapting the calibration techniques to be completed by an end user in the field.

2. Techniques for performing and updating the calibration while the navigation system is in use

3. Building up a fingerprint of the distortions in an entire operational space while the system is in use. Simultaneous localization and mapping (SLAM) techniques are a natural place to begin [87].

4. Using different Kalman models. With the structure of the navigation system in place, there are numerous possible ways to compose the state and measurement vectors. For example, some system states may be ultimately unnecessary, and/or extra states might need to be added to improve performance.

Bibliography

[1] H. Liu, H. Darabi, P. Banerjee, and J. Liu, "Survey of wireless indoor positioning techniques and systems," *Systems, Man, and Cybernetics, Part C: Applications and Reviews, IEEE Transactions on*, vol. 37, no. 6, pp. 1067–1080, Nov 2007. 2

[2] J. Kuipers, "Object tracking and orientation determination means, system and process," US Patent US 3 868 565 A, 02 25, 1975. 2, 24

[3] F. H. Raab, "Remote object position locater," US Patent US 4 054 881, 10 18, 1977. 2, 24

[4] J. B. Kuipers, *Quaternions and Rotation Sequences: A Primer with Applications to Orbits, Aerospace, and Virtual Reality*. Princeton University Press, 1999. 2, 14, 18, 25, 63, 81, 82, 106, 160, 162

[5] R. E. Kalman, "A new approach to linear filtering and prediction problems," in *Transaction of the ASME—Journal of Basic Engineering*, Mar 1960, pp. 35–45. 3, 119

[6] *LSM303DLHC Datasheet*, ST Microelectronics, April 2011. 7, 8, 47, 59, 136, 149

[7] A. Noureldin, T. Karamat, and J. Georgy, *Fundamentals of Inertial Navigation, Satellite-based Positioning and their Integration*. Springer Berlin Heidelberg, 2013. 8, 107, 109

[8] M. D. SHUSTER and S. D. OH, "Three-axis attitude determination from vector observations," *Journal of Guidance, Control, and Dynamics*, vol. 4, no. 1, pp. 70–77, 2015/01/06 1981. 9

[9] D. D. Frantz, A. D. Wiles, S. E. Leis, and S. R. Kirsch, "Accuracy assessment protocols for electromagnetic tracking systems," *Physics in Medicine and Biology*, vol. 48, no. 14, p. 2241, 2003. 15, 64

[10] D. Roetenberg, P. Slycke, and P. Veltink, "Ambulatory position and orientation tracking fusing magnetic and inertial sensing," *Biomedical Engineering, IEEE Transactions on*, vol. 54, no. 5, pp. 883 –890, may 2007. 20, 27, 28, 30, 120, 166

[11] M. Ikits, J. Brederson, C. Hansen, and J. Hollerbach, "An improved calibration framework for electromagnetic tracking devices," in *Virtual Reality, 2001. Proceedings. IEEE*, march 2001, pp. 63 –70. 21, 26, 30, 64

[12] D. Roetenberg, H. Luinge, C. Baten, and P. Veltink, "Compensation of magnetic disturbances improves inertial and magnetic sensing of human body segment orientation," *Neural Systems and Rehabilitation Engineering, IEEE Transactions on*, vol. 13, no. 3, pp. 395 –405, sept. 2005. 24, 27, 28, 30, 93, 120

[13] J. Kuipers, "Tracking and determining orientation of object using coordinate transformation means, system and process," US Patent US 3 983 474, 09 28, 1976. 24

[14] F. H. Raab, "Remote object position and orientation locator," US Patent US 4 346 384, 08 24, 1982. 24, 30

[15] F. Raab, E. Blood, T. Steiner, and H. Jones, "Magnetic position and orientation tracking system," *Aerospace and Electronic Systems, IEEE Transactions on*, vol. AES-15, no. 5, pp. 709 –718, sept. 1979. 24, 30

[16] M. A. Nixon, B. C. McCallum, W. R. Fright, and N. B. Price, "The effects of metals and interfering fields on electromagnetic trackers," *Presence: Teleoper. Virtual Environ.*, vol. 7, no. 2, pp. 204–218, Apr. 1998. 25

[17] V. V. Kindratenko, "A survey of electromagnetic position tracker calibration techniques," in *In Virtual Reality: Research, Development, and Applications*, 2000, pp. 169–182. 26, 30, 64

[18] G. Zachmann, "Distortion correction of magnetic fields for position tracking," in *Computer Graphics International, 1997. Proceedings*, June 1997, pp. 213–220, 251. 26

[19] M. A. Livingston and A. State, "Magnetic tracker calibration for improved augmented reality registration." *Presence: Teleoperators and Virtual Environments*, vol. 6, no. 5, p. 532, October 1997. 26, 64

[20] M. Ghazisaedy, D. Adamczyk, D. Sandin, R. Kenyon, and T. Defanti, "Ultrasonic calibration of a magnetic tracker in a virtual reality space," in *Virtual Reality Annual International Symposium, 1995. Proceedings.*, March 1995, pp. 179–188. 26, 64

[21] E. Prigge and J. How, "An indoor absolute positioning system with no line of sight restrictions and building-wide coverage," in *Robotics and Automation, 2000. Proceedings. ICRA '00. IEEE International Conference on*, vol. 2, April 2000, pp. 1015–1022 vol.2. 26, 30

[22] ——, "Signal architecture for a distributed magnetic local positioning system," *Sensors Journal, IEEE*, vol. 4, no. 6, pp. 864 – 873, dec. 2004. 26, 30

[23] E. A. Prigge, "A positioning system with no line-of-sight restrictions for cluttered environments," Ph.D. dissertation, Stanford University, 2005. 26, 28, 30

[24] D. Roetenberg, P. Slycke, A. Ventevogel, and P. Veltink, "A portable magnetic position and orientation tracker," *Sensors and Actuators A: Physical*, vol. 135, no. 2, pp. 426 – 432, 2007. 27, 28, 30, 120

[25] D. Roetenberg, C. Baten, and P. Veltink, "Estimating body segment orientation by applying inertial and magnetic sensing near ferromagnetic materials," *Neural*

Systems and Rehabilitation Engineering, IEEE Transactions on, vol. 15, no. 3, pp. 469 –471, sept. 2007. 27, 30, 120

[26] C. Hu, S. Song, X. Wang, M.-H. Meng, and B. Li, "A novel positioning and orientation system based on three-axis magnetic coils," *Magnetics, IEEE Transactions on*, vol. 48, no. 7, pp. 2211 –2219, july 2012. 30

[27] J. Dinale and J. Vrbancich, "Fast estimation of coil factor and orthogonality errors in tri-axial magnetic coil systems," *Measurement Science and Technology*, vol. 25, no. 10, p. 105901, 2014. 32, 65

[28] Google maps. [Online]. Available: https://www.google.com/maps/@35.91543, -84.1348,530m/data=!3m1!1e3 34, 154

[29] G. A. Aydemir and A. Saranl, "Characterization and calibration of mems inertial sensors for state and parameter estimation applications," *Measurement*, vol. 45, no. 5, pp. 1210 – 1225, 2012. 40

[30] Z. Xiaoming, C. Guobin, L. Jie, and L. Jun, "Calibration of triaxial mems vector field measurement system," *Science, Measurement Technology, IET*, vol. 8, no. 6, pp. 601–609, 2014. 41, 53

[31] S. Bonnet, C. Bassompierre, C. Godin, S. Lesecq, and A. Barraud, "Calibration methods for inertial and magnetic sensors," *Sensors and Actuators A: Physical*, vol. 156, no. 2, pp. 302 – 311, 2009. 41, 44, 45, 50

[32] T. Pylvänäinen, "Automatic and adaptive calibration of 3d field sensors," *Applied Mathematical Modelling*, vol. 32, no. 4, pp. 575 – 587, 2008. 41, 44, 61

[33] C. Foster and G. Elkaim, "Extension of a two-step calibration methodology to include nonorthogonal sensor axes," *Aerospace and Electronic Systems, IEEE Transactions on*, vol. 44, no. 3, pp. 1070–1078, July 2008. 41, 44, 49, 50

[34] J. Vasconcelos, G. Elkaim, C. Silvestre, P. Oliveira, and B. Cardeira, "Geometric approach to strapdown magnetometer calibration in sensor frame," *Aerospace and Electronic Systems, IEEE Transactions on*, vol. 47, no. 2, pp. 1293–1306, April 2011. 42, 44

[35] G. Strang, *Linear Algebra and Its Applications; 4th Ed.* Belmont, CA: Brooks/Cole, 2006. 42, 45, 79

[36] Q. Li and J. Griffiths, "Least squares ellipsoid specific fitting," in *Geometric Modeling and Processing, 2004. Proceedings*, 2004, pp. 335–340. 44

[37] D. A. Turner, I. Anderson, J. Mason, and M. G. Cox, "An algorithm for fitting an ellipsoid to data," 1999. 44

[38] G. Calafiore, "Approximation of n-dimensional data using spherical and ellipsoidal primitives," *Systems, Man and Cybernetics, Part A: Systems and Humans, IEEE Transactions on*, vol. 32, no. 2, pp. 269–278, Mar 2002. 44

[39] J. M. G. Merayo, P. Brauer, F. Primdahl, J. R. Petersen, and O. V. Nielsen, "Scalar calibration of vector magnetometers," *Measurement Science and Technology*, vol. 11, no. 2, p. 120, 2000. 44, 45

[40] D. Gebre-Egziabher, G. Elkaim, J. David Powell, and B. Parkinson, "Calibration of strapdown magnetometers in magnetic field domain," *Journal of Aerospace Engineering*, vol. 19, no. 2, pp. 87–102, 2015/07/20 2006. 44, 50

[41] M. J. Todd and E. A. Yldrm, "On khachiyan's algorithm for the computation of minimum-volume enclosing ellipsoids," *Discrete Applied Mathematics*, vol. 155, no. 13, pp. 1731 – 1744, 2007. 45

[42] (2015, November) Python. [Online]. Available: https://www.python.org 46, 150

[43] (2015, July) Scipy.org scipy.optimize.leastsq. [Online]. Available: http://docs.scipy.org/doc/scipy-0.15.1/reference/generated/scipy.optimize.leastsq.html 46, 57, 62, 80, 85

[44] J. J. Moré and S. J. Wright, *Optimization Software Guide*, ser. Frontiers in Applied Mathematics. Philadelphia: Society for Industrial and Applied Mathematics, 1993. 46

[45] J. Včelák, P. Ripka, A. Platil, J. Kubík, and P. Kašpar, "Errors of amr compass and methods of their compensation," *Sensors and Actuators A: Physical*, vol. 129, no. 1–2, pp. 53–57, 5 2006. 50

[46] X. Li and Z. Li, "A new calibration method for tri-axial field sensors in strap-down navigation systems," *Measurement Science and Technology*, vol. 23, no. 10, p. 105105, 2012. 53

[47] A. Mizutani, K. Rosser, and J. Chahl, "Semiautomatic calibration and alignment of a low cost, 9 sensor inertial magnetic measurement sensor," *Proc. SPIE*, vol. 7975, pp. 797 517–797 517–8, 2011. 53

[48] Z. Ding, H. Cai, C. Yu, and W. Zhang, "Novel low cost calibration methods for mems inertial/magnetic integrated sensors," in *Guidance, Navigation and Control Conference (CGNCC), 2014 IEEE Chinese*, Aug 2014, pp. 505–511. 53

[49] (2015, June) Magnetic field calculators. [Online]. Available: http://www.ngdc.noaa.gov/geomag-web/ 55, 102

[50] J. L. Crassidis, K.-L. Lai, and R. R. Harman, "Real-time attitude-independent three-axis magnetometer calibration," *Journal of Guidance, Control, and Dynamics*, vol. 28, no. 1, pp. 115–120, 2015/09/01 2005. 61

[51] J. Metge, R. Mégret, A. Giremus, Y. Berthoumieu, and T. Décamps, "Calibration of an inertial-magnetic measurement unit without external

equipment, in the presence of dynamic magnetic disturbances," *Measurement Science and Technology*, vol. 25, no. 12, p. 125106, 2014. 61

[52] V. Kindratenko, "Calibration of electromagnetic tracking devices," *Virtual Reality: Research, Development, and Applications*, vol. 4, no. 2, pp. 139–150, 1999. 64

[53] Z. F. Syed, P. Aggarwal, C. Goodall, X. Niu, and N. El-Sheimy, "A new multi-position calibration method for mems inertial navigation systems," *Measurement Science and Technology*, vol. 18, no. 7, p. 1897, 2007. 64

[54] H. D. Black, "A passive system for determining the attitude of a satellite," *AIAA Journal*, vol. 2, no. 7, pp. 1350–1351, 2015/09/18 1964. 74, 102, 108

[55] (2015, September) Triad method. [Online]. Available: https://en.wikipedia.org/wiki/Triad_method 74, 102, 108

[56] J. Epstein and E. L. Schucking, "Geometry of the su(3) group," *International Journal of Theoretical Physics*, vol. 23, no. 3, pp. 197–216, 1984. 85

[57] S. R. Hedemann, "Hyperspherical Parameterization of Unitary Matrices," *ArXiv e-prints*, Mar. 2013. 85

[58] C. Spengler, M. Huber, and B. C. Hiesmayr, "A composite parameterization of unitary groups, density matrices and subspaces," *Journal of Physics A: Mathematical and Theoretical*, vol. 43, no. 38, p. 385306, 2010. 85

[59] T. Tilma and E. C. G. Sudarshan, "Generalized euler angle parametrization for su (n)," *Journal of Physics A: Mathematical and General*, vol. 35, no. 48, p. 10467, 2002. 85

[60] C. Jarlskog, "A recursive parametrization of unitary matrices." *Journal of Mathematical Physics*, vol. 46, no. 10, p. 103508, 10 2005. 85

[61] C. A. Brannen. (2008, October) Unitary matrix parameterization. [Online]. Available: https://carlbrannen.wordpress.com/2008/10/09/a-new-parameterization-for-3x3-unitary-matrices/ 85

[62] J. G. Proakis, *Digital Communications*, 3rd ed. WCB/McGraw-Hill, 1995. 96

[63] H. Zhao and Z. Wang, "Motion measurement using inertial sensors, ultrasonic sensors, and magnetometers with extended kalman filter for data fusion," *Sensors Journal, IEEE*, vol. 12, no. 5, pp. 943 –953, may 2012. 99

[64] P. D. Groves, *Principles of GNSS, Inertial, and Multisensor Integrated Navigation Systems*. Norwood, MA, USA: Artech House, 2007. 100

[65] F. Liu, J. Li, H. Wang, and C. Liu, "An improved quaternion gauss–newton algorithm for attitude determination using magnetometer and accelerometer," *Chinese Journal of Aeronautics*, vol. 27, no. 4, pp. 986 – 993, 2014. 102

[66] R. G. Brown and P. Y. C. Hwang, *Introduction to Random Signals and Applied Kalman Filtering: With MATLAB Exercises and Solutions; 4th Ed.* New York, NY: Wiley, 2012. 106, 119, 120, 125, 131, 134

[67] Y. Bar-Shalom, T. Kirubarajan, and X.-R. Li, *Estimation with Applications to Tracking and Navigation*. New York, NY, USA: John Wiley & Sons, Inc., 2002. 106, 119, 130, 132, 138, 140, 142, 143

[68] J. F. Wagner and T. Wieneke, "Integrating satellite and inertial navigation—conventional and new fusion approaches," *Control Engineering Practice*, vol. 11, no. 5, pp. 543–550, 5 2003. 107

[69] G. Welch and G. Bishop, "An introduction to the kalman filter," University of North Carolina at Chapel Hill, Tech. Rep., July 2006. 119

[70] R. van der Merwe and E. A. Wan, "Sigma-point kalman filters for integrated navigation," *Proceedings of the 60th Annual Meeting of The Institute of Navigation*, pp. 641–654, June 2004. 120

[71] S. Julier, J. Uhlmann, and H. Durrant-Whyte, "A new approach for filtering nonlinear systems," in *American Control Conference, Proceedings of the 1995*, vol. 3, 1995, pp. 1628–1632 vol.3. 120, 121

[72] R. van der Merwe, "Sigma-point kalman filters for probabilistic inference in dynamic state-space models," Ph.D. dissertation, Oregon Health and Science University, April 2004. 121

[73] (2015, September) Pykalman. [Online]. Available: http://pykalman.github.io 121, 150

[74] C. F. V. Loan, "Computing integrals involving the matrix exponential," in *IEEE Transactions on Automatic Control*, vol. 23, no. 3, June 1978, pp. 395–404. 131

[75] A. A. Clifford, *Multivariate error analysis: a handbook of error propagation and calculation in many-parameter systems.* New York: John Wiley and Sons, 1973. 139, 141

[76] H. H. Ku, "Notes on the use of propagation of error formulas," in *Journal of Research of the National Bureau of Standards. Section C: Engineering and Instrumentation*, vol. 70C, no. 4. National Bureau of Standards, 1966, p. 263. 139, 141

[77] (2015, September) Propagation of uncertainty. [Online]. Available: https://en.wikipedia.org/wiki/Propagation_of_uncertainty 139

[78] (2015, November) Msp430f5438a. [Online]. Available: http://www.ti.com/product/msp430f5438a 149

[79] (2015, November 4) Scipy. [Online]. Available: http://scipy.org 150

[80] (2015, November) Numpy. [Online]. Available: http://www.numpy.org 150

[81] (2015, November) Matplotlib. [Online]. Available: http://matplotlib.org 150

[82] (2015, November) jedit. [Online]. Available: http://jedit.org 150

[83] E. Foxlin, "Inertial head-tracker sensor fusion by a complementary separate-bias kalman filter," in *Virtual Reality Annual International Symposium, 1996., Proceedings of the IEEE 1996*, mar-3 apr 1996, pp. 185 –194, 267. 166

[84] S. Godha and G. Lachapelle, "Foot mounted inertial system for pedestrian navigation," *Measurement Science and Technology*, vol. 19, no. 7, p. 075202, 2008. 166

[85] E. Kraft, "A quaternion-based unscented kalman filter for orientation tracking," in *Information Fusion, 2003. Proceedings of the Sixth International Conference of*, vol. 1, 2003, pp. 47–54. 166

[86] T.-L. Chen, "Design and analysis of a fault-tolerant coplanar gyro-free inertial measurement unit," *Microelectromechanical Systems, Journal of*, vol. 17, no. 1, pp. 201–212, Feb 2008. 190

[87] G. Tuna, K. Gulez, V. Gungor, and T. Veli Mumcu, "Evaluations of different simultaneous localization and mapping (slam) algorithms," in *IECON 2012 - 38th Annual Conference on IEEE Industrial Electronics Society*, Oct 2012, pp. 2693–2698. 191

Vita

Benjamin (Ben) Prothro was born in the coastal town of Mobile, Alabama. After attending high school at a local institution, he stayed in the town of his birth, and in 1998 he earned a Bachelor of Science degree in Electrical Engineering from the University of South Alabama, graduating Summa Cum Laude with the highest GPA in the College of Engineering.

Immediately thereafter, he enrolled at the Georgia Institute of Technology where he earned a Master of Science degree in Electrical and Computer Engineering with a focus on digital signal processing, communications systems, and analog electronics. He finished his degree in only one year with a GPA of 3.82.

After graduating, he began his career in digital signal processing and algorithm development where he worked for about six years before the next phase of his career.

Wishing to add breadth to his technical repertoire, in 2005, he began working on a Doctor of Philosophy degree in analog integrated circuits. This work was under the tutelege of Dr. Benjamin Blalock at the University of Tennessee. During this time, familial responsibilities required him to simultaneously maintain outside employment where he worked in a variety of capacities related to electronic systems development.